WIRELESS AND ELECTROMECHANICAL APPROACHES FOR STRAIN SENSING AND CRACK DETECTION IN FIBER REINFORCED CEMENTITIOUS MATERIALS

by

Tsung-Chin Hou

A dissertation submitted in partial fulfillment
of the requirements for the degree of
Doctor of Philosophy
(Civil and Environmental Engineering)
in The University of Michigan
2008

Doctoral Committee:

Assistant Professor Jerome P. Lynch, Chair
Professor Carlos E. S. Cesnik
Professor Victor C. Li
Associate Professor Gustavo J. Parra-Montesinos

To my mom and my brother for their great support.

Acknowledgements

This thesis is completed with great assistance offered from many people. The first one is my advisor, Prof. Jerome Lynch. His guidance, inspiration and encouragement have trained me to be a successful researcher in academics. Without his support, I would have never gained such a valuable experience and obtain this achievement at the University of Michigan. He is not just my thesis advisor, but more than that, he is one of my best friends that plays an important role in my life. It is my lifelong pleasure of having him as my PhD advisor.

Next, I would like to express my appreciation to my committee members: Prof. Victor Li, Prof. Gustavo Parra-Montesinos and Prof. Carlos Cesnik. They have offered great advice including research ideas, experimental techniques, and data analysis during my study period. They have also broadened my vision by improving my thesis study to have a greater contribution to the field of civil engineering. I should also acknowledge the financial support by National Science Foundation under grant number CMS-0421180 and CMS-0528867.

Next, I would like to thank my officemates: Kenneth Loh, Andrew Swartz, Andy Zimmerman, Junhee Kim and Niki Fanouraki. I appreciate their guidance and support offered during these past years. I am lucky to have been able to work with them and I really enjoyed it. Also, to my best friend and my roommate, Min-Yuan Cheng; I am very glad of spending my master and doctoral study with him. Best friends are lifelong teachers. Also to the many others not mentioned above, I am pleased to have had them participate in my PhD study.

Last but not least, I want to draw my sincere appreciation to my mom, Bo-Li Lai, my late father, Jen-Zr Hou and my brother, Tsung-Min Hou. I would never have attempted my PhD study without their great love and unyielding support. As a family member, I owe them everything.

Table of Contents

List of Figures

List of Tables

Abstract

High performance fiber reinforced cementitious composites (HPFRCC) are novel cement-based construction materials with excellent mechanical behaviors. Among those, high ductility and crack resisting are two of the most important features. As these new materials begin to be introduced into practice, there is a need to monitor the health and performance of structures and structural elements made of them. With current sensing technologies either incapable of accurately measuring cracking or too expensive to install, new sensing paradigms are needed. This thesis explores two novel approaches to sensing strain and cracking in HPFRCC structural elements: wireless sensors and the use of HPFRCC materials as their own sensor platform. First, wireless monitoring systems are explored because they are relatively low-cost and easy to install. An order of magnitude cheaper than conventional tethered sensors, wireless sensors can be installed in high density within a single structure. Illustration of a wireless monitoring system using a large number of wireless sensor nodes is provided using the Grove Street Bridge located in Ypsilanti, Michigan. The computational resources of the wireless sensor are leveraged to locally process response data recorded from an HPFRCC element. Damage index methods previously tailored for HPFRCC structural components are embedded into the wireless sensors for automated damage detection. The utility of locally processing response data at the sensor is validated using a cyclically loaded HPFRCC bridge pier.

While wireless sensors are capable of automated data interrogation, they do not fully quantify cracking in HPFRCC elements. To address this limitation, the inherent electromechanical properties of HPFRCC materials are harnessed. Specifically, HPFRCC materials are piezoresistive; in other words, their bulk resistivities change with strain. This work undertakes detail experimental evaluation of the electromechanical properties of one class of strain-hardening HPFRCC: engineered cementitious composites (ECC). First, the piezoresistive properties of ECC are quantified through two- and four-point probe methods. While strain can be accurately measured in the material's elastic regime, microcracking during strain hardening prevents correlations between resistivity and strain to be accurately made. Electrical impedance tomography (EIT) is proposed to map the spatial distribution of ECC bulk conductivity in two-dimensions using repeated electrical measurements taken at the specimen boundary. Hence, EIT conductivity maps can serve as a tool for measuring strain fields in ECC plate elements as well as for imaging cracking in fine detail. This material-level sensing approach holds tremendous promise for future structural health monitoring applications. The EIT sensing approach can also be applied to any semi-conductive material to map conductivity. The universality of the approach is illustrated using a carbon nanotube composite material as a sensing skin, or appliqué, for structural health monitoring.

Chapter 1

Introduction

1.1 Fiber Reinforced Cementitious Composites

Cementitious materials, including concrete, are one of the most widely used materials for the construction of civil engineering structures. Such materials are composed mainly of cement, aggregate, sand, water and other supplements such as fly ash and silica fume. Concrete in particular is widely used because of its high compressive strength. Due to a lack of tensile strength, steel is commonly included in the design of concrete structures to provide tensile strength, shear capacity and ductility. Steel reinforced concrete (R/C) has been in general use in the United States for more than 100 years and is today governed by a number of standard codes including the ACI Building Code Requirement (*e.g.*, ACI 318-08) (MacGregor and Wight, 2005).

While concrete has been a highly successful material for civil structures, some challenges do exist when constructing and maintaining concrete structures. For example, for structures exposed to high shear demands (*e.g.*, seismically loaded structures), extensive transverse reinforcement is often needed for critical regions of the structure (MacGregor and Wight, 2005). Furthermore, closely spaced transverse reinforcement can also be necessary to properly confine the concrete and to prevent local buckling of longitudinal reinforcement bars. Extensive transverse reinforcement can lead to dense and congested

reinforcement detailing; steel congestion is expensive to construct and can lead to concrete placement problems during casting (Parra-Montesinos, 2005).

Another long-term challenge of concrete structures is that concrete's brittle nature leads to cracks. Regardless of their origin, cracks are a major issue for R/C structures exposed to the environments. Specifically, cracks represent a path of least resistance for moisture and corrosive ionic agents (*e.g.*, ions from de-icing salts) to enter a concrete element. Exposure of buried bare steel reinforcement to moisture and ionic agents can lead to corrosion of the steel reinforcement. Corrosion of reinforcement results in a loss of steel bar cross-section and can cause tensile loading to the concrete in the reinforcement vicinity as iron oxides deposit on the steel surface (Du *et al.*, 2007). Such tensile loading causes more cracks and can result in spalling of the concrete covering the reinforcement. In particular, many existing highway bridge decks in harsh environmental regions of the United States suffer from deck cracking and severe corrosion of buried reinforcement (Hyman, 2005). Newer construction typically adopts epoxy coated steel reinforcement for crack prone bridge decks; the epoxy coating protects the steel reinforcement when cracking exposes it to water and ions.

One solution to these challenges (lack of ductility, corrosion of buried reinforcement, reinforcement congestion) is to consider the use of new materials in the design and construction of civil structures. For example, new cement-based materials that fundamentally address the brittle behavior of ordinary concretes are desired. Towards this end, fiber reinforced cement (FRC) was first investigated in the second half of the twentieth century (Balaguru and Shah, 1992). Short fibers, typically steel or polymeric, were proposed for inclusion in regular cement matrices to offer crack resistance and ductility. While ductility and enhancement of tensile strength was achieved, early FRC materials required relatively high volume fractions of fibers (leading to challenges in achieving homogeneous FRC materials) and achieved ductility through strain softening in tension (Figure 1-1b). By the mid-1990's, a more promising FRC material using a relatively smaller volume fraction of short fiber ($V_f < 2\%$) and attaining ductility through strain hardening was achieved. Termed high-performance fiber reinforced cementitious

composites (HPFRCC), this class of material has excellent tensile behavior (*e.g.*, ultimate tensile strength up to 15 MPa) and extreme tensile ductility up to several hundred times than that of conventional FRC (Figure 1-1c) (Naaman, 1998; Naaman and Reinhardt, 1996). A unique characteristic of the material is its ability to dissipate tensile load energy through the formation of fields of dense micro-cracks (*i.e.*, as defined by crack widths of less than 100 μm) instead of localizing into large cracks common in ordinary concrete structural materials (Li, 2003a). An additional advantage of tight microcracks is that microcracks offer less opportunity for moisture and ions to enter an HPFRCC structural element compared to the large cracks in concrete. This translates into greater corrosion resistance and enhanced long-term durability (Sahmaran and Li, 2008).

1.1.1 High Performance Fiber Reinforced Cementitious Composites

HPFRCC are a special class of FRC that resolves the post-cracking strain softening behavior of tensile loaded FRC elements. Specifically, a small volume fraction, often less than 2%, of short fibers are included in a cement matrix; fibers can be steel, carbon, or polymeric (Li *et al.*, 2002; Naaman, 2003). The key to achieving strain hardening behavior of tensile loaded HPFRCC elements is in the design of the fiber-cement interface. Some fibers, such as Torex, tailor the geometry of the fiber to achieve an interface conducive to strain hardening (Naaman, 1987). Another approach is the chemical modification of the surface of the fiber to achieve a chemical bond between the fiber and cement that achieves strain hardening (Li *et al.*, 2001). This approach is commonly taken for polymeric fibers. Optimization of the fiber-cement interface often entails the use of micro-mechanics and fracture theory to achieve a material in which fibers reinforce the cement matrix and favor arresting the growth of cracks by bridging cracks (Figure 1-2). By arresting cracks at the outset of their formation, tensile strain energy is dissipated by distributed fields of microcracks instead of localizing into a few macro-cracks.

Structural elements such as coupling beams in shear walls (Wight *et al.*, 2006), bridge decks (Kim *et al.*, 2004; Naaman and Chandrangsu, 2004), retaining walls (Kunieda and Rokugo, 2006), and extruded pipes (Stang and Pedersen, 1996) have all been proposed as

potential field applications that could benefit from the use of HPFRCC materials. Today, a number of structures employ HPFRCC materials including the Mihara Bridge (Hokkaido, Japan), the Grove Street Bridge (Ypsilanti, Michigan) (Li *et al.*, 2005) and Roppongi Pacific Tower (Tokyo, Japan). It is expected that more structures will be designed using HPFRCC materials for critical structural elements in the near future. As this new ductile cement-based material begins to be employed in actual structures, opportunities exist for monitoring the crack resistance of HPFRCC structural elements and providing quantitative data that can be used to accurately investigate the resiliency of the material under harsh field conditions. Field loading scenarios are impossible to recreate in the laboratory; hence monitoring HPFRCC structures in the field is necessary to further advance the material for practical uses.

As HPFRCC materials continue to field application as structural elements, monitoring the mechanical behavior of such elements during their operational lifetime is of great interest. For example, accurate measurement of strain fields could be used to estimate how far an HPFRCC structural element has been loaded, and how much residual capacity remains. Tracking the propagation of cracks can also provide engineers with information on where unusual, overly wide cracks are; this is of great concern when engineers consider long-term durability issues such as corrosion and spalling. While strain can be measured and cracking can be assessed in the laboratory, *in situ* monitoring of actual structures employing HPFRCC materials allows engineers to observe the material behavior under the complex loading scenario of an actual structure. Also, long-term observation (on the order of decades) also provides the data necessary to fairly assess the material's durability. Developing non-visual inspection techniques that track the formation of strain fields as well as quantify crack properties when HPFRCC materials are placed in operational structures is the core work of this thesis study. While the sensing methods presented are applicable to any HPFRCC material, this thesis selects just two HPFRCC materials that have found use in actual civil infrastructure construction. First, an HPFRCC material based on the use of Spectra fiber is explored. The second material, Engineered Cementitious Composites (ECC), is based on the use of polyvinyl alcohol (PVA) fibers. Table 1-1 summarizes the components of both HPFRCC materials.

1.2 Health Monitoring Technologies for Civil Structures

Recent structural catastrophes such as the sudden failure of the I35 Mississippi Bridge (Minneapolis, MN) in August 2007 (Figure 1-3) have called public attention to complexities of managing the health and safety of large-scale civil infrastructure systems over their operational lifespans. In the case of the I35 Mississippi Bridge, the bridge had been previously flagged by structural inspectors as "structurally deficient" due to corrosion, poor welding details, inoperable bearings and fatigue cracking in steel elements (MnDOT, 2007). Although the Federal Highway Administration (FHWA) has vigilant inspection measures in place for highway bridges (*i.e.* bi-annual inspection of all highway bridges), bridge failures do occur. With current inspection methods based simply on visual inspection, there is a clear need for sensing technology that can add greater objectivity to existing inspection procedures (Moore *et al.*, 2001).

Structural health monitoring (SHM) is an emerging technology that is designed to automate the process of tracking the health of operational structures. Structural health monitoring systems consist of three parts: sensors, automated damage detection algorithms, and automated health prognosis algorithms. Clearly, sensors are needed to record the response of the structure to its loading. Sensors can also be used to sense the structure's operational environment. Using the data collected by the sensors, algorithms embedded in the system are used to identify the existence, location and severity of damage. If damage is diagnosed, the last component of the SHM system is designed to estimate the margin of safety for the structure and its remaining operational life if damage has been revealed. Currently, structural damage detection and health prognosis algorithms are mostly determined using observed mechanical responses, such as changes of global-scale modal features, component-level loss of structural stiffness and degradation of load-carrying capacity.

The greatest advances in SHM have been found in the sensing technology used to record structural behavior. In particular, powerful new technologies such as micro electromechanical systems (MEMS) are revolutionizing the field with smaller, more accurate and cheaper sensors (Bryzek, 1996). Other advances include fiber optic sensors (Merzbacher *et al.*, 1996), wireless sensors (Lynch and Loh, 2006) and self-sensing materials (Chung, 2003). Similarly, major advances have been made in the realm of damage detection algorithms. For example, the seminal reviews by Doebling *et al.* (1996) and more recently by Sohn *et al.* (2004) provide excellent overviews of the available damage detection algorithms. While sensors and damage detection algorithms continue to mature, the prognosis technologies remain to lag in development. Prognosis remains as one of the major challenges to successfully implementing SHM systems in the commercial domain.

Early work in the SHM field was born out of the field of modal analysis. As a result, early sensors employed for SHM were accelerometers while damage detection algorithms were based on structural modal properties (*e.g.*, modal frequency, modal damping, and mode shapes). Such methods are essentially based on the global response of the system. Therefore, they have been found to lack sufficient sensitivity to small or mild structural damage since small amounts of damage have little impact on the global stiffness of the structure (Doebling *et al.*, 1996). For civil structures, structural redundancy inherent in most structures renders global damage detection methods even less sensitive.

Today, there is an awareness that global damage detection methods are not sufficient for reliable SHM. Damage is by its very nature a local anomaly in a structure. Hence, current research and development efforts are focused on sensor technologies and data interrogation algorithms that explore localized regions of the structure (Sohn *et al.*, 2004). For example, an emerging new approach to SHM is the use of acoustic and ultrasonic stress waves for damage identification (Rose, 2002). Using piezoelectric actuators and sensors mounted to the surface of a structure, elastic stress waves are introduced; propagation of such waves are observed so as to identify damage along the propagation path (Kim and Sohn, 2006; Raghavan, 2007).

As HPFRCC materials begin to be used in the field, SHM technologies that can provide a complete assessment of the health of HPFRCC structural elements are direly needed. As previously mentioned, tracking strain states and crack propagation during the operational lifetime of HPFRCC elements would provide engineers with information necessary to more accurately evaluate a structural element's health, its safety margin, and anticipated future performance. While many response characteristics could be monitored and used to advance understanding of a material, this thesis selects crack assessment as a high priority response characteristic to monitor. Crack assessment is selected because multiple cracking is one of the major features of HPFRCC materials and quantification of cracking can lead to a better understanding of the energy dissipation mechanisms. Also, quantifying cracks can be useful for identifying those cracks that are associated with a reduction in the strength, capacity and durability of the structure (*i.e.* "structural damage"). Crack monitoring can also be a powerful management tool since identification of cracks could alert engineers to locations of potential future corrosion of buried reinforcement bars.

Cracking can result from a variety of factors including externally applied loads, shrinkage, poor construction methods, among many others. When making an assessment of the general state of health of such structures, cracks must be reliably quantified and their significance determined. For example, small cracks affecting only the external aesthetic of the structure should be differentiated from those that reduce its strength, stiffness and long-term durability (ACI, 1998). Detailed visual inspection of the surface of the structure remains a common method for detecting cracks; systematic crack mapping allows inspectors to monitor the progression of cracks and to hypothesize the nature of their origins (Bungey *et al.*, 2006). After suspicious cracks are encountered, nondestructive (*e.g.*, ultrasonic inspection) and partially destructive (*e.g.*, core holes) testing can be carried out by trained inspectors to determine crack features that may fall below the structural surface (ACI, 1998). However, all of these methods require the use of trained personnel to execute, rendering them as tedious, time consuming, and expensive.

Compared to other nondestructive methods, utilization of the electrical properties of cement-based materials for crack detection has garnered less attention from the civil engineering community. Cementitious materials have bulk conductivities that place them in the range of semi-conductors; they can therefore carry electrical currents when needed. Historically, the electrical properties of cement-based materials have been investigated for tracking the formation of microstructural properties during hardening (Han *et al.*, 2005) and to quantify the potential for corrosion of buried steel reinforcement (Lauer, 2004). The electrical properties of cementitious materials can also be used to identify crack and damage of cement-based structural elements (Chung, 2003). A primary focus of this thesis is to harness the full potential of the electrical properties of HPFRCC materials to identify strain states and cracking in HPFRCC structural elements.

1.3 Research Objectives and Scope of Work

This thesis seeks to investigate sensor technologies that can quantify the cracking phenomenon of HPFRCC materials. Current advances in SHM sensor technologies offer many promising and exciting technologies that can be used for monitoring the health of HPFRCC structures. As shown in Figure 1-4, the thesis begins by investigating the use of wireless sensing technology for monitoring HPFRCC structures. Because wireless sensors are an order of magnitude cheaper than traditional wired sensors (Lynch and Loh, 2006), it is conceivable future wireless monitoring systems will be deployed with very high sensor densities (100's of sensors in a structure). With embedded computing ability, damage index algorithms are encoded into the wireless sensors so as to demonstrate how these sensors can autonomously provide real-time health assessment and damage evaluation of HPFRCC structural elements. The objectives of this phase of the study are:

- Illustrate the reliability of wireless sensors when used to record the static and dynamic response of an actual civil structure (*e.g.* a standard highway bridge).
- Demonstrate the ability of using wireless sensors to monitor the response of a single HPFRCC structural element, such as a bridge pier.

- Reveal the advantages of embedding data processing algorithms within a wireless sensing unit for damage detection of an instrumented structural element.

While existing damage detection algorithms provide an estimate of the health of an HPFRCC structural element, they generally do not provide sufficient details pertaining to more local response characteristics such as cracking patterns. In particular, such algorithms can not distinguish between cracks that reduce the capacity of a structural element from those that do not directly represent mechanical degradation but might cause long-term issues such as corrosion. Hence, the core of this thesis is focused on the development of a new sensing approach that uses the intrinsic electromechanical properties of HPFRCC materials. Better understanding of electromechanical properties will be leveraged to develop a self-sensing technique for HPFRCC materials that is capable of imaging, in rich detail, the spatial orientation of cracking. The objectives of this phase of the work can be summarized as follows:

- Characterize the electromechanical properties of HPFRCC materials so that their self-sensing functionality is established.
- Use the self-sensing ability of HPFRCC to track strain in tensile loaded HPFRCC elements.
- Apply electrical impedance tomography (EIT) to develop a multi-dimensional (2D or 3D) map of HPFRCC conductivity.
- Illustrate how spatial interpretations of EIT-derived conductivity maps precisely reveal crack locations and offer a rough estimate of crack widths.

The generality of the EIT formulation allows it to be easily applied to other materials whose electrical properties change with strain. Specifically, EIT is applied to image the mechanical response of carbon nanotube-polymer composites which are similar in concept to HPFRCC. Here, the carbon nanotube is the fiber that mechanically reinforces a polymeric matrix. The objective of this final phase of the study is to:

- Establish carbon nanotube composites as a multifunctional material that can be used for sensing applications.

- Apply carbon nanotubes as a "sensing skin" capable of monitoring damage to skin-coated structural elements.

1.3.1 Thesis Outline

Chapter 2 begins by exploring a sensing technology suited for measuring the behavior of HPFRCC structures at global and component length-scales. Wireless sensors proposed by Wang *et al.* (2005) are used for monitoring large-scale operational civil structures at low-cost. The Grove Street Bridge (Ypsilanti, MI), which contains an ECC link-slab structural element, is instrumented to monitor its response to controlled traffic loading. Modal analysis algorithms are encoded into the wireless sensors for real-time modal identification of the bridge. The computational capabilities of the wireless sensors are further explored for damage detection of instrumented HPFRCC structural elements. Specifically, a bridge pier with non-seismic detailing is constructed from a HPFRCC material using Spectra fibers to provide the desired ductility and shear strength necessary for repeated cyclic seismic loading. The recorded displacement responses are then used as inputs to damage index models embedded in the wireless sensor core. The damage index quantifies the mechanical damage accumulated in the HPFRCC bridge pier using a 0 to 1 scale (with 1 being the total failure of the pier). It is believed that this approach offers a very good estimate of damage degrees in the HPFRCC structural element. However, it only provides a rough summary of the damage situation; damage details such as neither crack locations, nor their dimensions (*e.g.* length, depth and width) are offered by the damage index method.

To more accurately assess strain fields and cracking damage in HPFRCC structural elements, the thesis seeks a new approach at the material-scale. Specifically, correlation between the electrical properties of cementitious materials and mechanical behavior is considered as a novel approach to automated health monitoring of HPFRCC structures. In Chapter 3, the electro-mechanical relationship between the electrical conductivity of HPFRCC materials and strain are quantified so as to establish the materials as a self-sensing material platform. Uncertainties in the electrical measurement due to the nature of external probing (*i.e.* contact impedance) and internal material properties (*i.e.*

polarization) are explored and resolved. Only when these two critical uncertainties are resolved can an accurate linkage between mechanical response and electrical material properties can be made.

Since in theory a measurement for strain can be made wherever the material is, a novel approach to measuring conductivity over spatial areas is introduced in Chapter 4. Termed electrical impedance tomography (EIT), the approach offers very detailed two- and three-dimensional maps of conductivity for structural elements instrumented with electrodes upon their surface. In Chapter 5, the EIT approach is used to reconstruct conductivity maps of HPFRCC plate and beam test specimens offering a direct measurement of strain fields and cracking in them. Comparisons of the strain obtained from EIT maps and external sensors (*e.g.* strain gages) are made. EIT is also rich in identifying conductivity inhomogeneities such as those associated with cracks. Furthermore, cracking severity can also be quantified by calculating the amount of conductivity reduction in the EIT maps.

In the last phase of this study, a new multifunctional composite using carbon nanotube (CNT) and polymeric matrices is proposed as a "sensing skin" for monitoring structural health. The spatial sensing technology is illustrated by using universality of the EIT approach to measure the two-dimensional conductivity of CNT-based sensing skins. In Chapter 6, the sensing skins are applied to the surface of ECC and metallic structural elements to monitor strain, impact damage and corrosion.

Finally, Chapter 7 offers a summary of the sensing approaches proposed in this thesis for HPFRCC structures. Specifically, the novel methods of using a material (and its electromechanical properties) as its own sensor are summarized. The major scientific contributions of the thesis to the field of structural health monitoring are also highlighted. In addition, future research needs and possible new avenues of research pursuit are identified for the SHM and structural engineering fields.

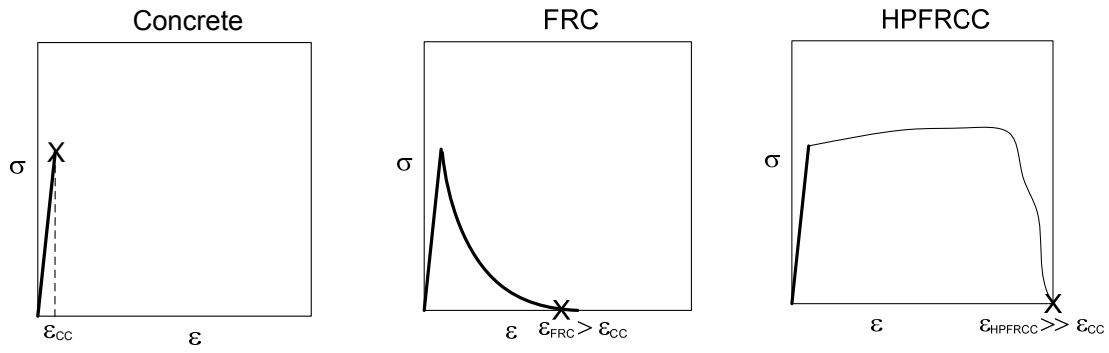

(a) (b) (c)

Figure 1-1: Tensile stress-strain behavior of: (a) ordinary cement; (b) fiber reinforced cements (FRC); (c) high-performance fiber reinforced cementitious composites (HPFRCC).

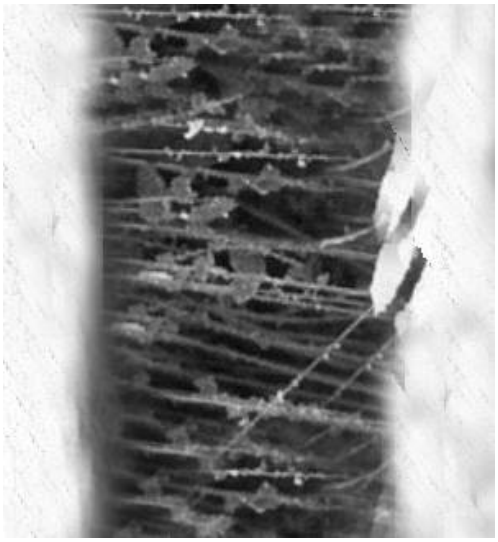

Figure 1-2: Microscopic image of polymeric fibers bridging a crack in ECC, a special HPFRCC material known for its high ductility and damage resilience (source: ACE-MRL).

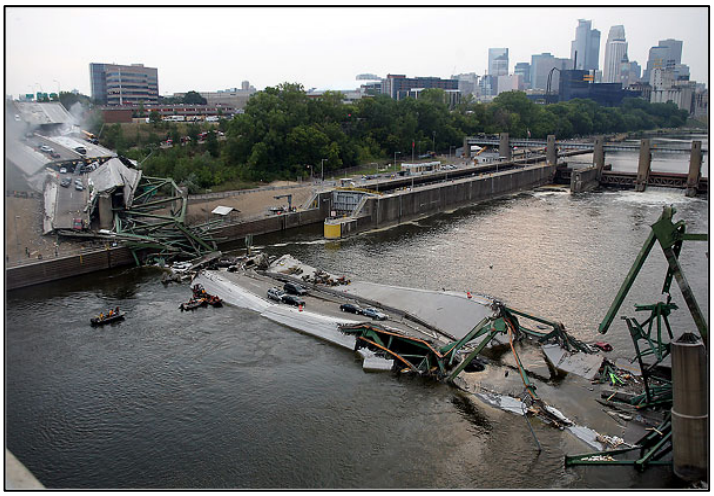

Figure 1-3: Collapse of the I35 Mississippi Bridge, Minneapolis, MN, August 2007 (source: Associated Press).

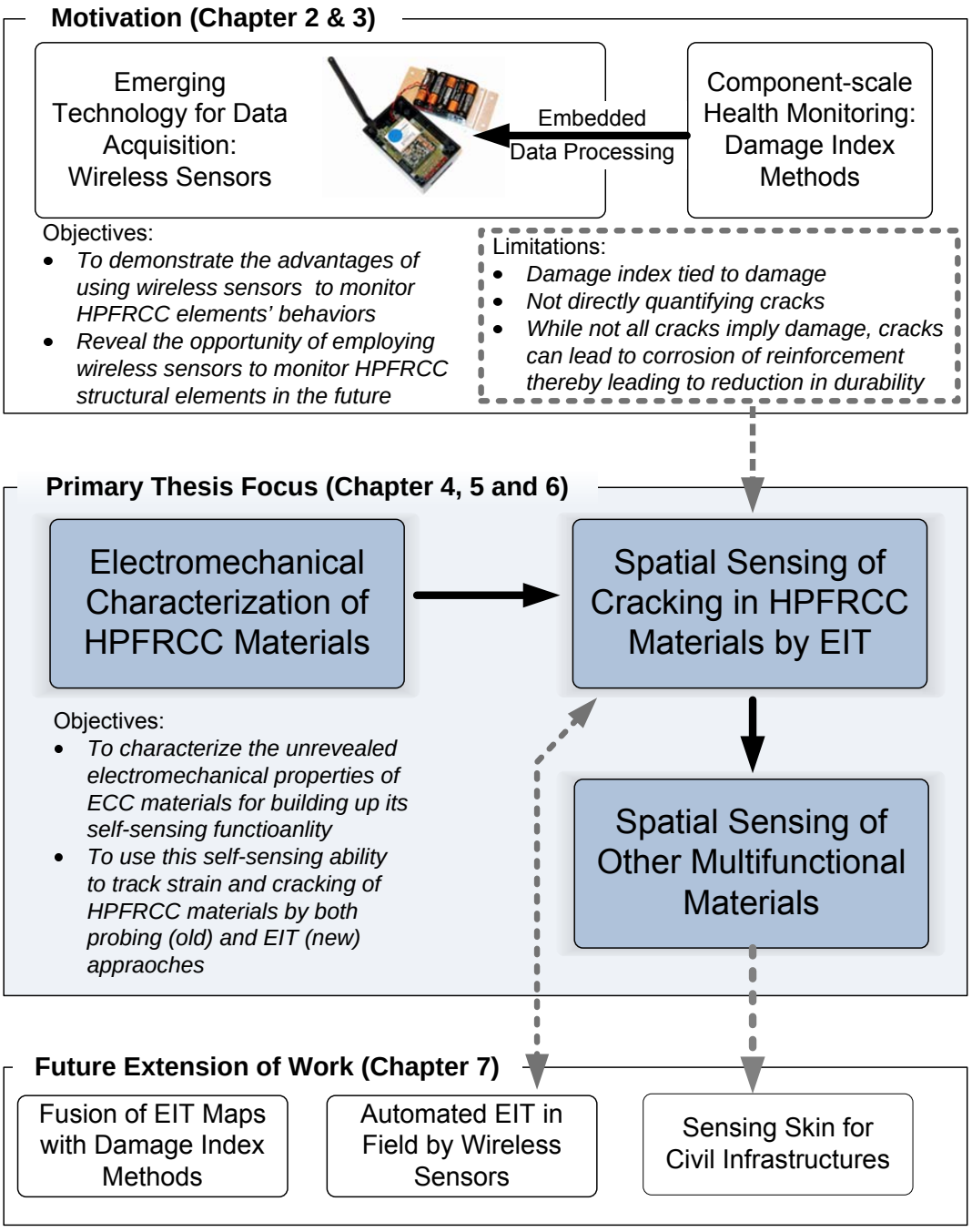

Figure 1-4: Research objectives and overall scope of the thesis work.

Table 1-1: Comparison of two different HPFRCC materials for civil infrastructures

	Spectra HPFRCC	**ECC**
Fiber Type	3.8 cm Spectra	1.2 cm PVA
Fiber Volume Fraction	1.5%	2.0%
Cement Weight Ratio	1.00	1.00
Fly Ash Weight Ratio	0.15	1.20
Sand Weight Ratio	1.00	0.80
Water Weight Ratio	0.50	0.58
Total Weight Ratio	2.65	3.58

Chapter 2

Wireless Sensor Networks for Performance Evaluation of HPFRCC Elements

2.1 Introduction

As HPFRCC materials transition from the laboratory to field applications, it is important that their long-term behavior be recorded. In addition, by monitoring the behavior of HPFRCC elements, damage could be detected, thereby facilitating timely and cost-effective repairs. Sensors permanently installed in HPFRCC elements can provide the data necessary to evaluate behavior and identify the onset of damage. In this chapter, emerging sensor technologies, such as wireless sensors, are explored as possible candidates for monitoring the behavior and health of HPFRCC structural elements.

Structural health monitoring has been proposed by the structural engineering community to assist owners by monitoring their structures for signs of deterioration. The monitoring system is responsible for the reliable collection of data pertaining to the structural response and environment (*e.g.*, temperature) using sensors installed in and around the structure of interest. Once data is collected by the monitoring system, damage detection algorithms can automate the task of interrogating the data for signs of structural distress and deterioration. Today, the majority of structural monitoring systems offered by the commercial sector are tethered (*i.e.* use wires). Extensive lengths of coaxial wire are installed in the structure to provide a direct communication link between sensors and a

centralized data repository. Unfortunately, the installation and maintenance of wires in complex civil structures can be expensive; published data suggest the cost of structural monitoring systems can be in excess of a few thousand dollars per sensor channel (Celebi, 2002). Often times, this cost is beyond the reach of facility owners with limited budgets. Hence, for structural monitoring to be more broadly adopted, the cost of the monitoring system must be reduced. Furthermore, high cost also drives the adoption of low sensor densities in a large civil structure. A handful of sensors in a multi-story building or a long-span bridge are often insufficient to effectively monitor such a complex engineered system, especially if the identification of damage is sought.

Wireless sensors have the potential to radically change how future structural health monitoring systems are deployed in operational civil structures. Initial interest in wireless sensors was prompted by the use of wireless communication for data transfer in the monitoring system. Clearly, the elimination of extensive lengths of wire give wireless monitoring systems the advantage of easier installations and substantially reduced costs (Lynch and Loh, 2006). While initial excitement was prompted by the clear cost advantage of wireless communication, the real paradigm shift associated with wireless sensors is the embedded computing available in most platforms. Specifically, microcontrollers included in the hardware design of wireless sensors can be utilized to perform local data processing at the sensor itself. This computing feature is what sets wireless sensors apart from traditional sensors interfaced to a cable-based monitoring system where computing power is concentrated to the centralized data repository.

This chapter explores the use of an academic wireless sensor prototype for structural health monitoring of HPFRCC structures and structural elements. In the first part of the chapter, the low-cost wireless sensor proposed by Wang *et al.* (2007) is described. Next, the platform is taken to the field to monitor the response of a highway bridge employing an ECC link slab in its design. The wireless monitoring system is shown capable of reliably recording the global and component response of the bridge to a prescribed set of loads. With the accuracy and reliability of the wireless monitoring system established, the chapter turns its focus to the embedded computing available at the wireless sensor.

For the instrumented highway bridge, embedded modal analysis algorithms are illustrated. Using ambient vibration input, the embedded algorithms determine the bridge mode shapes from which the "soft-joint" behavior of an ECC link slab can be evaluated.

With the wireless monitoring system established as a reliable sensing tool, the thesis then explores an algorithmic approach well suited for tracking damage in HPFRCC elements. A damage detection algorithm based on a damage index method proposed by Kratzig *et al.*, (1989) is adopted to assess the flexural and shear damage of an HPFRCC bridge pier under prescribed cyclic loading. Using the embedded damage index method, the wireless sensor demonstrates its ability to serve as a novel sensing system for health monitoring of HPFRCC structural elements utilized in seismic regions.

The goals of the chapter can be summarized as follows:

- Introduce wireless sensors as a low-cost and reliable sensor technology for monitoring large-scale infrastructure systems.
- Validate the performance of wireless sensors in monitoring the behavior of HPFRCC elements in operational structures.
- Showcase the sensor-side computing ability of wireless sensors when damage detection algorithms are embedded.

2.2 Wireless Sensors for Structural Monitoring

Many researchers have explored the use of wireless sensors within structural monitoring and structural health monitoring systems. For example, Straser and Kiremidjian (1998) are early proponents for the adoption of low-cost wireless sensors in structural monitoring systems. Since their seminal study, a wide range of academic wireless sensor prototypes have been proposed by Lynch (2002), Casciati *et al.* (2003), Shinozuka (2003), among others. In addition to these efforts, other researchers have explored the application of generic wireless sensor solutions offered by the commercial sector to civil structures. A particularly popular wireless sensor platform, termed the "Mote" system,

was developed at UC-Berkeley and commercialized by companies such as Crossbow and Intel. Researchers such as Ruiz-Sandoval *et al.* (2003), Clayton *et al.* (2005), Nagayama *et al.* (2007), and Pakzad *et al.* (2008) have applied Crossbow MICA Mote wireless sensors to monitor lab and field structures (for example, Pakzad *et al.* (2008) deployed over 40 Crossbow Motes to the Golden Gate Bridge for ambient vibration measurement of the bridge deck).

In this study, an academic wireless sensor designed explicitly for structural monitoring of civil structures is adopted. Because the wireless sensor is low-cost, it would allow a structure's owner the opportunity to include a large number of sensors in a single structure at a relatively low-cost. This high density could be advantageous for structures employing HPFRCC structural elements since it would allow the monitoring system to monitor the global behavior of the structure in addition to the behavior of select structural elements (*e.g.* HPFRCC elements). The wireless sensor prototype was first proposed by Wang *et al.* (2007). Designed explicitly for structural monitoring applications, the wireless sensor employs commercial off-the-shelf electrical components, including an 8-bit low-power microcontroller, 16-bit multi-channel analog-to-digital converter, and long-range wireless transceiver. When fully assembled (as shown in Figure 2-1), the wireless sensing unit is both low-cost (less than $200 per unit) and compact (10 by 6 by 2 cm^3). The wireless sensor offers end-users a transparent 4-channel sensing interface to which any type of analog sensor can be attached; to date, accelerometers, strain gages, linear displacement transducers and geophones have all been successfully used. Once data is collected by the internal 16-bit analog-to-digital converter (ADC), the digitized data can be stored by the microcontroller (Atmel ATmega128) in the wireless sensor's 128 kB static random access memory (SRAM) bank. The role of the ATmega128 microcontroller is twofold: first, software embedded in the microcontroller is needed to coordinate the activities of the wireless sensor. Second, the computing authority offered by the microcontroller can be used for self-interrogation of structural response data. The final element of the wireless sensor design is the inclusion of the long-range 2.4 GHz Maxstream XStream wireless radio. This radio is capable of line-of-sight communication ranges of 180 m when operated indoors; when used outdoors, this range is in excess of

5000 m. Fully assembled, the wireless sensor is powered by 5 AA batteries that are estimated to have a life expectancy of over 1 year when use of the wireless sensor is duty cycled (Wang *et al.*, 2007). The performance attributes of the wireless sensor are summarized in Table 2-1.

2.3 Validation of Wireless Sensors on the Grove Street Bridge

The first step to transitioning the aforementioned wireless sensor to industrial use is to validate its performance on a full-scale operational civil structure. For this purpose, a highway bridge is selected for monitoring by a network of wireless sensors installed in the bridge. The highway bridge selected was the Grove Street Bridge located in Ypsilanti, Michigan; in 2005, the bridge was under reconstruction offering opportunities to monitor the bridge during controlled truck loading and ordinary traffic. A key feature of the bridge is that an ECC link slab element is installed during reconstruction. Hence, the Grove Street Bridge also offers an opportunity to also validate the ability of wireless sensors to monitor the performance of the ECC link slab under controlled loading.

2.3.1 Grove Street Bridge

The Grove Street Bridge, shown in Figure 2-2a, is located in Ypsilanti, Michigan and carries two opposing lanes of traffic over Interstate 94. The two-lane highway bridge, designed in the late-1960's, is primarily a steel girder-concrete deck composite structure with a 42° skew angle. The 23 cm. concrete bridge deck is supported by 10 built-up steel girder sections to which shear studs are welded on the top flange surface. The bridge is designed to carry traffic using 4 independent spans. The north and south spans (denoted herein as Spans 1 & 4) are designed as cantilever bridge spans. Each cantilever span is 20.1 m long with one end supported by a bridge abutment and at the other by a pier situated 2.4 m from the span edge. The two inner spans (denoted herein as Spans 2 & 3) are each supported at one end by the north and south cantilever spans using pinned link plates as shown in Figure 2-2b. The opposite ends of Spans 2 & 3 share a concrete pier at the bridge center.

Prior to 2005, the bridge deck was separated into 4 independent slab sections. For example, Spans 1, 2, 3 and 4 had their own deck slabs that were discontinuous between adjacent slabs. Between adjacent spans were traditional expansion joints that allowed for thermal expansion and contraction of the deck during the winter and summer seasons. However, over time the expansion joints failed resulting in serious deterioration of the bridge deck including severe cracking and subsequent corrosion of buried steel reinforcement and the steel girders supporting the deck. In 2005, the custodian of the bridge, the Michigan Department of Transportation (MDOT), decided to reconstruct the bridge deck and to repair the corroded bridge girders.

During the design of the renovated Grove Street Bridge, MDOT decided to remedy the recurrent problem of poorly maintained expansion joints by eliminating the expansion joint at the center of the bridge (between Spans 2 and 3). In lieu of an expansion joint over the center pier, a soft and flexible "link slab" element was proposed to render the deck continuous (Li *et al.*, 2005). The center expansion joint was selected because cracking associated with the failure of this joint had led to corrosion and deterioration of the girder bearings at the pier. The expansion joints between Spans 1 and 2 and between Spans 3 and 4 were considered less critical because the girder bearings were not situated below the expansion joints. The link slab renders the deck continuous over the discontinuous girders as shown in Figure 2-2c; however, the link slab is designed to be a relatively soft joint (*i.e.* stiffness of the link slab is much smaller than that of the concrete deck-steel girder composite section) so as to not restrain the rotational movement of the span ends (Caner and Zia, 1998). While past link slabs have been constructed from concrete, the Grove Street's link slab is designed using ECC. ECC is selected because of its tensile ductility and damage resilience.

2.3.2 Link Slab Element Using ECC

The design of the link slab was conducted by the Michigan Department of Transportation (MDOT) in collaboration with researchers from the University of Michigan's Advanced Civil Engineering Materials Research Laboratory (ACE-MRL) (Li *et al.*, 2005). Their

design employs ECC M-45 and follows the link slab design guidelines offered by Caner and Zia (1998) that were originally formulated for concrete link slabs. The link slab is designed to be sufficiently flexible (offering almost no rotational restraint) to permit the spans on both sides of the link slab to behave as simply supported elements. To ensure the stiffness of the link slab is sufficiently low, it is recommended to debond the link slab from the ends of the steel girders for a length (L_{dz}) of at least 5% of the total simply supported span length (see Figure 2-3a).

The link slab element is designed to accommodate the strain induced by live load, shrinkage, and temperature; its design also restrains crack growth using the standard AASHTO (American Association of State Highway and Transportation Officials) crack control specifications. AASHTO also specifies the rotation angle of the simply supported bridge spans should not exceed 0.00375 rad under specified truck loadings (generally, H and HS series trucks). In the ECC link slab designed for the Grove Street Bridge, the ECC is designed to operate in its elastic region (pre-strain hardening) under the maximum permissible rotation (0.00375 rad).

2.3.3 Instrumentation of the Grove Street Bridge

To validate the design guidelines used by the Michigan Department of Transportation, MDOT requested a short-term monitoring study be conducted on the reconstructed Grove Street Bridge. Specifically, MDOT sought the dynamic properties (modal parameters including natural frequencies and mode shapes) of the bridge and two specific static response parameters of the actual link slab element: 1) maximum rotation at the ends of the link slab, and, 2) the maximum tensile strain of the link slab top surface under static live loading conditions (HS25 trucks as presented in Figure 2-4a).

To measure the acceleration response of the bridge to ambient traffic loading, a set of accelerometers are installed along the bridge length. The microelectromechanical system (MEMS) Crossbow CXL02 accelerometers are selected for use in this study. The CXL02 accelerometers, with an acceleration range of ± 2g, noise floor of 0.5 mg and sensitivity of 1 V/g, are ideal for dynamic structural monitoring. Sixteen accelerometers are evenly

distributed across the bridge as shown in Figure 2-5 so as to fully capture the dynamic modes of the structure. To ensure the MEMS accelerometers are properly affixed to the bridge deck, each sensor is bonded to the deck surface using epoxy. Each accelerometer is interfaced to one wireless sensor which is used to record the accelerometer output, digitize the output and to communicate the reading to a central data repository; a simple laptop situated on the south end of the bridge near sensor location A9 serves as the repository during the testing campaign. To improve the performance of the MEMS accelerometers, a custom made signal-conditioning circuit that amplifies each accelerometer output by 20 is integrated with each accelerometer-wireless sensor pair. Figure 2-6 presents a picture of a typical wireless sensor-accelerometer pair.

Once the relative rotation, θ, in the link slab is determined, the top surface strain in the link slab element can be calculated by:

$$\varepsilon = \frac{2\theta c}{L_{dz}} \tag{2.1}$$

where c is the distance from the cross section neutral plane to the top plane of the link slab. To experimentally validate this relationship for an ECC link slab, the rotations of the steel girders beneath the ECC slab are measured. To obtain an accurate measurement of beam end rotations, two linear variable differential transducers (LVDT) are mounted to the web of a steel girder as shown in Figure 2-7a. The LVDTs are mounted to the top and bottom portions of the girder web roughly 0.9 m apart. First, aluminum blocks to which the LVDTs can be screwed are epoxy mounted to the girder webs. To attach the LVDTs to the adjacent girder, another set of aluminum blocks are attached to the adjacent girder's web. Small hooks are screwed into these additional blocks so that a piece of fishing string can be attached between the LVDTs and the hooks. With one LVDT measuring the relative displacement of the girder top and another measuring the relative displacement of the girder bottom, an accurate means of measuring beam rotation is derived. Beneath the reconstructed southbound half width section are 5 steel girders; the second and third girder counting from the side of the bridge are instrumented with a

pair of LVDTs. A short shielded cable is used to connect each LVDT directly to a wireless sensor. One wireless sensor is used to record the displacements of two LVDTs mounted to a single girder; in total, two wireless sensors are installed to measure the rotation of the two girders.

The strain response of the ECC link slab element is also monitored using strain gages mounted to the continuous longitudinal steel reinforcement running parallel to the link slab width. Two buried steel reinforcement bars are selected as shown in Figure 2-8a. The reinforcement bars are located approximately 4.3 m from both sides of the link slab element. In total, three strain gages are installed on each bar roughly 0.6 m apart with the center-most gage in the center of the link slab. To install the strain gages, the epoxy coating on the reinforcement steel is removed and thin film strain gages (Texas Measurements FLA-5) are mounted to a flat surface machined on the steel face. The gage factors of these 120 Ω strain gages are 2.0 while their gage lengths are 5 mm. After the strain gages are securely mounted (Texas Measurements CN bonding adhesive), epoxy is recoated upon the bar to protect it from long-term corrosion (Figure 2-8b). The wires that originate from the gages are carried to the slab's top surface where they connect to the wireless sensors situated on the top deck of the bridge. A Wheatstone bridge circuit is required to convert strain gage readings (*i.e.*, changes in resistance) to a voltage signal compatible with the wireless sensor (0-5V). A separate signal conditioning board is designed and fabricated that allows 120 Ω strain gages to be connected to a Wheatstone bridge circuit. The bridge circuit also amplifies the bridge output by 50 before superimposing it upon a 2.5 V output that is connected to the wireless sensor.

2.3.4 Acceleration Response of the Grove Street Bridge to Vehicular Loading

The acceleration response of the reconstructed bridge is measured under ordinary traffic conditions which includes mostly cars and, in some rare instances, heavy trucks or buses. As presented in Figure 2-9, the acceleration response of the Grove Street Bridge from ordinary traffic is of a high quality when sampled at 200 Hz. In the representative time-histories presented in Figure 2-9, cars crossing the bridge at the posted speed limit (45

km/hr) result in peak accelerations of roughly 6 mg. Data is continuously collected for the duration of a few hours.

Embedded in the computational cores of the wireless sensor prototypes are a number of different algorithms that allow the wireless sensors to process their own measurement data (Lynch, 2007). For system identification, the fast Fourier transform (FFT) is embedded for the local calculation of the complex-valued Fourier spectrum using structural acceleration data. In addition to the FFT, a peak picking algorithm is also embedded so that model frequencies can be automatically estimated from Fourier spectra. The combination of the FFT and peak picking algorithms will provide the wireless monitoring system with the capability to estimate modal frequencies as well as the mode shapes of the bridge. Provided an output-only structural response data set, it is assumed that the traffic crossing the Grove Street Bridge provides a broadband excitation source (Brownjohn *et al.*, 2003). By assuming the system input is broadband, the Fourier spectrum calculated by the wireless sensors can be treated as frequency response functions (FRF) which offer direct measure of the system's modal features.

Example FRFs (4096 point) calculated by the wireless monitoring system are presented in Figure 2-10. The wireless sensor peak picking algorithm identifies the frequencies corresponding to the bridge's first three modes at 2.91, 3.22, 3.39, 4.35 Hz. After determination of the modal frequencies, the wireless sensors wirelessly transmit the imaginary component of their Fourier spectra at those four modal frequencies. If the modal frequencies are assumed to be well spaced and the structure lightly damped, the imaginary component of the Fourier spectra at modal frequencies are proportionally scaled to the structure's mode shape (Peeters and Ventura, 2003). Commonly termed operational deflection shapes (ODS), the ODS are equivalent to the structural mode shapes for a broadband input. During collection of ambient vibration data, the Grove Street Bridge wireless monitoring system calculates the mode shapes of the bridge using the distributed computational resources of the wireless monitoring system. The calculated mode shapes are presented in Figure 2-11: mode 1 (2.91 Hz) is primarily a flexural mode, mode 2 (3.22 Hz) is dominated by torsion, and mode 3 (3.39 Hz) and

mode 4 (4.35 Hz) are higher order flexural modes. Each of the mode shapes suggest that the ECC link slab serves as a "soft-joint". In all four mode shapes, the link slab element (shaded in Figure 2-11) remains horizontal; thus, it can be concluded that the presence of the link slab stiffness does not significantly alter the dynamic nature of the bridge's main spans.

2.3.5 Static Response of the Grove Street Bridge to HS25 Trucks

Static load testing is performed on the reconstructed bridge using trucks loaded to offer a distribution of weight equivalent to an HS25 truck (Figure 2-4a). Two six-axel carting trucks (Figure 2-4b) are selected because their weights have the same load effect as the HS25 design load. Each truck, prior to arrival, is driven to a local highway weigh station (Grass Lake, Michigan) where each axel weight is measured. The approximate weights of the axels, starting with the first axel in the front of the truck, are 80.2, 71.2, 71.2, 57.9, 57.9, and 57.9 kN, respectively. During static load testing, the southbound side of the bridge is closed while the northbound lane is left open for single lane traffic flow (only light traffic is permitted on the bridge with heavy trucks barred during testing). With the southbound lane closed, the two six-axel trucks are placed on the southbound side of the bridge but at opposite ends (Figure 2-12). Based upon influence line analysis, the maximum induced rotation at the ends of the link slab occurs when the two trucks are moving toward the link slab and stopped at a point where their first axles are roughly 10.7 m away from the link slab center (Figure 2-12b). The two trucks are located on opposite sides of the link slab element to ensure symmetry in loading.

The trucks are driven onto the bridge from opposite sides at a slow speed (8 km/hr) until they reach their final positions 10.7 m from the link slab center. As the trucks proceed onto the bridge, the strain gages and LVDTs are recorded using 8 wireless sensors installed on the bridge deck (6 wireless sensors are reserved for the six strain gages while 2 wireless sensors record the girder rotations each from 2 LVDTs). Bridge response data is collected at 50 Hz by the wireless sensors and wirelessly transmitted to the system data repository.

As presented in Figure 2-13, the rotation measurement of the girders beneath the link slab as measured from the LVDTs are of a high quality. For the set of LVDTs installed upon the second girder, the point when the trucks ride upon the simply supported spans adjacent to the link slab can be identified at 14 seconds; the trucks come to a stop with maximum girder rotations attained (6.33×10^{-4} rad.) at 20 seconds. Using Equation 2.1, the strain in the center of the top face of the link slab is estimated to be 41 με. Similar results are found for the third girder with a calculated rotation of 7.61×10^{-4} rad and estimated link slab strain of 50 με. These results correspond well to data collected from strain gages mounted to the buried steel reinforcement. For example, for strain gage S5 which is the center-most gage on the reinforcement bar in the southbound portion of the bridge, the maximum strain measured during the test was 32 με (Figure 2-13c) which is a bit shy of the estimated 41 με (22% difference). In addition, the measure strain response is extremely small compared to the noise inherent in the strain gage measurement. More confidence could be placed in the strain measurement if the signal-to-noise ratio was improved.

The field study conducted on the Grove Street Bridge using wireless sensors accomplished the goal of proving the feasibility and cost-effectiveness of wireless structural monitoring systems. Also, the computing capability of the wireless sensors was shown capable of deriving global structural properties of the system such as mode shapes. The low rotational stiffness of the link slab element could be observed from the mode shapes calculated in-network. In the next section, embedded algorithms tailored for damage detection are presented. Such algorithms could be used to monitor the health of HPFRCC structural elements.

2.4 Damage Evaluation of HPFRCC Elements Using Wireless Sensors

During the design of earthquake-resistant reinforced concrete (R/C) structures, a certain amount of the structure's seismic energy is anticipated to be dissipated through inelastic deformations of R/C members. During such seismic excitations, R/C structural elements

should maintain their structural integrity and should be able to withstand the local accumulation of inelastic deformations without collapse. In order to assess the global structural integrity of critical structural elements and to quantify the level of structural safety, quantitative damage measurements taken of structural members are necessary. In general, damage is defined as a degradation of the mechanical functionality of a structure. For example, damage of a flexural element could be the degradation of flexural stiffness and ultimate strength. Such parameters may degrade during regular operational loading as well as during seismic events. Regardless of the origin, quantification of the degradation is necessary for assessing condition of the structure.

Many damage models have been proposed by the research community for tracking the progress of damage in cyclically loaded R/C structural elements (for example, Park and Ang (1985) and Kratzig *et al.* (1989)). A large number of these damage models correlate damage of a structural element to specific structural response parameters such as deformation, internal forces or dissipated hysteretic energy. These models place their assessment of structural health on a scale from 0 to 1. Such damage indexes suggest the member is in its virgin state when the index is 0 and severely damaged (to the point of failure) when the index achieves a value of 1 (or greater). Damage index models are a powerful tool for providing a rough measure of the health of a structural element immediately following a seismic event. For example, a rough picture of the degree of damage can be used by owners to prioritize the inspection of their structures.

An accurate damage index model based solely on the response history of an R/C structural element under cyclic loading has been proposed by Kratzig *et al.* (1989). The characteristics of this damage index model are simply described as follows. By referring to the measured structural response, for example, as shown in Figure 2-14, positive and negative peak responses in each cycle of the total response history are isolated. These response values should be physically representative of the damage evolution of the structure (*e.g.* dissipated energy). The damage model is divided into positive and negative indexes, D^+ and D^-, in order to account for the unsymmetrical response of a structural element. At each peak, the damage index is calculated based on the current and

previous peak values. As part of calculating the damage index at each peak, the set of peaks that include the current and previous peaks must be appropriately classified as "primary" or "follower" half-cycle peaks. A primary half-cycle (PHC) corresponds to a peak response that is greater than that of any of the previous peaks. However, if the structural response within a half-cycle has a peak less than the maximum structural response in any of the previous half-cycles, then the cycle is denoted as a follower half-cycle (FHC). This is done to account for the damage accumulation during cyclic loading with PHC peaks representing newly evolved damage and FHC peaks representing accumulated damage to the R/C structural element.

To better understand the PHC and FHC naming convention, consider Figure 2-14. If the damage index is calculated at positive peak number 2, this peak is labeled as a PHC peak because it is larger than peak 1; peak 1 is labeled as a FHC peak. If the damage index is calculated at peak 3, it is larger than peaks 2 and 1 and is therefore labeled as a PHC peak. In contrast, peaks 1 and 2 are labeled as FHC peaks. Now, if the damage index is to be determined at peak 4, peak 4 is smaller than peak 3. As a result, peak 4 is labeled as a FHC along with peaks 2 and 1 while peak 3 retains the designation of the PHC peak.

An additional feature of the Kratzig damage index model is the use of the total structural capacity of monotonically loaded structural members up to failure to serve as a normalizing factor of the model. The accuracy of this damage model for R/C flexural elements is validated by finite-element simulation and experimental results as reported by Kratzig *et al.* (1989). In a similar manner, damage index models describing the health of HPFRCC structural members in both flexure and shear are devised in this study and are largely based on the model proposed by Kratzig *et al.* (1989).

2.4.1 Damage Index for HPFRCC Elements

A damage index model is sought that will be capable of tracking the damage of HPFRCC structural elements. The model must use response data that can be accurately measured in real civil structures. Furthermore, the computational demands of the model should be kept reasonable to ensure that the wireless sensor platform installed in the structure will

be able to execute the model within a reasonable time frame. The original Kratzig *et al.* (1989) model was based on dissipated seismic energy over the cyclic loading time history. However, such a model is difficult to use in the field because the dissipation of seismic energy cannot be directly quantified or measured. Mehanny and Deierlein (2001) have proposed a modification of Kratzig's model using element drift instead of seismic energy. Drift measures rectify the damage index model with the field of performance-based design that is shaping current and future design codes to evaluate structural performance as a function of drift responses. With state-of-the-art monitoring systems capable of accurately measuring member and/or structural drifts using displacement transducers and arrays of accelerometers (Celebi *et al.*, 2004) installed in a structure, drift measures are easier to acquire in the field than dissipated energy.

To provide an accurate damage index model for HPFRCC components, two distinct modes of mechanical behavior in HPFRCC members must be captured. When HPFRCC elements are dynamically loaded, a substantial percentage of dynamic energy is released through the formation of dense fields of micro-scale cracks in the cementitious matrix and through the inelastic deformation of the reinforcing steel. These microcracks are sufficiently small that fibers included in the composite material bridge the cracks and arrest their growth. During this mode of mechanical behavior, HPFRCC components exhibit excellent ductility and durability. At a certain level of strain, the strength of the fiber-matrix interface decays, resulting in the pullout of fibers and the formation of large cracks in the material. After fiber pullout occurs, energy is primarily dissipated by inelastic deformation of the reinforcing steel and thus, the post-fiber pullout behavior of an HPFRCC element is similar to the behavior of an ordinary R/C element. To instill these two modes of behavior in a damage model for HPFRCC components, two separate indexes are proposed by Canbolat *et al.* (2004) for each mode of behavior.

2.4.1.1 Pre-Fiber Pullout Damage Index

The HPFRCC damage model calculates individual damage indexes for the positive and negative drift directions, D^+ and D^-, respectively. Both indexes are symmetrical of one

another and only differ in the peaks (positive versus negative) they consider for their calculation. The positive index is defined as (Canbolat *et al.*, 2004):

$$D^{+} = \frac{\left(\delta^{+}_{PHC}\right)^{\alpha} + \left(\sum \delta^{+}_{FHC}\right)^{\beta}}{\delta^{+}_{Monotonic} + \left(\delta^{+}_{FiberPullout}\right)^{\alpha} + \left(\sum \delta^{+}_{FHC}\right)^{\beta}} \tag{2.2}$$

Drift peaks are labeled as either primary half-cycle (PHC) peaks or as follower half-cycle (FHC) peaks, denoted as δ^{+}_{PHC} and δ^{+}_{FHC}, respectively. The PHC and FHC peaks follow the definition as previously described in Section 2.4. To better illustrate the naming convention, a portion of an HPFRCC coupling beam drift time-history is used (Canbolat *et al.*, 2004). As shown in Figure 2-15, five consecutive drift peaks in the positive direction are numbered. Half-cycle peak "2" is larger than the previous half-cycle peak "1"; to calculate the damage index, $D+$, at peak "2", the peak is a PHC peak and is used for the variable δ^{+}_{PHC}. Because peak "2" is the new PHC, peak "1" is now labeled as a follower half peak and added to the sum of FHC peak drifts. Similarly, to calculate the damage index at peak "3", peak "3" is larger than peak "2" and is used as the primary half-cycle drift, δ^{+}_{PHC} , while peak "2" is added to the summation of FHC peaks. At peak "4", the peak drift is smaller than peak "3" and is immediately labeled as an FHC. In calculating the damage index at this peak, peak "3" would remain as the PHC peak drift while peak "4" is added to the summation of FHC peaks.

The numerator of the damage index is normalized by three terms. Similar to the model proposed by Kratzig *et al.* (1989), the monotonic maximum drift capacity, $\delta^{+}_{Monotonic}$, and the sum of FHC peak drifts are normalizing terms for the damage model. The peak drift at fiber pullout, $\delta^{+}_{FiberPullout}$, is used as the third normalizing term of the model (Canbolat *et al.*, 2004). The weighting terms, α and β, allow the damage model to be tuned to empirical data taken of HPFRCC elements tested in the laboratory. At the completion of each full cycle, the positive and negative damage indexes are combined to form a single damage index:

$$D = \sqrt[\gamma]{\left(D^{+}\right)^{\gamma} + \left(D^{-}\right)^{\gamma}} \tag{2.3}$$

Again, γ is a tuning parameter of the model.

2.4.1.2 Post-Fiber Pullout Damage Index

Once fiber pullout occurs in an HPFRCC element, its behavior is distinctly different from that prior to fiber pullout; as such, a different mechanistic damage model is warranted. To be consistent with the previous damage index model, the index proposed in Equation 2.2 is modified by removing from the denominator the peak drift at which fiber pullout occurs, $\delta^{+}_{FiberPullout}$. The positive damage index for the post-fiber pullout model is:

$$D^{+} = \frac{\left(\delta^{+}_{PHC}\right)^{\alpha} + \left(\sum \delta^{+}_{FHC}\right)^{\beta}}{\delta^{+}_{Monotonic} + \left(\sum \delta^{+}_{FHC}\right)^{\beta}} \tag{2.4}$$

The combination of positive and negative damage indexes proposed by Equation 2.3 is also used for the post-fiber pullout model. The same tuning constants, α, β, and γ, of the pre-fiber pullout model are used in the post-fiber pullout model. A damage index value of 1 (or greater) indicates failure of the HPFRCC component. Here, failure is defined as large-macro-crack localizing, and the steel reinforcement is behaving in a highly nonlinear manner.

2.4.2 Damage Index Model Embedded into Wireless Sensing Systems

The simplicity of the damage index model is well paired to the computational resources readily available on most wireless sensing platforms. In this study, the prototype wireless sensor introduced in Section 2.2 is employed. The damage index proposed for monitoring damage in HPFRCC elements is encoded in software and embedded in the wireless sensor's microcontroller. Wireless sensors could be installed with HPFRCC elements to record their cyclic response during seismic events and to determine the degree of damage in the element by autonomously executing the damage index model. By providing a measure of component damage in a structure, the overall global integrity

of the structural system can be determined in real-time and reported to the appropriate structures' managers and owners. Others have proposed the coupling of damage index models with sensors. For example, Mita and Takahira (2004) report the design of a radio frequency identification (RFID) wireless damage index sensor that determines the damage index based on the buckling of a thin wire. In contrast, the approach proposed in this study is calculation of the damage index in software by an "intelligent" or "smart" sensor.

Embedded firmware is written for the wireless sensor to allow it to autonomously execute the proposed damage index model. As shown in Figure 2-16, once the cyclic drift response of an HPFRCC component is measured and recorded, the wireless sensor determines the positive and negative response peaks and labels them as PHC and FHC peaks. Using the drift peaks that are smaller than the maximum drift before fiber pull-out, the positive and negative damage indexes are calculated using Equation 2.2. Once a peak drift exceeds the fiber pullout drift, the post-fiber pullout damage index model of Equation 2.4 is employed. The total damage index of the component is calculated for each peak by using Equation 2.3.

2.4.3 Damage Evaluation of an HPFRCC Bridge Pier

Cantilever concrete bridge piers are vulnerable during seismic loading with the pier base being the most critical region since this is where plastic hinges will be formed under the action of earthquake-induced displacements. Damage in plastic hinge regions may include large flexural and diagonal cracks, concrete crushing and spalling, and reinforcement buckling. All of these conditions could lead to premature structural performance degradation when bridges are undergoing displacement reversals. Within current codes (ACI-318, 2008), shear strength attributed to the concrete is typically insufficient and a vast amount of closely spaced transverse steel reinforcement is required to ensure desired shear strength of the member, to provide confinement to the concrete, and to prevent longitudinal reinforcement from buckling, especially in potential plastic hinge regions. Unfortunately, this large amount of transverse reinforcement can lead to unavoidable reinforcement congestion and concrete placing problems. Unlike buildings

which have a large number of plastic hinges within a single structure, bridge structures are typically less structurally redundant and have fewer plastic hinges than buildings. As a result, plastic hinges play a more critical role in the structural behavior.

The strain hardening property of HPFRCC under tension renders the material strong in shear. As such, it can be used to provide bridge piers, and flexural members in general, with sufficient shear strength so as to reduce current shear steel reinforcement detailing mandated by building codes (Parra-Montesinos, 2003). In addition to its strength in shear, HPFRCC is capable of providing support to the longitudinal bars, as well as an increased displacement capacity due to its excellent ductility both in tension and compression. In HPFRCC materials, concentrated macro-cracks only occur under large displacements when the strength of the fiber-matrix interface is exceeded (this is referred to as damage localization). Although no seismic design guidelines have yet been developed for the reasonable use of HPFRCC in plastic hinge regions of reinforced concrete structural members, studies of HPFRCC behavior within plastic hinge regions of reinforced concrete flexural members have been conducted (Parra-Montesinos and Chompreda, 2007).

For the purpose of investigating the performance of HPFRCC materials in bridge pier bases under large displacement reversals, a circular bridge pier specimen with a 40.6 cm diameter is constructed of HPFRCC material and tested in the laboratory under quasi-static lateral loading. The dimensions of the HPFRCC column roughly represent a 1/3-scaled specimen of a true pier. The bridge pier specimen prepared in this study is designed with non-seismic transverse steel reinforcement detailing as shown in Figure 2-17a because of the anticipated shear strength of the HPFRCC material. The longitudinal reinforcement provided in the bridge pier specimen corresponds to a reinforcement ratio of 2.6% while the volumetric ratio of spiral reinforcement is 0.56%. Note that a spiral pitch of 15.2 cm is provided, which is substantially larger than the maximum allowed in reinforced concrete members reinforced by spirals (which typically is on the order of 3 to 8 cm) (ACI-318, 2008). The HPFRCC material is prepared by combining a 1.5% volume fraction of 3.8 cm Spectra fibers with a cement-based mixture, as detailed in Table 1-1.

For the rectangular supporting pedestal and the top square loading cap, a normal weight regular concrete mixture is used since these elements are not of mechanical interest in this study. Because no fibers bridge the interface between the bridge pier base and the base block, additional longitudinal reinforcement is placed at the HPFRCC concrete interface so as to relocate the potential plastic hinge to roughly 16 cm above the interface. This allows the full capacity of the HPFRCC material to be utilized under lateral loading.

The final test specimen is composed of three parts, including the concrete base which is 61 x 61 x 183 cm (width, depth and length), a 1.02 m tall HPFRCC column, and a top loading block whose dimensions are 40.6 x 40.6 x 40.6 cm, leading to a shear span-to-diameter ratio of 3.0. Construction of the whole test specimen is divided into three stages. Regular concrete is first poured in formwork to create the supporting base. The 40.6 cm diameter HPFRCC column is then constructed to a total height of 1.02 m above the base. Last, the cubic cap is poured after the HPFRCC column. Grade 420M steel bars are used for both the longitudinal and spiral reinforcement. The compressive strength (f'_c) of regular concrete and HPFRCC test cylinders are measured to be 34.5 MPa and 41.8 MPa, respectively.

2.4.3.1 Instrumentation

A key element of the proposed study is the extensive use of wireless sensors to collect the response of the pier under quasi-static loading. The HPFRCC bridge pier specimen is instrumented with several LVDTs at the pier base (the plastic hinge region) so as to investigate its flexure and shear behavior under reversed cyclic loading. The LVDTs are interfaced to the wireless sensors for data collection. Also, a total of 20 strain gages are mounted on the surface of the longitudinal and transverse reinforcement within the HPFRCC pier to monitor strains during load testing. Strain is measured by both wireless sensors and a cable-based data acquisition system native to the lab. The displacement data collected by the LVDTs at the base will be used to calculate the shear and flexural deformation components in the pier plastic hinge. To be able to differentiate between shear and flexure, 4 LVDTs are mounted to the side of the pier base (in a plane parallel to the loading direction). As shown in Figure 2-18a, 2 LVDTs are placed in an X-

configuration while the remaining two are placed parallel and orthogonal to the pier longitudinal axis. An additional set of LVDTs are installed to the front and back sides of the pier to measure plastic hinge rotations, as shown in Figure 2-18b.

2.4.3.2 Damage Index Model for HPFRCC Bridge Pier

In order to differentiate between the damage caused by shear and flexural responses during cyclic loading, separate damage index models for both the shear and flexural deformation of the HPFRCC bridge pier will be developed. In this study, the structural response parameter used as the input to the damage index model will be the lateral displacements of the bridge pier base that correspond to shear, U_s, and flexure, U_f, as shown in Figure 2-19. Figure 2-20a shows the X configuration of LVDTs instrumented at the bridge pier base. Referring to Figure 2-20b, the horizontal displacements, U_1 and U_2, contain both shear and flexural components that should be differentiated in order to evaluate the structural behavior attributed to shear and that to flexure. If only first order shear deformation is considered, it is assumed that the lateral displacement due to flexure is equal on each side of the pier. Suppose the original undeformed horizontal and vertical lengths of the instrumented pier panel are a and b, respectively (in this study, a is 32 cm and b is 30 cm), then U_1 and U_2 can be treated as a single variable, U_t, that can be expressed as:

$$U_t = \frac{L_1^2 - L_2^2 - a^2}{2a} \tag{2.5}$$

Also, L_1 corresponds to one of the deformed diagonal distances of the LVDT X-configuration. Similarly, L_2 corresponds to the deformed vertical distance as can be referred from Figure 2-20b. Based on the geometry shown in Figure2-20b, the associated vertical displacements, V_1 and V_2, can be obtained once the total lateral displacement is calculated, which can be expressed as:

$$V_1 = \sqrt{\left(L_3 + a - U_t\right) \times \left(L_3 - a + U_t\right)} - b \tag{2.6}$$

$$V_2 = \sqrt{(L_2 + U_t) \times (L_2 - U_t)} - b \tag{2.7}$$

Here, L_3 corresponds to other deformed diagonal distance of the LVDT X-configuration, as shown in Figure 2-20b.

***Flexural Deformation*:**

In analyzing the flexural deformation of plastic hinge regions of bridge piers under lateral loading, the plastic hinge rotation, θ, is first calculated and then used to estimate the corresponding flexural deformation. Generally, the hinge rotation is associated with the vertical displacements, V_1 and V_2, and the horizontal distance between them, a, which results in:

$$\theta = \frac{V_1 - V_2}{a} \tag{2.8}$$

Because of the moment gradient in the bridge pier and the fact that flexural cracking is more concentrated towards the lower portion of the plastic hinge region, a distance from the top of the LVDTs X-configuration to the center of rotation of 2/3 of the total vertical length, b, is assumed. Then, the flexural displacement of the pier base, U_f, can be expressed as:

$$U_f = \rho \theta b \tag{2.9}$$

where ρ is equal to 2/3 and is consistent with the value used by others (Ali and Wight, 1990; Thomsen and Wallace, 1995).

***Shear Deformation*:**

Since the total lateral displacement contains flexural and shear displacements, the later term, U_s, can be easily obtained once the flexural displacement is calculated from Equation 2.9. Therefore, shear deformations is extracted out from the measured total lateral deformation once the flexural deformation (Equation. 2.9) is known:

$$U_s = U_t - U_f \tag{2.10}$$

***Flexural Damage Index Model*:**

After the flexural deformation of the pier has been determined from the LVDT measurements, the damage index characterizing the damage due to flexure is calculated. The damage index model uses the peak flexural displacement, U_f, of the pier base in both the positive and negative directions as an input. The damage index model calculated at each positive peak is an adaptation of the damage index model proposed by Mehanny and Deierlein (2001):

$$D_f^+ = \frac{\left(U_{f,PHC}^+\right)^\alpha + \left(\sum U_{f,FHC}^+\right)^\beta}{U_{f,Monotonic}^+ + \left(\sum U_{f,FHC}^+\right)^\beta} \tag{2.11}$$

where $U^+_{f,PHC}$ is the positive peak flexural displacement of the primary half-cycle (PHC), $U^+_{f,FHC}$ is the positive peak flexural displacement of the follower half-cycles (FHC), and $U^+_{f,Monotonic}$ is the monotonic maximum flexural displacement capacity. As will be presented later in the shear damage index model, fiber pullout has been experimentally observed to play negligible influence on flexural behavior of HPFRCC structural elements. Thus, the flexural damage index model does not consider fiber pullout as a normalizing factor. In this study, $U^+_{f,Monotonic}$ was not obtained at the end of the test because the maximum applied displacement (corresponding to 10% drift) was at the maximum capacity of the actuator. Therefore, the maximum flexural displacement corresponding to the monotonic limit of the HPFRCC material is assumed to be 140% of the flexural displacement at 10% drift. Once the flexural damage indexes of both the positive and negative directions for the full cycle are completed, they are combined into a single flexural damage index:

$$D_f = \sqrt[\gamma]{\left(D_f^+\right)^\gamma + \left(D_f^-\right)^\gamma} \tag{2.12}$$

The weighting terms, α, β, and γ, allow the damage model to be tuned to empirical data taken of HPFRCC elements tested in the laboratory. Assuming that the damage induced by the PHCs and FHCs in both loading directions in HPFRCC members is "identical" to that in reinforced concrete members, the damage index weighting terms determined for concrete elements by Mehanny and Deierlein (2001) are used in this study ($\alpha=1$, $\beta=1.5$, and $\gamma=6$).

***Shear Damage Index Model*:**

The shear damage index uses the shear displacement of the pier base extracted from the total lateral deformation measured using the LVDTs. However, for an HPFRCC bridge pier, shear behavior of the pier before and after fiber pullout are much different and need to be discussed separately. Before fiber pullout, a fiber bridging mechanism allows the HPFRCC material to contribute to the total shear strength; in that case the shear stiffness and strength of the pier is larger than that after fiber pullout. Therefore, another term in the denominator accounting for the fiber pullout mechanism should be used in the shear damage index (Canbolat *et al.*, 2004). Fiber pullout has been experimentally observed to play a major role in the behavior of HPFRCC structural elements in shear while fiber pullout has negligible influence on flexural behavior. As a result, the shear displacement of the pier, $U_{s,FiberPullout}$, is used as a third normalizing term so as to differentiate the two different mechanisms of the shear behaviors of HPFRCC bridge piers. For example, shear damage index in the positive direction before fiber pullout can be expressed as:

$$D_s^+ = \frac{\left(U_{s,PHC}^+\right)^\alpha + \left(\sum U_{s,FHC}^+\right)^\beta}{U_{s,Monotonic}^+ + \left(U_{s,FiberPullout}^+\right)^\alpha + \left(\sum U_{s,FHC}^+\right)^\beta} \tag{2.13}$$

After fiber pullout, the shear displacement of the pier at fiber pullout is removed because the material behaves in a fashion similar to reinforced concrete:

$$D_s^+ = \frac{\left(U_{s,PHC}^+\right)^\alpha + \left(\sum U_{s,FHC}^+\right)^\beta}{U_{s,Monotonic}^+ + \left(\sum U_{s,FHC}^+\right)^\beta} \tag{2.14}$$

Similar to the flexural damage index model, a single damage index will be calculated at the end of each cycle once the positive and negative indexes are calculated:

$$D_s = \sqrt[\gamma]{\left(D_s^+\right)^\gamma + \left(D_s^-\right)^\gamma} \tag{2.15}$$

Damage index models have been previously fitted to the response parameters of HPFRCC elements dominated by shear action (Canbolat *et al.*, 2004). The weighting terms derived for those elements are adopted in this study (α=*0.9*, β=*3*, and γ=*7*).

2.4.3.3 Cyclic Lateral Load Test of the HPFRCC Bridge Pier

The seismic behavior of the HPFRCC bridge pier is evaluated through a quasi-static laboratory load test. A 450kN actuator, which will provide lateral displacement reversals, is attached to the cubic block constructed at the top of the bridge column. Cyclic loading is slowly applied to the specimen under displacement control; at the displacement peaks, the test is paused to allow for tracing crack patterns manually on the pier surface using markers. As shown in Figure 2-21a, the HPFRCC bridge pier specimen is subjected to drift levels (the lateral displacement divided by the distance between the pier base and the loading point) ranging from 0.25% to 10%. The corresponding lateral force versus drift response of the HPFRCC bridge pier is shown in Figure 2-21b.

As shown in Figure 2-21b, the bridge pier maintains its lateral strength up to 10% drift in its positive loading direction, which is an extremely large displacement for such a structural component. Damage in the bridge pier consists of a dense array of hairline flexural and diagonal cracks, which formed during the first few loading cycles (<2.0% drift). At 4.0% drift, damage localization occurs at one of the flexural cracks, leading to significant widening of that crack at larger drift demands. However, the opening of such a crack does not compromise the integrity of the specimen because flexural resistance does not rely on the tensile behavior of the HPFRCC material. Further, the HPFRCC material maintains its integrity through the test, being effective in providing confinement to the longitudinal reinforcement even after damage localization. Even though a peak

shear stress demand of 2.7 MPa ($0.42\sqrt{f_c'}$) is imposed on the bridge pier specimen, only hairline diagonal cracks formed throughout the test. As a result, total damage of the bridge pier specimen can be considered minor since no shear-related damage and strength decay occured. As shown in Figures 2-22a and 2-22b, there is no spalling or crushing of the HPFRCC in the plastic hinge region during the test. This is mainly due to the excellent tensile and compression properties of the HPFRCC material, which also provides excellent confinement to the longitudinal reinforcement bars, thereby preventing them from buckling during large displacement reversals. The results from the bridge pier test suggest that minor post-earthquake repairs would be needed in HPFRCC bridge piers after a major earthquake with no interruption of bridge service.

2.4.3.4 Damage Index Models Embedded into Wireless Sensors

In order to validate the ability of wireless sensors to monitor structural damage evolution under cyclic loading of HPFRCC elements, the structural response time-history of the X-configuration of LVDTs is stored into the wireless sensors' memory. To account for the different shear behaviors of HPFRCC bridge pier due to fiber pullout mechanism, $U_{s,FiberPullout}$ and $U_{s,Monotonic}$ are selected based on empirical data taken from other shear dominant HPFRCC elements tests (Canbolat *et al.*, 2004). In this study, $U_{s,FiberPullout}$ and $U_{s,Monotonic}$ are chosen to be 0.28 cm and 1.12 cm corresponding to 1% and 4% shear strain, respectively.

Figure 2-23 shows the final damage index calculated by the wireless sensing unit for both flexure and shear. Although the HPFRCC bridge pier specimen maintains its structural integrity and does not exhibit a decay in load carrying capacity even at the end of the test (10% drift), a wide flexural crack is observed in the plastic hinge region at the pier base, which is related to moderate flexural damage, as denoted by the damage index value of 0.4. However, no major diagonal cracks are observed during the test, which implies that the shear damage of the bridge pier specimen is minor. The minor damage is consistent with the calculated damage index value of 0.2. Based on the low damage index values, the bridge pier has not experienced significant damage and still has capacity for additional load cycles and/or greater lateral displacement demands.

2.5 Conclusions and Summary

This chapter has illustrated the power of using wireless sensors to monitor HPFRCC structural elements in both the field (Grove Street Bridge) and laboratory (bridge pier). A major contribution of this work is that it tests a prototype wireless sensor designed for SHM applications; given the novelty of HPFRCC materials, tracking their performance and health under realistic loading is critical in the material's future development. Clearly, low-cost sensor technologies like wireless sensors open up opportunities for closely monitoring HPFRCC structures in the near future.

In the Grove Street Bridge field testing, wireless sensors are employed for both dynamic and static monitoring of the structural responses. Using ambient vibration as the input to the bridge, both the acceleration responses are recorded and the corresponding mode shapes are computed by the wireless sensors. Through the embedded modal analysis algorithm, the wireless sensors have validated the "soft-joint" performance of the ECC link slab. The static monitoring also showcases the reliable data acquisition possible with wireless sensors, especially when recording signals corresponding to small (noise dominated) structural responses. Wireless sensors have shown its advantages including low-costs, possibility for dense installation of sensing nodes, and local data interrogation capabilities. These attributes are attractive for monitoring HPFRCC structural elements in future field deployments.

The HPFRCC bridge pier study further validates the wireless sensor's computing power for rapid evaluation of the damage evolution of HPFRCC structural elements under cyclic loading. Damage index methods original proposed by Kratzig *et al.* (1989) and Mehanny and Deierlein (2001) were modified and encoded into the computing cores of wireless sensors. Using displacement responses as the input, wireless sensors with embedded damage index models have provide a rough damage evaluation of the HPFRCC bridge pier. The key contribution of this study is that it reveals the opportunity of using wireless

sensors to track the evolution of damage in HPFRCC structural elements. This work suggests that wireless sensors could be employed in the future for autonomous damage detection of HPFRCC structural elements after seismic events. Theoretical models should be explored to provide a guideline for the appropriate *a priori* selection of the model parameters. Future development of the damage index models should also focus on providing the appropriate tuning parameters (α, β, and γ) of the damage indexes for specific structural elements.

For tracking damage in HPFRCC structural elements, existing damage detection algorithms such as the aforementioned damage index method provide a rapid and rough assessment of damage. However, these methods are not able to provide detailed crack information. Locations and severity of cracks are desired so that engineers can evaluate if repair is needed. As a result, a damage detection technology based on the electro-mechanical properties of cementitious materials is investigated and developed in the remainder of this thesis so as to resolve the current limitations of damage detection algorithms.

Figure 2-1: A low-cost wireless sensor whose hardware design is optimized for structural monitoring of civil infrastructure systems.

(a)

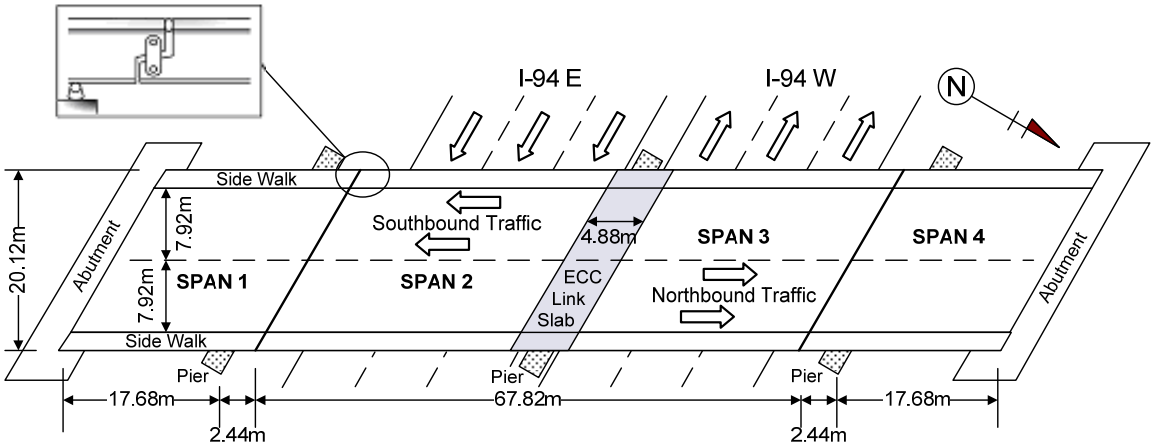

(b)

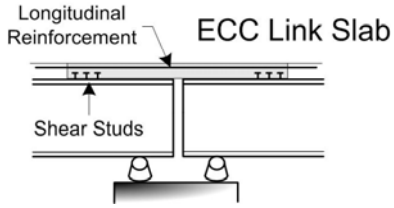

(c)

Figure 2-2: Grove Street Bridge, Ypsilanti, Michigan: (a) picture of bridge; (a) top view schematic; (c) link slab section detail.

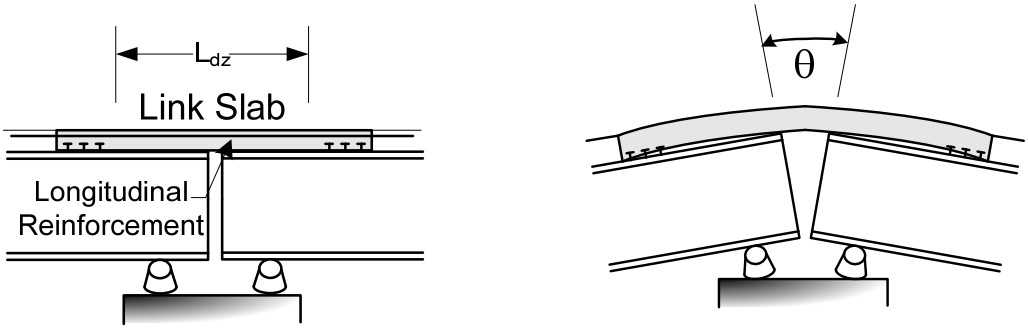

(a) (b)

Figure 2-3: (a) Link slab and the debonded length (L_{dz}) denoted; (b) rotation of girders beneath the ductile link slab.

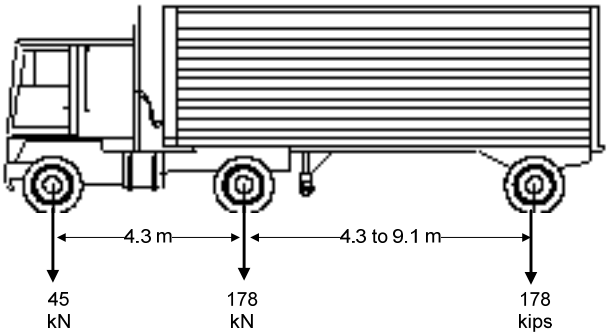

(a)

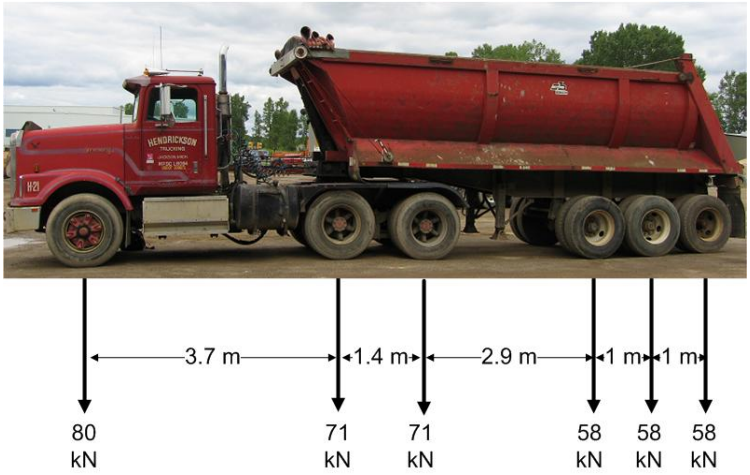

(b)

Figure 2-4: (a) HS25 AASHTO truck load; (b) approximate HS25 truck utilized during load testing.

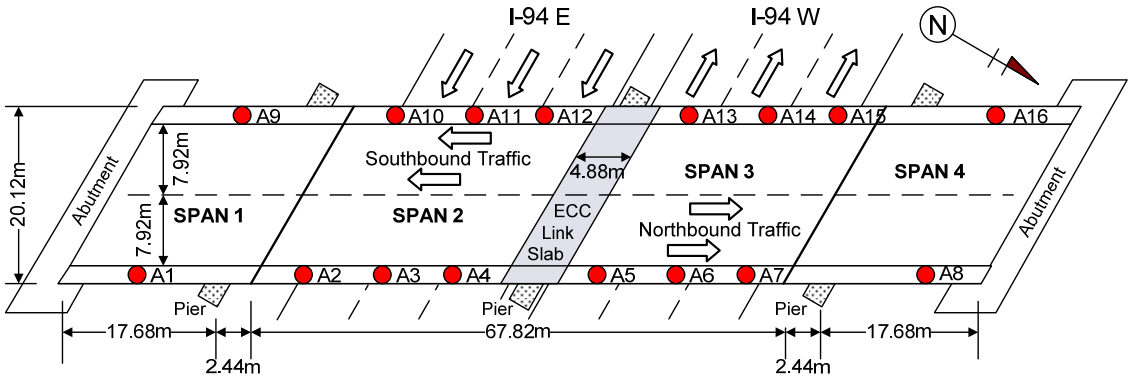

Figure 2-5: Installation of accelerometers along the Grove Street Bridge length during ambient dynamic testing.

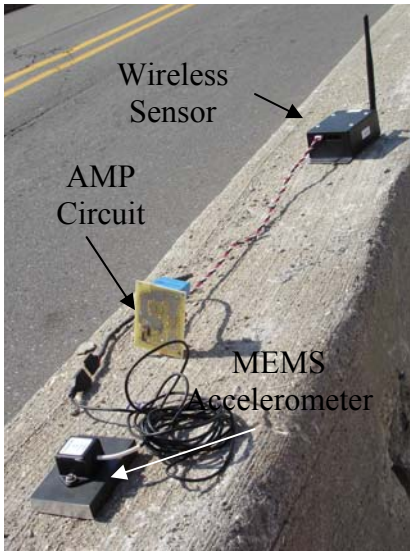

Figure 2-6: Crossbow MEMS accelerometer is shown in the foreground; the wireless sensor is shown with an amplification circuit connected between the accelerometer and wireless sensor.

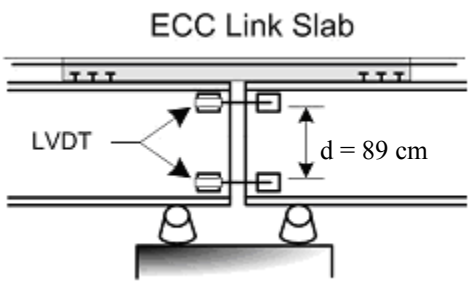

(a) (b)

Figure 2-7: (a) Location of installation of LVDTs to measure girder rotations; (b) actual installation upon the top of the second Grove Street southbound girder.

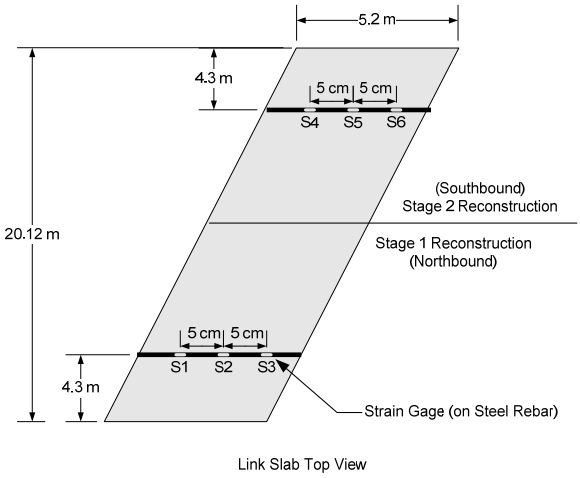

(a) (b)

Figure 2-8: (a) Location of strain gages mounted to two buried steel reinforcement bars; (b) epoxy covered strain gages on actual reinforcement bars on the Grove Street Bridge.

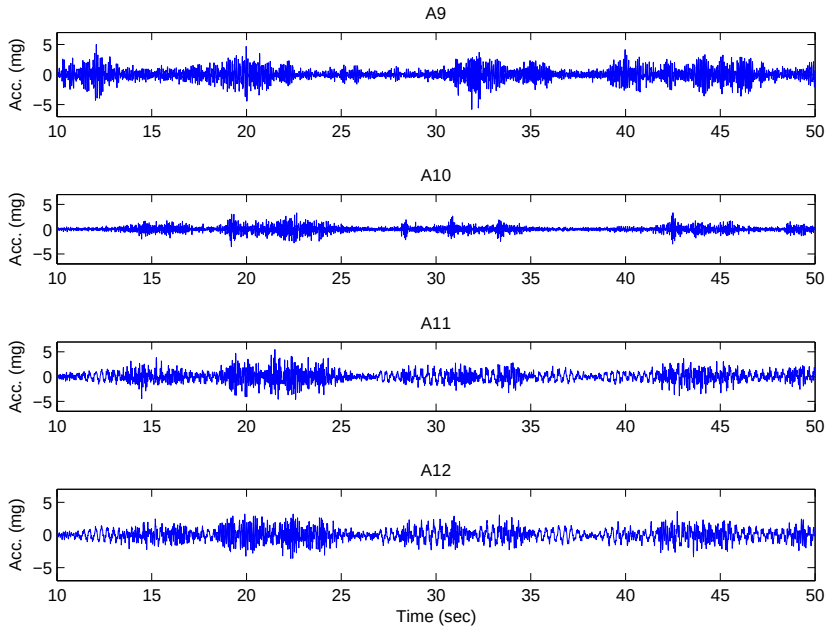

Figure 2-9: Ambient response data of the Grove Street Bridge to ordinary traffic conditions.

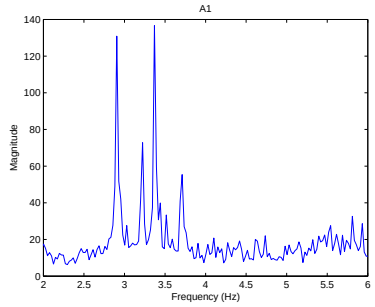

(a)

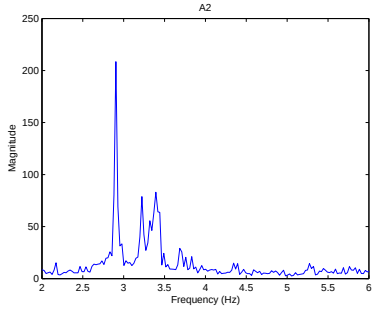

(b)

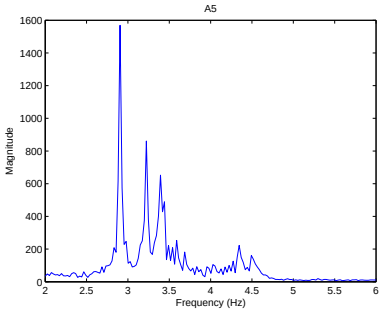

(c)

Figure 2-10: Dynamic test 1 responses at sensor locations (a) A1, (b) A2, and (c)A5: frequency response spectrum magnitude as calculated by the wireless sensors.

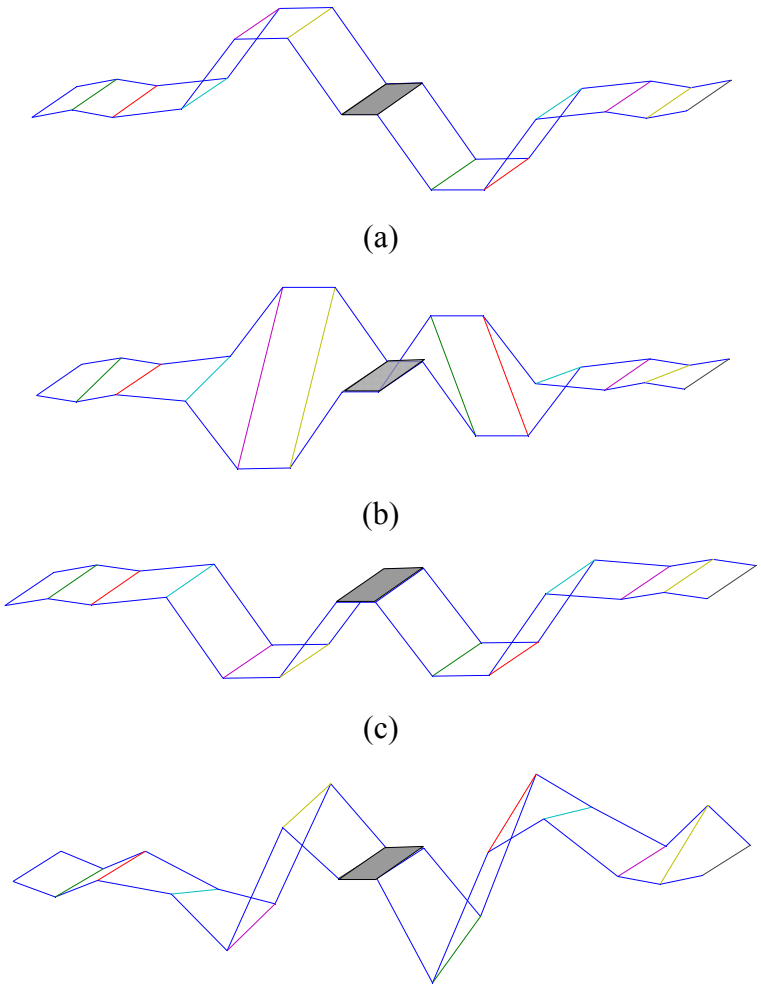

(a)

(b)

(c)

(d)

Figure 2-11: First four modes of the Grove Street Bridge: (a) Mode 1 at 2.91 Hz; (b) Mode 2 at 3.22 Hz; (c) Mode 3 at 3.39 Hz; (d) Mode 4 at 4.35 Hz.
Note, link slab element is shaded in light gray.

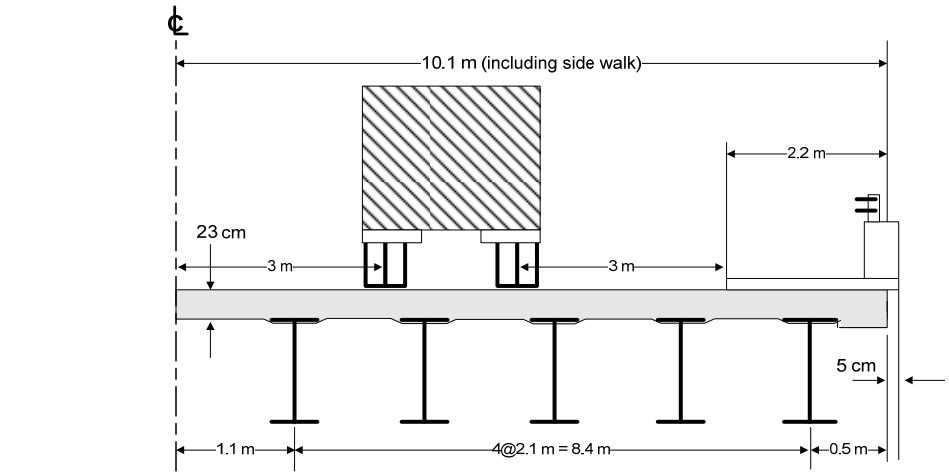

(a)

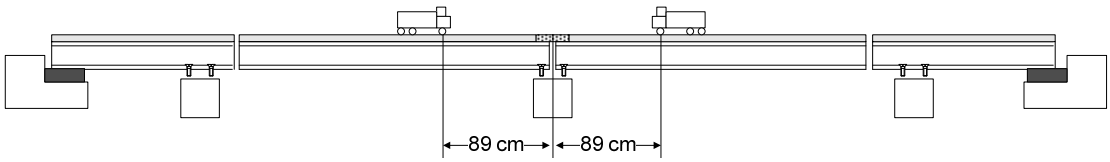

(b)

Figure 2-12: Static load testing using HS25 trucks: (a) transverse and (b) longitudinal truck locations.

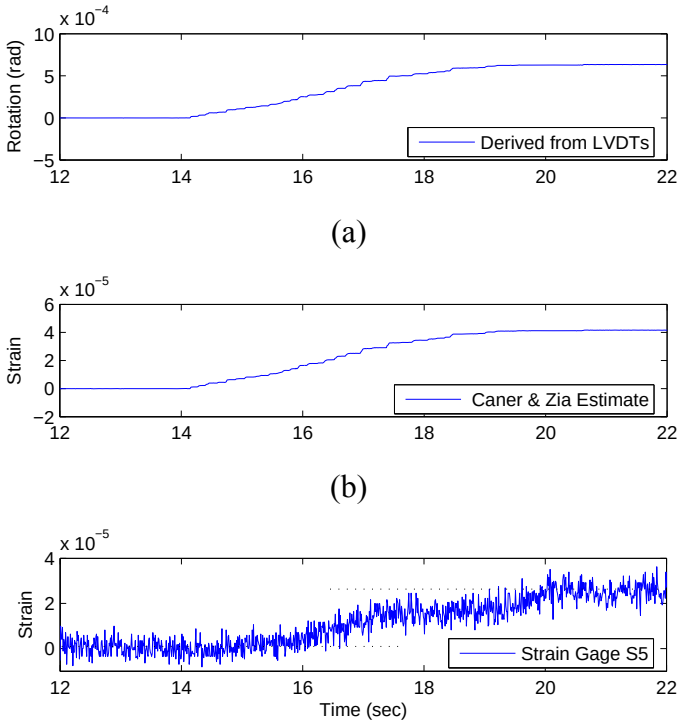

Figure 2-13: (a) Girder 2 (beneath the southbound) rotation calculated from top and bottom girder LVDTs; (b) estimated strain based on link slab rotation (Caner and Zia 1998); (c) measured strain in center of link slab reinforcement bar.

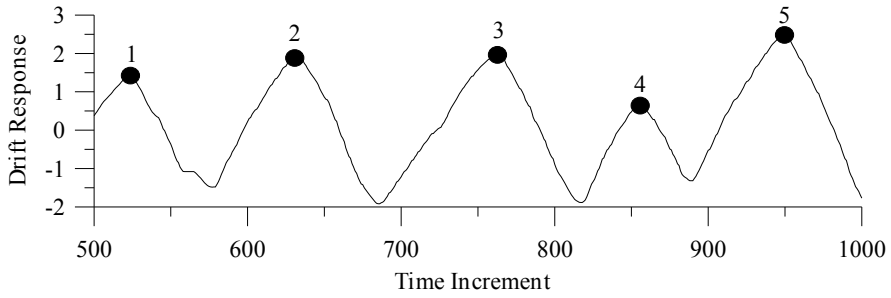

Figure 2-14: A period of drift response of cyclically loaded structural elements.

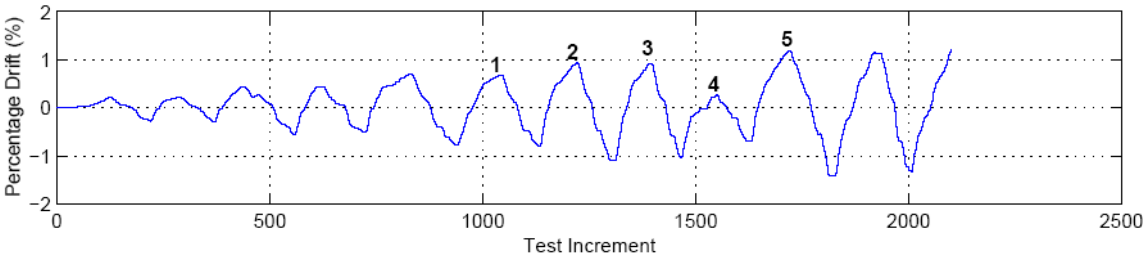

Figure 2-15: Drift response of cyclically loaded HPFRCC coupling beam (Canbolat *et al.*, 2004).

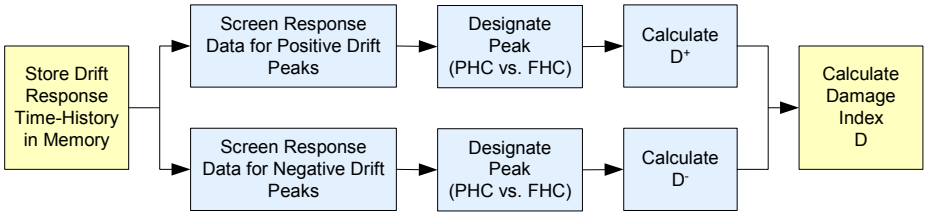

Figure 2-16: Embedded firmware for calculation of the damage index.

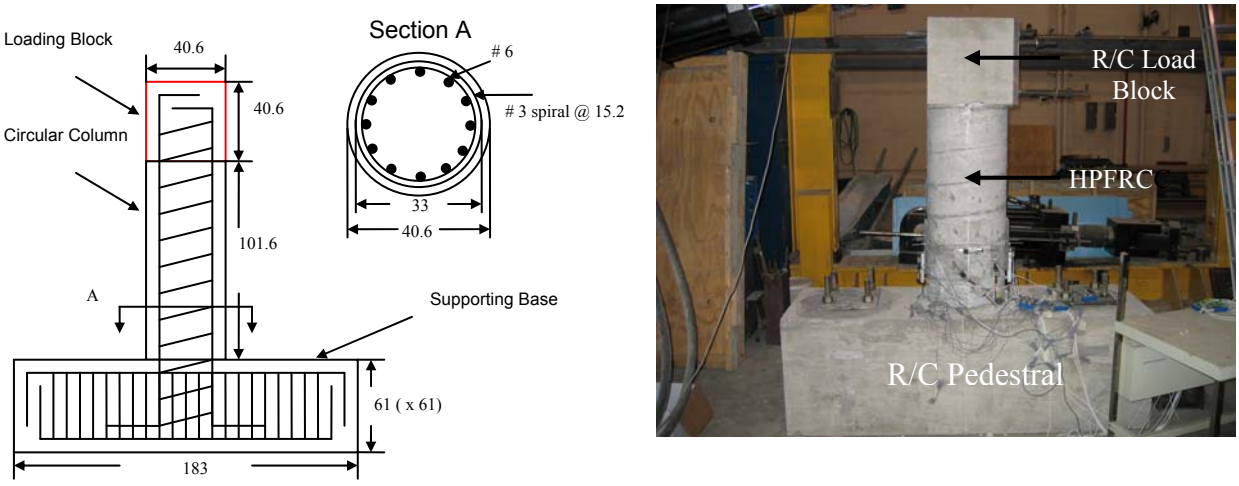

(a) (b)

Figure 2-17: Geometry and reinforcement detailing of the bridge pier (units shown are cm), (b) the completed HPFRCC bridge pier.

(a) (b) (c)

Figure 2-18: (a) LVDTs instrumentation at the pier base, (b) two LVDT pairs mounted to the front and back pier faces, and (c) a wireless sensing unit mounted to the top of the concrete support pedestal.

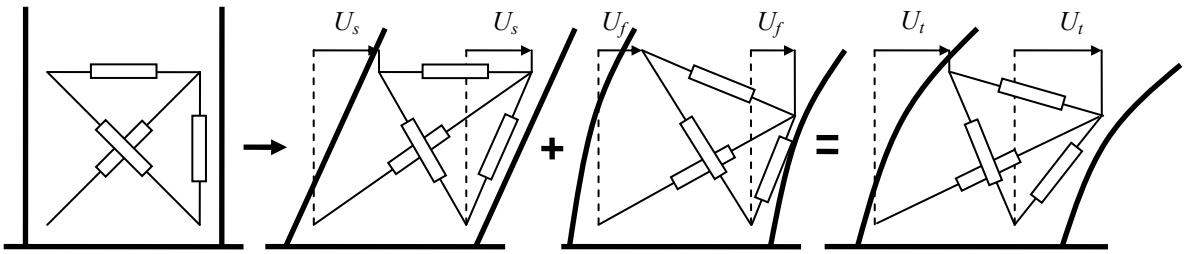

(a) (b) (c) (d)

Figure 2-19: Combination of shear and flexural deformations in plastic hinge region of bridge pier specimen.

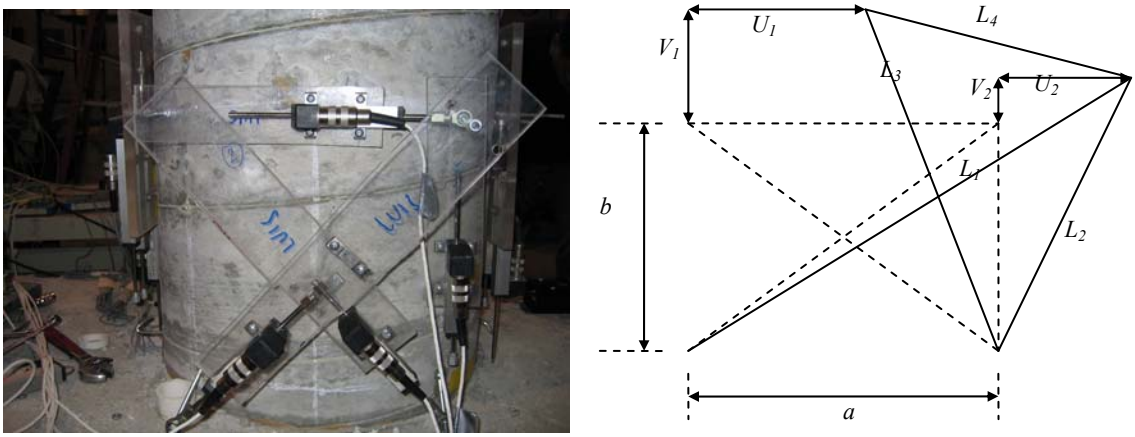

(a) (b)

Figure 2-20: (a) Instrumentation of the LVDTs at the pier base, and (b) measurements of the total deformation.

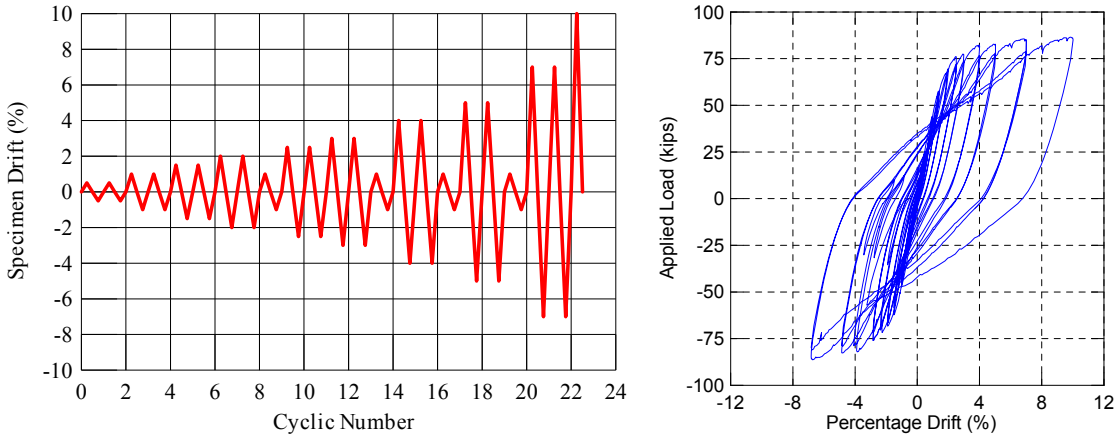

(a) (b)

Figure 2-21: (a) Applied loading, and (b) the corresponding shear force-drift response.

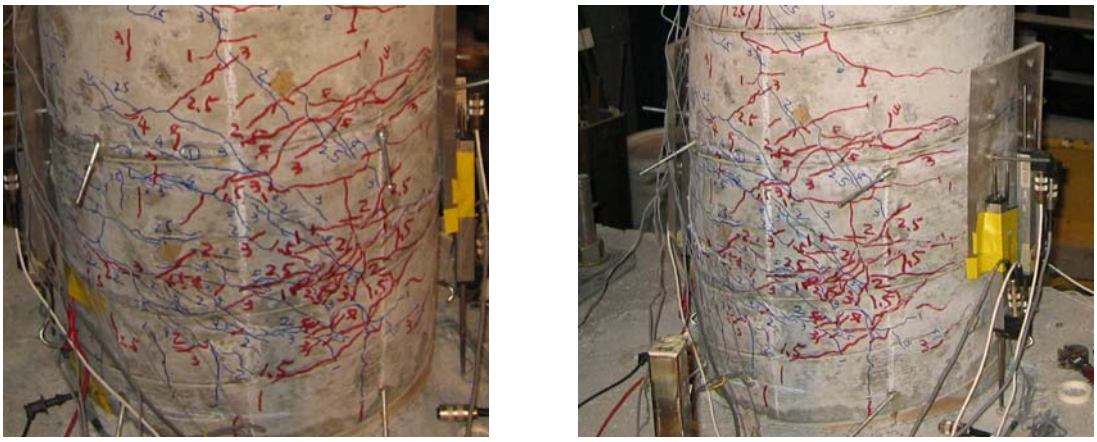

(a) (b)

Figure 2-22: (a) Crack pattern at 4% drift at the base (b) Crack pattern at 10% drift at the base.

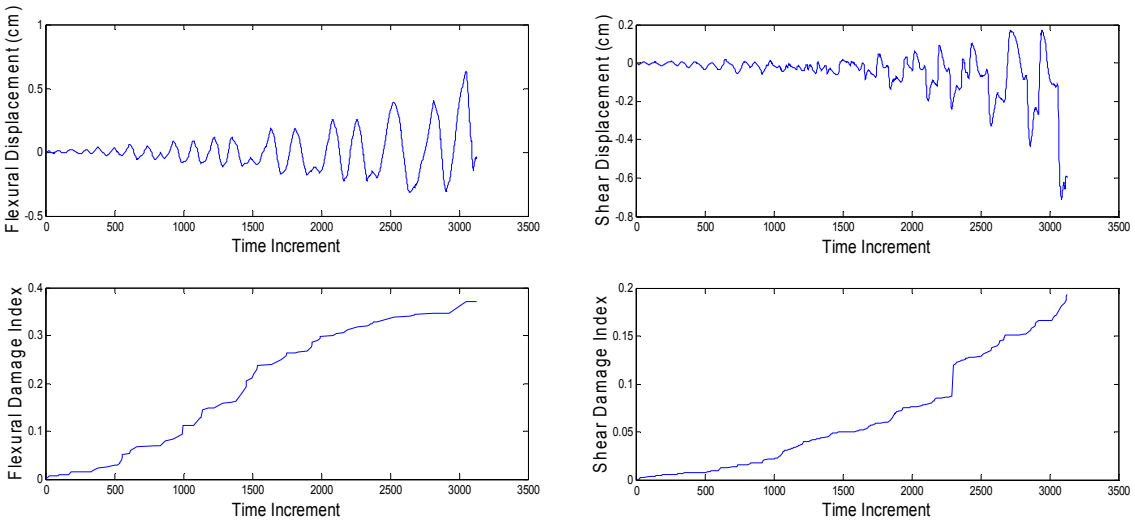

(a) (b)

Figure 2-23: HPFRCC bridge pier damage index for (a) flexural deformation and (b) shear deformation.

Table 2-1: Performance specifications of the wireless sensor prototype

Attribute	Specification
Sensing Channels	*4*
Sample Rate	*100 kHz*
Sensor Inputs	*0 – 5 V*
Memory for Embedded Algorithms	*128 kB*
Memory for Data Storage	*128 kB*
Clock Frequency	*8 MHz*
Radio Carrier Band	*2.4 GHz*
Communication Range (outdoor/indoor)	*180 m/ 5 km*
Power Source (Lithium-ion recommended)	*5 AA Batteries*
Power Consumption (radio off/radio on)	*150 mW/ 380 mW*

Chapter 3

Self-Sensing Multifunctional Cementitious Materials

3.1 Introduction

In Chapter 2, some promising sensing (*e.g.* wireless sensors) and damage detection (*e.g.* damage index algorithms embedded in the wireless sensors) technologies were explored for monitoring FRCC element's behavior and health in the field and laboratory settings. The low-cost attribute of wireless sensors was particularly attractive since structural owners can elect to install a higher density of sensors in a single structure for the same cost as a tethered monitoring system. As a result, individual structural elements (*e.g.* beams, columns, joints) can be instrumented with sensors. With damage inherently a local phenomenon, component-level sensing is better scaled for damage detection. Of particular interest in this thesis is the identification and characterization of crack damage in FRCC elements.

While the damage index methods presented in Chapter 2 can serve as a means of rapidly assessing the degree of cracking-induced damage in cementitious structural elements, they do not provide detailed data on cracks such as their location and severity (*i.e.* width). Such crack information is needed when owners must decide if repair of the damaged elements are required. Priorities should be given to cracks that are deemed critical to the structure's functionality (*e.g.* safety, stability). Furthermore, identification of cracks can also be used to evaluate the long-term sustainability of cement-based structural elements.

For example, cracks that do not reduce the load capacity or stiffness of a structural element might still be a problem with respect to corrosion of buried steel reinforcement. Hence, detection and characterization of all cracks is critical. Unfortunately, minor cracks that do not affect the global structural integrity of the system (but that pore as risks for corrosion) are nearly impossible to detect for observation of the behavior of the system. By considering the limitations of sensing and damage detection technologies studied in Chapter 2, the remainder part of this thesis provides a novel alternative for sensing strain and cracking in cement-based structural elements by using their electromechanical properties. This approach will prove capable of detecting serious as well as minor cracks.

This chapter begins by exploring the piezoresistive properties of FRCC materials. Knowledge of the piezoresistive (*i.e.*, strain induced resistivity changes) properties of FRCC materials is needed to accurately measure their electrical response to load and to correlate changes to strain and cracking damage. As will be presented in subsequent chapters (Chapters 4 and 5), the electrical properties of cementitious materials will be leveraged to provide spatial images of strain fields and cracks in high performance fiber reinforced cementitious composites. Highly detailed images of strain and cracking allow engineers to quantify local damage in critical HPFRCC structural elements.

Before introducing the electromechanical characterization methods that will be used, this chapter begins with a survey of the existing sensing technologies available for crack detection in cementitious structural elements. While many of these methods have been successfully employed in actual civil structures, this thesis will offer a novel approach to crack detection based on the electrical properties of cementitious materials. Towards this end, a detailed description of the techniques available for accurately measuring the bulk conductivity of cement-based materials will be reviewed. Major issues related to the presence of electric fields within cementitious materials must be considered when interpreting the electrical measurements. Other critical issues such as the electrochemical reaction that occurs at the electrode-cement interface are also investigated. Finally, the conductivity of HPFRCC materials are correlated to strain and cracking in uniaxially

loaded plate elements. It should be mentioned that although in this study only a specific type of HPFRCC (ECC M-45) is investigated, using the electromechanical properties of a material for autonomous damage detection can be applied to many other cement-based materials (*e.g.* concrete). Other researchers have also begun to study the piezoresistivity of FRCC materials with the aim of using them as their own sensors (Chung, 2001; Reza *et al.*, 2003; Hou and Lynch, 2005b; Li *et al.*, 2006). The addition of sensing functionality with mechanical functionality has led to FRCC materials being classified as a multifunctional material platform (Chung, 2003).

The objectives of this chapter can be summarized as follows:

- Characterize the bulk conductivity of ECC materials during the hydration process.
- Explore the self-sensing abilities of cementitious materials by using their electromechanical properties.
- Build a foundation for sensing strain fields and identifying crack damage in HPFRCC elements using electrical methods.
- Identify issues that would cause errors in the electrical measurement made of HPFRCC materials.
- Illustrate changes in the conductivity of ECC plate elements under tensile loading.

3.2 Review of Existing Technologies for Crack Detection

Cracking in cement-based structures, such as those constructed of reinforced concrete, can result from a variety of factors including externally applied loads, shrinkage, poor construction methods, among many others. When making an assessment of the general state of health of such structures, cracks must be reliably quantified and their significance determined. For example, small cracks affecting only the external aesthetic of the structure should be differentiated from those that reduce its strength, stiffness and long term durability (ACI, 1998). Detailed visual inspection of the surface of the structure remains a common method for detecting cracks; systematic crack mapping allows inspectors to monitor the progression of cracks and to hypothesize the nature of their

origins (Bungey *et al.*, 2006). After suspicious cracks are encountered, nondestructive (*e.g.*, ultrasonic inspection) and partially destructive (*e.g.*, core holes) testing can be carried out by trained inspectors to determine crack features below the structural surface (ACI, 1998). However, all of these methods require the use of trained personnel to execute, rendering them tedious and expensive. In contrast, automated sensor technologies are needed for permanent installation so that accurate assessments of cracking could be made without requiring a trained professional to visually inspect the structure.

A variety of approaches have been proposed for automated structural health monitoring of concrete structures. Generally, many of these approaches call for the installation of external sensors to measure global and local structural responses to loading. Early work explored the use of vibration measurements (*e.g.*, accelerations) to identify global modal properties that change when structural damage is present. Particularly for civil structures, environmental variability often hinders accurate correlation of modal property changes to damage (Doebling *et al.*, 1998). Alternatively, local structural measurements including strain and deformation have also been proposed for crack detection. Based on the applied structural loading and the corresponding component response, various damage index methods (for example, those presented in Chapter 2) have been proposed for the quantification (often on a scale from 0 to 1) of cracking degree in concrete structural elements (Park and Ang, 1985; Kratzig *et al.*, 1989). While damage index methods like those presented in Chapter 2 perform well when predicting cracks in laboratory elements, the inability to precisely measure loads on full-scale concrete structures renders this approach difficult to apply in more practical settings.

Perhaps the best approach for automated structural health monitoring of concrete structures entails the adoption of the sensors available in the nondestructive evaluation (NDE) field. In particular, passive and active stress wave approaches have been proposed for NDE evaluation of concrete structures. Acoustic emission (AE) sensing is foremost amongst the passive stress wave methods. AE employs piezoelectric elements to capture the stress waves generated by cracks (Quyang *et al.*, 1991; Shah and Choi,

1999); while AE has played a critical role in the laboratory, its success in the field has been limited to only a handful of applications (Mindess, 2004). In contrast, active stress wave methods have proven more accurate for crack detection in the field. This approach entails the use of a piezoelectric transducer to introduce a pulsed ultrasonic stress wave into a concrete element and using the same transducer or another to measure the pulse after it has propagated through the element. For example, pulse-echo (using one transducer) and pitch-catch (using two transducers) techniques have all been proven robust in characterizing cracks in actual concrete structures (Carino, 2004). A direct extension of the active stress wave approach is the electromechanical impedance spectra method. This approach measures the electromechanical impedance spectrum of a piezoelectric transducer to detect cracking in the vicinity of the surface mounted transducer (Park *et al.*, 2000; Park *et al.*, 2006). With digital photography rapidly maturing, many researchers have also adopted the use of charge-coupled device (CCD) cameras to take photographic images of concrete structural elements; subsequent application of digital image processing techniques automates the identification of crack locations and widths (Toussaint *et al.*, 2005; Lecompte *et al.*, 2006).

Compared to other NDE methods, utilization of the electrical properties of cement-based materials for crack detection has garnered less attention from the civil engineering community. Historically, electrical properties have been investigated for tracking the formation of microstructural properties during hardening (Han *et al.*, 2005) and to quantify the potential for corrosion of buried steel reinforcement (Lauer, 2004). In contrast, this study will utilize the electrical properties of cementitious materials as a novel approach to automated strain monitoring and crack detection of cementitious civil structures.

3.3 Electrical Conduction in Cementitious Materials

3.3.1 Flow of Electricity in Cementitious Materials

Conductivity (σ) is a fundamental material property that quantifies the ability of the material to carry a current when placed in an electrical field. Specifically, the current flow density, **J**, is linearly proportional to the electric field, **E**, through conductivity, σ, (Mayer and Lau, 1990):

$$J = \sigma E \tag{3.1}$$

Resistivity (ρ), the inverse of conductivity ($\rho=1/\sigma$), is the volumetric resistance, R, of a unit cube as measured across one dimension. Resistivity is reported in terms of Ω-m while conductivity is reported using the units S-m^{-1} (Ω^{-1}-m^{-1}). With conductivities ranging from 10^{-3} to 10^{-6} S-cm^{-1}, cementitious materials are generally classified as semiconductors (Whiting and Nagi, 2003). In cement, the current generated by an electric field is based on ionic conduction. The high concentrations of calcium, potassium, and sodium salts within the pore water and water-cement gel are mobilized by the elastic field to create current (Hansson and Hansson, 1983). Since the ions in water are the primary charge carrier, the conductivity of cementitious materials naturally exhibits strong dependency on the moisture content of the material.

The electrical conductivity of cementitious materials can be varied with the inclusion of conductive fibers such as carbon and steel fibers. Conductive fibers provide additional paths for electrical current to travel through the cement matrix thereby raising the conductivity of the bulk material. Therefore, the electrical properties of FRCC materials using conductive fibers are the combination of the cement matrix and the fibers within it. The physical interface that lies between the conductive fibers and the cement matrix is also known to play a role in the electrical properties of the composite material. Researchers have found that the electrical conductivity of the fiber-matrix interface is frequency dependent (Reza *et al.*, 2003; Peled *et al.*, 2001). For example, direct current (DC) and low frequency alternating current (AC) tests reveal that the fiber-matrix interface is characterized by a high impedance. As a result, the composite conductivity is dominated by the electrical properties of the cement. As the AC frequency is raised, the

interface impedance lessens and the composite's electrical properties are strongly influenced by the conductivity of the fibers (Reza *et al.*, 2003).

It has been found that the mechanical deformation, specifically tensile strain, will induce a detectable change in the electrical conductivity of a cementitious material. Furthermore, research done in the piezoresistivity of FRCC materials has revealed that due to the absence of large aggregates and the presence of conductive fibers, piezoresistive behaviors are fairly linear as well as repeatable (Chung, 2003). This is mainly due to conductive fibers that bridge the cracks that form from tensile strain. For example, if an FRCC specimen with fibers is sustaining cracking as shown in Figure 3-1, the electrical current, *i*, will not travel through region "1" since both the matrix and fibers are separated from each other. In contrast, the fiber bridging mechanism depicted in region "2" allows the electrical current to pass across the matrix crack via conductive fibers. As a result, the increased electrical resistivity is partially or even fully reversible once the crack is closed upon compression of the material. If nonconductive fibers are used, then region "2" is similar to region "1" with no current passing across the crack. For completeness, consider region "3"; the electrical conductivity of the uncracked region is attributed to the cement matrix and the fibers (if conductive).

3.3.2 Electrical Measurements

Considerable attention has been paid in recent years to measuring and interpreting the electrical properties of cement composites including concrete. Specifically, the electrical properties of cement can be used to assess the microstructural details of the material (Han *et al.*, 2005). For example, very early work in the field explored correlations between direct current (DC) conductivity measurements and the setting times of Portland cement composites (Calleja, 1953; Hammond and Robson, 1955). More profound insight to the hydration process has been gained since the 1990's through the use of electrical impedance spectroscopy (EIS). EIS measures conductivity as a function of the angular frequency of an applied alternating current (AC) signal (McCarter and Brousseau, 1990). Impedance spectra obtained by EIS can be used to track hydration processes, identify the porosity of cured cement, and characterize interfacial properties (*e.g.*, cement-steel or

cement-aggregate interfaces). The electrical properties of cement also serve as a basis for assessing the corrosion potential of reinforced concrete (Lauer, 2004). When reinforcement steel corrodes, the cement conductivity is a measure of how easy it is for ions to flow between the anodic and cathodic sites of the buried steel reinforcement. It has not been until very recently that the electrical properties of cementitious materials have been explored for damage detection including the identification of cracking (Peled *et al.*, 2001; Chung, 2001; Hou and Lynch, 2005a).

Multiple measurement methods have been proposed for measuring the conductivity of cement-based materials. In general, the measurement methods proposed can be broadly classified as either two-point or four-point probe methods. In the two-point probe methods (Figure 3-2a), two electrodes are used to apply an electrical current, I, and to also measure the corresponding drop in voltage, V, across the cement specimen. Electrodes must be in intimate contact with the cement-based specimen to induce an ionic current within the specimen. Metallic electrodes can either be surface mounted using conductive gels and pastes, or they can be embedded directly into the wet concrete prior to hardening (Whiting and Nagi, 2003). If a direct current (DC) is applied across the specimen area, conductivity can be calculated,

$$\sigma = \frac{I}{V}\frac{L}{wh} \tag{3.2}$$

where L, w and h correspond to the electrode spacing, specimen width, and specimen height, respectively. While two-point DC probe measurements are easy to take, they do suffer from two major drawbacks. First, contact impedance at the electrode-cement interface in the two-point probe method introduces a time-dependent reduction in conductivity. Contact impedance originates from the electrochemical reactions that naturally occur in the test specimen in the vicinity of the electrode (Vilhunen *et al.*, 2002). For example, electrons flowing into a specimen at the electrode induce pore water to decompose into hydrogen (H_2) and hydroxide ions (OH^-) (Hansson and Hansson, 1983). Similarly, free hydroxide ions can react at the other electrode to produce electrons (e^-)

that then flow into the electrode as well as producing oxygen (O_2) and water (H_2O). These reaction byproducts accumulate at the electrode-specimen interface resulting in a back electromagnetic field. The second drawback of DC two-point methods is the measurement error introduced by polarization of the specimen. Polarization is the separation of positive and negative ions trapped within the cement pores; as ions separate, less current is carried resulting in a reduction in the conductivity measurement (Hansson and Hansson, 1983). As a result, alternating current (AC) is preferred since contact impedance and polarization effects do not have sufficient time to develop under an alternating field (Whiting and Nagi, 2003). When AC signals are used in the two-point probe method, Equation 3.2 is still valid using the amplitude of the current and voltage.

The four-point probe method is the preferred approach for measuring the conductivity of cement-based materials (Millard, 1991). As the name suggests, the four-point probe method employs four independent electrodes along the length of a specimen (Figure 3-2b). The two outer-most electrodes are used to drive an electric current (DC or AC) into the medium while the two inner electrodes are responsible for measuring the electrical potential developed over the length, L. Again, if it is assumed the cross-sectional area of the specimen is w by h, then Equation 3.2 is still valid. In the four-point probe method, the effects of contact impedance are minimized because the measurement and excitation electrodes are separated. As a result, four-point probe methods provide a more consistent measurement of electrical conductivity when compared to two-point probe methods.

A specialized version of the four-point probe method is the Wenner technique (Gower and Millard, 1999). Although this approach was originally developed for *in-situ* measurement of soil conductivity, it has been widely applied to measurements in cementitious materials. In the Wenner technique, four electrodes equally spaced (by a) along a straight line are applied to the surface of a cementitious specimen, as shown in Figure 3-3. If the specimen is assumed to be an infinite half-space, then conductivity can be calculated (Millard, 1991):

$$\sigma = \frac{I}{V}\frac{L}{2\pi a} \tag{3.3}$$

Both DC and AC electrical excitations can be used, but generally AC excitations greater than 100 Hz are preferred (Han *et al.*, 2005). Some care must be exercised when using the Wenner technique. For example, test specimens must be sufficiently thick (generally, thicknesses 4 times greater than the electrode spacing) to ensure the assumption of an infinite half space is valid. Similarly, measurements must be made away from specimen edges and corners.

Electrical impedance spectroscopy (EIS) is a more sophisticated electrical characterization technique based on AC signals. Similar to the aforementioned four-point probe measurement method, two probes are employed to apply an AC current to the specimen while two inner electrodes measure voltage (Figure 3-4a). In EIS, a frequency response analyzer (FRA) is adopted to measure both the amplitude and phase of the voltage measurement relative to the applied current (Barsoukov and Macdonald, 2005). Using amplitude and phase, the complex-valued impedance of the material can be measured as a function of applied AC frequency, ω. The frequency is varied from low to high frequencies with complex impedance,

$$Z = \frac{V_A \sin(\omega t + \theta)}{I_A \sin(\omega t)} \tag{3.4}$$

plotted on the complex plane. The real and imaginary components are associated with the conductivity and capacitive properties of the specimen, respectively. For many cementitious materials, the impedance plot consists of two semi-circular traces as shown in Figure 3-4b. Such distinctive impedance plots permit the use of equivalent parallel resistor-capacitor (RC) circuits (Figure 3-4c) to model the electrical behavior of the material. The low-frequency semi-circular trace ($\omega_1<\omega<\omega_2$) corresponds to the behavior of the electrode while the high frequency trace ($\omega_2<\omega<\omega_3$) corresponds to that of the cementitious material (Han *et al.*, 2005).

3.4 Conductivity of Fiber Reinforced Cementitious Materials

Before the piezoresistivity of high performance fiber reinforced cementitious materials can be characterized, the conductivity of the material prior to loading should be quantified. While 2- and 4-point probe methods will be used, interpretation of conductivity results will be necessary. Specifically, measurements of bulk conductivity will exhibit a variation in time. Time dependency is a direct result of the measurement technique and the dielectric properties of the material itself. Changes in conductivity due to the dielectric properties of the material are termed polarization.

Within the pores of cement-based materials is both water and ions. Under an applied steady (static) electric field, the positive and negative ions separate with positive ions attracted to the higher potential and negative ions attracted to the lower potential. Similarly, the water (H_2O) molecules rotate so that the apparent positive charge of the water molecule is closest to the higher potential, while the apparent negative charge is closest to the lower potential. As the molecules move to be in their lowest energy state, the measured conductivity will decrease. This change in electrical conductivity is often viewed as an intrinsic feature of the material and has been used to understand the materials' chemical, rheological and mechanical properties. For example, researchers have studied the dielectric properties of cement mixtures to better understand the hydration process in freshly cast cement (McCarter and Brousseau, 1990). For example, the dielectric property of cement undergoes a significant change during the first 24 hours of curing (McCarter and Afshar, 1984; McCarter and Afshar, 1985). Different cementitious admixtures and their rates of polarization have been investigated by Cao and Chung, 2004).

When making conductivity measurements of cementitious materials, the different measurement techniques (*i.e.* 2-point probe and 4-point probe) lead to different bulk conductivities. First, consider the case of the 2-point probe method (Figure 3-2a) using

direct current (DC). As shown in Figure 3-5, the measurement of resistivity (inverse of conductivity) from the first 600 seconds of an ECC specimen reveals an exponential increase. This is due to polarization of the material. As the DC current is applied to the test specimen, resistivity slowly rises due to the alignment of dipoles (*e.g.*, ions, water) in the material. In contrast, consider the case of the 4-point probe resistivity measurement history using DC current and the same specimen. Again, an exponential increase in resistivity is observed; such an increase is due to material polarization. However, two observations can be made. First, it appears that the polarization occurring during 2-point probing is greater than that during the 4-point test. Second, the initial and final (steady-state) resistivity values are not in agreement with one another. Both observations are a direct result of contact impedance at the electrode-cement interface.

Contact impedance is a phenomenon that occurs at the probing electrode. Under an applied current, an electrochemical response occurs at the electro-specimen boundary creating a capacitive double layer (Hansson and Hansson, 1983). This high impedance layer is characterized by a high resistance and a high capacitance. The resistance appears as a large increase in resistivity at the initial start of the 2-point probe test. As time progresses, the capacitive double layer at the point of contact also absorbs some of the applied current, just as a capacitor would. As the capacitive double layer charges, the resistivity measurement slowly rises. This is why the exponential rise in resistivity is much greater than that for the 4-point probe test. Since in the 4-point probe test, the voltage measurement is made at probes separate from the probes used to apply current, the effects of contact impedance are minimal.

3.4.1 Resistivity Measurement of ECC Specimens

In this section, the measured resistivity of M-45 ECC test specimens is investigated using both 2- and 4-point probe methods. In the first part of the resistivity study, 2-point and 4-point probe methods using direct current (DC) is adopted. These sets of test are conducted to quantitatively compare polarization at the electrode and of the material. The results will verify that using the 4-point probe method provides a more accurate resistivity measurement. The second part of the study adopts the 4-point probe method to

monitor the resistivity of ECC specimens at multiple degrees of hydration; namely, at 1, 7, 14, 21, 28, and 35 days after casting. Polarization calibration curves are fit to the experimental data to provide a polarization database for M-45 ECC during the critical hydration period (1 to 35 days). The last part of the study investigates the use of alternating currents (AC) in the 4-point probe method as a means of minimizing the polarization of ECC materials.

A total of 6 M-45 ECC test specimens roughly 7.5 x 1.25 x 1.25 cm^3 in size are cast. M-45 ECC material is constructed from a combination of Type III Portland cement (cement to water ratio of 0.53), silica sand, fly ash, and short polyvinyl alcohol (PVA) fibers. In the specimens constructed, only a 2% volume fraction of PVA fibers is included in the cement matrix so as to provide strain-hardening and ultra-ductility. In addition, no aggregates are present thereby rendering the material as electrically homogeneous. An adequate amount of superplasticizer is also used in casting the ECC specimens in order to increase the workability of the mixtures and to guarantee all of the fibers are well dispersed. After 1 day of curing, electrodes made of copper tape are applied to the specimen surface using silver paste; the electrical tape is applied around all four sides of the specimen, roughly 4 cm apart, as shown in Figure 3-6. Current is applied to the specimen using a DC current source (Keithley 6221) while voltage measurements are made using a digital multimeter (Agilent 34401A). The first set of DC 2-point and 4-point resistivity measurements is made one day after casting. A direct comparison between the 2- and 4-point probe measurements will be made for the 1 day old specimens. Then 2-probe measurements are repeated every seven days until 35 days are reached.

Figure 3-7 shows the time history of measured resistivity by 2-point (Figure 3-7a) and 4-point (Figure 3-7b) probing of the six 1-day old specimens. The aforementioned polarization and contact impedance affects can be seen in both plots. At t=0, the measured resistivity by the two methods is distinctly differently. The 2-point probe measurement is nearly 4.5M Ω-cm greater than that of the 4-point probe measurement. This difference is due to the high resistance associated with the contact impedance common to the 2-point probe measurement. There is also a distinguished difference in

the rate of increase of the measured resistivity by the two methods. The 4-point probe measurement has a lower rate of increase; this exponential rise is due to the polarization of the cement material. In contrast, the 2-point probe resistivity rises at a much higher rate because both the material and capacitive double layer at the contact must charge. Regardless, both resistivity measurements plateau off after about 600 seconds. A clearer picture of this is gained if the average resistivity of all six specimens is plotted for both the two and four point methods (Figure 3-7c).

Since polarization is caused by the movement of ions within cementitious materials, the degree of hydration in the material would significantly impact the mobility of the ionic carriers in the pores. Therefore, the exponential rise in resistivity in both measurement approaches would change as the cement specimen matures after casting. This phenomenon has given opportunity to use the polarization behavior as an indirect means of monitoring the hydration level of cementitious materials; however, no much related work has been conducted so far. As hydration is more relevant to the material itself than the electrode/material interface, the 4-point probe DC method is used to measure the material polarization. Similar to the past set of test, 10 M-45 ECC specimens with the dimensions 7.5 x 1.25 x 1.25 cm^3 are prepared. The cast specimens are then permitted to cure. After one day, four copper tape electrodes are mounted to the specimen. At 1, 7, 14, 21, 28, and 35 days, a 4-point probe resistivity measurement is made for each specimen. The magnitude of direct current (DC) used during 4-point probing is varied from 500 nA to 5 μA.

Figure 3-8 shows the resistivity measurement of all 10 specimens over the first 600 seconds of data collection. For the test specimens tested on the first day, the initial resistivity is about 158 kOhm-cm and grows to around 200 kOhm-cm (resistivity plus material polarization) after 600 seconds of DC charging. Moreover, both the initial resistivity (at t=0) and magnitude of polarization are seen to increase as the samples cure. For example, the initial resistivity of the specimens at 14 days is about 524 kOhm-cm and exponentially increases to about 720 kOhm-cm after 600 seconds of DC measurement. For specimens tested 35 days after casting, the initial resistivity is 652 kOhm-cm and

increases to about 880 kOhm-cm after 600 seconds of polarization. It should be noted that both initial resistivity and polarized resistivity reported in this study are under the case of 100% relative humidity (RH) curing environments. For cementitious materials that are naturally cured in air and not in a 100% RH environment, the initial resistivity and polarization may vary due to the variations in moisture contents that may occur over the test time period.

The higher initial and polarized resistivity encountered as the specimens cure can be easily explained. Since more and more ions are trapped by the hardening hydration by-products, it is harder to mobilize the ions, which is consistent with a higher resistivity. It can also be observed from Figure 3-8 that as the hydration level increases, polarization requires more time to reach its saturation level. This explanation is consistent with the slower mobility of the ionic carriers within the cementitious material as they cure. It can be concluded that at the early stage (*i.e.*, the first 24 hours) the electric properties of the cementitious material are characterized more by their initial resistivity, however, as the hydration process proceeds, the polarization properties of the material become more pronounced.

The general trend in the 4-point probe resistivity measurement is fairly consistent. Therefore, it can be accurately modeled for the M-45 ECC material for the different levels of hydration. The experimental data of Figure 3-8 is used to find the best fit exponential model of the following form:

$$\rho = \rho_0 + a_1\left(1 - e^{-\left(\frac{t}{a_2}\right)^{a_3}}\right) \tag{3.5}$$

Here, ρ_0 is the initial resistivity (at t=0) while a_1, a_2, and a_3 are model parameters fit to the experimental data. Time, t, is in units of seconds. For each hydration level, the model parameters (ρ_0, a_1, a_2, a_3) are tabulated in Table 3-1. The first 600 seconds of the modeled resistivity are presented in Figure 3-9a. In Figure 3-9b, the initial (ρ_0) and

steady state resistivity are plotted as a function of curing time. Both parameters seem to have their own steady-state values of about 600 kΩ-cm and 900 kΩ-cm, respectively.

The previous tests (2-point and 4-point probe measurements using a DC source) have shown the impact of both the electrode and material polarization on the resistivity measurement of the cementitious material. Both effects are time dependent and require a certain time duration before reaching their saturation limits. It has also been shown that by employing the 4-point probe method, the polarization of the capacitive double layer at the electrode boundary is removed. However, using a DC current, the 4-point probe still has the issue of material polarization. Since material polarization is due to the separation of charge caused by the presence of external electric fields (which in this study is introduced by the current injection), this charge separation can be mitigated, or even eliminated, if the direction of the ionic structure reorientation is reversed. Hence, by using an alternating current (AC) in lieu of a DC current, the material polarization effects can be nearly eliminated.

In order to investigate the ability of AC to stabilize the resistivity measurement (eliminate the polarization effect) three of the M-45 ECC specimens from the DC 4-point resistivity tests are subjected to different AC frequencies with resistivity measured for 300 seconds. Cast specimens are tested 14 days after casting. The magnitude of the AC current amplitude is configured to be 50 μA with the signal frequency varied from 10 Hz to 100 kHz. Plotted in Figure 3-10 is the measured resistivity of the three M-45 ECC specimens over 300 seconds. Clearly, the resistivity measurement is itself fluctuating at the same oscillation as the AC signal. Clearly, at lower frequencies the amplitude of variation is greater since the specimen has more time to polarize before polarity of the electrical signal is reversed. As frequency increases, the amplitude reduces suggesting a lower error in the resistivity measurement. Important to note, the higher AC frequencies (f>1 kHz) have amplitudes reducing asymptotically to mean measured resistivity. If the amplitude of the resistivity measurement is considered an “error” inherent to the technique, it is clear that the error is reduced as higher AC frequencies are adopted.

Figure 3-11 reveals a fairly linear relationship between percent error and AC frequency when plotted on a log-log scale.

3.5 Piezoresistivity Monitoring of HPFRCC Structural Components

The previous section characterized the electrical properties of ECC, a highly ductile HPFRCC material. As previously reported, such materials are piezoresistive with their resistivity changing in relation to strain. This thesis is the first to explore the piezoresistivity of ECC materials; the work sets a scientific foundation for the use of the material as a self-sensing material for structural health monitoring as will be presented in subsequent chapters.

The piezoresistivity study is divided into 3 parts. First, the 4-point probe DC resistivity method is employed to monitor ECC resistivity during monotonic tensile load. Specimens are pre-charged for 1 hour in order to reach the polarization saturation before the application of load. The purpose of this set of tests is to illustrate the piezoresistive behavior of ECC materials under fully polarized conditions. The second phase of the study employs the 4-point probe AC method to monitor the piezoresistivity of ECC under monotonic tensile load. With the application of an AC current with a frequency greater than 1 kHz, material polarization will be nullified as illustrated in the previous section (3.4). The last phase of the piezoresistivity study employs the 4-point probe AC resistivity measurement method to monitor ECC specimens under cyclic loading. Specimens are placed under tension and compression reversals with the change in material resistivity recorded.

3.5.1 Experimental Methods

To investigate the piezoresistive properties of the ECC material, ten plate elements are constructed from the M-45 variation of ECC for axial loading. The dimensions of each plate are 30 x 7.5 x 1.25 cm^3 as shown in Figure 3-12a. Prior to axial loading, copper tape is wrapped around the specimen at the four locations shown in Figure 3-12a. These

four copper tape pieces will serve as the current and voltage electrodes for the 4 probe resistivity measurement. The Keithley 6221 current supply is used while voltage is measured using Agilent 34401A digital multimeter. When ready for testing, the specimens are clamped in a MTS load frame for application of uniaxial loading (3-12b). All specimens are loaded with very low loading rates ranging from 0.013 to 0.064 mm/second. The stroke of the load frame is recorded so that strain measurements can be made since access.

Before experimentation using the plates begins, validation tests are performed to compare the strains obtained from the load frame stroke, OptoTrak optical measurement system, and metal foil strain gages. Figure 3.13a shows the instrumentation sketch of the strain validation test. As seen in Figures 3-13b, 3-13c and 3-13d, there exists a certain discrepancy between the three strain measurements. Strains measured by the OptoTrak system and by the strain gages in strong agreement with each other through all of the regions (Region 1 to 5); however, the strain obtained by the frame stroke differs from the strain gages and OptoTrak system. For strain level below 0.1%, the difference between the three strain measurements is quite small. However, after 0.1%, there seems to be a major difference in the frame-derived strain and that measured by the OptoTrak and strain gage systems. At around 0.2%, this change stabilized. The behavior of the comparison between 0.1% and 0.2% is mainly due to the slipping of the clamp ends of the MTS load frame, which would lead to a larger measurement of the load frame stroke. Therefore, the strain calculated from the stroke of the load frame is not a very accurate measure for strain. However, stroke strain will be used in this study for all the tested ECC specimens due to instrumentation congestion.

3.5.2 DC Monotonic Loading Test

Although material polarization is common to DC-based 4-point probing, the approach can still be used if the element is “pre-charged”. In other worlds, if prior to loading the 4-point probe method is initiated but given sufficient time to achieve a steady-state, then the material is considered pre-charged. Only after pre-charging can the piezoresistive tests be done. In this study, three ECC specimens (after 14 days curing) are pre-charged

ahead of the application of mechanical loading so as to fully polarize the material. The three specimens will be denoted as Specimen DC-1, DC-2 and DC-3. Based on the results of section 3.4.1, an ECC specimen at the 14 day hydration level would reach the polarization plateau after 10 minutes using a DC current of 500 nA. As a result, all three specimens are subjected to 1 hour of a 500 nA DC current, so as to guarantee that no additional polarization effect would exist during mechanical loading. For the following two phase of the piezoresistivity characterization tests (namely, the AC piezoresistive tests), the experimental set up is kept the same as the one used here.

Figure 3-14a shows the polarization and piezoresistivity results for ECC specimen DC-1. As seen, resistivity experiences tremendous change during the first few hundred seconds and reaches a plateau after about 2000 seconds. Once the tensile loading is initiated at t = 3600 sec, the electrical resistivity responds immediately to the tensile load. Since polarization has been saturated before mechanical loading, any increase in the resistivity is now considered as strain-induced (*i.e.* the piezoresistive effect). Figure 4-14b replots the piezoresistivity response for t=3600 to 7200 seconds which corresponds to the time of axial loading. Although the electrical resistivity increases as the specimen is axially strained, it is obvious that the relationship between electrical resistivity and mechanical strain is not fully linear. The primary reason for this difference is due to the occurrence and location of cracks.

First, consider the plate element loaded only in its elastic regime as shown in Figure 3-14c (t=3600 to 4500). Clearly, the change in bulk resistivity is perfectly linear. This is because the plate element has not yet cracked. However, after the strain hardening regime has begun, the resistivity increase is no longer linear due to cracking. When cracks occur in between the two inner electrodes, these cracks effectively contribute to the growth of the material resistivity in the sense that the crack is blocking current flow to some extent. What is an interesting characteristic of the resistivity time history plot is that it is piecewise linear. Distinct regions where the resistivity-strain plot is linear are denoted in Figure 3-15b by dots A through H. Each linear segment is due to a given crack state.

Figure 3-15 to 3-17 show the piecewise piezoresistive behavior of specimens DC-1, DC-2 and DC-3, respectively. The associated gage factors (the percent change in resistivity divided by strain) for each segment of the piecewise linear resistivity-strain curve are also summarized in Table 3-2. As can be observed, the gage factors of M-45 ECC when using 4-point DC probing are generally lower during the elastic regime (A-B). The gage factors for all three specimens in the elastic range are consistent at about 6; this elastic gage factor is about half the value of the ones encountered in the strain-hardening range. It should be noted that these gage factors are well above those associated with traditional metal foil strain gages which typically have gage factors of 2 to 3 (Perry and Lissner, 1962).

Figure 3-17c through 3-17h shows the cracking pattern of specimen DC-3 at loading point B through G, respectively. By observing Figure 3-17c, it is evident that prior to the first cracking, changes of resistivity are mainly due to the elastic deformation of the HPFRCC specimen. During the strain-hardening stage, resistivity changes are caused by the development of new micro-cracks as well as the opening of existing cracks along the HPFRCC specimen. Once damage localization occurs (at point F), resistivity changes are then induced by the growth (*i.e.* widening) of the localized crack. The dependency of the gage factor on damage state could be potentially used to crudely estimate component health based on electrical resistivity measurement if strain is known.

3.5.3 AC Monotonic Loading Test

It has been shown that employing high frequency AC current would effectively mitigate and potentially eliminate polarization effects. Based on the results in Section 3.4.1, when the AC frequency exceeds 1 kHz, polarization resistivity would be nullified. In this phase of the study, 4-point probe AC methods are used to measure the resistivity changes resulting from strain as ECC specimens are subjected to monotonic tensile loading. Again, three M-45 ECC specimens that are cured for 14 days are used. The aforementioned Keithley 6221 current generator is set-up to output an AC current with the frequency and magnitude configured to be 5 kHz and 50μA, respectively. The tensile

strain rate is still kept slow (0.013 to 0.064 mm/second) so as to allow insightful observation of the material piezoresistivity during loading. The three specimens are labeled as specimen AC-1, AC-2 and AC-3.

Figure 3-18a and Table 3-3 show the piezoresistivity results of Specimen AC-1. Again, resistivity-strain linearity does not hold over the entire loading process due to cracking. By observing the associated cracking patterns at each loading point (Figure 3-18b through 3-18i), it can be concluded that one of the reasons leading to the fluctuation of estimated gage factors is the location of cracks. The resistivity varies in a piecewise linear fashion as the crack state of the material changes due to load. Gage factors for each segment vary significantly from 13 to 96 in the strain hardening stage. If micro-cracks are generated within the region between inner and outer electrode pairs, larger gage factors are obtained. In particular, in segments B-C, D-E, F-G and G-H most new micro-cracks are generated within the region delineated between the electrode pairs resulting in gage factors well above 70. The averaged gage factor is roughly 16 in the elastic stage and 60 in the strain hardening stage. Both are much higher than the gage factors obtained from the DC probe measurement taken in Section 3.5.2. The higher sensitivity encountered when employing AC current rather than DC current, may be due to the reactance of cementitious materials. Reactance, X, which is the imaginary part of the complex impedance and appears only when AC is applied:

$$Z = R + iX \tag{3.6}$$

where Z is the complex impedance, R is resistance and X is reactance. Under DC measurement, the impedance, Z, is equal to resistance, R. Researchers have argued that reactance is more sensitive to the mechanical strain for certain types of cementitious materials (Fu *et al.*, 1997). However, more work well beyond the scope of this study is needed to justify this statement. Figure 3-19 summarize the piezoresistivity results of the ECC specimens (specimens AC-1, AC-2, AC-3) and Table 3-4 shows the averaged gage factors. Compared to the gage factors obtained in section 3.5.2, 4-point probe AC

measurements give the best sensitivity (highest gage factors) than any other probe technique.

3.5.4 AC Cyclic Loading Test

In the previous two sets of tests, all of the ECC specimens are loaded monotonically. While linear strain-resistivity behaviors of the fiber reinforced cementitious material can be observed, the tests do not reveal if the behavior is reversible during cyclic loading. Reversibility of the piezoresistive phenomena is important if the strain measurement of ECC elements loaded by earthquakes or other cyclic loading scenarios is sought. To observe the change in resistivity under reversed cyclic loading, a set of uniaxial tests are carried out on ECC plates with both tension and compression cyclically applied. These plates are constructed using the same bath of ECC previously used in the monotonic test. However, the specimens tested cyclically have been cured for 28 days in 100% RH. Changes in resistivity during loading will be observed by 4-point AC probing. All AC details remain the same as for the monotonic tensile tests (Section 3.5.3). The cyclic loading history to be applied to the plate specimens is shown in Figure 3-20; specimens are referred to as specimen AC-C1, AC-C2, and AC-C3.

Figure 3-21 to 3-23 document the experimental results of the three cyclically loaded ECC specimens. The material piezoresistive sensitivity shows different magnitudes when in the elastic (the first two-half cycles) and strain hardening (the later cycles) stages. The elastic tensile gage factor is determined to be about 30. This is higher than the elastic gage factor determined during the AC monotonic tests. Therefore, it can be concluded that the amount of hydration has a strong influence on the elastic gage factor. Changes of the material resistivity also experience a slope jump when strain hardening is initiated, which coincide with the observations made during the previous monotonic tests. This observation is opposite to that made in the elastic regime. It is believed that since cracking has greater control over the tensile gage factor during strain hardening, the hydration level has little effect resulting in gage factors (~60) consistent with those obtained during the monotonic test. Moreover, material resistivity under compressive loading does not seem to vary as significantly as under tensile loading. This leads to a

much lower gage factor when ECC specimens are in compression than in tension, as shown in Table 3-5. One can also observe that as the loading reversals proceed, material resistivity does not entirely recover to the original value. Table 3-6 compares all the piezoresistivity results presented.

3.6 Piezoresistivity Test on Large-Scale Bridge Pier Specimen

In order to illustrate the possibility of using the electromechanical methods studied in this chapter to monitor the behavior of large-scale HPFRCC structural elements, the bridge pier tested in Chapter 2 is instrumented with electrical probes. Figure 3-24a illustrates the instrumentation of LVDTs along with copper electrodes at column base. The four copper electrodes will be used to make 4-point DC resistance measurement of the base region of the pier. The presence of the LVDTs (oriented to measure longitudinal deformation) in this region will permit resistance measurements to be compared to the average strain. It should be mentioned that in this case the measured resistances are not converted into resistivity since the probes are not surrounding a volume of the HPFRCC material. Rather, electrodes are mounted only on a limited portion of the bridge pier perimeter surface; hence, resistivity/conductivity calculation using Equation 3.2 is not valid. This is done to avoid mounting electrodes along the entire column perimeter. Regardless, the resistance measurements can still be used to observe the piezoresistive behavior of the HPFRCC bridge pier. Figure 3-24b shows the relationship between the LVDT readings and the measured resistances when the bridge pier is cyclically loaded for the first few cycles of the load schedule detailed in Figure 2-21a. As observed in this figure, there exists a strong correlation (roughly linear) between longitudinal deformation and electrical resistance in both the positive and negative directions. It should be mentioned that below the surface of the HPFRCC material is a dense network of steel reinforcement (longitudinal and transverse). As witnessed by the results presented in Figure 3-26(b), the presence of steel below the HPFRCC cover does not seem to strongly interfere with the piezoresistive behavior of the bridge pier. This result positively

indicates that this electromechanical sensing method can be broadened for field application in more general types of cement-based structural elements.

3.7 Conclusions and Summary

This chapter has successfully illustrated the self-sensing ability of cementitious materials using their electromechancial properties. The promising results suggest that this approach could serve as a novel sensing technique for quantifying the strain, cracking and damage state of HPFRCC structural elements. In particular, ECC materials are employed in this study to showcase their piezoresistive behaviors under static and cyclic loadings. Traditional 2-point and 4-point probing methods are introduced in this chapter and their differences are analyzed. Influences of using DC and AC as the excitation source are also investigated. Electrochemical effects present at electrode-cement interfaces are also identified. Based on the electrical measurement results presented in this chapter, the following conclusions can be made:

- Electrical measurement errors exist in both the electrode-cement interfaces (contact impedance) and cement interior (material polarization). Contact impedance, which is primarily caused by the electrochemical reactions occurring at the electrode-cement interface when currents are injected, would result in a resistivity measurement several magnitudes larger than the bulk resistivity of ECC materials. This effect can be easily resolved by employing 4-point instead of 2-point probing methods.
- Material polarization, which is caused by the separation of ion concentrations due to the presence of electric fields, grows with time but would eventually reach a saturation state over time. The polarization characteristics (rate, amplitude, *etc.*) of M-45 ECC materials are calibrated in this study for monitoring the hydration level as well as estimating the unpolarized bulk resistivity. Similarly, material polarization can be eliminated by simply using high frequency AC currents. The measuring errors can be controlled down to 0.01% if AC currents of more than 1k Hz are applied.

- In this chapter, strain, cracking and damage states of HPFRCC materials are evaluated by observing the changes in measured resistivity when loaded. For ECC M-45 materials, resistivity experiences significant changes (different gage factors) in the strain hardening stage (multiple micro-cracking) than during elastic deformation (prior to first cracking). In particular, changes in resistivity are primarily caused by the degree of cracking. As a result, this approach can be used to offer a rough and quick assessment of the strain and cracking state of HPFRCC structural elements in the field.
- When using electrical measurements to monitor the strain, cracking and damage of cement-based materials, 4-point probing methods using high frequency AC currents are preferred. The results in this study show that the impact of contact impedance and material polarization are minimized leading, to more consistent resistivity measurements. In addition, elimination of the contact impedance also offers larger gage factors.
- Experimental results on a large-scale HPFRCC bridge pier also suggest that the electrical measurement can be adopted for more general types of cement-based structural elements such as those with steel reinforcement and aggregates present. However, more specific study in this area is needed.

This chapter conclusively illustrates the self-sensing ability of HPFRCC materials. The strain is monitored during the elastic response regime by the resistivity measurements. Damages can also be interpreted during strain hardening by the changing of gage factors. However, these resistivity measurements do not provide information on crack locations and distributions. Accurate identification of these cracking details is needed for cementitious structural elements so as to correctly estimate their service conditions and to expedite repair work when required. Based on this consideration, a two-dimensional spatial sensing technique using electrical impedance tomography (EIT) will be introduced and explored in the following chapters.

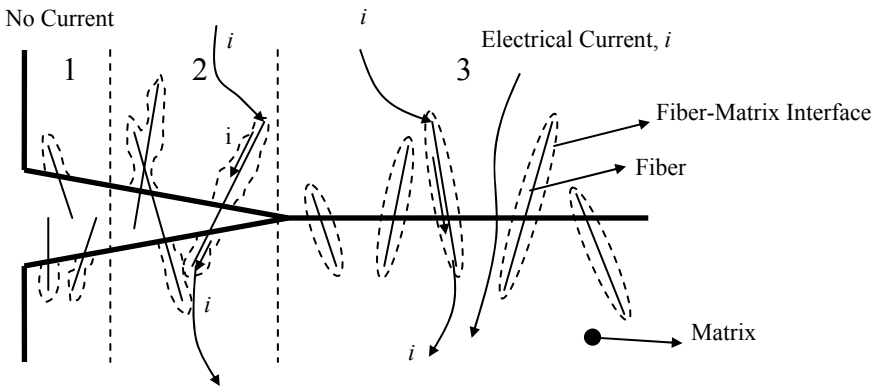

Figure 3-1: Electrical current passing through three ECC states: 1) post-fiber pullout, 2) fiber bridged cracks, and 3) uncracked.

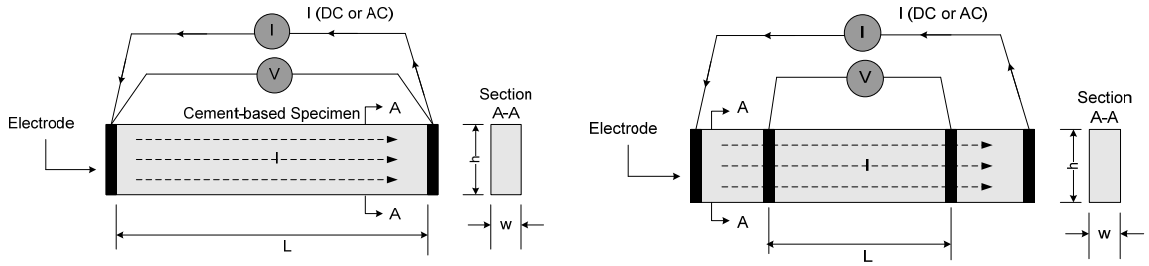

(a) (b)

Figure 3-2: Conductivity measurement based upon the (a) two-point and (b) four-point probe techniques.

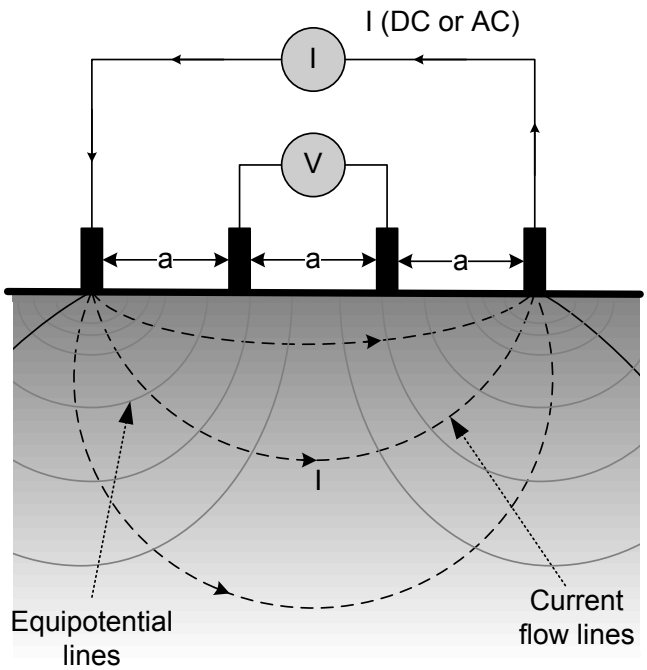

Figure 3-3: Wenner technique: a four-point probe conductivity measurement based upon surface contact (adapted from Millard, 1991).

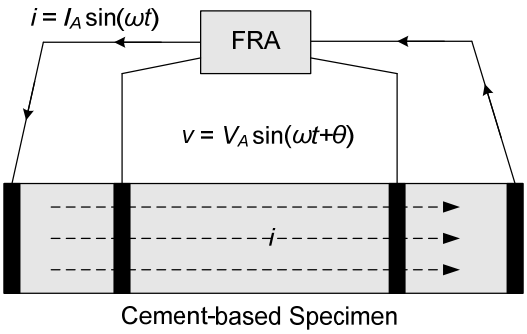

(a)

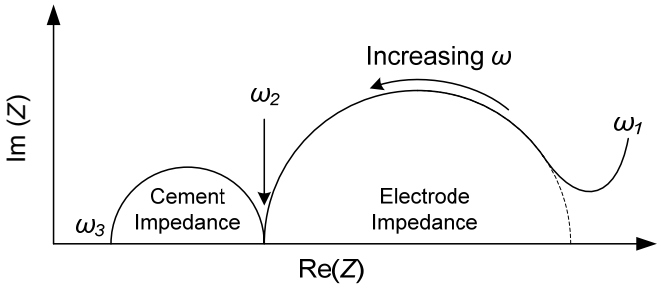

(b)

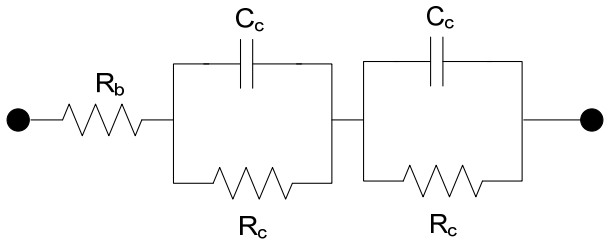

(c)

Figure 3-4: Electrical impedance spectroscopy: (a) experimental set-up; (b) typical impedance plot on the complex plane (adapted from Han, *et al.* (2005)); and (c) equivalent circuit model.

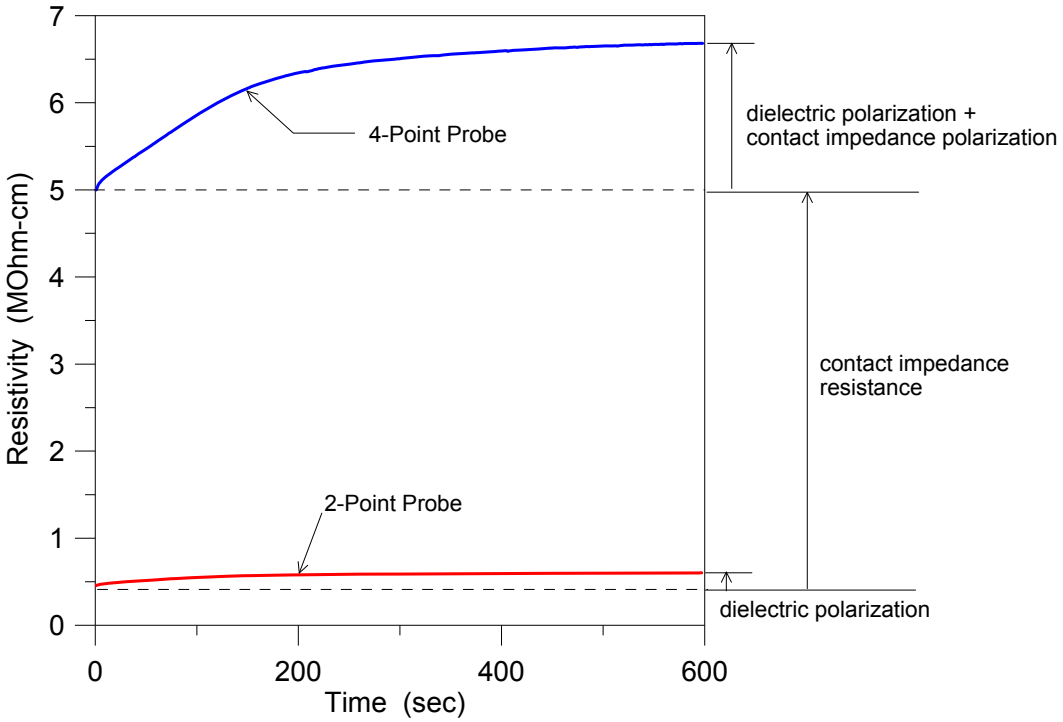

Figure 3-5: Polarization effects evident from DC-based 2-point probe and 4-point probe resistivity measurement methods applied to an ECC (M-45) specimen.

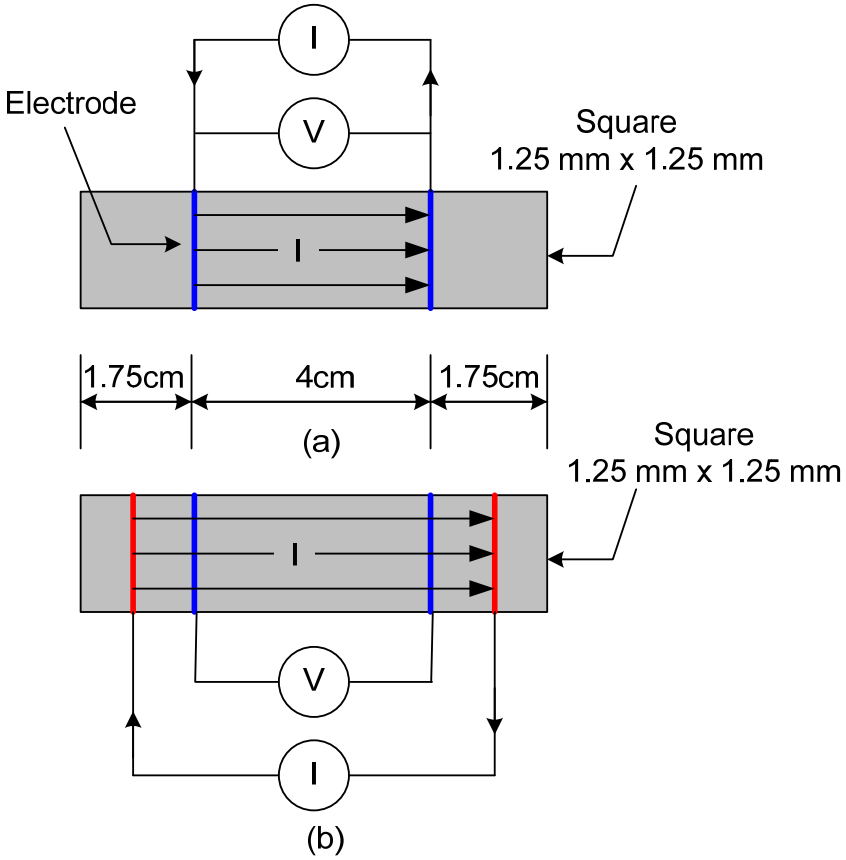

Figure 3-6: Electrode instrumentation for the 2-point probe (a) and 4-point probe (b) methods of resistivity measurement.

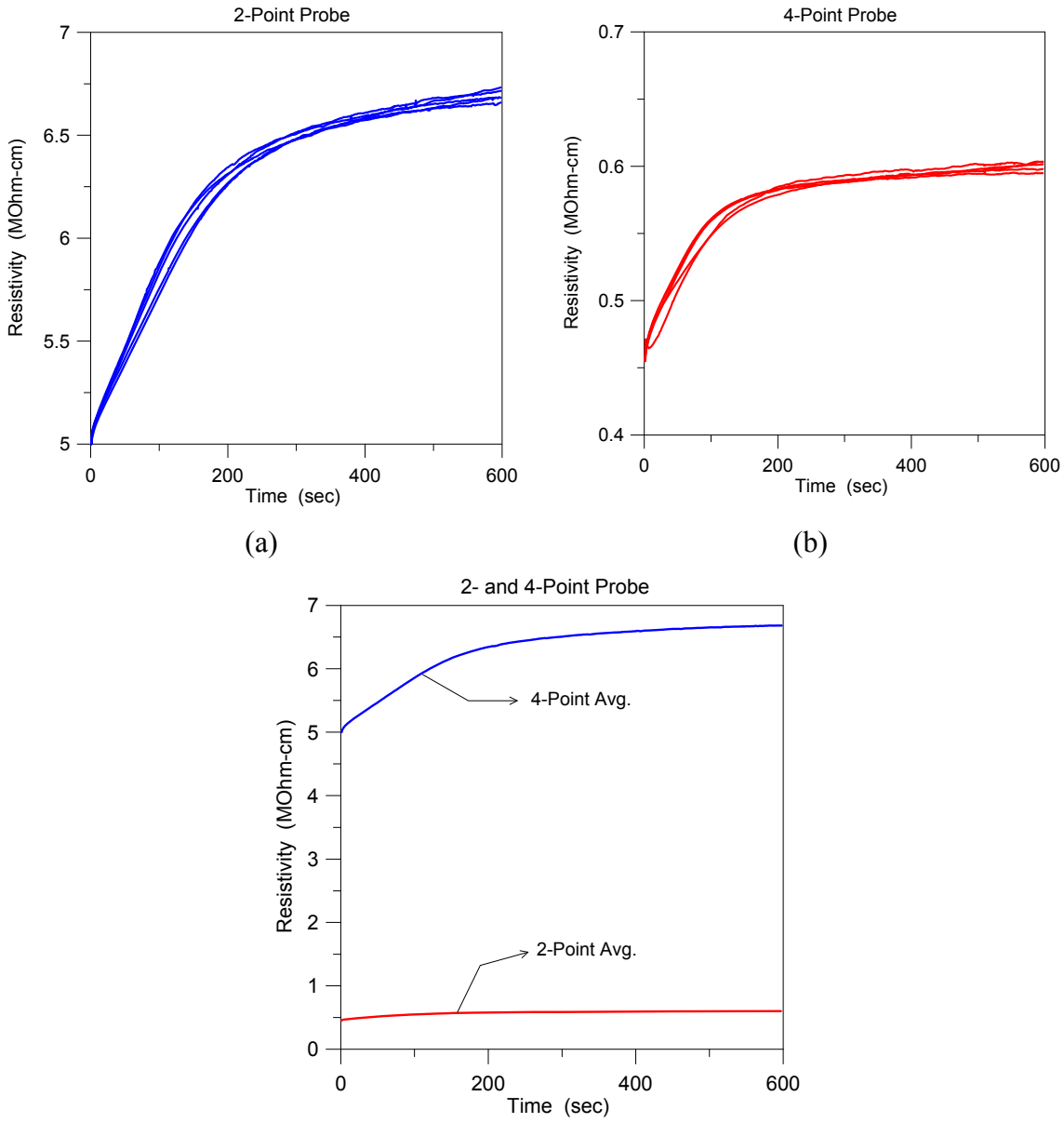

Figure 3-7: The first 600 seconds resistivity measurement of six 1-day old specimens by (a) 2-point and (b) 4-point probe methods and an average comparison of them (c).

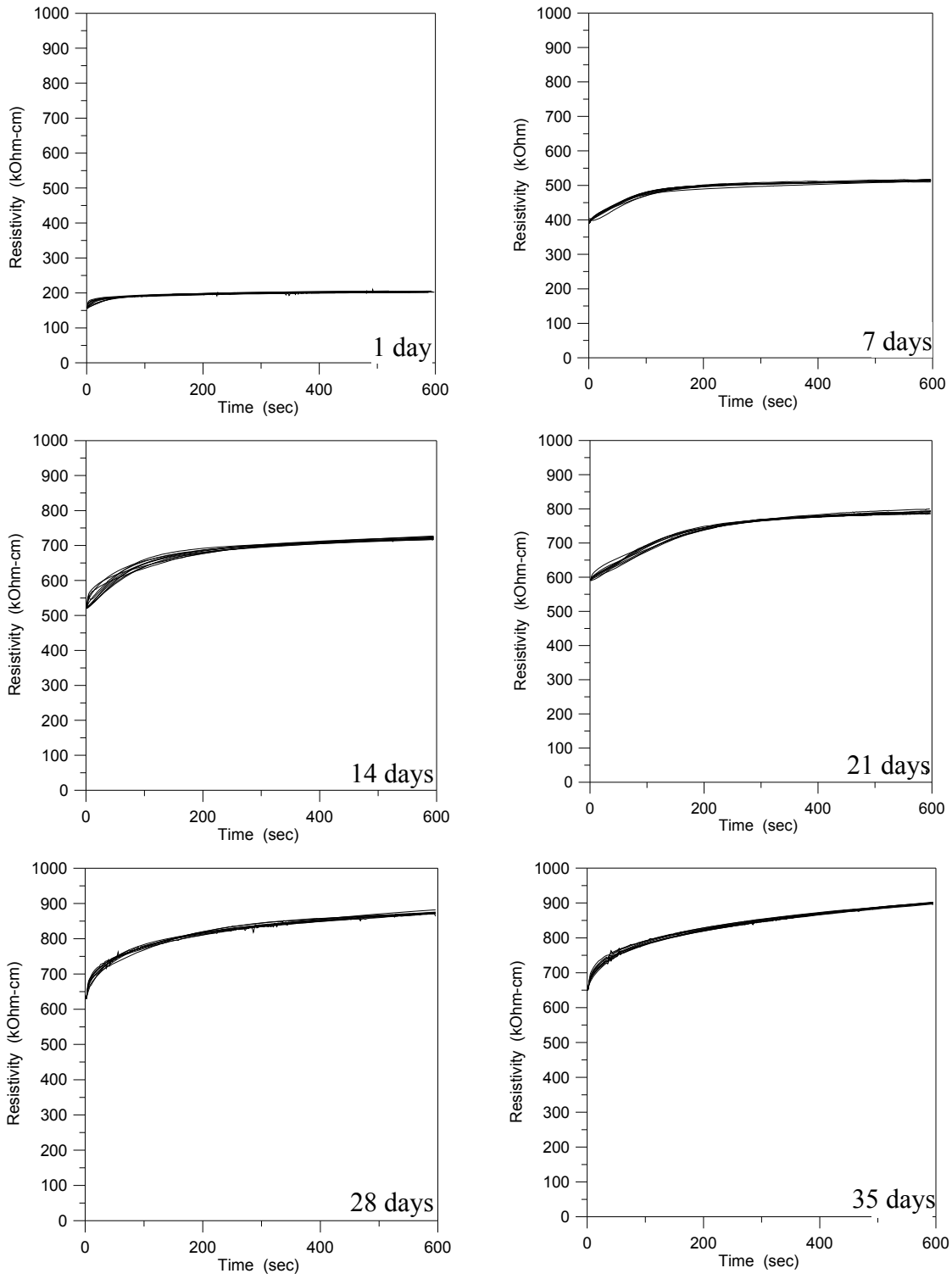

Figure 3-8: Resistivity measurement of ten M-45 ECC specimens by 4-point probing. Measurement repeated six times over the 35 day hydration period.

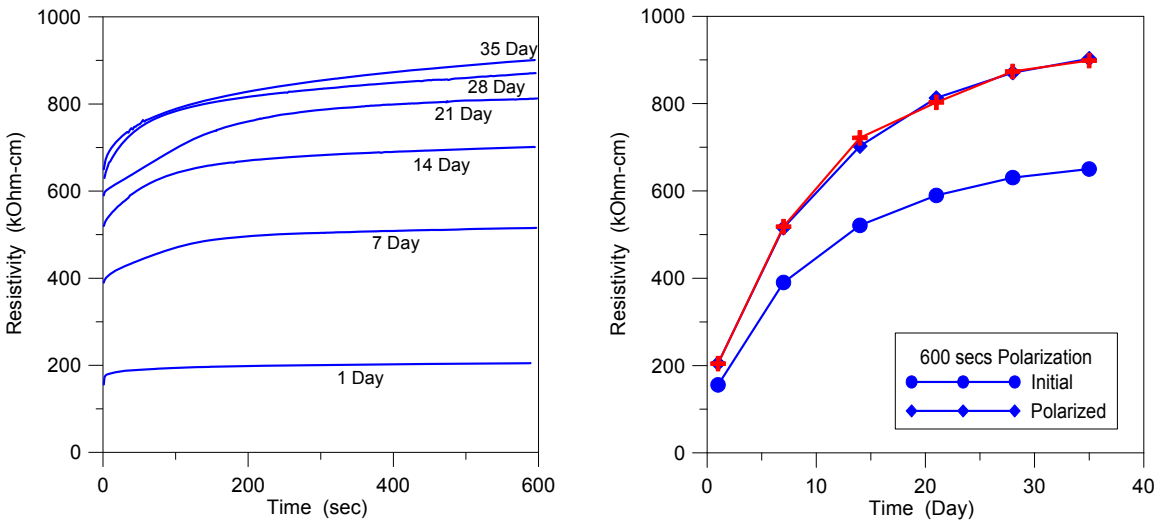

(a) (b)

Figure 3-9: (a) Resistivity calibration curves of the ECC M-45 material for different hydration levels (b) The initial and steady state resistivities for the ECC M-45 material as a function of cure time (in days).

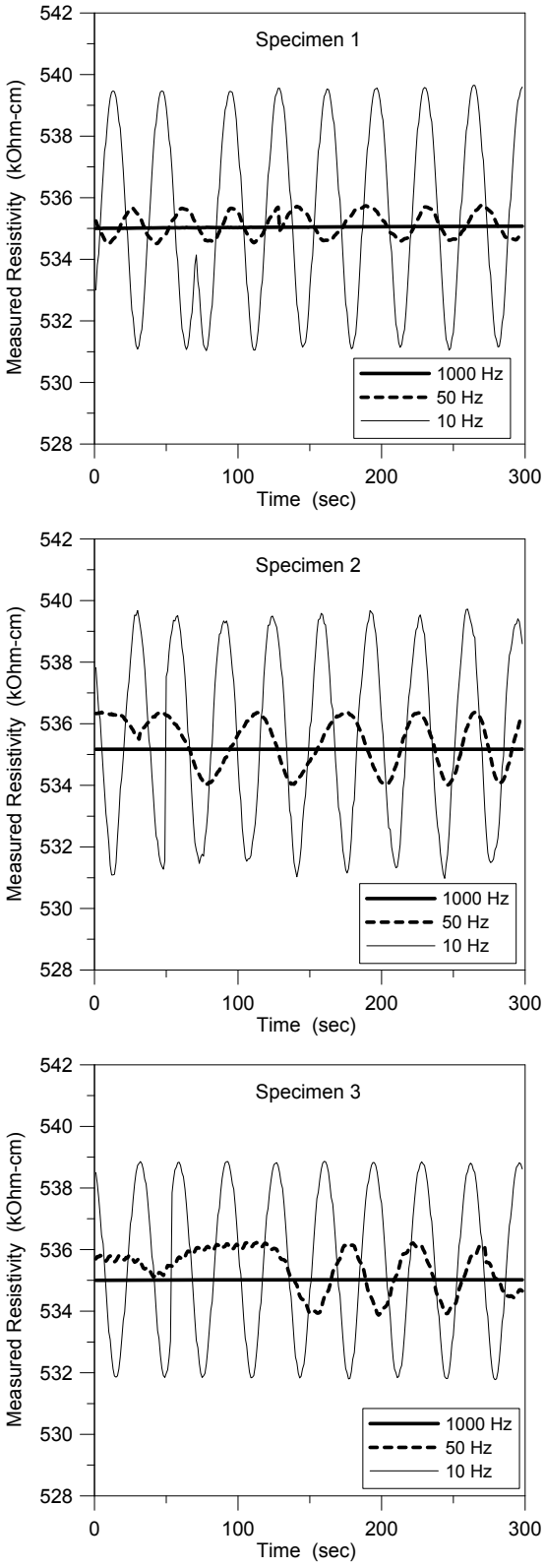

Figure 3-10: Resistivity measurement of three ECC M-45 specimens over 300 seconds with each specimen experiencing AC frequency from 10 Hz to 100 kHz.

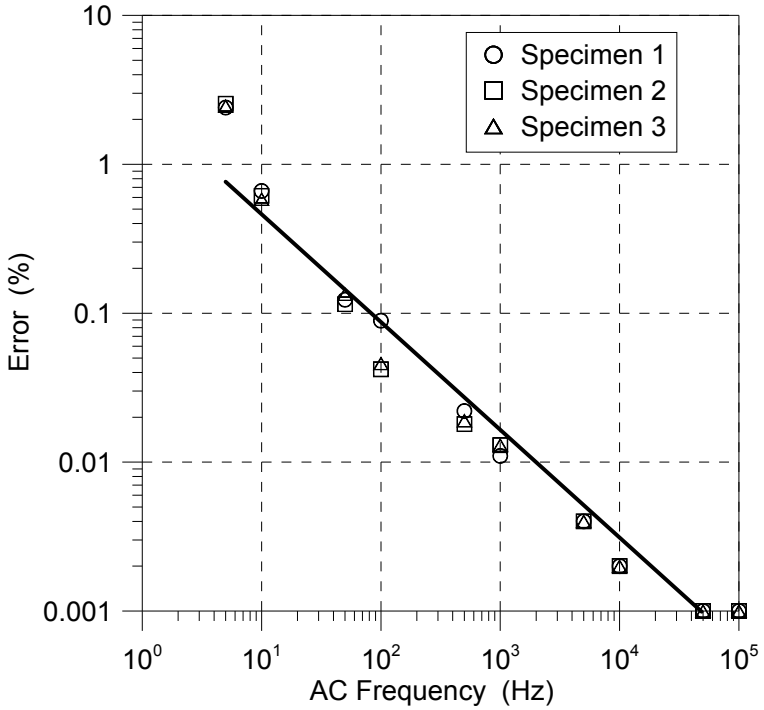

Figure 3-11: Comparison of the measured resistivity error versus the applied AC frequency used in the 4-point probe measurement.

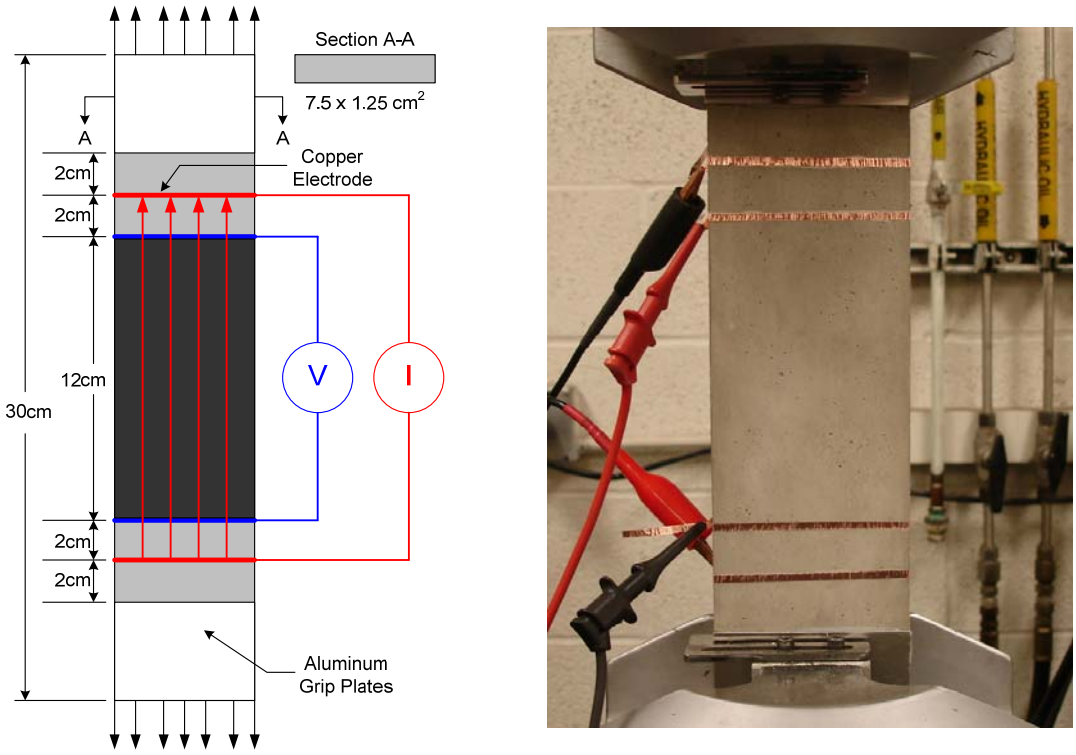

(a) (b)

Figure 3-12: ECC plate element for piezoresistivity quantification: (a) plate dimensions; (b) plate loaded in on MTS load frame.

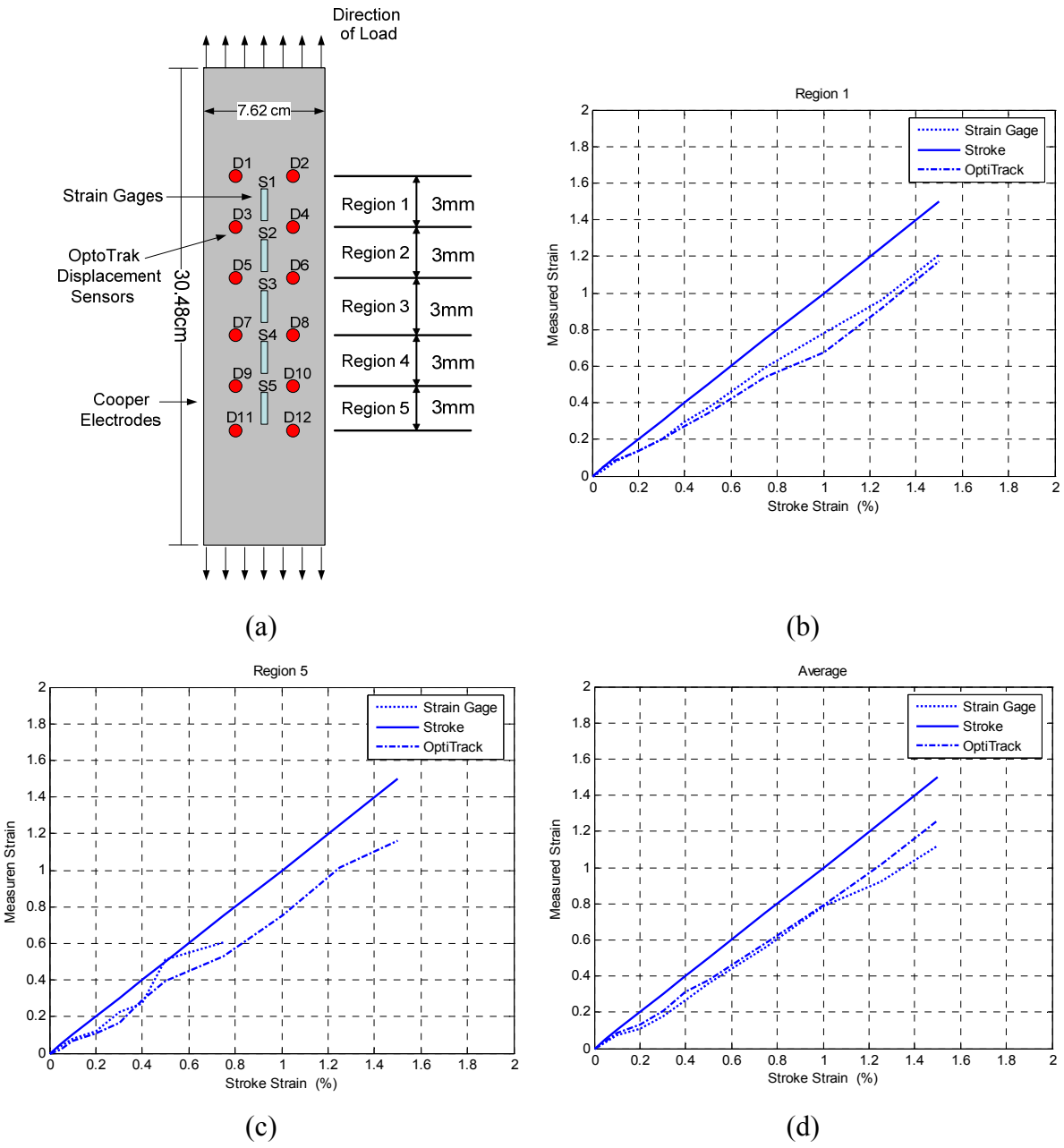

Figure 3-13: (a) Instrumentation for comparison of strain measurements; (b) comparison of the three strain measurements at region 1 (load frame stroke, OptoTrak and strain gages); (c) at region 5; and (d) average over region 1 through 5.

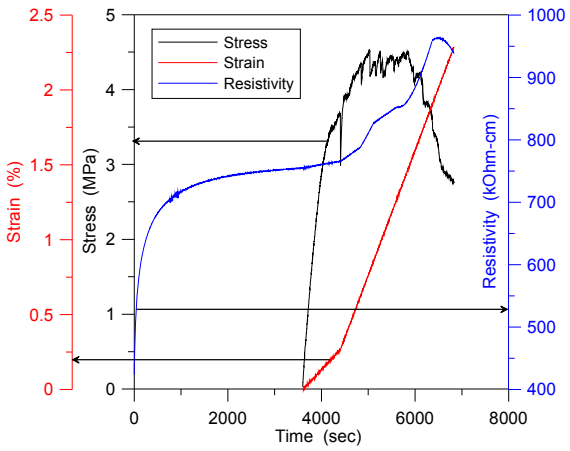

(a)

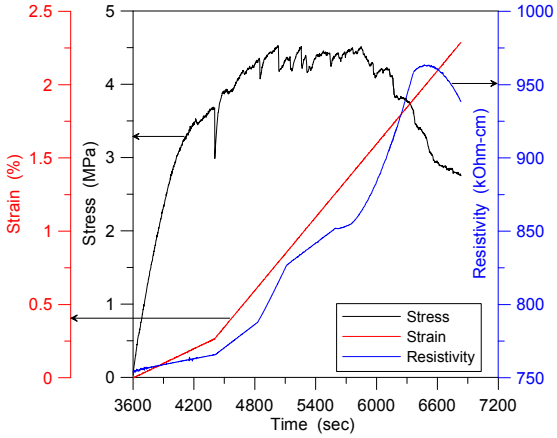

(b)

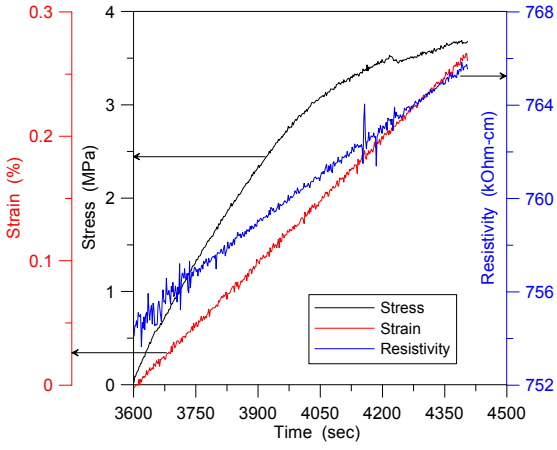

(c)

Figure 3-14: Piezoresistivity test results of ECC specimen DC-1 under monotonic loading: (a) full time horizon; (b) for t = 3600 to 7200 seconds; (c) for t = 3600 to 4500 seconds.

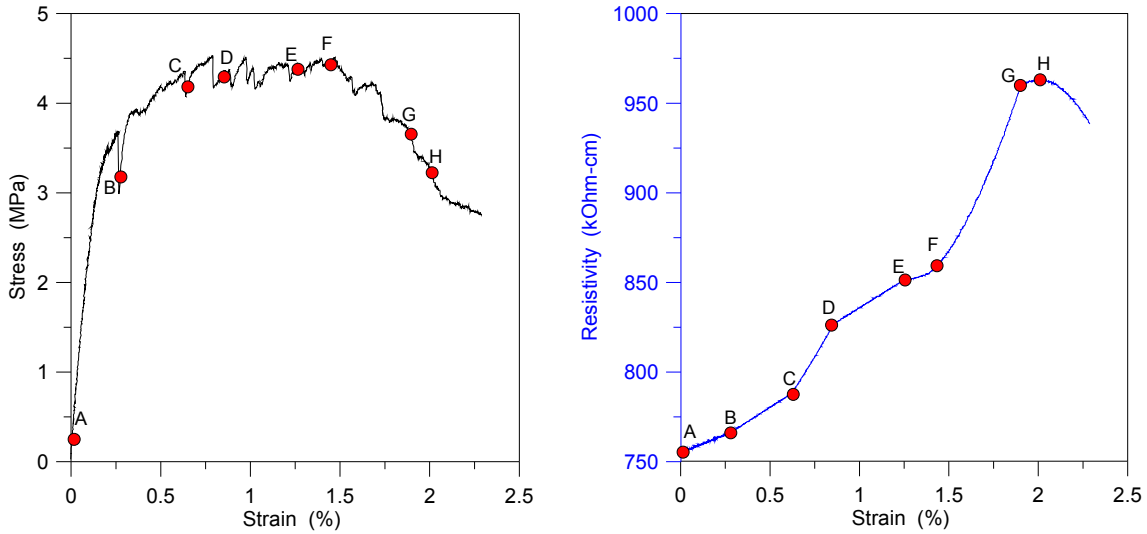

(a) (b)

Figure 3-15: Piezoresistivity result of ECC M-45 specimen DC-1 measured by the DC 4-point probe method during monotonic loading: (a) stress-strain curve; (b) resistivity-strain curve.

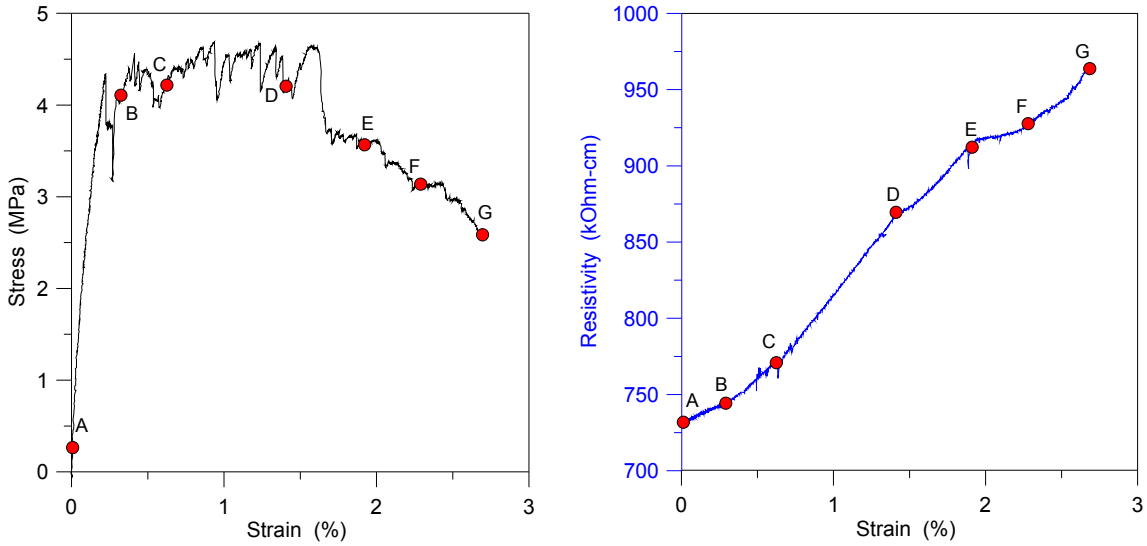

(a) (b)

Figure 3-16: Piezoresistivity result of ECC M-45 specimen DC-2 measured by the DC 4-point probe method during monotonic loading: (a) stress-strain curve; (b) resistivity-strain curve.

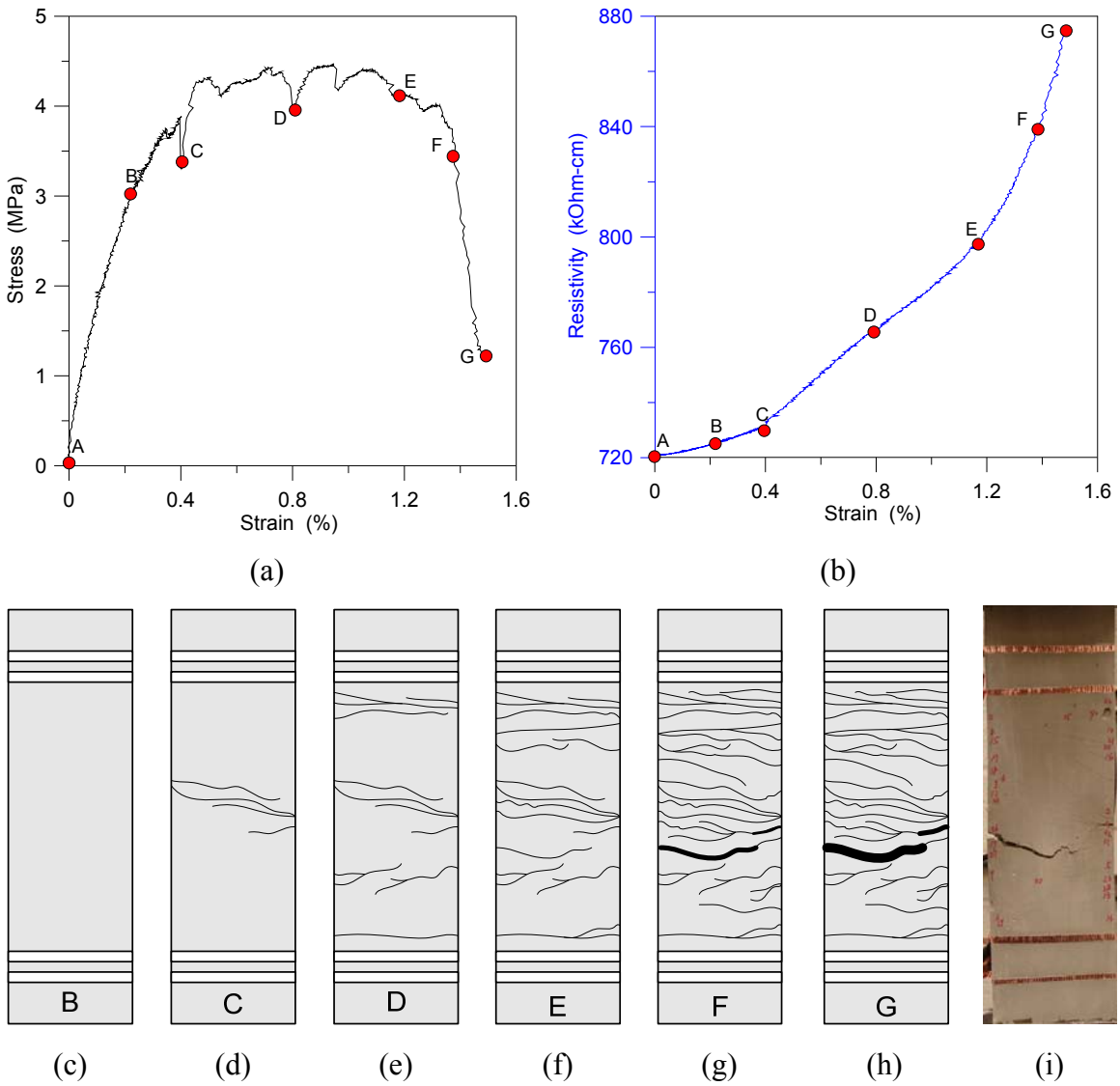

Figure 3-17: Piezoresistivity result of ECC M-45 specimen DC-3 measured by the DC 4-point probe method during monotonic loading: (a) stress-strain curve; (b) resistivity-strain curve; (c) to (h): cracking patterns at loading point B through G, respectively; (i) photo of the specimen after crack localization (at point G).

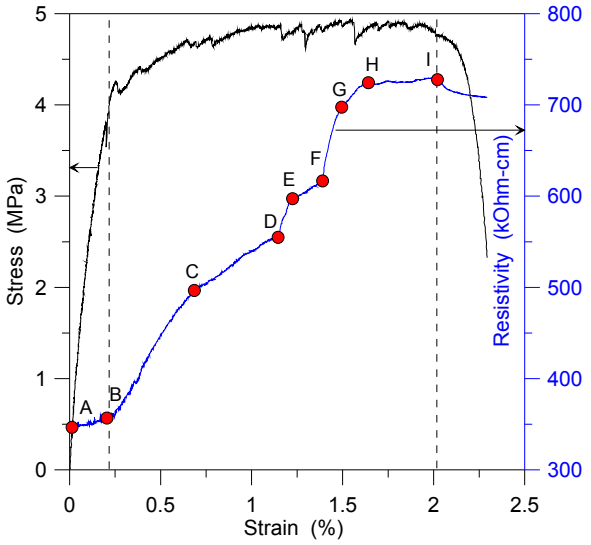

(a)

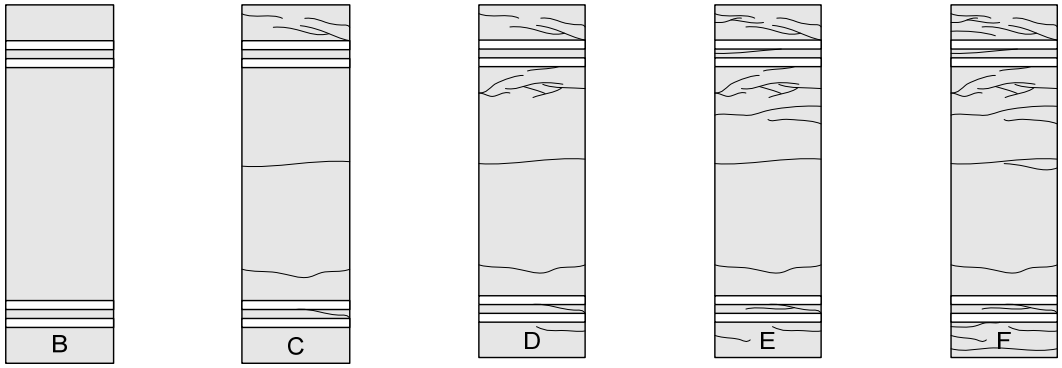

(b) (c) (d) (e) (f)

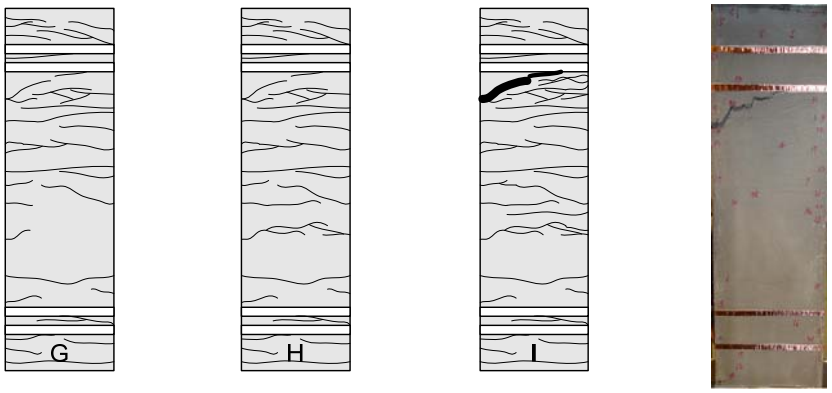

(g) (h) (i) (j)

Figure 3-18: (a) Piezoresistivity result of ECC M-45 specimen AC-1 under 4-point probe AC monotonic loading; (b) to (i): cracking patterns at loading point B through I, respectively; (j) photo of the specimen after crack localization.

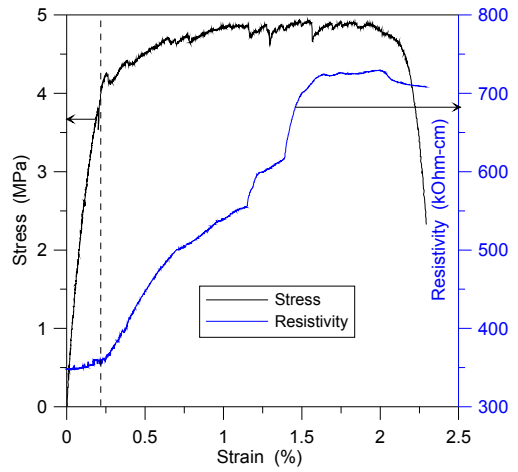

(a)

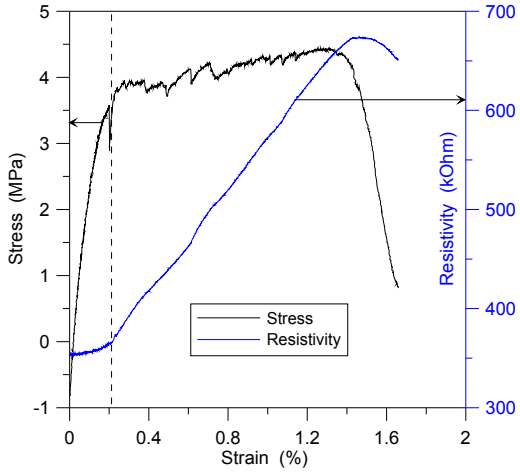

(b)

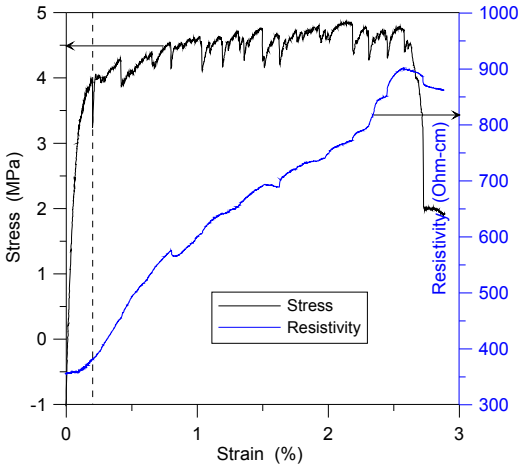

(c)

Figure 3-19: Piezoresistivity results for 3 M-45 ECC specimens with resistivity measured by 4-point AC probing: (a) specimen AC-1; (b) specimen AC-2; (c) specimen AC-3.

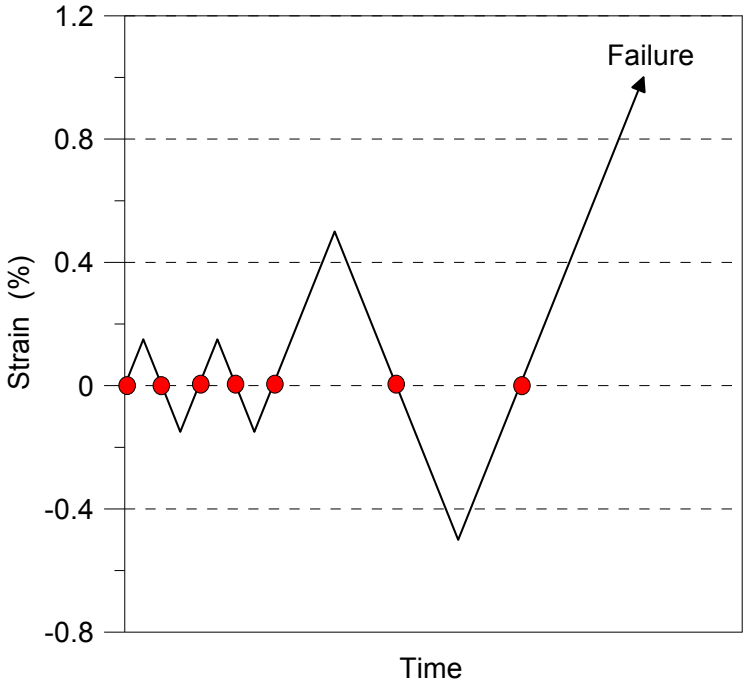

Figure 3-20: Loading history of 4-point probe AC cyclic loading test.

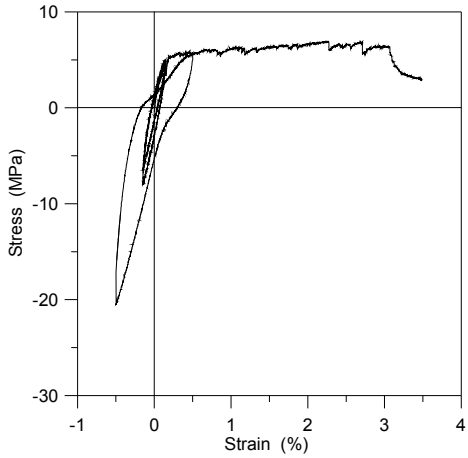

(a)

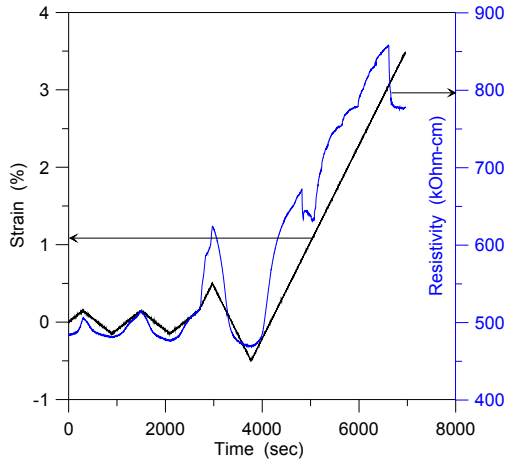

(b)

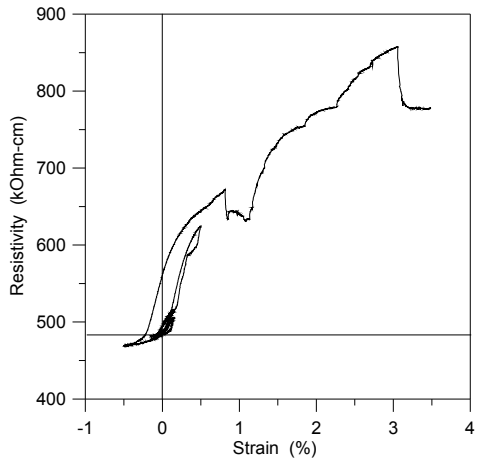

(c)

Figure 3-21: Cyclically loaded Specimen AC-1C: (a) stress-strain plot; (b) strain and resistivity time histories; (c) resistivity-strain plot.

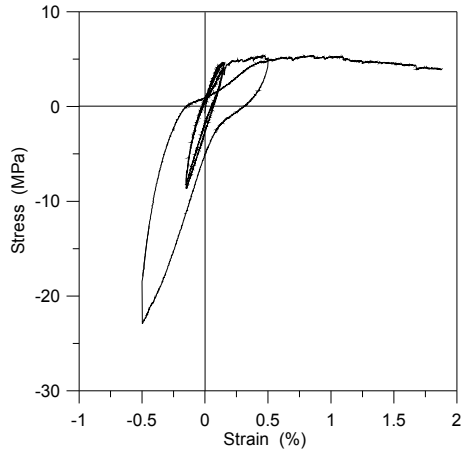

(a)

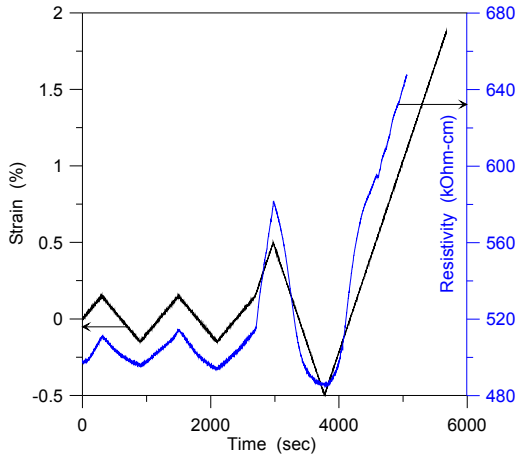

(b)

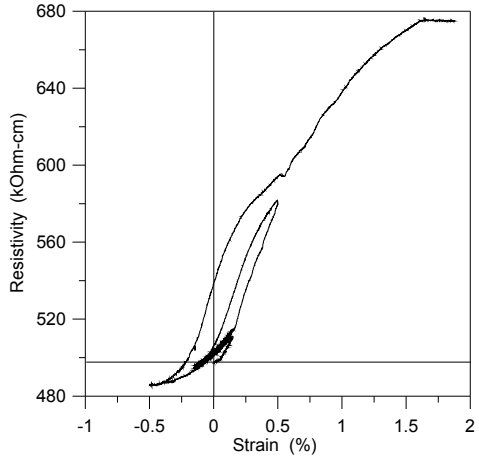

(c)

Figure 3-22: Cyclically loaded Specimen AC-2C: (a) stress-strain plot; (b) strain and resistivity time histories; (c) resistivity-strain plot.

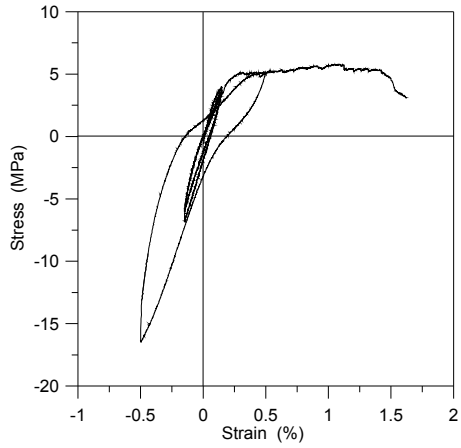

(a)

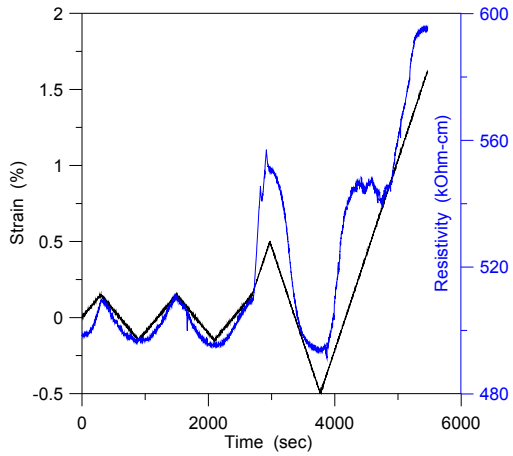

(b)

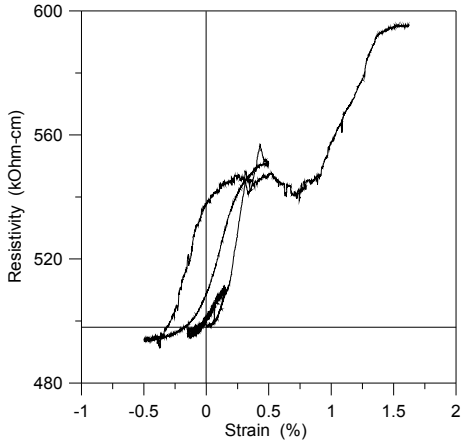

(c)

Figure 3-23: Cyclically loaded Specimen AC-3C: (a) stress-strain plot; (b) strain and resistivity time histories; (c) resistivity-strain plot.

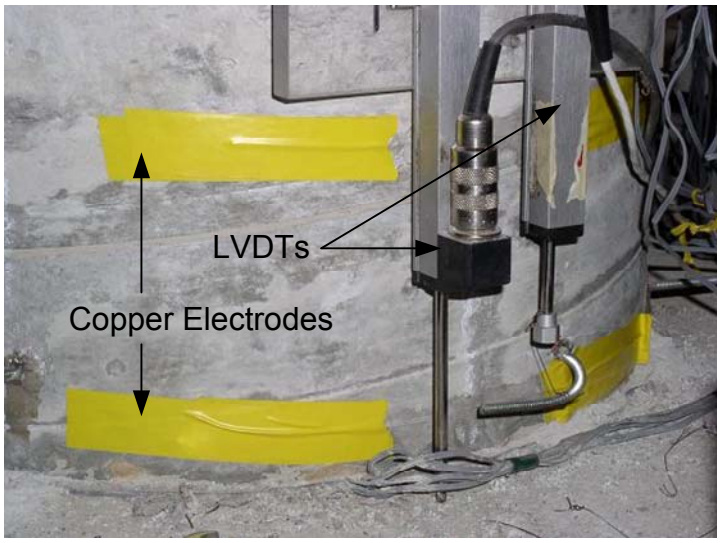

(a)

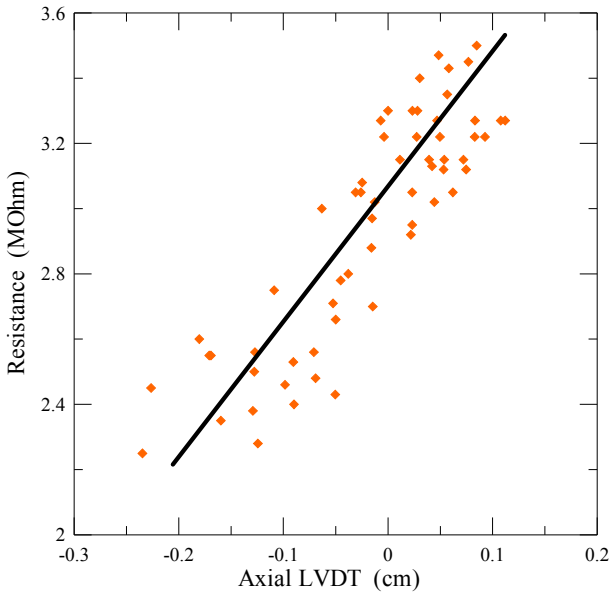

(b)

Figure 3-24: (a) Instrumentation of LVDTs and copper electrodes at bridge pier base; (b) axial LVDT-electrical resistance relationship.

Table 3-1: Parameters of Equation 3.5 for different hydration levels

Hydration Level (days)	**1**	**7**	**14**	**21**	**28**	**35**
ρ_0 (kOhm-cm)	155	393	524	587	628	652
a_1	60	135	205	235	320	330
a_2	125	110	115	205	270	325
a_3	0.35	0.65	0.85	0.80	0.45	0.55

Table 3-2: Gage factors of M-45 ECC based on 4-point DC probe measurement

	Linear Segments						
Specimen	A-B	B-C	C-D	D-E	E-F	F-G	G-H
DC-1	6.32	8.78	15.27	12.06	10.83	16.14	9.64
DC-2	6.55	9.53	13.39	11.64	8.32	12.58	N/A
DC-3	5.56	7.77	11.39	13.64	15.32	22.58	N/A

Table 3-3: Gage factors of M-45 ECC based on 4-point AC probe measurement of specimen AC-1

	Linear Segments							
	A-B	B-C	C-D	D-E	E-F	F-G	G-H	H-I
Gage Factor	16.16	78.92	37.23	89.42	36.13	96.56	72.63	13.09

Table 3-4: Average gage factors of M-45 ECC for 4-point AC probing under monotonic loading

	Specimen			
	AC-1	**AC-2**	**AC-3**	**Avg.**
Gage Factor (Elastic)	16.16	15.33	16.32	15.94
Gage Factor (Strain Hardening)	59.52	64.28	61.91	61.93

Table 3-5: Average gage factors of M-45 ECC for 4-point probe AC probing under cyclic loading

	Specimen			
	AC-1C	**AC-2C**	**AC-3C**	**Avg.**
Gage Factor (Elastic-Tension)	32.57	34.06	30.58	32.40
Gage Factor (Strain Hardening)	65.62	68.45	62.73	65.61
Gage Factor (Elastic-Compression)	6.31	5.65	5.17	5.71

Table 3-6: Averaged gage factors of piezoresistivity study of M-45 ECC

Loading State	**4-Point DC Monotonic Loading**	**4-Point AC Monotonic Loading**	**4-Point AC Cyclic Loading**
Elastic-Tension	6.14	15.94	32.40
Strain Hardening	13.36	61.93	65.61
Elastic-Compression	N/A	N/A	5.71

Chapter 4

Electrical Impedance Tomography

4.1 Introduction

The two- and four-point probe methods presented in Chapter 3 suffer from inherent limitations when used to characterize the electrical properties of cementitious materials. Specifically, they do not provide a measurement of material conductivity at a given point. Rather, they measure the average conductivity between the electrodes. Therefore, if the electrodes are spaced too far apart, inhomogeneities that may exist between the electrodes are not directly observed since their influence on the conductivity measurement is averaged out.

In theory, the electro-mechanical properties of cementitious materials can be used to sense the strain response of a structure everywhere the material is. For example, should a mapping of conductivity over the area of a cement element be sought, the Wenner technique can be employed. Numerous vendors sell hand-held equipment to make four-point probe conductivity measurements based on the Wenner technique (Bungey *et al.*, 2006). However, repeated measurement across a structural element can be both labor-intensive and time-consuming. An autonomous means of measuring the spatial distribution of FRCC conductivity is sought. Since FRCC materials are piezoresistive, as was illustrated in Chapter 3, conductivity maps could be used to measure two-

dimensional strain fields within an FRCC structural element. Furthermore, cracks are physical inhomogeneities that block the flow of electricity. Cracks would therefore appear as regions of near zero conductivity within the conductivity maps. Electrical impedance tomography (EIT) is proposed for mapping the spatial distribution of conductivity over structural surfaces. EIT has been widely adopted for anomaly detection in geophysical exploration (Zhdanov and Keller, 1994), biomedical imaging (Webster, 1990; Holder, 2005) as well as in other fields.

EIT is a more sophisticated approach to measuring material conductivity than that of the two- and four-point probe methods. Unlike the probe methods, EIT is a combination of both electrical probing followed by the use of analytical models describing the flow of electricity in the test specimen. Therefore, conductivity mapping by EIT can be broken down into three major parts. First, the specimen under study is stimulated by a regulated alternating current (AC) while electrical voltages are measured along the specimen boundary. Second, an analytical model that predicts the boundary voltages to the same AC stimulation is formulated; this model if often referred to as the forward problem since the distribution of conductivity is assumed known at the problem outset. However, the conductivity distribution is unknown *a priori*; hence, the inverse problem is solved by varying the assumed conductivity distribution of the forward problem until convergence between experimental and model boundary voltages is achieved. Figure 4-1 summarizes the EIT approach to conductivity determination.

In this chapter, EIT is proposed for sensing FRCC structural elements. Before describing the specific application of the method to FRCC structures, the chapter will summarize the EIT framework. First, the analytical problem describing electrical flow in conductive and semi-conductive bodies is presented. Second, the finite element formulation of the forward problem is introduced to offer a numerical approach to solving the forward problem. Third, the inverse problem of determining FRCC conductivity using electrical measurements made on the element boundary is described. Finally, some limitations of EIT are discussed, especially as they apply to FRCC materials.

4.2 Mathematical Formulation of the Forward Problem

In this section, we begin by first presenting the analytical model that describes the relationship between electrical current and potential. Essentially, we will describe how electrical potential develops along the boundary of a test specimen in response to a known applied current and specimen conductivity distribution. Since conductivity is assumed known, this problem formulation is termed the "forward problem". Excellent reviews of the forward problem formulation for electrical conduction problems are numerous in the literature. This section serves as a brief review of the forward problem; however, the reader is referred to more extensive summaries offered by Vauhkonen (1997), Borcea (2002), and Holder (2005).

4.2.1 Derivation of the Laplace Equation

Electrical impedance tomography (EIT) finds its origins in the field of electro-magnetic (EM) theory. Maxwell equations (which consist of four equations) describe the inter-relationship between electrical and magnetic phenomenon and hence serve as the cornerstone of the EM field. Two of the four equations are used to describe the flow of electrical currents in a conductive body, Ω. First, Faraday's Law of Induction describes how an electrical current is induced in a conductive medium due to changes of magnetic flux:

$$\varepsilon = -\frac{\partial \Phi_m}{\partial t} \tag{4.1}$$

where

$$\Phi_m = \int_{\mathrm{A}} \mathbf{B} \cdot d\mathrm{A} \tag{4.2}$$

ε is the induced electromotive force (emf) and Φ_m is the magnetic flux in a prescribe area A over which a magnetic field **B** is present (see Figure 4-2). Similarly, the emf is associated with an electric field **E** acting over the same area A such that:

$$\oint \mathbf{E} \cdot d\mathrm{S} = \varepsilon \tag{4.3}$$

Equation 4.1, 4.2 and 4.3 can be combined to relate the electric field to the magnetic field:

$$\oint \mathbf{E} \cdot d\mathrm{S} = \int_{\mathrm{A}} -\frac{\partial}{\partial t}\mathbf{B} \cdot d\mathrm{A} \tag{4.4}$$

By Stokes Theorem:

$$\oint \mathbf{E} \cdot d\mathrm{S} = \int_{\mathrm{A}} (\nabla \times \mathbf{E}) \cdot d\mathrm{A} \tag{4.5}$$

therefore,

$$\nabla \times \mathbf{E} = -\frac{\partial}{\partial t}\mathbf{B} \tag{4.6}$$

The second of Maxwell's equations is Ampère's Law which relates the magnetic field, **B**, to electric current:

$$\oint \mathbf{B} \cdot d\mathbf{S} = \mu_0 (I + I_d) \tag{4.7}$$

Where I is current, I_d is "displacement" current due to a magnetic field, and μ_0 is the permeability of free space. Current over area A is defined as:

$$I = \int_{\mathrm{A}} \mathbf{J} \cdot d\mathrm{A} \tag{4.8}$$

with **J** defined as current density. Current density is directly related to electric field through Ohm's law, $\mathbf{J} = \sigma\ \mathbf{E}$. Here, σ, is the conductivity of the material. The displacement current, I_d, is associated with the electric field, **E**, through the permittivity of free space, ε_0:

$$I_d = \varepsilon_0 \frac{\partial \Phi_e}{\partial t} \tag{4.9}$$

where Φ_e is the electric field flux:

$$\Phi_e = \int_{\mathrm{A}} \mathbf{E} \cdot d\mathrm{A} \tag{4.10}$$

Combining Equation 4.7, 4.8 and 4.9, then:

$$\oint \mathbf{B} \cdot d\mathbf{S} = \mu_0 \int_{\mathrm{A}} \mathbf{J} \cdot d\mathrm{A} + \mu_0 \varepsilon_0 \int_{\mathrm{A}} \frac{\partial}{\partial t} \mathbf{E} \cdot d\mathrm{A} \tag{4.11}$$

By Stokes Theorem:

$$\int_{\mathrm{A}} (\nabla \times \mathbf{B}) \cdot d\mathrm{A} = \mu_0 \int_{\mathrm{A}} \left(\mathbf{J} + \varepsilon_0 \frac{\partial \mathbf{E}}{\partial t} \right) \cdot d\mathrm{A} \tag{4.12}$$

The magnetic field can be normalized by the permeability of free space to yield the magnetic field strength $\mathbf{H} = \mathbf{B}/\mu_0$. In a similar fashion, the electric field multiplied by the permittivity of free space is termed the electric displacement $\mathbf{D} = \varepsilon_0\ \mathbf{E}$ for non-dispersive, linear, isotropic media. The integrand of Equation 4.12 can be rewritten to derive:

$$\nabla \times \mathbf{H} = \mathbf{J} + \frac{\partial \mathbf{D}}{\partial t} \tag{4.13}$$

Consider the case of when an alternating current (AC) is present in the conductive medium. If the AC signal is characterized by the harmonic frequency, ω, then the electric and magnetic field strength vectors can be written as:

$$\mathbf{E}(t) = \mathrm{Re}\left(\mathbf{E}(\omega)e^{i\omega t}\right) \tag{4.14}$$

$$\mathbf{H}(t) = \mathrm{Re}\left(\mathbf{H}(\omega)e^{i\omega t}\right) \tag{4.15}$$

The time varying electric and magnetic field strength functions (Equation 4.14 and 4.15, respectively) can be substituted into Equation 4.6 (Faraday's Law) and Equation 4.13 (Ampère's Law) to yield:

$$\nabla \times \mathbf{E}(\omega) = -i\omega\mu\mathbf{H}(\omega) \tag{4.16}$$

$$\nabla \times \mathbf{H}(\omega) = i\omega\varepsilon\mathbf{E}(\omega) + \mathbf{J} \tag{4.17}$$

The current density, **J**, of Equation 4.17 can consist two parts. First, the flow of current in the conductive medium is one part ($\mathbf{J_c} = \sigma\mathbf{E}$); however, if at a point of interest, an external current source is applied, $\mathbf{J_s}$, :

$$\mathbf{J} = \mathbf{J}_\mathbf{s} + \sigma\,\mathbf{E} \tag{4.18}$$

Thus, reconsidering Equation 4.16 and 4.17, the following equations are derived:

$$\nabla \times \mathbf{E}(\omega) = -i\omega\mu\mathbf{H}(\omega) \tag{4.19}$$

$$\nabla \times \mathbf{H}(\omega) = (\sigma + i\omega\varepsilon)\mathbf{E}(\omega) + \mathbf{J}_\mathbf{s} \tag{4.20}$$

In order to simplify the derivation, EIT is assumed to be operated under low frequency or static electric fields. For that case, the terms $\omega\varepsilon$ and $\omega\mu$ can be neglected. Therefore, the

capacitive effect in Equation 4.20 can be neglected (Baker, 1989; Barber and Brown, 1984):

$$\omega\varepsilon\mathbf{E}(\omega) \approx 0 \tag{4.21}$$

Equation 4.19 and 4.20 can now be rewritten as:

$$\nabla \times \mathbf{E}(\omega) = 0 \tag{4.22}$$

$$\nabla \times \mathbf{H}(\omega) = \sigma\mathbf{E}(\omega) + \mathbf{J_s} \tag{4.23}$$

The electric field, **E**, is related to the scalar electric potential, ϕ, and the magnetic vector potential, $\mathbf{A_m}$:

$$\mathbf{E} = -\nabla\phi(\omega) - \frac{\partial \mathbf{A_m}}{\partial t} \tag{4.24}$$

The magnetic field, **B**, is equal to the curl of the magnetic vector potential, $\mathbf{A_m}$:

$$\mathbf{B} = \nabla \times \mathbf{A_m} \tag{4.25}$$

In Equation 4.24, the rate of change in the magnetic vector potential as a function of time reflects the contribution of magnetic induction to the electric field. However, the effect of magnetic induction is often neglected since (Vauhkonen, 1997):

$$\omega\mu\sigma L_c\left(1 + \frac{\omega\varepsilon}{\sigma}\right) << 1 \tag{4.26}$$

where L_c is a characteristic length over which the electric field has a significant variation. Hence, the electric field is typically considered related only to the electric potential:

$$\mathbf{E} = -\nabla\phi(\omega) \tag{4.27}$$

Considering this fact, Equation 4.23 can now be rewritten as:

$$\nabla \times \mathbf{H}(w) = \sigma\nabla\phi(w) + \mathbf{J}_s \tag{4.28}$$

The curl of the magnetic field strength is divergence free. Hence,

$$\nabla \cdot (\nabla \times \mathbf{H}) = 0 \tag{4.29}$$

Furthermore, it is assumed in the EIT formulation that current is applied only on the boundary of the conductive body. Therefore, within the body itself, $\mathbf{J_s} = 0$. Combining this fact with Equation 4.29, the Laplace Equation describing the electrical behavior of a conductive body is derived:

$$\nabla \cdot (\sigma\nabla\phi) = 0 \tag{4.30}$$

The Laplace Equation serves as the cornerstone of the forward problem. In other words, given a spatial description of conductivity, σ, the electrical potential, ϕ, at any point can be determined for a given applied current. Next, the behavior of the body on its boundary is further explored.

4.2.2 Electrode Boundary

The Laplace Equation (Equation 4.30) is used to describe the flow of electricity within the body, Ω. In electrical impedance tomography, electrical sources are applied to the boundary of the body, $\partial\Omega$. Let us consider in more detail the behavior of the body at its boundary. First, let us consider Figure 4-3a. Here, an electrical current, I, is applied on the body boundary. The point of application of the current is highlighted in Figure 4-3b. Over the volume, V, enclosing the section of the boundary where the current is applied, we can consider the divergence of the source current (Vauhkonen, 1997):

$$\int_V \nabla \cdot \mathbf{J}_s dV = -\int_V \nabla \cdot \sigma \mathbf{E} dV \tag{4.31}$$

By Green's theorem, the divergence over the volume can be converted to the projection of the vector field on the normal vector, **n**:

$$\int_V \nabla \cdot \mathbf{J}_s dV = \oint_S \mathbf{J}_s \cdot \mathbf{n} dS \tag{4.32}$$

$$\int_V \nabla \cdot \sigma \mathbf{E} dV = \oint_S \sigma \mathbf{E} \cdot \mathbf{n} dS \tag{4.33}$$

Therefore,

$$\oint_S \mathbf{J}_s \cdot \mathbf{n} dS = -\oint_S \sigma \mathbf{E} \cdot \mathbf{n} dS \tag{4.34}$$

While Equation 4.34 performs the integral over the surface of the enclosed volume, V, the current is on the outside portion of the volume and the electric field is present on the inside portion. As the volume is shrunk to an infinitesimally small volume, (V→0), Equation 4.34 becomes:

$$-\mathbf{J}_s \cdot n\big|_{OUTSIDE} = \sigma \mathbf{E} \cdot \mathbf{n}\big|_{INSIDE} \tag{4.35}$$

If I is the normal component of the source current density, $\mathbf{J}_s$, then:

$$-I = \sigma \mathbf{E} \cdot \mathbf{n} \tag{4.36}$$

More compactly, since $\mathbf{E} = -\nabla \phi$, then:

$$I = \sigma \nabla \phi \cdot \mathbf{n} \tag{4.37}$$

In effect, Equation 4.37 describes the relationship between the electric potential at the body that develops due to the externally applied current, *I*.

Additional boundary conditions must be stated for the body. The first boundary condition establishes the electric potential, *v*, on the body boundary (Borcea, 2002):

$$\phi(\mathbf{x}) = v(\mathbf{x}) \qquad \text{for } \mathbf{x} \in \partial\Omega \tag{4.38}$$

This condition is termed the Dirichlet Boundary Condition. The second boundary condition established a conservation of current along the boundary:

$$\oint_{\partial\Omega} I d\mathrm{S} = 0 \tag{4.39}$$

Termed the Neumann Boundary Condition, this condition states that whatever current goes into the body must come out.

The application of current on the body boundary can be modeled as either a continuous function or discretely. The model describing the boundary current as a continuous function is termed the continuum model. In effect, this model does not localized current to electrodes as the other models will do. The continuum model employs Equation 4.30, 4.38 and 4.39. While this model is easy to implement, it does ignore the complexities of electrodes, leading to severe discrepancies between experimental and analytical boundary data (Cheng *et al.*, 1988). In additional to ignoring electrode effects, another difficulty is the infeasibility of providing a continuous current pattern along the body boundary in practice.

An alternative approach to defining current continuously is to localize current to electrodes. In this approach, the boundary is discretized into a set of electrodes upon which current can be applied and voltages measured. First, the boundary of the medium is divided into a finite set of sections. The Neumann Boundary Condition (Equation 4.39) can then be rewritten as:

$$I = \begin{cases} \dfrac{\overline{I_i}}{|Ae_i|} & \text{on } e_i,\ i = 1,2,\ldots L \\ \\ 0 & \text{otherwise} \end{cases} \tag{4.40}$$

Here $\bar{I}_i$ is the total current applied to the i^{th} electrode, e_i. Ae_i is the area of i^{th} electrode while L is the total number of electrodes along the body boundary. This model is termed the gap model. Although this model resolves the need for the definition of a continuous pattern on $\partial\Omega$, it still underestimates the conductivity of the body because it ignores shunting effects and contact impedance at the electrode-body interface (Vauhkonen, 1997).

To resolve the influence of shunting at the electrode-body boundary, the following boundary is considered:

$$\phi = v_i \qquad \text{on } e_i,\ i = 1,2,\ldots L \tag{4.41}$$

Where v_i is the measured voltage on the i^{th} electrode. This equation reflects the fact that the electric potential on a highly conductive electrode should be constant. Hence, Equation 4.30, 4.40 and 4.41 together are the so called shunt model. This model, however, has a tendency to overestimate the medium conductivity because again, contact impedance at the body-electrode interface is not considered (Somersalo *et al.*, 1992).

Contact impedance is an electrical impedance introduced at the interface between an electrode and the conductive body (for example, its impact on measurements of ECC conductivity was encountered in Chapter 3). Specifically, it is an electrochemical reaction that occurs when electricity is applied at the interface (Hansson and Hansson, 1983). The electric potential associated with the contact impedance, z_i, at the i^{th} electrode can be written as:

$$\phi_{CI} = z_i \sigma \nabla \phi \cdot \mathbf{n} \tag{4.42}$$

Hence, Equation 4.41 is rewritten as:

$$\phi + z_i \sigma \nabla \phi \cdot \mathbf{n} = v_i \qquad \text{on } e_i,\ i = 1,2,\ldots L \tag{4.43}$$

Furthermore, the total applied current of Equation 4.40 is rewritten in the form:

$$\int_{\mathrm{Ae_i}} \sigma \nabla \phi \cdot \mathbf{n} d\mathrm{A} = \overline{I_i} \qquad \text{on } e_i,\ i = 1,2,\ldots L \tag{4.44}$$

Finally, in locations where we do not have an electrode, the following condition holds:

$$\sigma \nabla \phi \cdot \mathbf{n} = 0 \tag{4.45}$$

When Equation 4.43, 4.44, and 4.45 are combined with the Laplace Equation (Equation 4.30), the complete electrode model is derived (Vauhkonen, 1997). To ensure the existence and uniqueness of a solution to the complete electrode model, two additional conditions are necessary:

$$\sum_{i=1}^{L} \overline{I_i} = 0 \tag{4.46}$$

$$\sum_{i=1}^{L} \overline{v_i} = 0 \tag{4.47}$$

The Complete Electrode Model, when properly tuned (i.e. selection of z_i), provides a model with excellent agreement with experimental boundary measurements. The EIT formulation based on each of the four models (continuum, gap, shunt and complete electrode) will offer different conductivities, with the complete electrode closest in

agreement with experimental data. For example, Figure 4-4 offers a direct comparison between the Continuum, Gap, Shunt and Complete Electrode Models (Somersalo *et al.*, 1992).

4.3 Finite Element Formulation of the Forward Problem

Generally, solving Equation 4.30 analytically is feasible only in the case of bodies defined by a homogeneous medium and those with symmetric geometries such as circular bodies (Pidcock *et al.*, 1995a; Pidcock *et al.*, 1995b). In cases where the body geometry is irregular and the body medium is conductively inhomogeneous, an analytical solution of the Laplace Equation is generally not plausible. As a result, numerical approaches must be employed to accurately solve Equation 4.30 in the forward problem formulation. There are several numerical approaches widely available that can be used, including the finite difference method (FDM), boundary element method (BEM) and finite element method (FEM). In this study, the finite element method is elected to numerically solve the Laplace Equation in the forward problem formulation.

FEM has proven to be a very powerful approach to obtaining a numerical solution to the Laplace partial differential equation when the medium is inhomogeneous and the body geometry is fairly irregular (Murai and Kagawa, 1985; Yorkey *et al.*, 1987; Jarvenpaa, 1996; Paulson *et al.*, 1992; Woo *et al.*, 1994). In this section, the FEM formulation of the Laplace Equation using the complete electrode model is presented. After the FEM solution is introduced, simple examples will be used to illustrate the power of the approach for modeling electrical phenomenon in conductive bodies.

The finite element method starts by discretizing the body Ω into a discrete set of finite elements. The electric potential at the vertices of the elements will be solved for, ϕ, with a total of N vertices defined over the entire body. With potential at the vertices defined, the electric potential everywhere else as defined by the location vector x is based on interpolation using a set of basis function, w_i:

$$\phi_{FEM}(\mathbf{x}) = \sum_{i=1}^{N} \phi_i w_i(\mathbf{x}) \tag{4.48}$$

The basis function w_i has a value of 1 on the vertex i but 0 at all the others. Any admissible basis function can be selected but generally polynomial functions are used because of their simplicity and accuracy.

Since w_i is not differentiable due to the cusp at the nodes, Equation 4.48 can not satisfy the partial differential Laplace Equation (Equation 4.30). Therefore, the weak formulation of Equation 4.30 is derived using variational methods. Multiplying Equation 4.30 by an arbitrary function, q, and integrating over the entire volume of the body leads to:

$$\int_V q(\nabla \cdot (\sigma \nabla \phi)) dV = 0 \qquad \text{in } \Omega \tag{4.49}$$

Based on Green's Theorem, the first of Green's three identities can be derived. Specifically:

$$\nabla \cdot (q \sigma \nabla \phi) = \nabla q \cdot (\sigma \nabla \phi) + q(\nabla \cdot (\sigma \nabla \phi)) \tag{4.50}$$

Green's first identity (Equation 4.50) can be rewritten to isolate the integrand of Equation 4.49:

$$q(\nabla \cdot (\sigma \nabla \phi)) = \nabla \cdot (q \sigma \nabla \phi) - \nabla q \cdot (\sigma \nabla \phi) \tag{4.51}$$

Therefore, Equation 4.49 can be rewritten as:

$$\int_V \nabla \cdot (q \sigma \nabla \phi) dV - \int_V (\nabla q \cdot \sigma \nabla \phi) dV = 0 \tag{4.52}$$

From Green's Theorem, the first term in Equation 4.52 can be rewritten as:

$$\int_V \nabla \cdot (q\sigma\nabla\phi) dV = \oint_S q\sigma\nabla\phi \cdot \mathbf{n} dS \tag{4.53}$$

If Equation 4.53 is substituted into Equation 4.52, the following result is obtained:

$$\int_V (\nabla q \cdot \sigma\nabla\phi) dV = \oint_S q\nabla\sigma\nabla\phi \cdot \mathbf{n} dS \tag{4.54}$$

Equation 4.54 is the weak formulation of the Laplace Equation.

The Dirichlet Boundary Condition at the body boundary $\partial\Omega$ combined with the complete electrode model (Equation 4.43) is considered at the i^{th} electrode:

$$\phi + z_i \sigma\nabla\phi \cdot \mathbf{n} = v_i \qquad \text{on } e_i, i = 1,2,\ldots L \tag{4.43}$$

The equation is rewritten as:

$$\sigma\nabla\phi \cdot \mathbf{n} = \frac{1}{z_i}(v_i - \phi_i) \qquad \text{on } e_i, i = 1,2,\ldots L \tag{4.55}$$

The right-hand side of the weak formulation of the Laplace Equation (Equation 4.54) is integrated over the boundary of the body. Since the integral is zero when there are no electrodes, the integral can be defined along the boundary where electrodes are present. In doing so, the condition described in Equation 4.55 can be used to rewrite the weak formulation of the problem:

$$\int_V (\nabla q \cdot \sigma\nabla\phi) dV = \sum_{i=1}^{L} \int_{e_i} \frac{1}{z_i}(v_i - \phi) q dS \tag{4.56}$$

Since the variable q is arbitrary, it is defined in a discrete manner similar to that used to define electric potential:

$$q = \sum_{i=1}^{N} q_i w_i \tag{4.57}$$

In Equation 4.56, there exist gradients for q and ϕ on the left-hand side. When considering the discrete formulation of ϕ and q, then their gradients are as follows:

$$\nabla \phi(\mathbf{x}) = \nabla\left(\sum_{j=1}^{N} \phi_j w_j(\mathbf{x}) \right) = \sum_{j=1}^{N} \phi_j \nabla w_j(\mathbf{x}) \tag{4.58}$$

$$\nabla q(\mathbf{x}) = \nabla\left(\sum_{i=1}^{N} q_i w_i(\mathbf{x}) \right) = \sum_{i=1}^{N} q_i \nabla w_i(\mathbf{x}) \tag{4.59}$$

The discrete formulations of ϕ and q and their gradients are included in Equation 4.56 to yield at node "i":

$$\sum_{j=1}^{N} \left\{ \int_{\mathrm{V}} \sigma \nabla w_i \cdot w_j d\mathrm{V} \right\} \phi_j + \sum_{k=1}^{L} \left\{ \int_{e_k} \frac{1}{z_k} w_i w_j d\mathrm{S} \right\} \phi_j - \sum_{k=1}^{L} \left\{ \int_{e_k} \frac{1}{z_k} w_i d\mathrm{S} \right\} v_k = 0 \tag{4.60}$$

An additional boundary condition to consider is the Neumann Boundary Condition (Equation 4.39). Since current is only applied at the electrodes, the boundary condition is restated:

$$\sum_{k=1}^{L} \overline{I_k} = 0 \tag{4.46}$$

Based on Equation 4.43 and 4.44, the applied current, $\bar{I}_k$, at the k^{th} electrode can be written as:

$$\overline{I_k} = \int_{e_k} \frac{v_k - \phi}{z_k} d\mathrm{S} \tag{4.61}$$

Therefore, upon substitution of Equation 4.48 in Equation 4.61, the following equation is derived:

$$\overline{I_k} = \int_{e_k} \frac{v_k}{z_k} d\mathrm{S} - \sum_{i=1}^{N} \left\{ \int_{e_k} \frac{1}{z_k} w_i d\mathrm{S} \right\} \phi_i \tag{4.62}$$

Generally, the contact impedance, z_k, is assumed constant over the entire electrode. Thus, Equation 4.62 becomes:

$$\overline{I_k} = \frac{v_k}{z_k} \int_{e_k} d\mathrm{S} - \sum_{i=1}^{N} \frac{\phi_i}{z_k} \left(\int_{e_k} w_i d\mathrm{S} \right) \tag{4.63}$$

The area of the electrode, Ae_k, is used to further simplify Equation 4.63:

$$\overline{I_k} = \frac{v_k}{z_k} Ae_k - \frac{1}{z_k} \sum_{i=1}^{N} \phi_i \left(\int_{e_k} w_i d\mathrm{S} \right) \tag{4.64}$$

Equations 4.60 and 4.64 serve as the governing equations of the FEM model. Let us define the following vectors:

$$[\Phi] = \{\phi_1, \phi_2, \ldots \phi_N\}^T \in \mathrm{R}^{N \times 1} \tag{4.65}$$

$$[V] = \{v_1, v_2, \ldots v_L\}^T \in \mathrm{R}^{L \times 1} \tag{4.66}$$

$$[\overline{I}] = \{\overline{I}_1, \overline{I}_2, \ldots \overline{I}_L\}^T \in \mathrm{R}^{L \times 1} \tag{4.67}$$

If Equation 4.60 is written for all N nodes, then the following is found:

$$[A_M][\Phi]+[A_Z][\Phi]+[A_W][V]=0 \tag{4.68}$$

where $[A_M]\in \mathrm{R}^{N\times N}$, $[A_Z]\in \mathrm{R}^{N\times N}$, and $[A_W]\in \mathrm{R}^{N\times L}$ and

$$A_{M\,ij}=\int_{\mathrm{V}}\sigma\nabla w_i\cdot w_j d\mathrm{V} \tag{4.69}$$

$$A_{Z\,ij}=\sum_{k=1}^{L}\frac{1}{z_k}\int_{e_k} w_i w_j d\mathrm{S} \tag{4.70}$$

$$A_{W\,ij}=\frac{1}{z_k}\int_{e_k} w_i d\mathrm{S} \tag{4.71}$$

If the conductivity is assumed to be constant over a given element, then Equation 4.69 is rewritten as:

$$A_{M\,ij}=\sum_{p=1}^{P}\sigma_p\int_{\mathrm{V_p}}\nabla w_i\cdot\nabla w_j d\mathrm{V_p} \tag{4.72}$$

where σ_p is the conductivity of the p^{th} element, and there are P elements defined by the N nodes.

Equation 4.64 can be written in matrix form as well:

$$[A_W]^T\{\Phi\}+[A_D]\{V\}=\{\bar{I}\} \tag{4.73}$$

where $[A_W]^T\in \mathrm{R}^{N\times L}$ is the transpose of $[A_W]$ and $[A_D]\in \mathrm{R}^{L\times L}$ and

$$[A_D] = \begin{bmatrix} \frac{Ae_1}{z_1} & & \\ & \ddots & \\ & & \frac{Ae_L}{z_L} \end{bmatrix} \tag{4.74}$$

Hence Equation 4.68 and 4.73 can be combined to derive one linear equation:

$$\begin{bmatrix} A_M + A_Z & A_W \\ A_W^T & A_D \end{bmatrix} \begin{Bmatrix} \Phi \\ V \end{Bmatrix} = \begin{Bmatrix} 0 \\ I \end{Bmatrix} \tag{4.75}$$

The large matrix [A]:

$$[A] = \begin{bmatrix} A_M + A_Z & A_W \\ A_W^T & A_D \end{bmatrix} \in R^{(N+L)\times(N+L)} \tag{4.76}$$

is generally sparse.

To illustrate, the system matrix [A] for a single triangular element will be derived. Suppose a triangular element of a uniform conductivity σ is as shown in Figure 4-5 where the electrode is placed along side 1-2 with contact impedance z. It is assumed that the length of side 1-2 and 2-3 are both a. The 1st order linear basis functions (shape functions) of a 2-D triangular element (Figure 4-6) are given as:

$$\begin{cases} w_1 = \left(1 - \frac{x}{a}\right)\left(1 - \frac{y}{a}\right) \\ w_2 = \frac{x}{a}\left(1 - \frac{y}{a}\right) \\ w_3 = \frac{xy}{a^2} \end{cases} \tag{4.77}$$

Shape functions of higher order can be found in Reddy (1993). For example, Figure 4-7 shows second order functions for a triangular element. For simplicity, the 1st order shape functions will be used in the following example.

Using Equation 4.69 for a planar triangular element:

$$\begin{aligned} A_{M,11} &= \sigma \int_0^a \int_0^a \nabla w_1 \cdot \nabla w_1 dxdy = \frac{1}{3}\sigma \\ A_{M,12} &= \sigma \int_0^a \int_0^a \nabla w_1 \cdot \nabla w_2 dxdy = -\frac{1}{6}\sigma \\ &\vdots \end{aligned} \tag{4.78}$$

which results in the following subsystem matrix A_M:

$$A_M = \sigma \begin{bmatrix} \frac{1}{3} & -\frac{1}{6} & -\frac{1}{6} \\ -\frac{1}{6} & \frac{1}{2} & -\frac{1}{6} \\ -\frac{1}{6} & -\frac{1}{6} & \frac{1}{3} \end{bmatrix} \tag{4.79}$$

Similarly, from Equation 4.70:

$$\begin{aligned} A_{Z,11} &= \sum_{l=1}^{L} \frac{1}{z} \int_S w_1 w_1 dS = \frac{a}{3z} \\ A_{Z,12} &= \sum_{l=1}^{L} \frac{1}{z} \int_S w_1 w_2 dS = \frac{a}{6z} \\ &\vdots \end{aligned} \tag{4.80}$$

The subsystem matrix A_Z is then:

$$A_Z = \frac{1}{z}\begin{bmatrix} \frac{a}{3} & \frac{a}{6} & 0 \\ \frac{1}{6} & \frac{a}{3} & 0 \\ 0 & 0 & 0 \end{bmatrix} \tag{4.81}$$

and A_W and A_D are:

$$A_W = A_{W,11} = -\frac{1}{z}\int w_1 d\mathrm{S} = -\frac{a}{2z}\begin{bmatrix} 1 & 0 & 0 \end{bmatrix} \tag{4.82}$$

$$A_D = A_{D,11} = \frac{a}{z}\begin{bmatrix} 1 & 0 & 0 \\ 0 & 0 & 0 \\ 0 & 0 & 0 \end{bmatrix} \tag{4.83}$$

In this thesis, there are 12 kinds of system matrices corresponding to the 12 type of triangular elements implemented (as shown in Figure 4-8). Their element system matrices are constructed following the similar rules to the ones used to formulate the matrices for the element of Figure 4-5.

Once the individual element matrices are constructed, they are assembled into the global system matrix [A] by standard finite element practice (Reddy, 1993). For example, suppose a rectangular body is meshed into 8 triangular elements, as shown in Figure 4-9. The process of assembling each local element system matrix into the global system matrix would yield the following:

$$\begin{aligned} [A] &= [A]_{(9+4,9+4)} \\ [\Phi]_{9\times 1} &= [\phi_1, \phi_2, \cdots \phi_9]^T \\ [V]_{4\times 1} &= [V_{e1}, V_{e2}, V_{e3}, V_{e4}]^T \\ [I]_{4\times 1} &= [-I, 0, 0, I] \end{aligned} \tag{4.84}$$

Solving Equation 4.75 (of the form $[A]\{x\}=\{b\}$) requires the inversion of $[A]$ to solve for $[V]$ and $[\Phi]$. This is the linear approximation of the forward problem. However, it should be mentioned that the system matrices, $[A]$ are usually sparse and ill-posed. Therefore, solving Equation 4.75 may require certain mathematical tools such as LU decomposition among others.

4.4 Inverse Problem

The purpose of the inverse problem, also known as image reconstruction, is to seek an appropriate conductivity distribution, σ, such that the mean square error between the predicted boundary voltages and the experimental values are minimized:

$$\begin{aligned} f(\sigma) &= \frac{1}{2}(\phi(\sigma)-v)^T(\phi(\sigma)-v) \\ &= \frac{1}{2}\|(\phi(\sigma)-v)\|^2 \end{aligned} \tag{4.85}$$

In this section, an iterative approach is introduced so as to minimize Equation 4.85. Here, ϕ is defined as the electrical potential at the boundary based on the prior conductivity distribution, σ, and v is the experimentally measured boundary voltages. In order to minimize the mean square error, f, we thus take the first derivative of Equation 4.85 with respect to σ and set it equal to zero:

$$f' = (\phi')(\phi - v) = 0 \tag{4.86}$$

where ϕ' is the Jacobian matrix of ϕ with respect to conductivity, σ, and is defined as:

$$\phi' = \frac{\partial \phi}{\partial \sigma} \tag{4.87}$$

Obviously, Equation 4.86 is nonlinear, often requiring methods such as Taylor series expansion to linearize it. Suppose for an arbitrary set of conductivities, σ_k:

$$f' \approx f'(\sigma_k) + f''(\sigma_k) h_k + h.o.t. \tag{4.88}$$

where h_k is the difference between σ and σ_k, ($h_k = \sigma - \sigma_k$), and *h.o.t.* denotes "high order terms" in the Taylor series expansion. Setting Equation 4.88 equal to zero and neglecting the high order terms would lead to an iterative expression of h_k:

$$h_k = -f''(\sigma_k)^{-1} f'(\sigma_k) \tag{4.89}$$

This iterative approach is also known as Newton-Raphson method. Here *f"* is known as the Hessian matrix and is defined as:

$$f'' = \phi'^T \phi' + \phi''^T \left[I_m (\phi - v) \right] \tag{4.90}$$

where I_m is an identity matrix with rank m.

Since the second derivative of potential, ϕ'', is very difficult to calculate in practice and is generally quite small compared to ϕ'; in most cases it is usually neglected (Narenda and Mehra, 1974). Therefore, the Hessian matrix, Equation 4.90, is further simplified as:

$$f'' \approx \phi'^T \phi' \tag{4.91}$$

Based on Equation 4.89, 4.90 and 4.91, an iterative expression of h_k is now derived:

$$h_k = -\left[\phi'(\sigma_k)^T \phi'(\sigma_k) \right]^{-1} \phi'(\sigma_k) \left[\phi'(\sigma_k) - v \right] \tag{4.92}$$

Therefore, at the k^{th} iteration, the conductivity distribution for the next step, σ_{k+1}, can then be calculated as:

$$\sigma_{k+1} = \sigma_k + h_k \tag{4.93}$$

This iterative formulation for minimizing the objective function is well known as the modified Newton-Raphson method or Gauss-Newton method (Narenda and Mehra, 1974). Convergence of the Gauss-Newton method is dependent on the validity of the assumption made to derive Equation 4.91, and the step size of h_k. In general, the Gauss-Newton method is capable of offering excellent computational performance and the same convergence properties as the Newton-Raphson method (Narenda and Mehra, 1974).

In most cases, the calculation of $[\phi'(\sigma)^T\phi'(\sigma)]^{-1}$ in Equation 4.92 is ill-posed in the sense that the largest eigenvalue is 6 orders (or even more) of magnitude larger than that of the minimum eigenvalue. This ill-posed condition constrains the accuracy of $[\phi'(\sigma)^T\phi'(\sigma)]^{-1}$; hence, conductivity updating is generally done in very small steps. Furthermore, if the initial conductivity distribution (σ_0) is far from the true distribution, the conductivity updating would proceed in an incorrect direction. Hence, prior knowledge of conductivity can be very useful in ensuring a stable and accurate conductivity distribution is found during image reconstruction.

In order to handle ill-posed condition of $[\phi'(\sigma)^T\phi'(\sigma)]^{-1}$, the second term in Equation 4.90 can be reconsidered for inclusion in the calculation of the Hessian matrix of f. However, the term is simplified by approximating it as:

$$\phi''^T\left[I_m(\phi - v)\right] \approx \lambda I_m \tag{4.94}$$

where λ is a positive scalar. By adding this term into Equation 4.88 (again the higher order terms are neglected), the iterative expression of h_k can be rederived as:

$$h_k = -\left[\phi'(\sigma_k)^T \phi'(\sigma_k) + \lambda_k I_m\right]^{-1} \phi'(\sigma_k)\left[\phi'(\sigma_k) - v\right] \tag{4.95}$$

Equation 4.95 combined with Equation 4.93 is widely termed the Marquardt method or, more generally, the Levenberg-Marquardt method (Levenberg, 1944; Marquardt, 1963). In this thesis, the Levenberg-Marquardt method is adopted. It should be noted that the scalar λ varies iteratively depending upon the value of the subsequent objective function. For example, λ is multiplied by 0.1 when $f_{k+1} < f_k$, and by 10 when $f_{k+1} > f_k$. If the studied medium exhibits a simple conductivity distribution (*i.e.* homogeneous), the ill-posed condition of $[\phi'(\sigma)^T\phi'(\sigma)]^{-1}$ vanishes and λ would shrink to zero. Therefore, the Levenberg-Marquardt method would be identical to the Gauss-Newton method.

4.5 Theoretical Limitation and Discussion of Other Issues

In EIT conductivity reconstruction, the existence and uniqueness of the final solution is guaranteed when the stated assumptions of the complete electrode model are satisfied. Specifically, Equation 4.46 must be satisfied to ensure a solution exists while Equation 4.47 must be satisfied to ensure it is a unique solution. In each iteration of the inverse process, the boundary conditions must be obeyed so as to obtain the global minimum of the objective function. Some other conditions necessary to arrive at a global minimum include the initial guess of the conductivity distribution and the assumptions on the nature of the contact impedance at the electrode-body boundary. The existence and uniqueness of a solution when using the complete electrode model are proved rigorously by Somersalo *et al.* (1992).

Theoretically, any tomographic imaging technology has certain limitations to its image resolution and accuracy. For EIT, the image resolution considers the smallest conductivity inhomogeneity that can be detected. Accuracy on the other hand relates to the dynamic range in which the conductivity can be correctly represented. Resolution of the image is mainly controlled by the number of boundary electrodes installed. In order to obtain a high-resolution conductivity image, a large number of electrodes are desired;

however, this will dramatically reduce the speed of the inverse process in an exponential manner. There also exists a threshold of the electrode number at which the image resolution can no longer be improved (Seagar *et al.*, 1987).

Limitations on image accuracy are attributed to the noise of the measurements and the conductivity contrast of the object. A measurement system with infinitely high dynamic range and free of measurement noise would offer very high sensitivity. However, such a measurement system is impossible to obtain. While there still exists no standard methods to quantitatively examine the sensitivity of the conductivity image, it is well accepted that a measurement system with noise levels of 10^{-6} are ideal for a 32 electrode system with image sensitivity (the lowest conductivity divided by the largest conductivity) of 0.002 (Seagar *et al.*, 1987). Other presented issues that would cause errors and restrain the image quality (resolution and accuracy) include the applied current pattern and the measurement strategy (Seagar and Brown, 1987; Cheng *et al.*, 1988; Kolehmainen and Vauhkonen, 1997), the reconstruction algorithms themselves (Breckon and Pidcock, 1988), electrode sizes and locations (Kolehmainen and Vauhkonen, 1997), contact impedance (Yorkey *et al.*, 1985; Kolehmainen and Vauhkonen, 1997), and the geometry of the object under study (Kolehmainen and Vauhkonen, 1997).

4.6 Conclusions and Summary

This chapter reviews the theoretical background of the EIT approach including the mathematical model governing the electrical behavior of a semi-conducting or conducting body. Furthermore, both the forward and inverse problems are rigorously posed. The complete electrode model (CEM) is generally used for the forward problem since it considers shunt effects as well as contact impedance, leading to simulation results that are nearly identical to the experimental results. Since an analytical solution to the complete electrode model exists only in the case of an object with simple geometries and symmetric conductivity distributions, discrete approaches (in this study, the finite element method) are required to obtain numerical solutions. For the inverse problem, the

Levenberg-Marquardt method is adopted to deal with the ill-condition of the Jacobian matrix ($\phi'(\sigma)$).

Compared to the probing methods introduced in Chapter 3, the EIT approach provides a spatial mapping of conductivity by repeatedly performing 4-point probing measurements along an object's boundary. By creating spatial conductivity maps, strain and cracking can be detected in a spatial manner. In the next chapter, the EIT approach is employed for strain and crack imaging in HPFRCC structural elements.

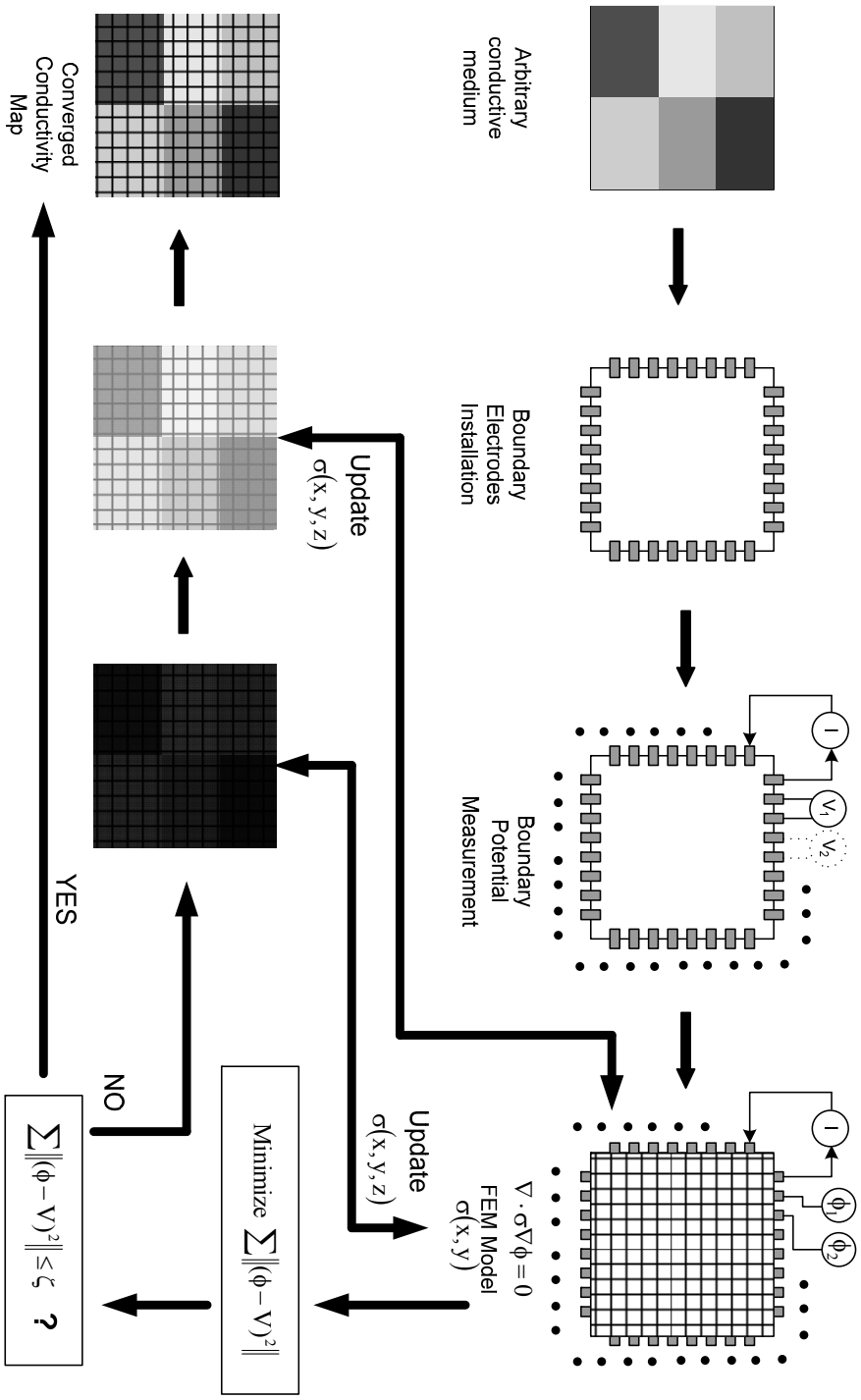

Figure 4-1: General procedure of electrical impedance tomography (EIT) conductivity determination.

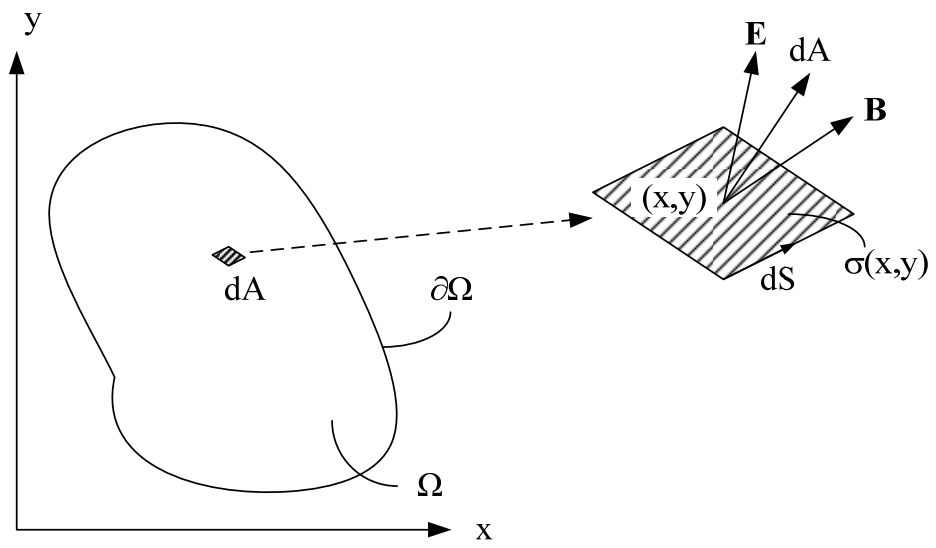

(a) (b)

Figure 4-2: (a) Conductive body, Ω; (b) the electric (**E**) and magnetic (**B**) vector fields acting over area, dA.

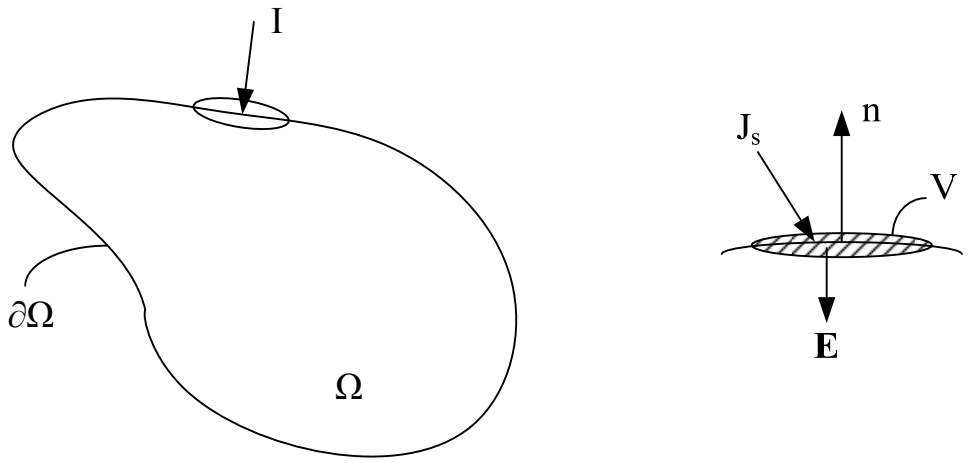

(a) (b)

Figure 4-3: (a) Body, Ω, with an applied current, I; (b) close-up view of boundary at the point current injection.

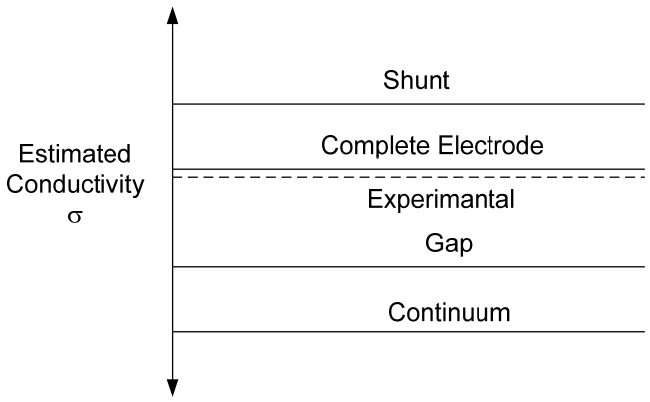

Figure 4-4: Comparison of predicted body conductivity, σ, using the continuum, gap, shunt and complete electrode models in the EIT formulation (after Somersalo *et al.*, 1992).

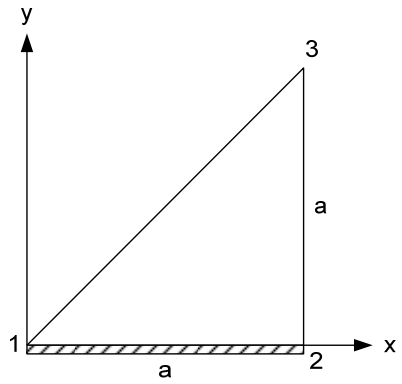

Figure 4-5: Triangular element with a uniform conductivity, σ, and an electrode placed along side 1-2.

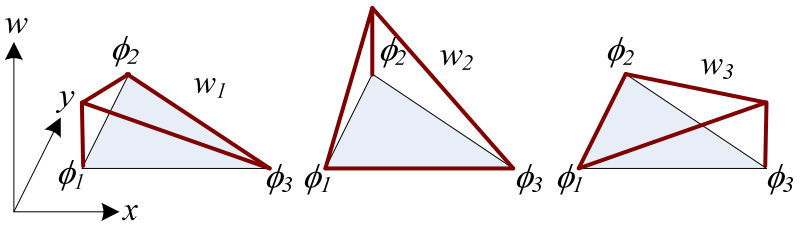

Figure 4-6: 1st order basis functions of 2-dimensional triangular elements.

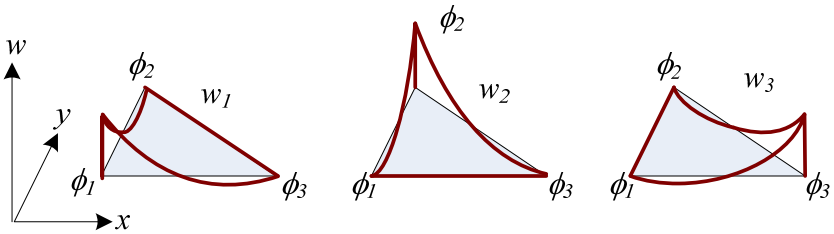

Figure 4-7: 2nd order basis functions of 2-dimensional triangular elements.

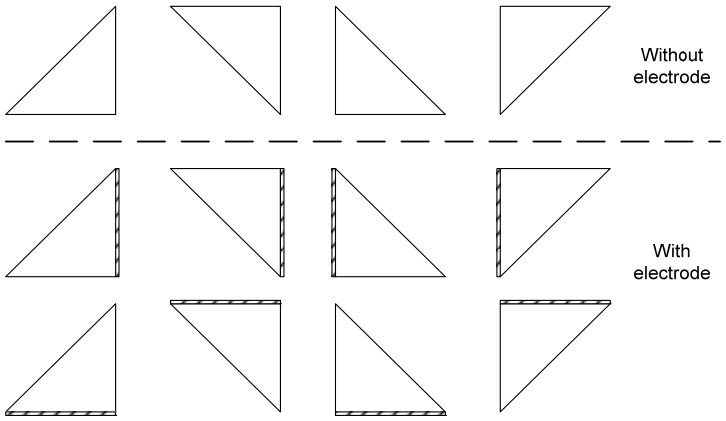

Figure 4-8: 12 types of triangular elements

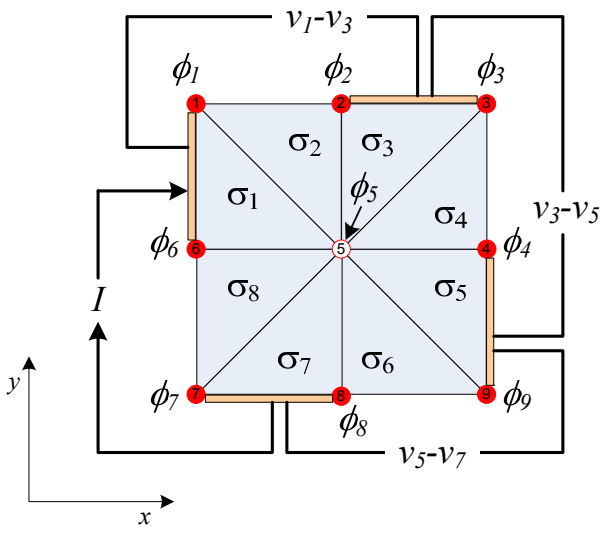

Figure 4-9: A rectangular medium with 9 nodes, 8 triangular elements, and 4 electrodes.

Chapter 5

Electrical Impedance Tomography-Based Sensing of Fiber Reinforced Cementitious Composite Materials

5.1 Introduction

In Chapter 3, the electrical methods currently used to monitor the mechanical properties of cementitious materials were presented. By using 2-point and 4-point probing methods, polarization effects and the piezoresistive behavior of fiber reinforced cementitious composites were monitored. These methods employed HPFRCC materials as their own sensor with bulk material resistivities correlated to strain, and damage. Although 2-point and 4-point probing methods provide quantitative information of a material's electrical response under loading, information pertaining to cracking (not just existence) is sought including the location, spacing, and width of cracks. More detailed information on cracking allows engineers the opportunity to determine if the crack reduces the strength of the structure or renders buried reinforcement vulnerable to corrosion.

The inherent benefit of leveraging the electrical properties of cement-based materials for sensing is their electro-mechanical response is everywhere the material is. Hence, there is potential to utilize the material as a fully distributed sensor in which strain and damage can be characterized over the full spatial dimensions of a structural element. Towards this end, electrical impedance tomography (EIT) is adopted to accurately measure the spatial distribution of electrical resistivity in FRCC materials using only electrical

measurements taken at the boundary of the element (Holder, 2005). Given the absence of large aggregates in FRCC materials, the electrical properties of FRCC structural elements are fairly homogeneous across their dimensions. Therefore, the EIT framework will offer spatial observation of the conductivity of the FRCC elements instrumented.

Compared to the traditional 2- and 4-point probe methods employed in Chapter 3, EIT is expected to offer more insightful observation of strain and crack fields distributed with cementitious structural elements. This chapter applies the EIT technique discussed in Chapter 4 to FRCC structural elements to produce multi-dimension conductivity maps that are correlated to strain. In addition to utilizing EIT to measure two-dimensional strain fields, the approach is also shown capable of visually observing the evolution of dense cracking in FRCC structural elements. In this study, only homogeneous FRCC materials (such as ECC) without coarse aggregates or steel reinforcement are investigated. However, EIT can still be applied to other types of cement-based structural elements including those with coarse aggregates and steel reinforcement.

The objectives of the chapter are:

- Apply EIT conductivity mapping to FRCC materials, specifically ECC.
- Correlate changes in conductivity to strain when ECC elements are loaded in their elastic regime.
- Observe cracking in EIT conductivity maps after strain hardening has initiated.
- Correlate conductivity changes due to cracking and crack widths.

5.2 Experimental Methods

5.2.1 ECC Test Specimens

In this study, structural elements constructed of ECC (Mix M-45), are adopted to evaluate the application of EIT sensing for the measurement of strain and the identification of cracking. Similar to the link slab element discussed in Chapter 2 and the piezoresistive study in Chapter 3, the ECC materials mix used in this study employs Type 1 Portland

cement, silica sand as a fine aggregate, fly ash and short polyvinyl alcohol (PVA) fibers for mechanical reinforcement. To control the growth of cracks and to attain strain hardening behavior in tension, the surface of the PVA fiber is chemically treated to tailor the micro-mechanical properties of the fiber-matrix interface (Li *et al.*, 2002). Only a relatively small amount of PVA fibers is necessary to attain optimal mechanical properties; in this study, a 2% volume fraction of PVA fibers is used. To build test specimens, wet ECC mixture is poured into molds where they remain for seven days to harden. Once seven days have passed, the specimens are removed from the molds and cured until testing, which occurs no earlier than 28 days after casting. The first set of test specimens constructed are ECC plates that are 30.5 cm long with cross sectional areas of 7.6 by 1.3 cm^2. The second specimen employed is an ECC beam which is more representative of a realistic structural element; however, no steel reinforcement is included. The beam is 140 cm long, 15.2 cm deep, and 7.6 cm wide. The plate specimens tested are shown in Figure 5-1a while the beam specimen tested is shown in Figure 5-2a.

5.2.2 Data Acquisition

To conduct EIT sensing on the test specimens, each specimen is instrumented with copper electrodes. Adhesive copper tape 6.3 mm wide and 0.7 mm thick (Ted Pella Inc. 16072 3M) is attached to the surface of the test specimens as shown in Figure 5-3a. To ensure the copper-cement contact is conductive, additional silver colloidal paste is used to attach the electrodes. AC electrical signals are applied to an adjacent set of electrodes using a high-precision current generator (Keithley 6221). As the AC current is applied to the element, electrical potential (voltage) is measured at all of the other electrodes using a standard laboratory data acquisition system (National Instruments). Standard shielded coaxial wires, roughly 1 m in length, are used to attach the data acquisition system to the copper electrodes. The complete experimental set-up is shown in Figure 5-3b. MATLAB is then used to execute the tomographic reconstruction process. The FEM model used during reconstruction for each test specimen consists of mesh of 384 triangular elements evenly distributed over the specimen.

Strain is also measured by three traditional methods for many of the loaded specimens. First, metal foil strain gages (Texas Measurements PFL series) with nominal resistances of 120 Ω and gage factors of 2.1 are installed to the surface of the ECC specimens using epoxy (Texas Measurements CN-Y). An additional approach to measuring strain is by optical methods using the OptoTrak Certus motion capture system. The system consists of a 3020 OptoTrak camera position sensor (111 cm x 31.5 cm x 21.5 cm), markers and a system control unit. The markers are reflective nodes (approximate diameter 1 cm) that are attached to the specimen surface using standard glue. Two-dimensional motion of the markers is accurately measured by the 3020 OptoTrak camera position sensor with a resolution of less than 10μm. To achieve this resolution, the camera is placed 2 m from the instrumented test specimens. The last approach is to calculate strain using the actuator displacement as measured by a load frame's linear variable differential transformer (LVDT).

5.2.3 Monotonic Tensile Loading

Four rectangular ECC plate specimens are prepared for monotonic tensile loading. First, thirty-two copper electrodes are attached to the sides of the plate as shown in Figure 5-1a. On the long sides of the specimen, twelve electrodes are attached to each side; the shorter sides each have four electrodes attached. The electrodes are installed in a manner such that they are equidistant from one another. The specimens are labeled as specimen MT1 through MT4. Twelve OptoTrak markers are glued to the front surface of specimen MT1; the markers are oriented in two vertical rows and separated by 3 cm from one another (Figure 5-1a). The marker orientation divides the plate specimen into five regions labeled as region 1 through 5. Along the vertical center line of the specimen, five metal foil strain gages are epoxy mounted; the gages are separated such that each region has its own strain gage.

Strain gages and OptoTrak markers are not installed on specimens MT2 through MT4. Due to instrumentation congestion, only the load frame displacement will be used to determine strain. However, it should be mentioned that this strain value will not be as accurate as the strain values obtained from the strain gages or OptoTrak displacement

sensors mounted on the tested specimen. The primary cause of the lack of accuracy is a slight slippage of the hydraulic clamps gripping the specimen at the beginning of the loading process.

Specimen MT1 is gripped by an MTS-810 load frame and monotonically loaded in tension. Prior to the application of axial load, the copper electrodes are used to perform EIT sensing of the specimen in the specimen's unstrained state. This data will be used to derive a baseline conductivity map of the unloaded plate specimen. The load frame is commanded to apply tension load to the plate with the actuator displacement controlled. Applied force and actuator displacement are recorded from which stress and strain of the specimen can be calculated. The actuator is paused at 0.05, 0.1, 0.2, 0.3, 0.4, 0.5, 0.75, 1, 1.25 and 1.5% strain (denoted as P1 to P10 in Figure 5-4a). When paused, EIT sensing is conducted so as to collect electrical data for reconstruction of conductivity maps of the instrumented specimen. In addition, the strain gage resistance and displacement of the OptoTrak markers are both measured. After 1.5% strain has been achieved, the test is terminated. Specimens MT2 through MT4 are also loaded by the MTS load frame with monotonic tensile loading. Again, before axial load is applied to the specimens, EIT sensing is conducted to obtain baseline tomographic data. Next, each specimen is loaded with the actuator operated in displacement control mode to strain levels of 0.5, 1 and 2.4% strain. At each strain level, the load is paused and EIT sensing conducted. After 2.4% strain, each specimen is loaded until failure. At the point of failure, EIT sensing is again performed in order to capture each specimen's failure mechanism.

5.2.4 Cyclic Axial Loading

Again, thirty-two copper electrodes are attached to the boundary of plate specimen CT1 in the same configuration as specimens MT1 through 4 (Figure 5-1a). Before the specimen is gripped in the MTS load frame, EIT sensing is performed to derive a baseline conductivity map of the unloaded specimen. The specimen is then gripped in the MTS load frame and two tension-compression cycles are applied. The specimen is cyclically loaded with the following peak strains: first, 0.32% strain in tension, second, 0.5% strain in compression, third, 1.2% strain is tension, forth, 1% strain in compression, and then

finally 2% strain in tension. After 2% tensile strain is achieved, the specimen is monotonically loaded in tension until failure. Along the two cycles of loading, the application of axial load is paused and EIT conductivity maps calculated.

5.2.5 Monotonic Three Point Bending

The ECC beam previously described is instrumented with thirty-two copper electrodes mounted to the bottom face of the beam. A section roughly 38.1 cm long and 7.6 cm wide is delineated in the center of the beam by the electrodes (Figure 5-2a). Twelve electrodes are attached along each of the long sides of this region while four electrodes are attached on each of the shorter sides. The beam is placed upon the bed of an Instron general purpose load frame (Instron 8500); rollers spaced 121.9 cm apart support the beam at the beam's two ends while an actuator applies load at the center of the top face. An EIT conductivity map is acquired prior to the application of load. Once load is applied, the test is paused when center span deflections of 0.2 and 0.6 cm are achieved so that EIT conductivity maps of the beam's lower face can be acquired. After the center displacement of 0.6 cm is achieved, the beam is loaded till failure. At the point of failure, an EIT conductivity map is acquired before the load is removed.

5.3 Reconstruction Results and Discussion

5.3.1 Specimen MT1

Specimen MT1 is monotonically loaded in tension in order to estimate the sensitivity of the piezoresistive effect of ECC materials. The stress-strain curve of the monotonically loaded plate is presented in Figure 5-4a. The plate initiates strain hardening at approximately 0.05% strain (as calculated from the load frame displacement). The application of tension is paused three times while the plate is in its elastic region (denoted as P1, P2 and P3). After strain hardening, the test is again paused as denoted by points P4 through P10. Each time the test is paused, an EIT conductivity map of the plate is obtained. The conductivity of the specimen is averaged across each of the specimen's five regions (where each region is defined in Figure 5-1a) and compared to the average

conductivity prior to the application of load (effectively at P0). The percent change in average conductivity versus the average strain (as calculated from the displacement of the top-most and bottom-most OptoTrak marker displacement) is plotted in Figure 5-4b for each specimen region. As can be seen in the plot, each region exhibits approximately a linear change in conductivity as a function of strain.

The OptoTrak sensor system also measures strain in localized regions of the specimen. As a result, for each of the regions defined by the location of the OptoTrak markers (regions 1 through 5), the localized strains measured by the OptoTrak camera are compared to the average resistivity of the region. To calculate the average resistivity change, the conductivity change of the triangular elements of the EIT conductivity map in a given region (Figure 5-5) are averaged and inverted. For each region of specimen MT1, averaged resistivity is plotted against the local strain as measured by the OptoTrak system in Figure 5-6. The piezoresistive effect is evident with resistivity increasing in tandem with strain. Furthermore, the resistivity changes are fairly linear with gage factors of 15.0, 14.3, 15.6, 15.4 and 15.4 for regions 1 through 5, respectively. Compared to the gage factors obtained in Chapter 3 (4 point probe AC), the gage factor obtained in this chapter using EIT is about 3 to 4 times lower. A primary reason of this could be the age of the specimens (MT1 through MT5), which is much older than the specimens used in Chapter 3. As a result, a significant portion of the moisture contents has dried out resulting in a rise in the bulk resistance. The second reason may attributed to the lower AC frequency (500~700Hz) used in this study than in Chapter 3 (5k Hz), which reduces the baseline conductivity and thus, exhibits lower variation at each strain level. The third reason, although not clear yet, could be attributed to the measurement technique.

5.3.2 Specimen MT2 - MT4

The next set of monotonic tensile tests are intended to validate the use of EIT as a means of capturing the evolution of damage (*e.g.*, cracking) in ECC structural specimens. Specimens MT2, MT3 and MT4 are therefore loaded monotonically in uniaxial tension until failure (damage localization). During loading, stress-strain responses are recorded as shown in Figures 5-7a, 5-8a and 5-9a, respectively. All three specimens undergo

strain hardening after reaching approximately 0.25% strain (as calculated from the load frame stroke). The low elastic modulus and high strain value at strain hardening initiation are attributed to the slippage of the gripping clamps. The high ductility of the ECC material is evident by the ultimate strain levels reached by each of the three plates; specimens MT2, MT3 and MT4 all fail at tensile strains in excess of 2.5%.

When the specimens achieve 0.25% strain, the application of load is paused and an EIT conductivity map is acquired. To observe a change in conductivity, the conductivity map acquired at point A (*i.e.*, unloaded) will be subtracted from those acquired during loading. As can be seen in Figures 5-7b, 5-8b and 5-9b, the maps of the change in conductivity of the specimens at point B reveal reductions in conductivity consistent with strain (*i.e.*, the piezoresistive effect). Furthermore, regions of micro-cracking which occur during strain hardening are evident in the conductivity maps (right column of Figure 5-7b, 5-8b and 5-9b). For example, in specimen MT2, a thin band of concentrated conductivity change in the center of the element (Figure 5-7b, left column) reveals the micro-cracking associated with the initiation of strain hardening (Figure 5-7b, right column). Specimens MT3 (Figure 5-8b) and MT4 (Figure 5-9b) also have regions of micro-cracking evident towards the left side of their EIT conductivity maps. The microcrack width at this stage of loading for all three specimens is estimated to be less than 30 μm (as measured by a crack gage).

Monotonic tensile loading of the specimens continues until 1% strain is achieved. At point C, the average conductivity of each specimen reduces consistently with strain. However, regions of micro-cracking where conductivity reductions are greater have grown significantly. For example, for specimen MT4 (Figure 5-9b, left column), the thin region of micro-cracking first witnessed at 0.25% strain has grown to occupy nearly half of the specimen at 1.0% strain. Similarly, in specimen MT2 (Figure 5-7b, left column), the region of micro-cracking is in the center of the specimen and occupies nearly half of the specimen length. The development of microcracking is also illustrated in the right column of Figure 5-7b, 5-8b, 5-9b. At this stage of loading, the maximum crack width is estimated to be 60 μm.

The tests are continued until damage localizes into large cracks (*i.e.*, failure). The large cracks can be seen in the EIT conductivity maps as major reductions in conductivity, some as large as 500 nS-cm^{-1}. For example, in Figure 5-7b, two large cracks can be seen in the EIT conductivity map at the two ends of specimen MT2. The cracks imaged in the EIT map precisely capture the location and geometric orientation of the true damage state of specimen MT2 as pictured in Figure 5-7c. The cracks in the test specimen are highlighted using a red felt-tip marker to enhance the comparison. For specimen MT3, the macro-crack forms in the center of the specimen as can be seen in the final EIT conductivity map (Figure 5-8b) and the picture of the final specimen (Figure 5-8c). Again, in specimen MT4, the ECC plate develops a large crack towards the left-side of the specimen (Figure 5-9c). This crack is successfully captured by the EIT conductivity map at 3.0% strain (Figure 5-9b).

Figure 5-10 summarizes the relationship between crack widths, manually measured using a crack gage, and changes in conductivity observed in the EIT maps of the three ECC specimens. As seen, for cracks with widths less than 140 μm (defined as microcracks), the conductivity drops are less than 150 nS-cm^{-1}. Furthermore, there exists a linear relationship between the log of the crack width with the conductivity change. For cracks with widths over 2000 μm (damage localization), the conductivity drops are as greater as 450 ns-cm^{-1}. These results serve as a reference data for using EIT conductivity maps to distinguish the severity of cracking in FRCC structural elements.

5.3.3 Specimen CT1

Plate specimen CT1 is loaded cyclically in axial tension and compression. Again, the distribution of change in specimen conductivity (*i.e.,* conductivity minus the baseline conductivity) is mapped at multiple points along the cyclic loading profile so as to observe changes in conductivity associated with repeated application of tension and compression. As can be observed in Figure 5-11a, the specimen is first loaded in tension until a tensile strain of 0.32% (point B). At this strain level, a narrow band of micro-cracking can be observed towards the left-side of the specimen with the maximum crack

width less than 30 μm, as shown in the EIT conductivity map of Figure 5-11b (followed by the cracking sketch at each loading point). As the specimen is unloaded back to 0% strain (point C), the change in conductivity in the region of micro-cracking recovers suggesting the closure of the cracks. The plate is then loaded in compression to 0.5% strain (point D). When loaded in compression, the narrow crack field once again becomes evident although the conductivity reduction is less pronounced than when the element is loaded in tension. Even though the cracks introduced in tension have closed, because they likely do not close perfectly, some conductivity reduction is expected. When the specimen is reloaded in tension to 1% strain (point F), the microcracks from point B reopen while additional microcracks form yielding a larger field of micro-cracking as well as larger crack widths (~60 μm) at the left-side of the specimen. When the ECC specimen is further loaded in tension to 1.3% strain (point G), a second field of microcracks emerges near the center of the specimen. At this stage, the maximum crack width is observed to be approximately 80 μm. Thereafter, the specimen is loaded to 1% strain in compression (point I). Again, the microcracks present in the specimen can still be observed in the EIT conductivity maps even though they have closed. This is likely due to their inexact closure, and the occurrence of some crushing at the crack surface. After achieving a peak compressive strain of 1%, the specimen is loaded in tension until failure, which occurs at 2.8% strain (point L). When loaded in tension, the micro-cracking field in the center of the specimen continues to grow until a large millimeter wide crack (~1.9 mm) is introduced on the right-side of the specimen at 2.8% tensile strain. At each loading point, the conductivity inhomogeneity in each EIT map reflects the region and degree of microcracking. Furthermore, the location and geometry of localized cracks are evident in the EIT conductivity map. The EIT conductivity map compares well with a photo of the failed specimen (Figure 5-11c).

Similar to the monotonic test, Figure 5-12 summarizes the observation of using EIT conductivity maps for monitoring the width of cracks developed in Specimen CT1. As shown, an exponential linearity exists when ECC M-45 is within the strain hardening stage. The conductivity drop in regions of cracking are less than 150 nS-cm^{-1} when the maximum crack width is less than 100 μm. Once the crack width begins to grow to a

millimeter or more (localization), the conductivity drop in the area of crack is as high as 480 nS-cm^{-1}.

At each point of cyclic loading, the percent change in conductivity is also averaged over the entire specimen. This percent change in conductivity is superimposed over the chronological plot of applied strain, as shown in Figure 5-13. The percent change in conductivity varies in linear proportion with strain when loaded in tension. If the gage factor of the specimen is calculated at the points of peak tension (points B, G, L), the gage factor is found to be 8.5, 13.1 and 15.4, respectively. The increase in gage factor is due to the accumulation of micro-cracking in the specimen. When the specimen is unloaded between successive tension-compression peaks, the accumulation of micro-cracking prevents the specimen from fully recovering its initial conductivity. As can be seen, in Figure 5-13, the residual change in conductivity at points C, E, H and J is 0.7, 1.0, 3.1 and 3.7%, respectively. When the element is placed in compression, the specimen conductivity still reduces, but at a much smaller rate in compression than when in tension. The effective gage factor for the element in tension is calculated at points D and I as -3.0 and -5.2, respectively.

5.3.4 Beam Specimen

In the last set of experiments, the ECC beam specimen is loaded in three point bending while EIT conductivity maps of the lower face of the beam are taken at four points along the monotonically applied force-displacement curve (denoted as points A, B, C and D in Figure 5-14a). The absolute EIT conductivity maps are presented in Figure 5-14c. The formation of cracking initiates at point B with a field of micro-cracking observable in the center of the EIT conductivity map. The field of micro-cracking appears to resemble a "V" shape with one side of the beam experiencing more micro-cracking than the other. Microcracking is anticipating at this part of the beam since the center of the EIT is the location of maximum tensile stress during three-point loading. As the load is applied further, the beam begins to soften at a deflection of 0.4 cm; softening is due to the localization of damage in the form of a macro-crack. At point C, the EIT conductivity map reveals the opening of the crack developing at the center of the beam; the crack

width is measured using a crack gage to be approximately 3 mm wide. The crack is further widened by displacing the beam to 0.9 cm (point D). At this point, the change in absolute conductivity is significantly greater (a reduction of 1600 nS-cm^{-1}). With the load still applied, the crack opening is approximately 5 mm. Pictures of the final cracked specimen are presented in Figure 5-14b.

5.4 Conclusions and Summary

This chapter introduces electrical impedance tomography (EIT) as a new nondestructive evaluation tool for strain sensing and crack detection of cementitious materials. EIT offers true multi-dimensional sensing that can be automated for unattended long-term operation in actual cement-based structures. In this chapter, EIT sensing is validated upon ECC specimens loaded in axial tension, axial compression and bending. EIT conductivity maps reveal the piezoresistive nature of ECC structural elements loaded in tension. The gage factor of ECC, as determined by EIT conductivity mapping, is shown to be between 13 and 15. While the piezoresistivity of cementitious materials have been proposed for self-sensing strain (Chung, 2003), the approach would be challenging to practically apply in actual field structures. As witnessed in this chapter, micro-cracking in the cementitious specimen alters the effective gage factor; gage factors are shown to increase with the accumulation of cracking. Other challenges also exist including the sensitivity of the material's electrical properties with environmental influences like temperature and humidity.

The more likely use of EIT sensing is for damage characterization of cement-based structures. As one of the few truly distributed sensing approaches, EIT has the ability to accurately locate cracks as well as quantify their geometric features. Based on the results presented in this chapter, the following conclusions can be made:

- As this chapter has shown, the geometric propagation of dense fields of microcracks, strain hardening, and crack localization in ECC elements were all

captured by the EIT conductivity maps. Unlike the probing methods mentioned in Chapter 3, this observation is spatial and distributed.

- The development of microcracking in the strain hardening stage is found to contribute to moderate conductivity reduction, while the localized cracks result in fairly larger conductivity drops. This indicates that by observing the conductivity maps, one can distinguish the location and severity of cracks.
- The results also suggest that one can estimate the crack width by simply observing the conductivity reduction in the EIT maps. Based on the data presented in this chapter, there exists an exponential linearity between the crack width and the conductivity reduction at the cracking area.
- When the FRCC materials are undergoing tension and compression reversals, the crack opening and closing are well reflected by the EIT conductivity maps. The effects of inexact closure of the cracks in compression are captured by the conductivity maps. This indicates that EIT can also capture the damage residuals of cementitious materials under tension and compression reversals.
- The purpose of using EIT spatial mapping is to provide detailed information on cracks (location and severity) as a supplemental tool for developing more complete damage detection algorithms (*e.g.* fusion with damage index methods) of HPFRCC structural elements.

This work largely restricted its application to two-dimensional surfaces of the ECC specimens. However, the EIT formulation is general and can be applied to three-dimensions. For example, electrodes mounted to the outer surface of structural elements would be capable of imaging the element's internal structure. This could be powerful for identifying cracks below the surface that are impossible to detect during visual inspection.

While this work lays a firm foundation for EIT sensing in civil structures, additional work is need to further develop this novel sensing technique. This chapter only considered the use of ECC materials for EIT sensing; other FRCC materials should be explored. The inclusion of conductive fibers in a cement matrix opens new and exciting avenues of exploration since fiber interfaces and volume fractions can be varied to adjust

the nominal conductivity and piezoresistive gage factor of the material. An additional advantage of conductive fibers is that FRCC materials using conductive fibers experience an increase in conductivity when loaded in compression (Chung 2003). This is in contrast to the polymeric fibers employed in this study; polymeric fibers are non-conducting resulting in decreases in conductivity when specimens are loaded in compression. Other challenges envisioned for EIT sensing is the inclusion of steel reinforcement in structural specimens. The presence of reinforcement steel in the structure could alter the EIT map. However, the location of reinforcement is generally known *a priori* and can therefore be included at the outset of the EIT inverse solution. This would preserve the accuracy of the EIT approach when mapping the conductivity of just the cementitious material.

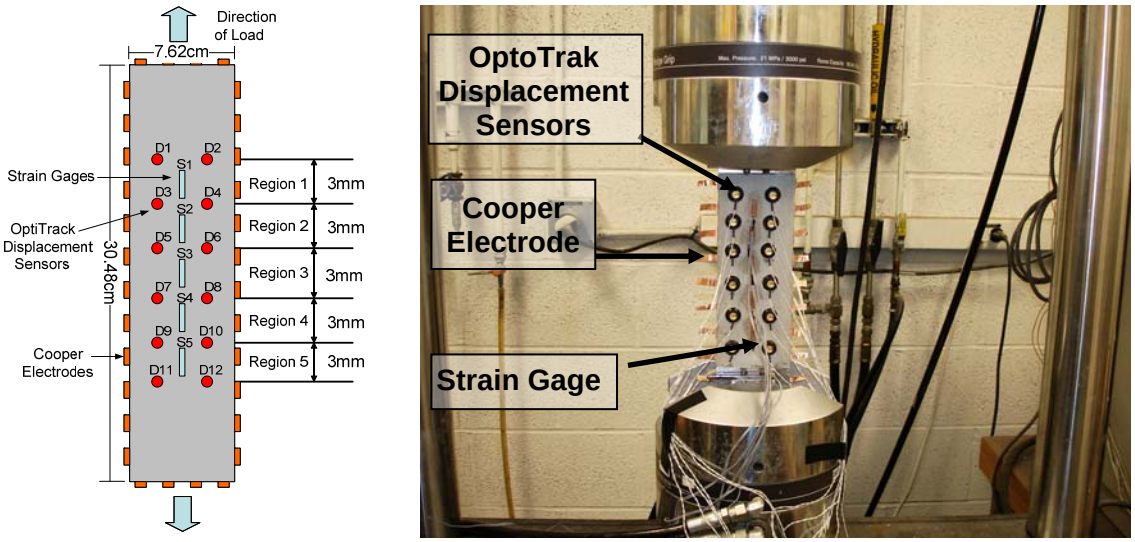

(a) (b)

Figure 5-1: (a) ECC plate specimen for monotonic and cyclic axial loading; (b) ECC plate specimen loaded into the tensile load frame.

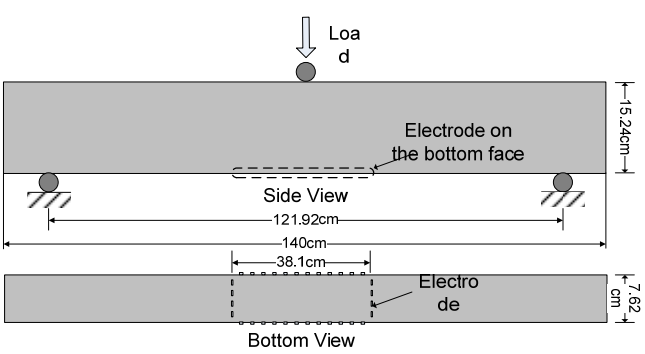

(a) (b)

Figure 5-2: Unreinforced ECC beam: (a) beam dimensions; (b) beam tested in three point bending.

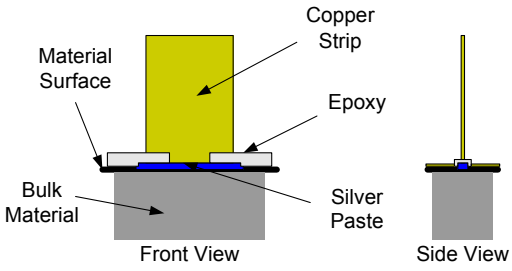

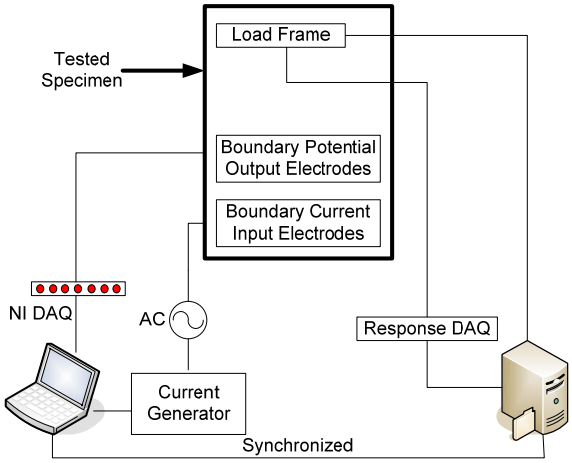

(a) (b)

Figure 5-3: (a) boundary electrode installation; (b) experimental setup.

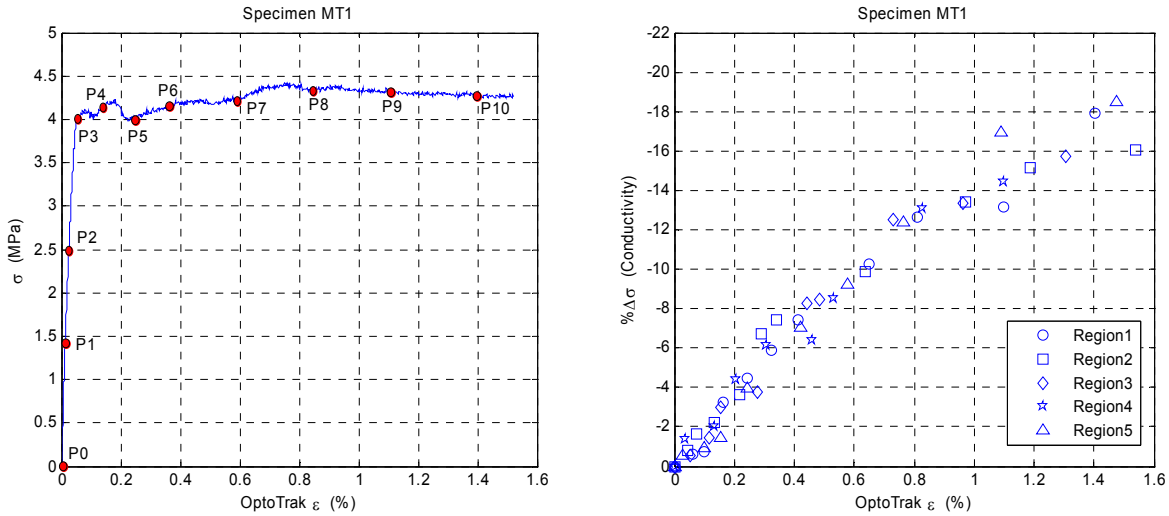

(a) (b)

Figure 5-4: Monotonic tensile loading of specimen MT1 : (a) stress-strain response ; (b) percentage change of conductivity as a function of the average specimen strain.

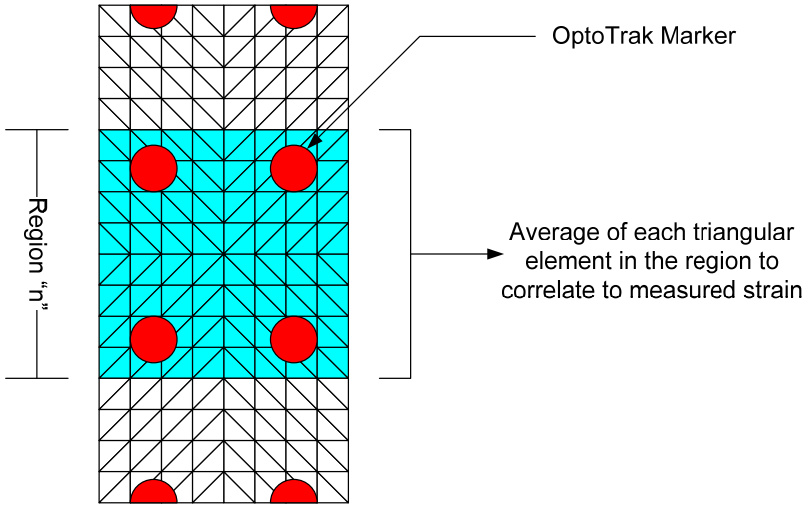

Figure 5-5: Calculation of average conductivity of a region using EIT-derived conductivity maps.

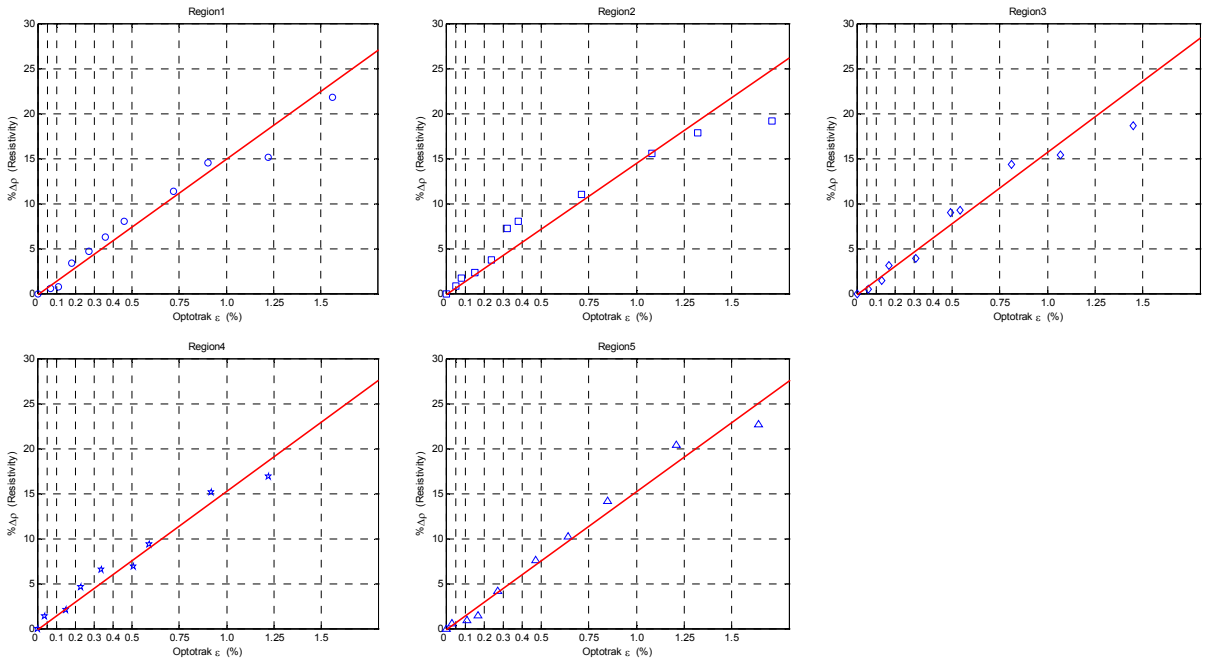

Figure 5-6: Change in average resistivity of region 1 through 5 versus strain as measured by the OptoTrak optical sensors installed in that region.

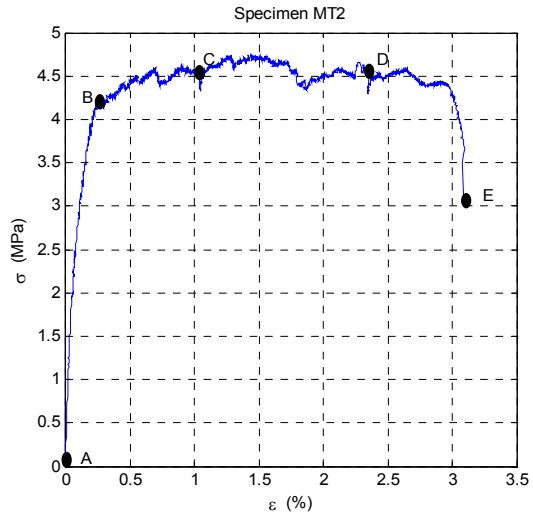

(a)

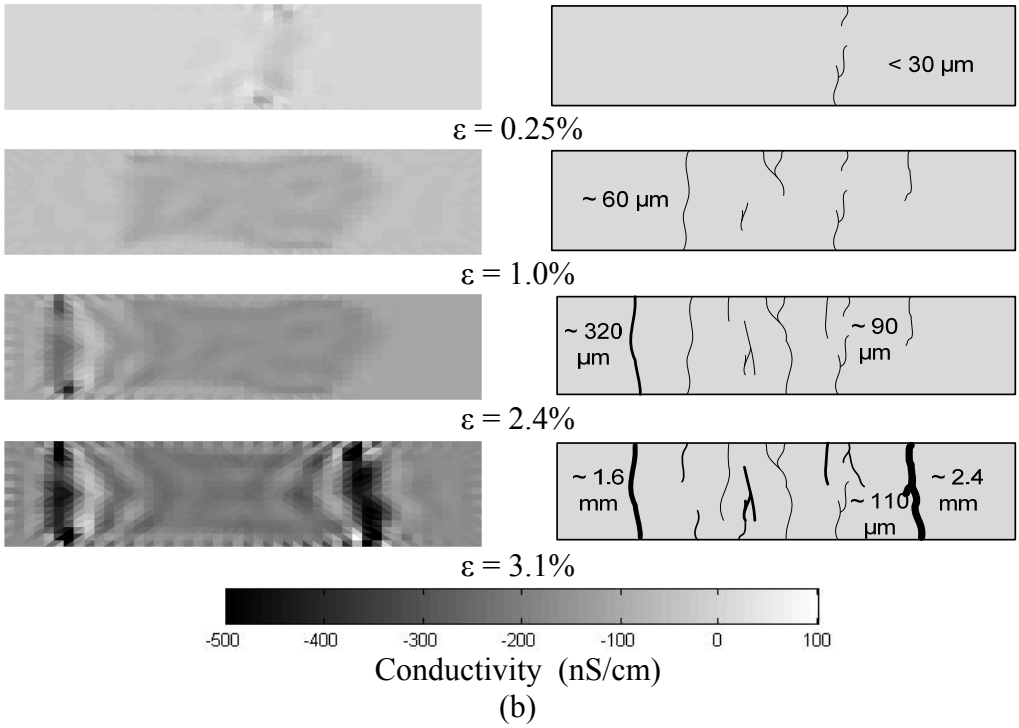

(b)

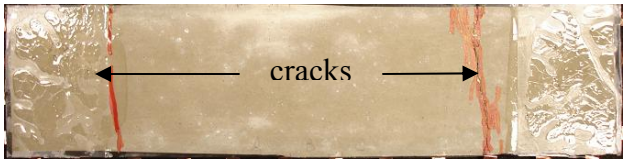

(c)

Figure 5-7: Monotonic tensile loading of specimen MT2: (a) stress-strain response; (b) change in conductivity (left) attributed to strain and cracking (right); (c) final specimen with cracks highlighted using a red felt-tip marker.

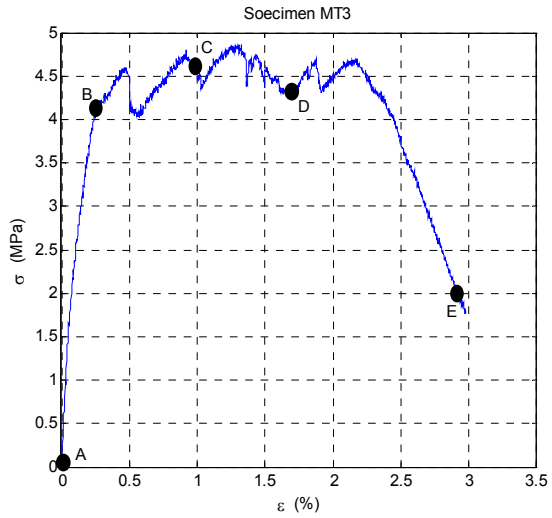

(a)

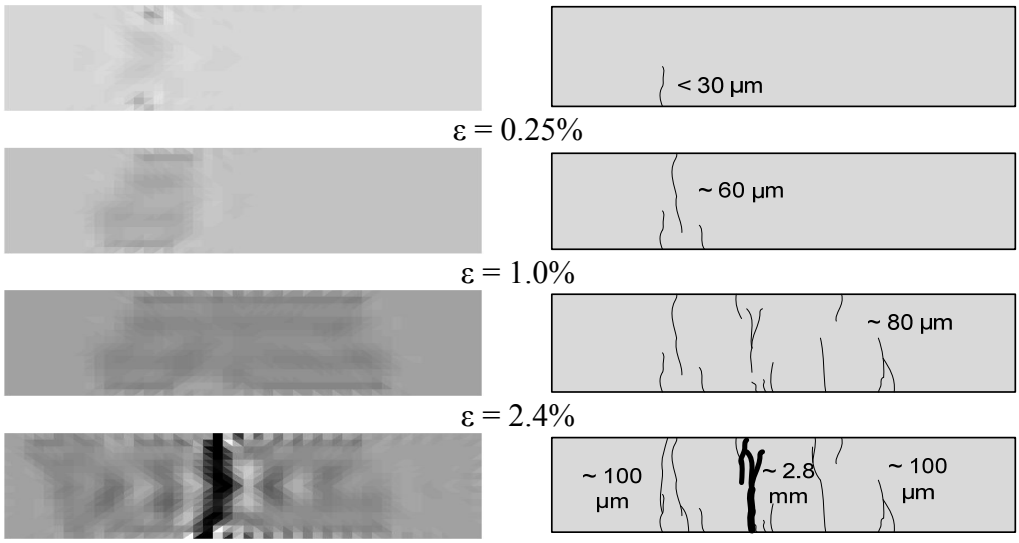

(b)

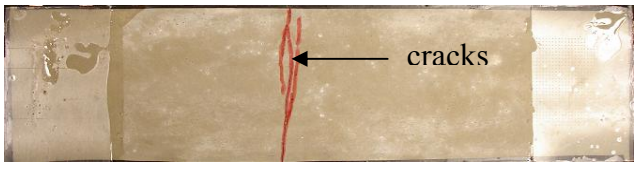

(c)

Figure 5-8: Monotonic tensile loading of specimen MT3: (a) stress-strain response; (b) change in conductivity (left) attributed to strain and cracking (right); (c) final specimen with cracks highlighted using a red felt-tip marker.

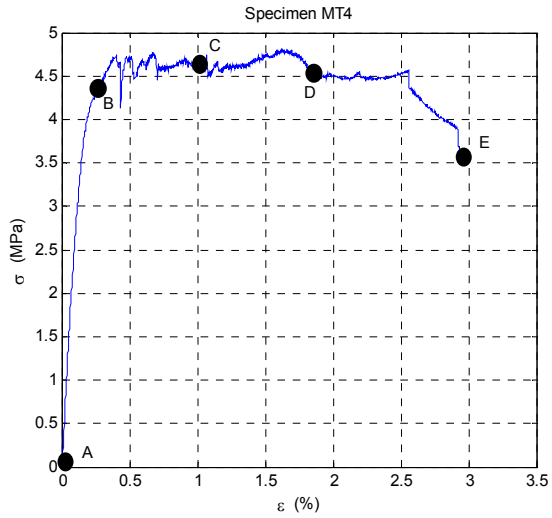

(a)

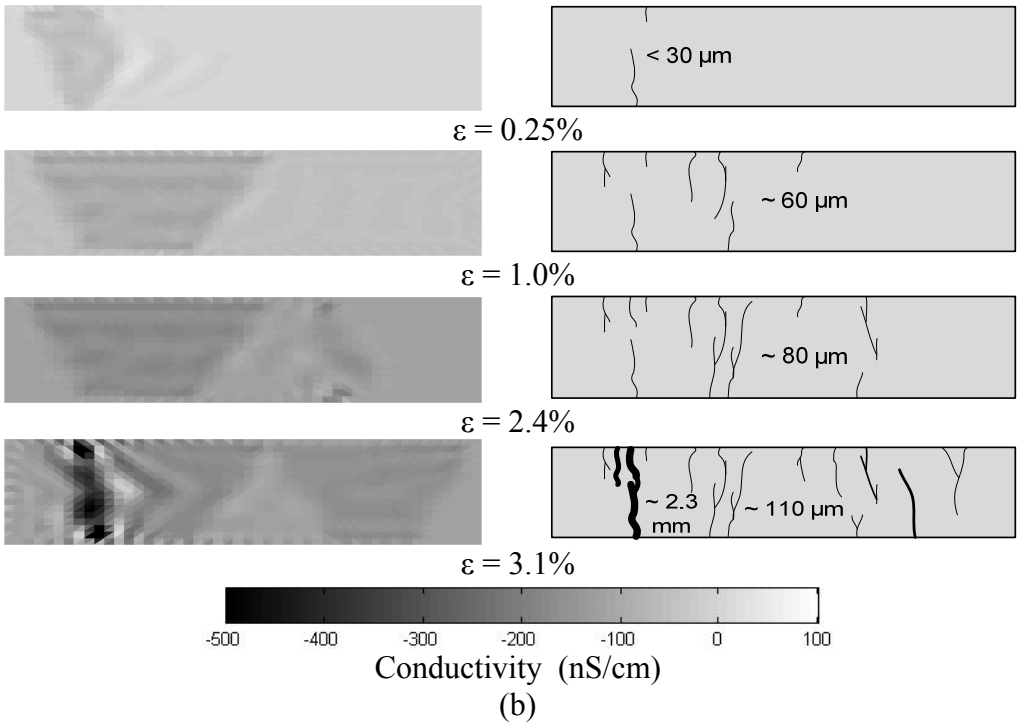

(b)

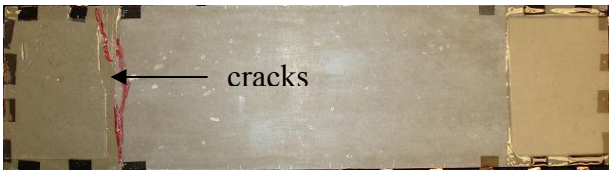

(c)

Figure 5-9: Monotonic tensile loading of specimen MT4: (a) stress-strain response; (b) change in conductivity (left) attributed to strain and cracking (right); (c) final specimen with cracks highlighted using a red felt-tip marker.

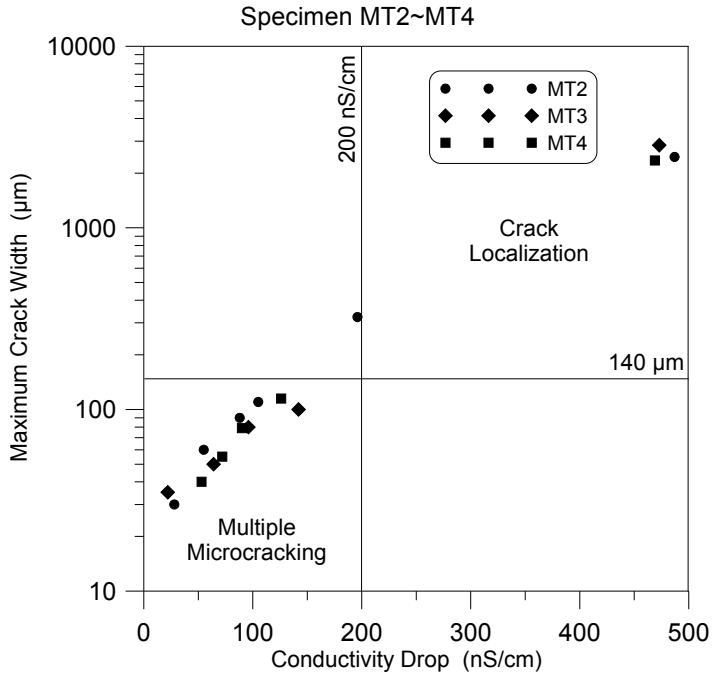

Figure 5-10: Plot of maximum crack width versus associated conductivity change (Specimen MT2 through MT4).

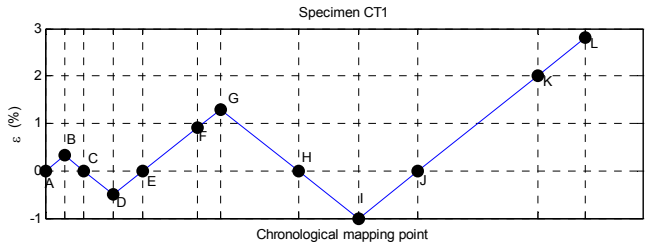

(a)

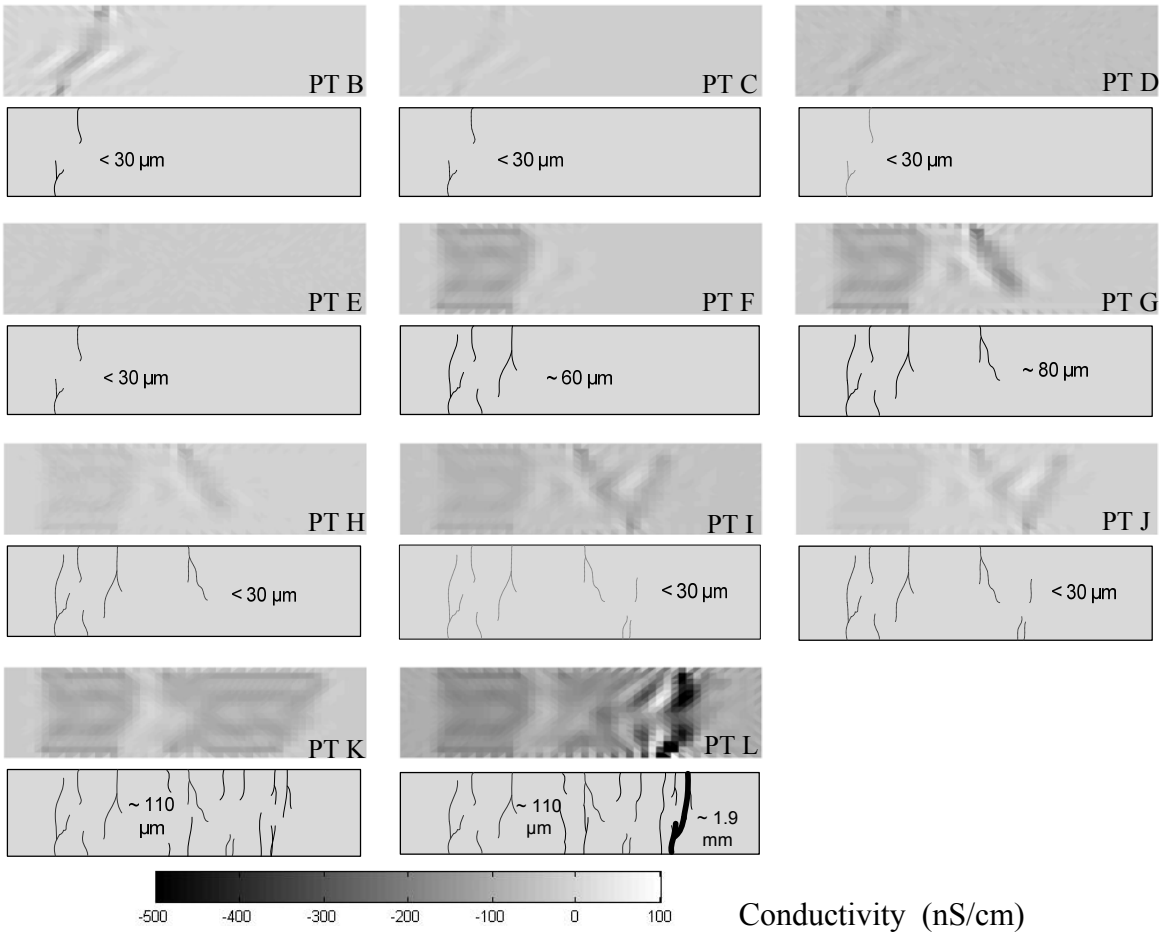

(b)

(c)

Figure 5-11: Cyclic axial loading of specimen CT1: (a) chronological application of tensile and compressive strain; (b) mapping of conductivity changes at points B through L; (c) picture of failed specimen (point L) with close-up views of cracking fields and fibers bridging a macroscale crack.

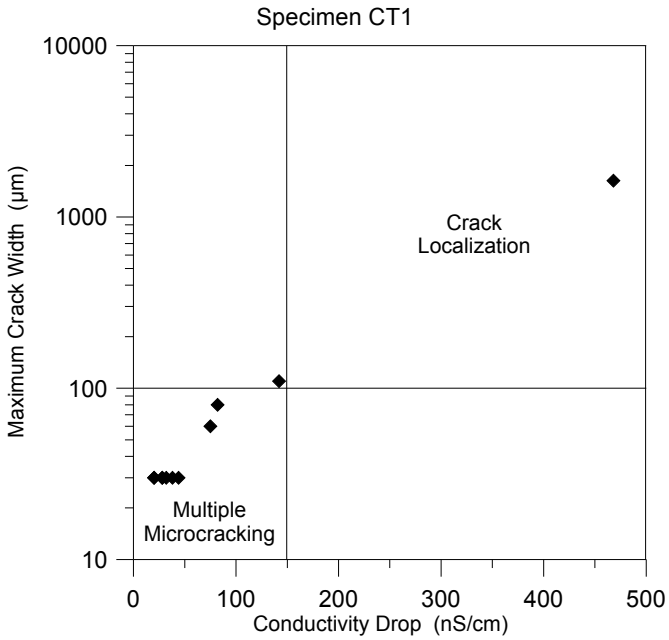

Figure 5-12: Plot of maximum crack width (under tension) versus conductivity change (Specimen CT1).

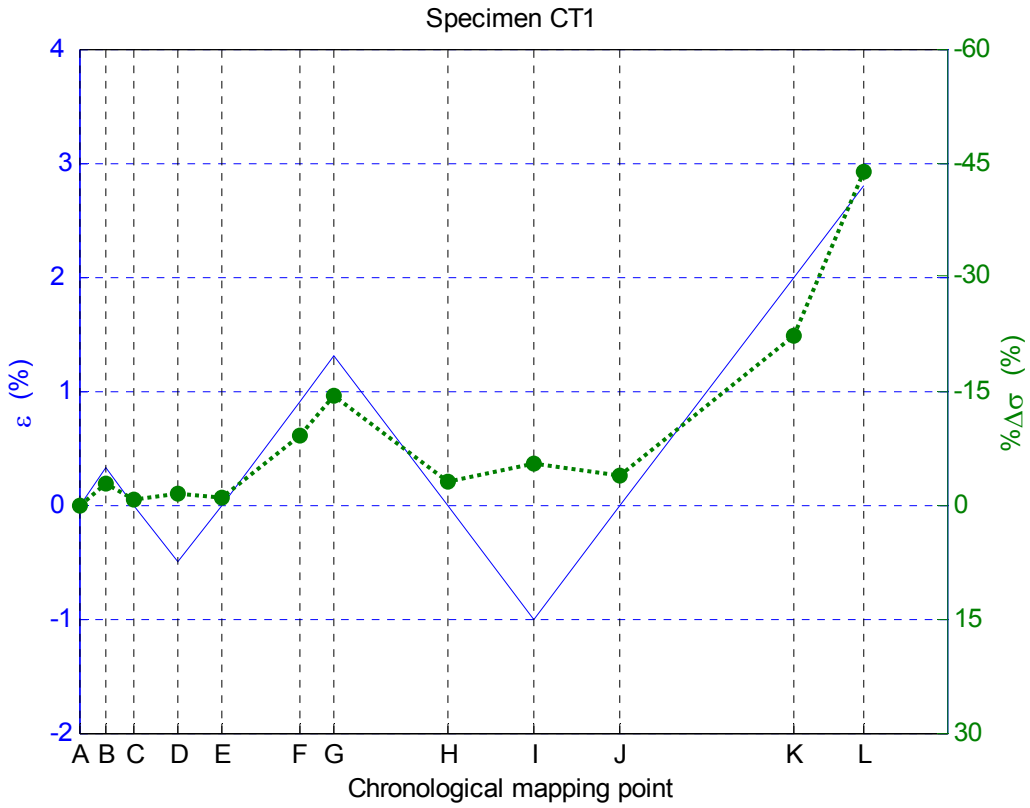

Figure 5-13: Average conductivity change for each load point superimposed with the applied strain pattern.

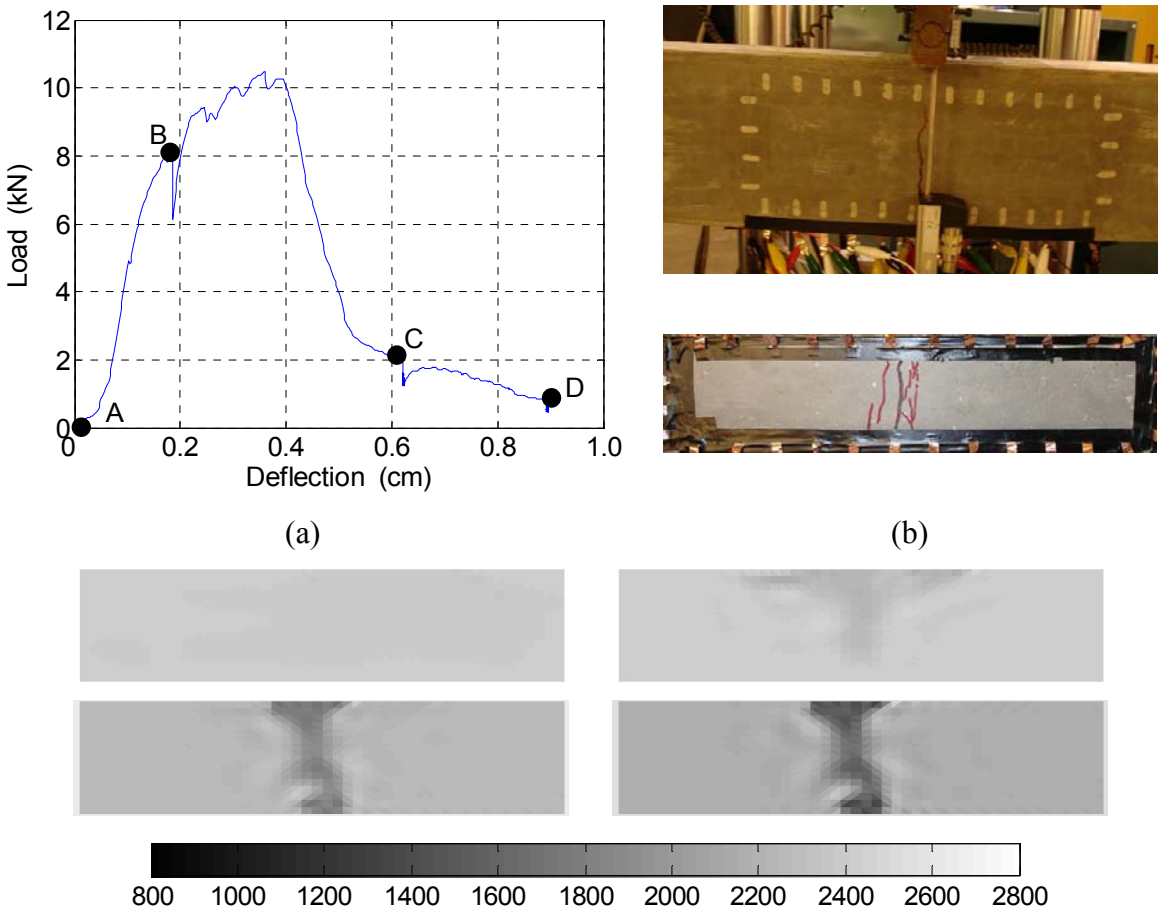

Figure 5-14: Beam specimen 1 under three-point bending: (a) load-deflection curves; (b) side and bottom face damage with cracks highlighted; (c) absolute conductivity maps at points A through D.

Chapter 6

Nano Level Damage Evaluation – Multifunctional Civil Engineering Sensors

6.1 Introduction

In the last chapter, the EIT distributed sensing approach proved powerful for imaging strain fields and crack patterns in fiber reinforced cementitious materials. However, the approach is sufficiently general that it can be applied to any multifunctional material with bulk conductivities in the semi-conductive and conductive ranges. In this chapter, the EIT sensing methodology is applied to a different class of multifunctional materials termed carbon nanotube (CNT) composites. CNT composites are emerging from the field of nanotechnology. The multi-disciplinary nanotechnology field explores the manipulation of matter at the molecular-scale so as to create macro-scale materials with desired mechanical, electrical, and/or chemical attributes.

The application of EIT to map the conductivity of CNT composite materials is novel for two reasons. First, spatial mapping of conductivity offers opportunities to assess the uniformity of the composite. Since CNT are a conductive inclusion in generally non-conductive polymers, the distribution of conductivity would be correlated to the dispersion of CNT within the polymetric matrix. Second, the seminal work of Loh *et al.*, 2007a) lays a scientific foundation for tailoring CNT composites for a variety of sensing application. With CNT composites capable of being used as strain, pH and corrosion

sensors, mapping of the composites conductivity allows the material to be used as a "sensing skin". This CNT-based skin would be an appliqué that can be applied to structural surfaces so as to monitor their performance.

In this chapter, a brief background on CNT composites is presented. The CNT composite used in this study is else described including its fabrication process. Next, films with regions of different conductivity are fabricated so that the EIT approach used to map the CNT composite can be validated. The chapter concludes with illustration of the CNT composite as a sensing skin for stain, cracking and pH measurements.

6.2 Multifunctional Carbon-nanotube Composite Sensors

Much interest has surrounded the development of CNT composites which are commonly composed of singlewalled (SWNT) and multi-walled carbon nanotubes (MWNT) embedded within a polymer matrix. CNT were first discovered in the early 1990's. Some of the impressive properties of SWNT (Figure 6-1) are their diameters (0.7 to 10 nm), high aspect ratio (104 to 105), high stiffness (1.1 TPa), and high tensile strength (60 GPa) (Saito *et al.*, 2004). Electrically, SWNT are either conductive or semi-conductive, depending upon the chirality (*i.e.* molecular orientation) of the nanotube. MWNT are essentially multiple concentrically aligned SWNT; MWNT have similar physical and mechanical properties as SWNT. However, MWNT are electrically conductive and are considered as metallic.

CNT composites take advantage of the impressive mechanical, electrical and physical properties of individual nanotubes to produce materials endowed with similar bulk properties (Skakalova *et al.*, 2005; Thostenson and Chou, 2006; Loh *et al.*, 2007a; Kang *et al.*, 2006; Zhang *et al.*, 2006). The inclusion of carbon nanotubes mechanically reinforce the polymeric matrix similar to way fiber reinforce the cementitious composites (*e.g.*, HPFRCC) previously investigated. Mechanically strong CNT composites that simultaneously exhibit conductivity changes to external stimuli (*i.e.* to pH (Loh *et al.*,

2007a), strain (Kang *et al.*, 2006; Zhang *et al.*, 2006), humidity (Yu *et al.*, 2006) and light (Valentini *et al.*, 2006)) have been reported, thereby allowing the material to also be used in a variety of sensing applications. Both strong and self-sensing, CNT composites are clearly a true multifunctional material.

The development of multifunctional CNT composites for sensing applications hinges on accurate monitoring of the bulk electrical properties of the material before, during and after exposure to external the stimuli including the conductivity changes. Various measurement techniques have been widely used to quantify the resistance of solid state and thin film materials such as CNT composites. Most common are direct current (DC) techniques (as previously described in Chapter 3) where a constant current, I, is injected into a sample while the voltage, V, across the sample is measured (Mayer and Lau, 1990). If the points of current injection and voltage measurement are collocated, the approach is termed the two-point probe method (Figure 3-1a). If the sample volumetric resistance, R, is low, contact impedance of the probes can introduce measurement errors. To minimize the influence of contact impedance, the four-point probe method (Figure 3-1b) separates the points of current and voltage measurements to acquire a more accurate measurement of sample resistance (Smits, 1958). Using knowledge of the specimen geometry (*e.g.*, film thickness), bulk material conductivity, σ, can be calculated using the measured resistance, R. To more precisely analyze the electrical properties of materials whose resistance is dependent on the frequency of an applied alternating current (AC), electrical impedance spectroscopy (EIS) can be used *in lieu* of DC probe methods (Barsoukov and Macdonald, 2005). In EIS, the amplitude and phase relationship between an applied AC signal and the measured voltage is encapsulated within an impedance measurement, $Z(\omega)$, where ω is the cyclic frequency of the injected current. Impedance is a complex valued electrical property of the specimen with the real and imaginary impedance components closely related to the resistance and capacitance of the specimen, respectively.

An inherent limitation of both DC probe and EIS methods is the assumption of relative homogeneity of the specimen's electrical properties between probe points. Should the electrical properties of a specimen be spatially inhomogeneous, both methods average the

spatial variations to provide an equivalent homogeneous resistance or impedance measurement. To offer spatial resolution of specimen resistance, adaptations of the DC probe methods have been offered. Scanning four-point probe methods have been proposed with probe measurements repeatedly made at equally spaced probe locations defined by a grid (Hansen *et al.*, 2003). Such an approach to mapping the material conductivity is similar to the Wenner techniques previously described for cementitious structural elements (see Chapter 4) Repeated 4-point probe measurements can be scaled down into a scanning electron microscope (SEM) environment to offer a spatial resolution of a few microns in thin film materials (Hasegawa *et al.*, 2002). Other established techniques include scanning spreading resistance microscopy which consists of a conductive atomic force microscope (AFM) tip that measures spreading resistance profiles across a specimen cross section as the AFM tip is scanned over the specimen (Xu *et al.*, 2002). While such methods provide a mapping of resistance over multiple dimensions, they require repeated and time-consuming measurements that are conducted at the macro- or micro-scales.

With the emergence of multifunctional thin film composites capable of sensing stimuli such as strain and pH (Loh *et al.*, 2007a), there is a need for analytical methods that can map the thin film resistance over multiple spatial dimensions. In this study, the novel approach to mapping the distribution of body conductivity based upon the electrical impedance tomographic (EIT) methods described in Chapter 4 are proposed for CNT composites. The method differs from scanning probe methods since electrical measurements need only be taken at the boundary of a specimen. EIT is especially powerful in applications where the CNT composite is implemented as a sensing skin, or appliqué, since mapping of film conductivity provides direct spatial depictions of the external stimulus inducing the conductivity changes. In this thesis, two-dimensional mapping of CNT composite thin film by EIT is proposed for various structural health monitoring applications. The method is validated by intentionally manufacturing films with defects consistent with non-uniform conductivity distributions. Furthermore, the use of nanotube-based composite thin films as a sensing skin is illustrated by mapping changes in film conductivity to strain, cracking, and pH exposure all using EIT.

6.3 Fabrication of Carbon Nanotube Composites

The fabrication of homogeneous nanostructured multifunctional thin films is attained via a layer-by-layer (LbL) self-assembly method (Decher and Schlenoff, 2003). Through alternate dipping of a charged substrate (*e.g.*, glass or silicon) in oppositely charged polyelectrolyte and suspended nanomaterial species, a thin film of controlled morphology with no phase segregation can be deposited one monolayer at a time. The alternate nanometer-thick mono-layers of polyelectrolyte and nanomaterials are held by weak interaction forces such as electrostatic and van der Waals forces. Through judicious selection of polyelectrolytic species used during LbL self-assembly, multifunctional nanocomposites have been successfully demonstrated (Loh *et al.*, 2007a).

A challenge associate with using CNT is their tendency to conglomerate and precipitate out of solution. The first step in the LbL self-assembly method is to create a stable, well dispersed solution of SWNT. While many different dispersive agents can be used, poly (sodium styrene-4-sulfonate) (PSS) with a high molecular weight ($M_w \approx 1{,}000{,}000$) is used. Deep tip sonication for 90 minutes is used to achieve adequate dispersion. The PSS molecules absorb to the surface of the SWNT departing an overall negative charge on the SWNT-PSS surface. In this study, 1% weight percent of PSS is used.

In this study, LbL assembly begins by dipping a charged glass substrate treated with piranha solution (3:7 by vol H_2O_2:H_2SO_4) in a cationic polyelectrolyte solution for 5 min. In particular, two alternative polycationic polymers are used; poly(aniline) emeraldine base (PANI) is used for pH sensing composites while poly(viny|alcohol) (PVA) is used for piezoresistive composites. Both PANI and PVA are used in quantities equal to 1.0% weight solution. Upon rinsing with 18 MΩ deionized water for 3 min followed by drying with compressed nitrogen for 10 min, the substrate, along with its adsorbed monolayer, is then immersed in the polyanionic SWNT-PSS solution. The substrate is held in the SWNT-PSS solution for 5 minutes before it is rinsed (3 min) and compressed air dried for 10 minutes. The rinsing and drying stages are necessary to free the substrate of any loose material not adequately absorbed to the film surface. The aforementioned

procedure yields one bilayer of the thin film and is denoted as $(A/B)_n$, where *A* and *B* represent the oppositely charged species and *n* represents the number of bilayers. Realization of electrically conductive and mechanically strong sensing skins for EIT spatial conductivity mapping is accomplished by fabricating $(SWNT\text{-}PSS/PANI)_{50}$, $(SWNT\text{-}PSS/PANI)_{100}$ and $(SWNT\text{-}PSS/PVA)_{50}$ thin films (Table 6-1). To verify the uniform morphology of the carbon nanotube composite, scanning electron microscopy (SEM) is employed to look at the thin film at micro- and nano- length scale. From the SEM image of Figure 6-2, it can be seen that only individual and small bundles of SWNTs are deposited in the polymer matrix composite during LbL self-assembly. Furthermore, the composite is defined by a fairly uniform morphology.

In order to ensure accurate EIT calculations of thin film conductivity, the precise thickness of each thin film specimen is measured using a J A Woollam spectroscopic ellipsometer. The entire set-up of the spectroscopic ellipsometer consists of a Base-160 sample holder with a QTH-200 light source connected to an EC-270 electronic control module and data acquisition system (DAQ). Since ellipsometry thickness measurements require thin films deposited on a reflective surface, LbL SWNT composites are fabricated onto a silicon substrate (with a 38 nm thick oxide layer). By taking 16 total ellipsometry thickness measurements at 16 unique locations throughout the thin film surface, the average film thickness and thickness variance are determined.

6.4 Boundary Electrical Measurement

Spatial conductivity mapping of CNT composite thin films by EIT is achieved by measuring current–voltage relationships across a thin film's boundary. In this study, electrical potential measurement of thin films is performed using electrical contacts made by drying colloidal silver paste (~1 mm wide) equidistantly spaced (~2 mm) between strip copper header pins and the film surface. For instance, SWNT multilayer thin film specimens roughly 25 × 25 mm^2 in area are instrumented with eight electrodes along each of the four sides of the film boundary (totaling 32 electrodes). In this study, electrode

placement is precise because of the use of header pins manufactured with a pin-to-pin spacing of 2 mm. However, should other electrode placement methods be used that lead to inaccurate placement, the electrode positions would be inconsistent with those specified in the EIT forward problem and minor distortions of the final conductivity map could occur. Upon drying (after 6 h), the aforementioned silver electrodes are connected to a National Instruments (NI) data acquisition system (DAQ). Minimization of experimental error is prevented by housing specimens in a customized wood platform to prevent undesirable detachments between electrodes and copper wires. Figure 6-4a gives a schematic view of electrode placement while Figure 6-4b shows a thin film specimen resting on the wood platform with 32 electrodes installed along its boundaries.

While many methods have been proposed to measure the actual boundary potential of a solid body (Holder, 2005), the adjacent electrode measurement technique is employed similar to that used when electrically stimulating HPFRCC elements in Chapter 6. By injecting a regulated alternating current using a current source (Keithley 6221) at a pair of adjacent electrodes, the NI DAQ with a rack-mounted multiplexed terminal block (NI BNC-2090) is employed to simultaneously measure the potential between the remaining pairs of electrodes. Upon determining the electrode boundary potentials, the current source and its corresponding current sink are shifted to the next adjacent electrode pair. The aforementioned process is cycled until all electrode pairs have been subjected to AC excitation. If the boundary has L electrodes, then the total number of independent boundary potential measurements made in the adjacent electrode technique is $L(L-1)/2$. Higher resolution (*i.e.* finer mesh) of conductivity mapping can be reached by increasing the number of electrodes, L, to obtain a larger set of independent boundary measurements.

6.5 Experimental Verification of EIT Imaging of CNT Composites

In this study, electrical impedance tomography is used to imaging the CNT composites fabrication. To the author's knowledge, this is the first time EIT has been applied to a nanoscale multifunctional material for distributed sensing purpose (Hou *et al.*, 2007b).

The experimental testing prescribed for this thesis can be broken down into three parts. First, the EIT conductivity mapping technique is validated by taking repeated two-point probe conductivity measurements over the entire thin film. Second, inhomogeneous thin films with regions of different conductivity are intentionally manufactured and imaged. Third, thin films with intentional "tears" (*i.e.* absence of material) are fabricated and imaged.

6.5.1 Comparison of EIT Conductivity to 2-Point Probe Conductivities

As presented in section 2, the EIT method can reconstruct an absolute measure of thin film conductivity simply through boundary potential measurements. While it has been demonstrated that relative conductivity changes can be accurately identified via EIT (section 4.1), no experimental data suggest the calculated conductivity map corresponds to the true conductivity of the thin film. Here, a validation case study is presented to directly compare EIT conductivity estimates to experimental data obtained using traditional DC two-point probing (Smits, 1958).

Similar to section 4.1, the validation of absolute thin film spatial conductivity is conducted using 25 × 25 mm^2 $(SWNT\text{-}PSS/PVA)_{50}$ thin films fabricated on a silicon substrate (Figure 7-5a). The pristine film is subjected to EIT to obtain its corresponding spatial conductivity map (where a total of 32 electrodes are used as described in section 3.4). Upon boundary potential measurements and EIT reconstruction, the thin film is physically sliced to form a 4 × 4 element grid with each element electrically isolated from all others (Figure 7-5b). By drying colloidal silver paste between each grid element, individual element resistance (R) is measured via an Agilent 64401A digital multimeter connected in a two-point probe fashion. Once resistance is obtained for a grid element, the multimeter electrodes are removed and applied to the corresponding electrodes of the next element. This is repeated until all 16 mesh resistances have been determined. Since film resistivity, ρ (or equivalently conductivity, σ) is dependent on thin film thickness (h), the thickness of each thin film element is measured using ellipsometry (as detailed in section 3.3). Resistivity, ρ, is calculated by:

$$\sigma = \frac{1}{\sigma} = \frac{R}{l} wh \tag{6.1}$$

where w is the element's width and l is the distance between the two-point probe electrodes.

The EIT reconstructed conductivity map using 32 boundary electrodes is compared to the conductivity measured for each of the mesh elements by two-point probing. To make a direct comparison, the triangular elements of the EIT conductivity map that fall within the domain of each grid element are averaged. As presented in Figure 6-5c, the average conductivity measured by EIT reconstruction is within 2.1% error of those measured by using two-point probe methods for each grid element. These results suggest the conductivity maps offered by EIT reconstruction are accurate as compared with more traditional conductivity measurement methods.

6.5.2 EIT Imaging of Thin Films with Inhomogeneous Conductivities

In order to demonstrate that the EIT technique can identify subtle changes in conductivity within the thin film structure, three levels of conductivity are encoded into a fourth specimen by controlling the number of bilayers deposited. From a previous study conducted by Loh *et al.*, 2007b, thin film conductivity increases in tandem with increasing number of bilayers deposited. Thus, fabrication of this fourth specimen with varied conductivity is accomplished by initially fabricating a $(SWNT\text{-}PSS/PVA)_{50}$ thin film. Upon mechanical etching of an 18 × 18 mm2 window in the middle of the film to form a region of zero conductivity, the LbL process continues to fabricate another $(SWNT\text{-}PSS/PVA)_{25}$ thin film structure over the etched 50-bilayer film. Again, mechanical etching is employed to remove a 9 × 18 mm2 window before another 25-bilayer thin film is deposited (Figure 6-6a); the final thin film structure consists of three different magnitudes of conductivity. Generally, darker regions of the back-lighted image (Figure 6-6b) suggest greater carbon nanotube deposition and hence increasing film conductivity. Using only a 32-electrode boundary set-up, EIT successfully identifies

major and minor conductivity variations due to different CNT deposition densities (Figure 6-6c).

6.5.3 EIT Imaging of Thin Films with Tears and Cuts

Validation of EIT conductivity mapping of LbL thin films is conducted by assessing conductivity homogeneity variations among four separate $(SWNT\text{-}PSS/PVA)_{50}$ thin film specimens. Following LbL fabrication, EIT is performed to obtain baseline conductivity maps (σ_{base}) for each thin film specimen. After the baseline conductivity maps are reconstructed, an intentional inhomogeneity is introduced within the film structure by physically etching straight, diagonal and L-shaped cuts into the film surface (Figures 6-7a, 6-7c and 6-7e) to create regions of zero conductivity. After etching, EIT is performed again on each thin film specimen to obtain the etched conductivity maps (σ_{etch}). These maps are then subtracted from σ_{base} to obtain associated pattern conductivity maps, $\sigma_{pattern}$. From Figures 6-7b, 6-7d and 6-7f, it can be observed that EIT can clearly identify the change in conductivity within the thin film structure. When compared with the back-lighted photographs of the three aforementioned thin film specimens, the experimental EIT conductivity maps (Figures 6-7b, 6-7d and 6-7f) correspond precisely with the photographs (Figures 6-7a, 6-7c and 6-7e).

6.6 Illustration of SWNT-PE Sensing Skins by EIT

In this section, thin film specimens are illustrated to show the distributed sensing abilities with respect to various types of external stimuli, such as strain, crack, impact and pH, to the CNT composites. Unlike traditional "point-like" sensors used in field, thin film specimens are employed as 2-dimensional sensing skins which are capable of identify different degrees of external stimuli within a single sensor. Sensing functionalities of the CNT composites are divided into four parts. First, thin film specimens are mounted onto cyclically loaded (tension and compression) PVC coupons and the associated EIT conductivity maps are constructed. Similarly, thin film specimens are epoxy fixed onto FRCC rectangular plates. The FRCC plates are then loaded cyclically till the cracks

occur. Unlike previous two parts, the third part test direct uses aluminum plates as the LbL substrates. Impact loading is introduced to the aluminum plates at the area CNT composites is manufactured, and the associated conductivity maps are produced. Last, thin films are modified by mounting five plastic wells to its surface using high-vacuum grease (Dow Corning). Each plastic well serves as a chamber for containment of the pH buffer solutions while boundary potentials are measured for 2D EIT conductivity mapping of the specimen, thereby allowing simultaneous sensing of different pH solutions on a single thin film specimen.

6.6.1 Strain Sensing

Previous studies of SWNT-PE thin film conductivity have revealed the piezoresistive nature of the nanocomposite material. As such, SWNT-PE thin films have been proposed for monitoring strain in structural elements to which the films are attached. A powerful feature of the LbL assembly process is that thin film piezoresistive properties (*e.g.*, gage factors) can be prescribed by varying the fabrication process (*e.g.*, concentration of constituent materials, dipping time, number of layers) (Loh *et al.*, 2007a). In this study, the change in conductivity due to strain over a large SWNT-PE thin film area is observed by EIT reconstruction.

Thin film specimen $(SWNT\text{-}PSS/PVA)_{25}$ is affixed to a ductile PVC rectangular tensile coupon element using CN-E epoxy (Tokyo Sokki Kenkyujo). The instrumented specimen is gripped at its two ends by an MTS-810 load frame and cyclically loaded in axial tension and compression. The PVC coupon is initially loaded in tension to a strain of 0.1%; once the desired strain is attained, the loading is paused while an EIT analysis is conducted. After the EIT analysis is completed, the specimen is again loaded in tension until a strain of 0.2% is attained. The conductivity map of the thin film SWNTPE specimen is determined by EIT at each 0.1% strain increment in a ±0.2% tension-compression cycle. After the 0.2% strain cycle, the specimen is loaded up to 2% strain with EIT conductivity maps determined at 8 intermediate strain levels. To appreciate the change in conductivity as a function of strain, the EIT conductivity maps are superimposed upon the strain-test number plot of Figure 6-8. The piezoresistive nature of

the SWNT-PE thin film is observed in the EIT conductivity plots with the film conductivity increasing in compression and decreasing in tension. Furthermore, the conductivity maps suggest the film is electrically homogenous even at high strain.

If the average conductivity at each load step is calculated and plotted as a function of strain (Figure 6-9), the change in conductivity is bilinear. When axial tensile strain is below 0.8%, the gage factor (defined as the percent change of average conductivity per unit strain) is 4.2. However, when the strain level increases beyond 0.8%, the gage factor rises to 11.3. It is hypothesized that the two distinct gage factors may be attributed to the displacement of carbon nanotubes within the film. When strain levels less than 0.8% are encountered, the distribution of carbon nanotubes is still above the percolation threshold with many carbon nanotube-to-carbon nanotube junctions present. As the material is strained beyond 0.8%, carbon nanotubes undergo large displacements resulting in the loss of many carbon nanotube-to-carbon nanotube junctions; as a result, at 0.8% strain, the carbon nanotube distribution drops below the percolation threshold resulting in a distinct change in the gage factor.

6.6.2 Crack Sensing

In this study, free-standing SWNT-PSS/PVA sensing skins chemically etched (using hydrofluoric acid) from their substrates are used to detect cracking in cementitious structural elements. The SWNT-PSS/PVA sensing skin is fabricated on a 2.5 cm wide glass substrate resulting in a skin roughly 2.5 by 2.5 cm^2 (Figure 6-10). Upon drying, the conformable SWNT-PSS/PVA sensing skin is affixed onto a 11.5 cm long, 3.8 cm wide, and 1.3 cm thick fiber reinforced cementitious composite (FRCC) coupon using CN-E epoxy (Tokyo Sokki Kenkyujo). In addition, eight 1 mm-diameter colloidal silver paste (Ted Pella) electrodes are painted along the skin boundary using a 2 mm spacing; eight electrodes are applied to each side of the square skin resulting in 32 electrodes (Figure 6-11).

Prior to testing, an initial EIT conductivity map of the mounted SWNT-PSS/PVA thin film is first obtained. Demonstration of the effectiveness of the 2-D SWNT-PSS/PVA

sensing skin is accomplished by applying a one-cycle tensile-compressive load pattern (with 5 mm m^{-1} peak strain) to the FRCC element. Following the one-cycle load pattern, monotonic tensile loading (to 20 mm m^{-1}) is applied to induce large cracks and to ultimately fail the specimen. A load frame is employed to execute the aforementioned load pattern while holding its displacement and load at 2.5 mm m^{-1} strain increments to allow for the application of electrical signals in the skin and EIT spatial conductivity mapping. To observe the formation of cracks in the underlying cementitious element, EIT-derived conductivity maps are subtracted from the initial unloaded map to provide a measure of relative conductivity changes attributed to strain and damage. It should be noted that unlike concrete which localizes damage to large cracks, FRCC structures exhibit strain-hardening behavior with the formation of micro-cracks during hardening (Li, 2003b).

The results corresponding to the tensile-compressive cyclic load test of an FRCC coupon are shown in Figure 6-12. Initially, during the first tensile loading cycle to 5 mm m^{-1} strain (Figure 6-12a); a crack develops at the bottom of the sensing skin (Figure 6-12g). The EIT results of Figure 6-12d accurately capture the location and size of this first crack. Based on previous studies, SWNT-PSS/PVA thin films have been shown to exhibit a decrease in thin film conductivity with increasing strain (Loh *et al.*, 2007a). It can be seen from the bottom of Figure 6-12d that regions of decreasing conductivity are identified, thereby signifying that a crack has occurred below the sensing skin at that location (due to large localized strain in the film). Furthermore, at the boundaries of the crack location, EIT identifies regions of increased conductivity that suggest stress and strain relaxation due to crack opening (Figure 6-12d). It should be noted that, typically, even a strain gauge cannot identify such detailed strain distributions.

Once the specimen is unloaded to its initial displacement (zero strain) (Figure 6-12b), the crack closes to make the surface appear as if no damage has occurred (Figure 6-12h). However, despite crack closure, the surface of the cementitious composite remains damaged. In fact, the EIT spatial conductivity map of the sensing skin shown in Figure 6-12e identifies regions of lower strain (increased skin conductivity) as compared with

when the specimen has been loaded in tension (Figure 6-12d). The results from Figure 6-12e suggest that despite crack closure, localized residual strain due to the previous crack opening still exists. Finally, when the cementitious composite and thin film specimen is loaded to 10 mm m^{-1} (Figure 6-12c), a larger crack develops at the top of the thin film (Figure 6-12i). EIT conductivity mapping of the sensing skin identifies this second crack; as shown in Figure 6-12f, the second crack is larger resulting in a more dramatic conductivity reduction.

6.6.3 Impact Sensing

As opposed to epoxy-mounting free-standing SWNT-PSS/PVA thin films to the surface of aluminum plates for impact damage monitoring, 75 mm long, 25 mm wide, and 3 mm thick aluminum plates are directly used as LbL substrates. Since aluminum is electrically conductive and may interfere with EIT boundary potential measurements, a 100-bilayer PSS/PVA insulating layer is initially deposited; then, the LbL method continues to deposit another 100-bilayer SWNT-PSS/PVA thin film as the sensing skin (Figure 6-13). Similar to crack monitoring in cementitious composites, 32 silver paste electrodes are deposited along the sensing skin boundary and an initial EIT spatial conductivity map is obtained for the skin (Figure 6-14).

After thin films are deposited onto the aluminum plates, simulation of impact damage is conducted by mechanically striking the back of the plate with a tapered aluminum rod. The contact area between the tapered rod and the aluminum plate is approximately 5 mm in diameter. As shown in Figure 6-14, the deformation of the aluminum plate and its deposited thin film resembles that of bending. However, at the center of the thin film, a small bulge due to direct impact of the tapered rod can be visually observed. The EIT algorithm is then executed to capture the spatial conductivity of the SWNT-PSS/PVA thin film after impact. Finally, the undamaged EIT conductivity map is subtracted from the post-impact EIT map to obtain a spatial image of the change in conductivity of the skin due to the impact damage.

As shown in Figure 6-15a, impact damage is created at the center of the rectangular SWNT-PSS/PVA sensing skin (which has been deposited directly on top of the

aluminum plate). Upon reconstruction of EIT conductivity maps for the undamaged and damaged specimens, the change in skin conductivity can be obtained. From Figure 6-15b, it is obvious that EIT conductivity mapping of the sensing skin can accurately identify the impact damage location and size (signified by the darker regions suggesting decreasing conductivity associated with high local strain at the impact point). It can be seen that a circular pattern is associated with the conductivity reduction which is similar to the size of the tapered aluminum rod used to strike the plate (0.5 mm diameter). Furthermore, bending of the aluminum plate can also be identified as shown in Figure 6-15b by a strip of reduced conductivity spanning from one side of the plate to the other through the impacted region.

6.6.4 pH Sensing

In previous work, $(SWNT\text{-}PSS/PANI)_n$ thin films have been shown to drastically increase in film resistance in tandem with increasing pH buffer solutions (pH 1–10) (Loh *et al.*, 2007a). With a pH sensitivity of approximately 20.66 k_ cm−2/pH, these thin films serve as ideal candidates for pH sensing in a wide variety of applications (*e.g.*, corrosion monitoring). The electrochemical response of $(SWNT\text{-}PSS/PANI)_n$ thin films have been characterized with entire films exposed to a single pH environment while two-point probe measurements are conducted (Loh *et al.*, 2007a). In contrast, EIT conductivity mapping offers a direct method of sensing pH variations across the entire thin film.

Demonstration of the potential functionality of $(SWNTPSS/PANI)_n$ thin films for distributed pH sensing is conducted using the experimental set-up described in section 3.5 (Figure 6-16a). Prior to the application of pH buffer solutions in the five wells, the conductivity map of the thin film is reconstructed by EIT. This map will serve as a baseline map to which further conductivity maps will be compared. To illustrate the use of $(SWNT\text{-}PSS/PANI)_n$ thin films for biological applications, a small range of pH buffer solutions ranging from 5 to 9 are pipetted into the five wells. The EIT derived conductivity maps of the thin film exposed to pH buffer solutions are subtracted from the baseline conductivity, thereby revealing changes in conductivity due to pH. First, the surface of the thin film is exposed to pH buffer solutions corresponding to pH values of 7,

7.5, 8, 8.5 and 9; Figure 6-16b reveals the conductivity of the $(SWNT\text{-}PSS/PANI)_{100}$ thin film decreases in linear proportion to pH. Second, the basic solutions are removed and acid buffer solutions with pH values 7, 6.5, 6, 5.5 and 5 are applied to the film surface. Figure 7-16c confirms the thin film undergoes an increase in the film conductivity in tandem with acidic pH. Figure 6-17 summarizes the sensitivity of $(SWNT\text{-}PSS/PANI)_n$ thin film composites to pH stimuli including earlier work conducted by the same group (Hou *et al.*, 2007a). As shown, a linear relation exists in the pH sensitivity of electrochemically active $(SWNT\text{-}PSS/PANI)_n$ thin films.

6.7 Conclusions and Summary

In this chapter, electrical impedance tomography is employed to map the two-dimensional spatial conductivity distribution among layer-by-layer assembled carbon nanotube–polyelectrolyte composite thin films. First, validation of conductivity inhomogeneity is performed on four $(SWNT\text{-}PSS/PVA)_{100}$ thin film specimens. By mechanically etching different patterns within three of the films and fabricating three regions of different conductivity in the fourth, EIT spatial conductivity can accurately identify regions of inhomogeneous conductivity. Furthermore, to ensure that the mapped conductivity corresponds to the true conductivity of the thin film specimen, EIT results are compared with those measured using a DC two-point probe technique. When comparing EIT measured conductivity to measurements taken by two-point probe techniques, strong agreement (within 2%) is encountered.

With the accuracy of the EIT conductivity reconstruction established, the chapter's focus turns to distributed sensing of SWNT composites. Strain, impact and crack sensing are all illustrated using SWNT-PSS/PVA sensing skins. Furthermore, pH sensing using the surface of a single $(SWNT\text{-}PSS/PANI)_n$ thin film specimen is also illustrated using EIT. The conductivity maps of the film exposed to different pH buffer solutions in five locations reveal the outline of the solution wells. Furthermore, the change in conductivity of the film surface immediately below each circular well is shown to be

linearly proportional to pH. The EIT method is clearly a powerful approach for measuring the conductivity of CNT-based sensing skins. The approach is elegant since repeated probe measurements need not be taken to measure thin film conductivity. As a result, multifunctional CNT composite films could be used in a variety of sensing applications where spatial depiction of conductivity changes to stimuli is desired (*e.g.*, corrosion monitoring of metallic surfaces). While multilayered carbon nanotube–polyelectrolyte composite films are used as case studies in this work, it should be noted that the EIT approach to distributed sensing is rather general and can be applied to map the conductivity of other nano engineered thin film materials.

This chapter only lays a foundation for EIT-based sensing of CNT composite skins. Further work is needed to mature the approach for actual deployment in civil engineering structures. For example, while the skin is piezoresistive, the directionality of strain must be correlated to the estimated conductivity changes. In addition, a sensitivity analysis is necessary to determine the relative size between the electrode spacing and spatial details like cracks sought. Finally, the long-term durability of the sensing skins is unknown. Before deployment to harsh field conditions, the mechanical durability of the skin must be extensively investigated.

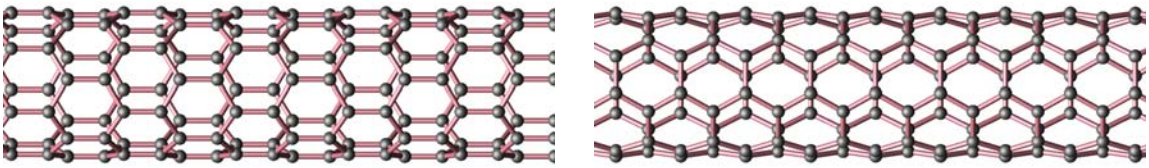

(a) (b)

Figure 6-1: (a) Semi-conducting and (b) metallic single-walled carbon nanotubes (Courtesy of V. H. Crespi, Penn State University).

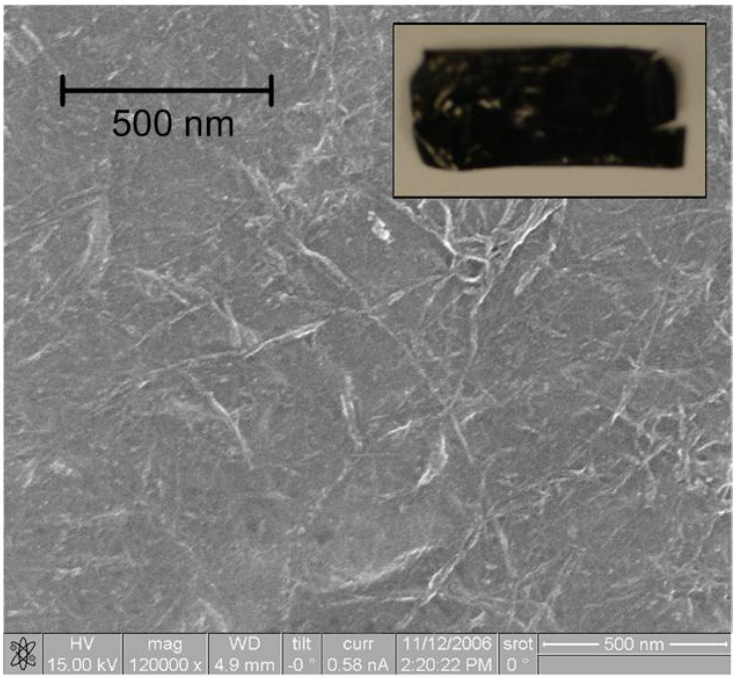

Figure 6-2: An SEM image of a $(SWNT\text{-}PSS/PVA)_{50}$ LbL thin film shows the selective deposition of individual and small bundles of nanotubes within the polymer matrix. Rinsing during layer-by-layer self-assembly removes excessively large agglomerated particles. The inset depicts the corresponding free-standing $(SWNT\text{-}PSS/PVA)_{50}$ thin film upon lift-off from its original glass substrate.

Figure 6-3: J. A. Woollam spectroscopic ellipsometers.

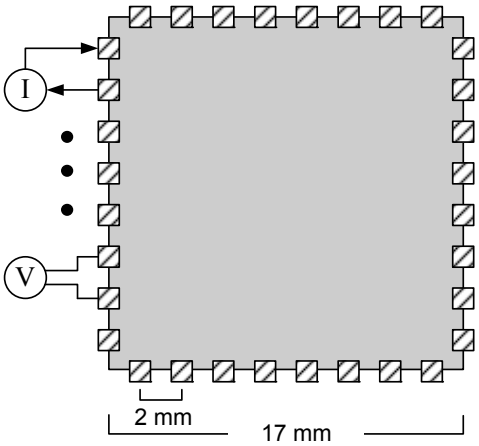

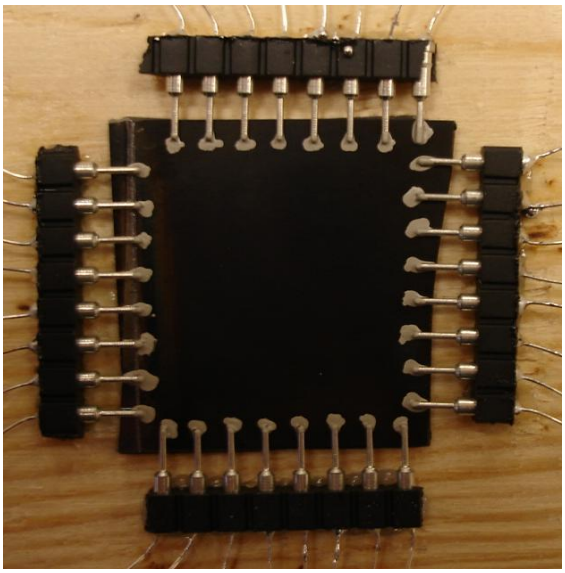

(a) (b)

Figure 6-4: (a) Illustration of boundary electrode placement for conductivity mapping; (b) LbL thin film specimen with boundary electrodes installed. The specimen is mounted to a wood stand to prevent detachment of copper wire from the thin film electrodes.

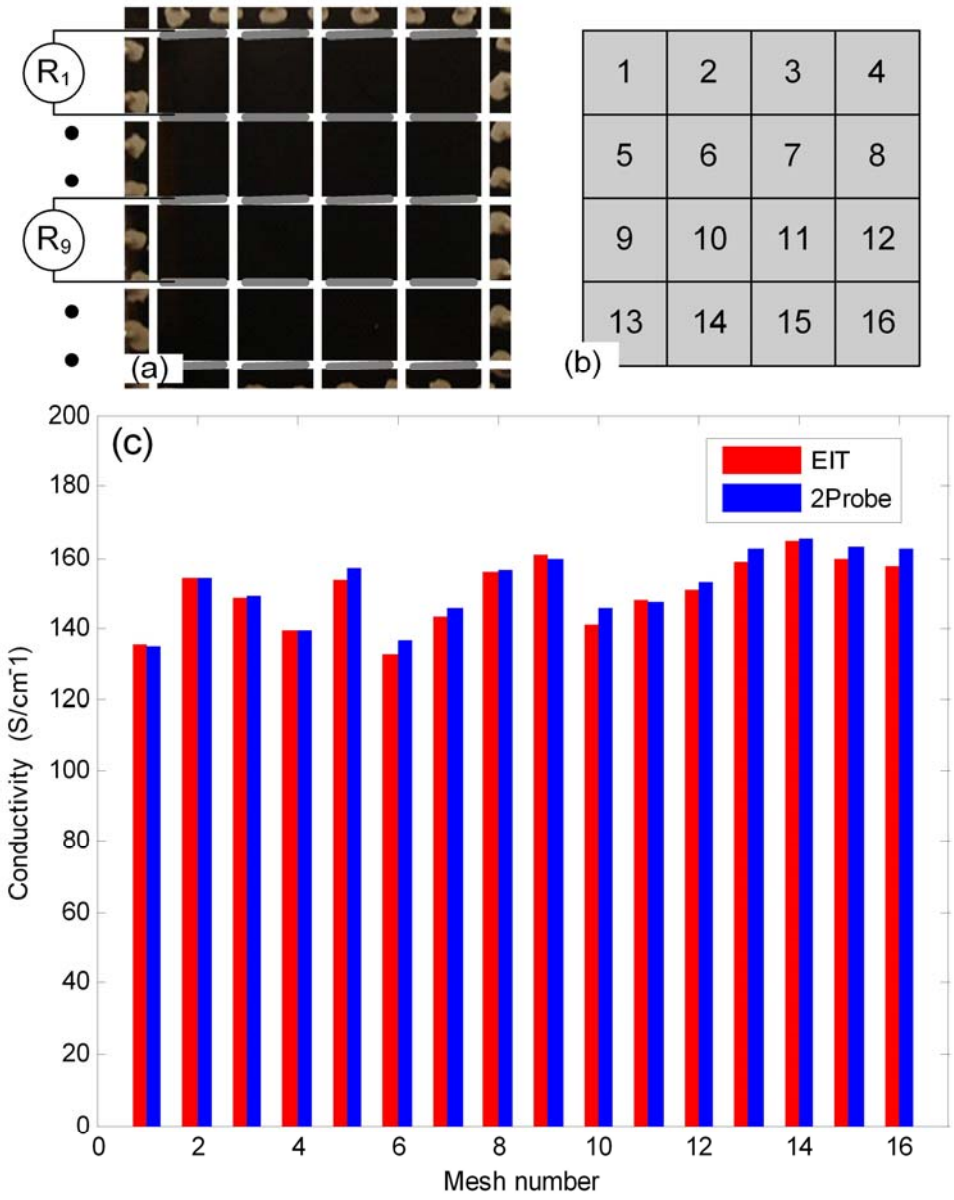

Figure 6-5: Thin film conductivity validation: (a) thin film specimen is equally meshed into 16 individual elements by physical slicing of the thin film; (b) the mesh number of (a); (c) the conductivity comparison of (a) between EIT and the two-probe method (average error is 2.1%).

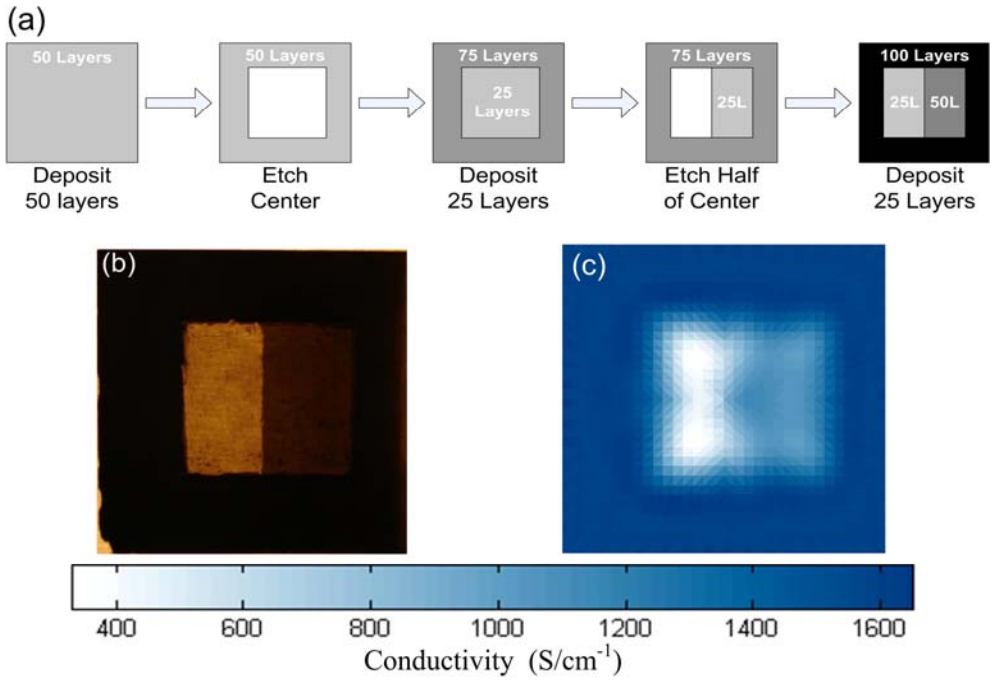

Figure 6-6: (a) Sequential deposition and etching process to structure three regions of different conductivity in a single thin film; (b) back-lighted image of thin film specimen with 3 dipping layers, 25 (left centre), 50 (right centre) and 100 layers (outer field); (c) is the conductivity map of (b).

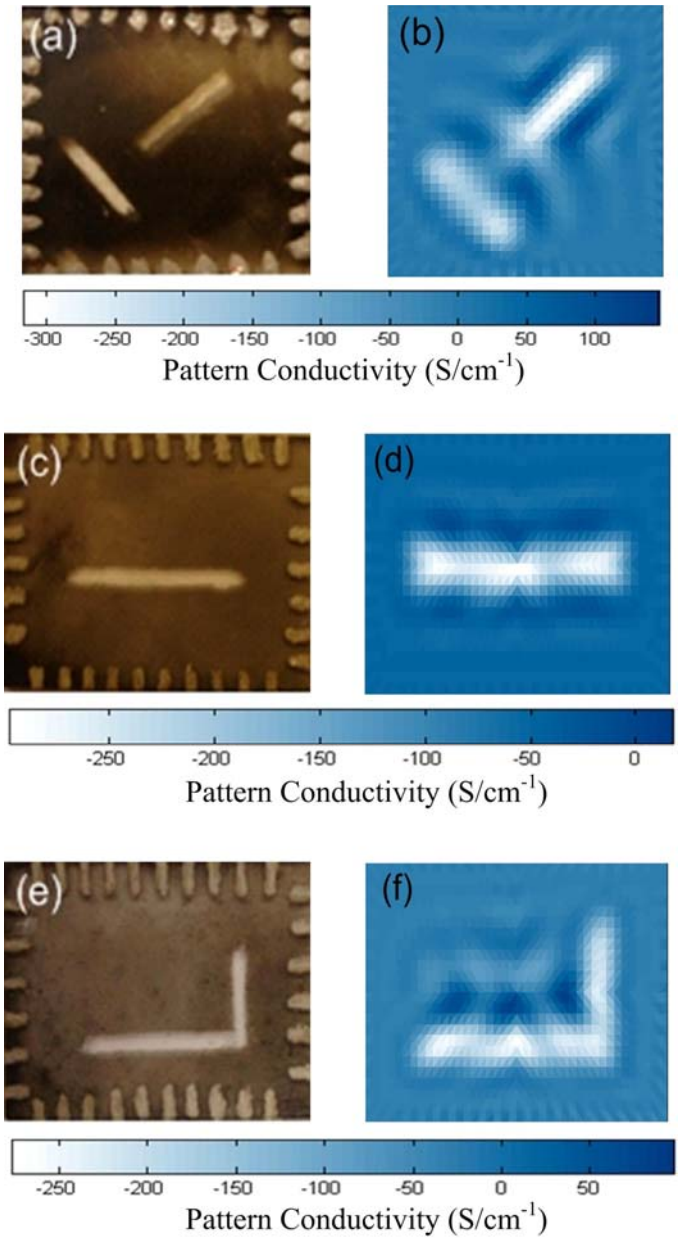

Figure 6-7: Pattern conductivity maps ($\sigma_{pattern}$) of three types of physically etched thin film specimens. (a), (c) and (e) are optical pictures of thin films with double slashes, straight line and L shaped etchings; (b), (d) and (f) are the corresponding pattern conductivity maps of (a), (c) and (e) with the color scale in units of S/cm.

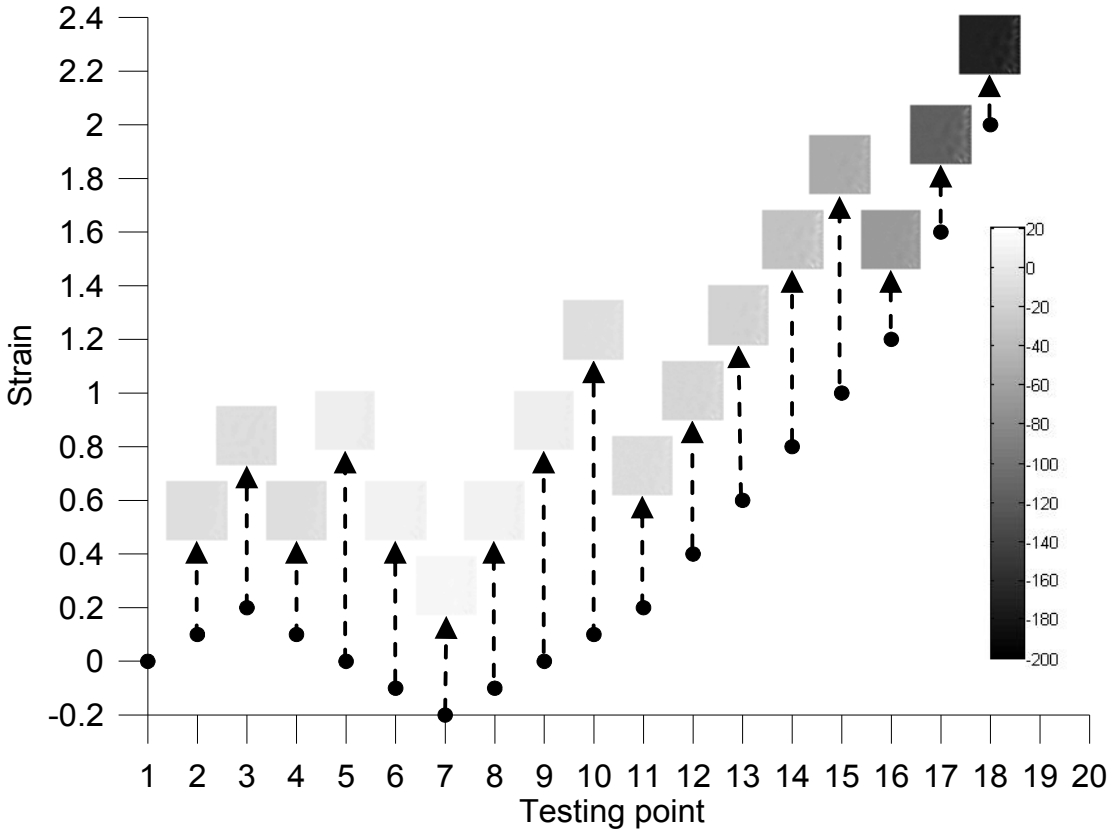

Figure 6-8: EIT conductivity maps as axial strain (compressive and tensile strain) is applied to the $(SWNT\text{-}PSS/PVA)_{25}$ specimen (gray-scale bar shows conductivity in terms of S/cm^{-1}).

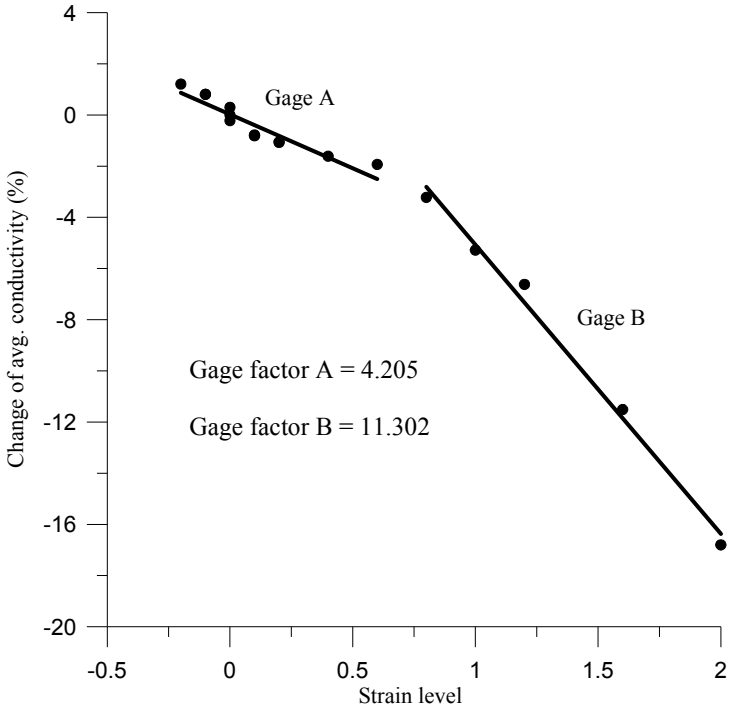

Figure 6-9: Change in thin film conductivity maps as axial strain (compressive and tensile strain) is applied (grayscale bar shows conductivity in terms of S/cm^{-1}).

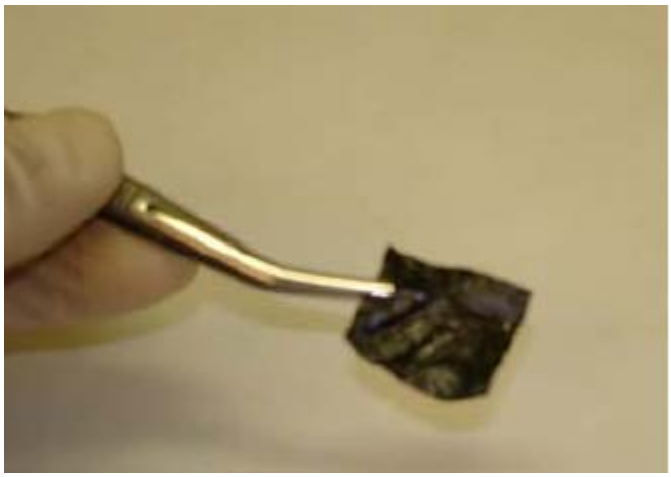

Figure 6-10: An example of a conformable free-standing LbL SWNT-PSS/PVA thin film after being etched from its glass substrate.

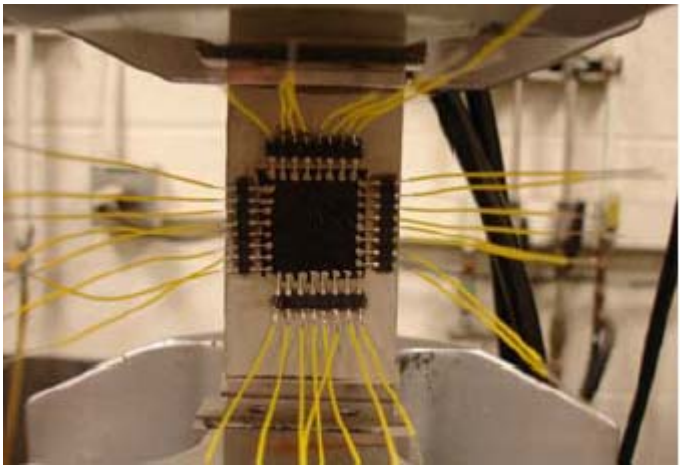

Figure 6-11: A cementitious coupon with a 2-D SWNT-PSS/PVA thin film strain and crack sensor mounted on the MTS-810 load frame.

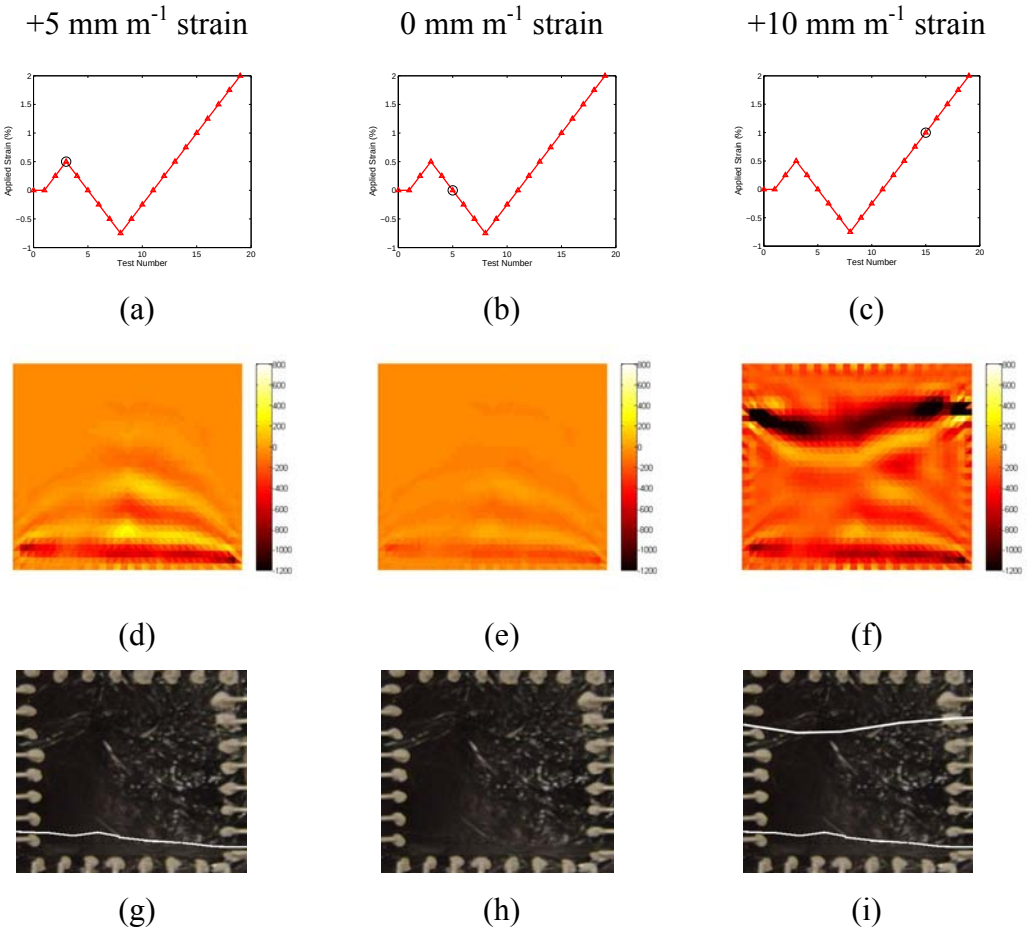

Figure 6-12: Free-standing SWNT-PSS/PVA thin films are epoxy-mounted to cementitious composites for 2-D EIT strain and crack sensing. During the first loading peak at 5 mm m^{-1} (a), EIT (d) and optical images (g) successfully identify the development of the first crack. Upon unloading to 0 mm m^{-1} (b), residual strain can be observed from the EIT conductivity map (e) despite the crack has closed (h). At 10 mm m^{-1} (c), both EIT (f) and optical images (i) identify the development of a larger second crack at the top of the thin film. (Note: EIT conductivity changes are measured in S cm^{-1}).

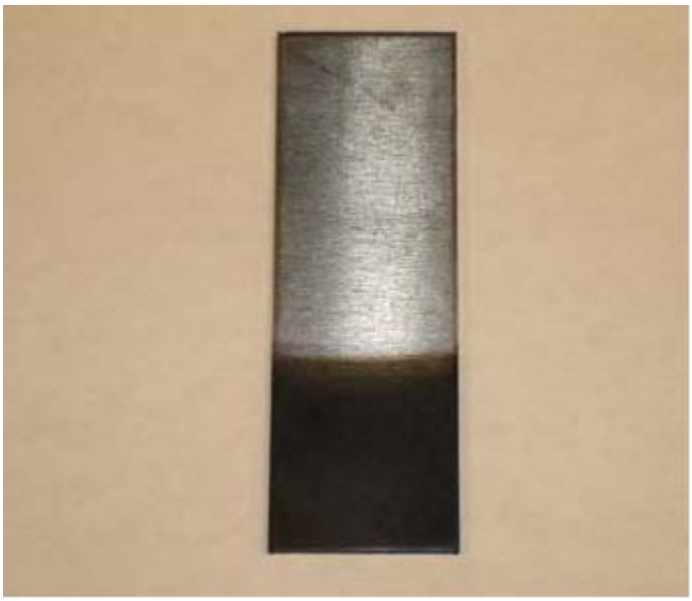

Figure 6-13: A 100-bilayer SWNT-PSS/PVA impact damage sensor assembled onto an aluminum substrate with a 100-bilayer PSS/PVA insulating layer underneath the thin film.

Figure 6-14: The specimen in Figure 6-13 is impacted with a tapered aluminum rod to cause bending and a bulge in the middle of the SWNT-PSS/PVA impact damage sensor.

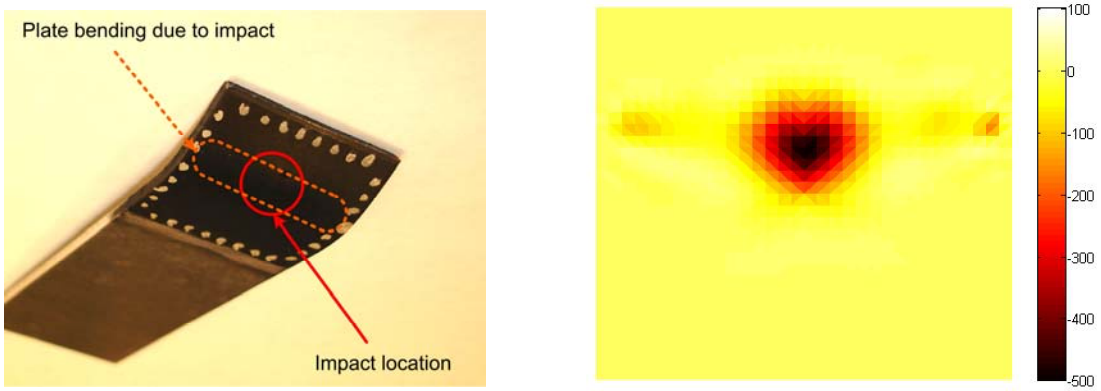

(a) (b)

Figure 6-15: (a) Image of impacted aluminum plate and sensing skin (damage located on upper-center location of thin film). (b) Corresponding EIT relative spatial conductivity mapping of SWNT-PSS/PVA sensing skin. Impact damage is detected at the upper-center location of the plate.

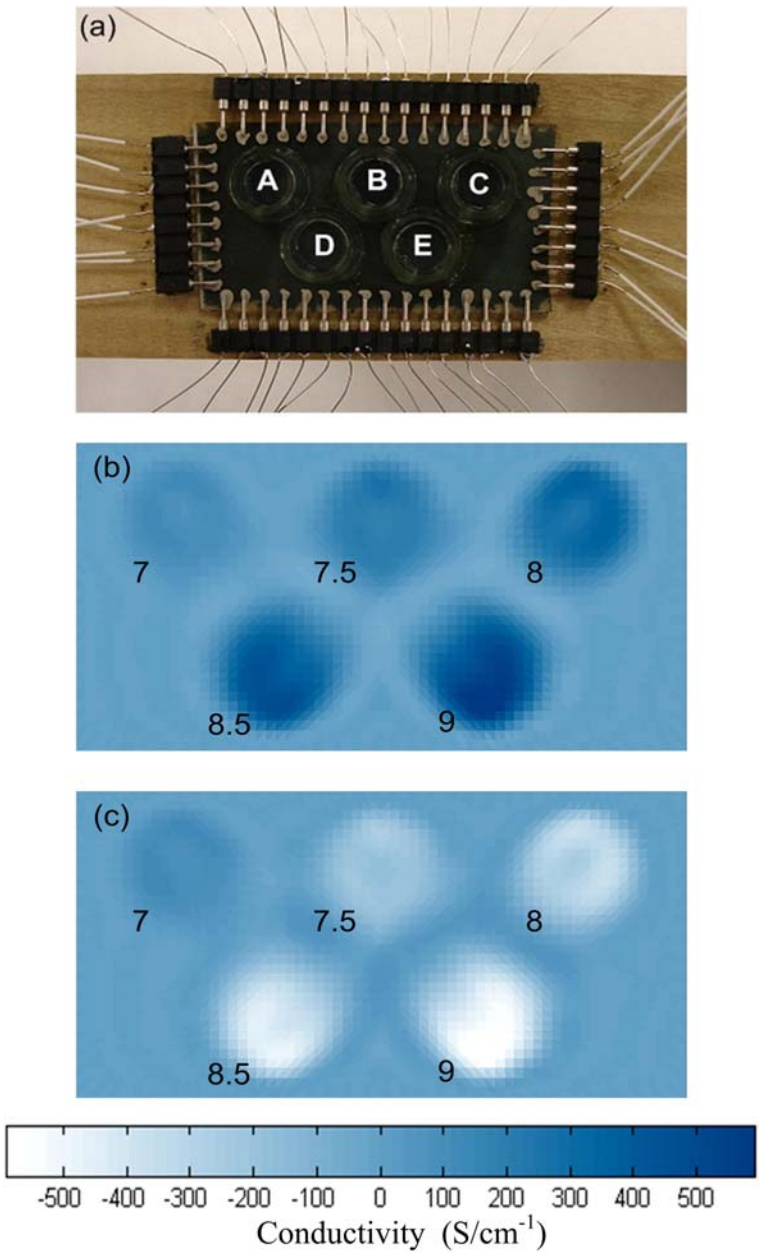

Figure 6-16: (a) $(SWNT\text{-}PSS/PANI)_{100}$ thin film under several magnitudes of pH stimuli; (b) change in spatial conductivity when pH in well A, B, C, D and E is 7, 7.5, 8, 8.5 and 9, respectively; (c) change in spatial conductivity when pH in well A, B, C, D and E is 7, 6.5, 6, 5.5 and 5, respectively.

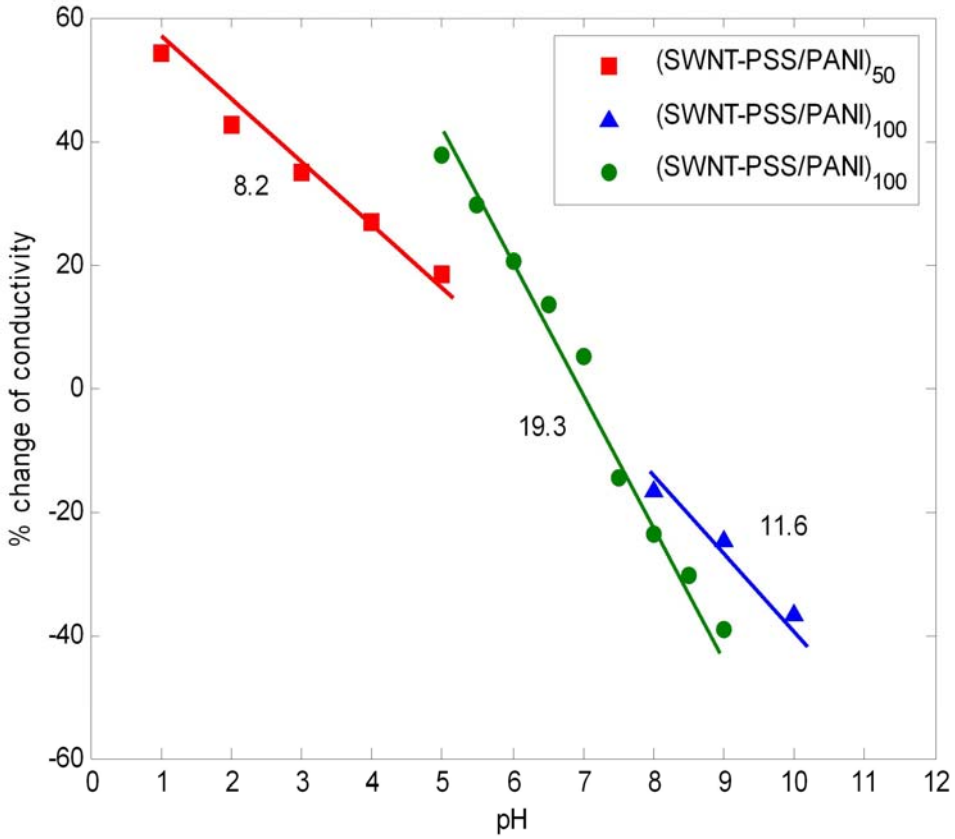

Figure 6-17: Sensitivity of three different (SWNT-PSS/PANI)$_n$ thin films under pH stimuli. All three films exhibit similar linear variations in conductivity as a result of pH buffer solutions applied to the film surface.

Table 6-1: Summary of LbL SWNT-composite thin films and their corresponding LbL constituents fabricated for EIT spatial conductivity mapping

Polycation	**Polyanion**	**Number of bilayers**	**Thin film characteristics**
1.0 *wt.* % PANI in 1.0 *vol.* % DMF	0.8 mg/mL SWNT in 1.0 *wt.* % PSS	50 and 100	Low conductivity and pH-sensitive
1.0 *wt.* % PVA	0.8 mg/mL SWNT in 1.0 *wt.* % PSS	50 and 100	High conductivity

Chapter 7

Concluding Remarks

7.1 Summary and Discussion

As high performance fiber reinforced cementitious composite (HPFRCC) materials begin to transition from the laboratory to the field, there is a need to monitor their behavior when exposed to realistic loads in operational civil structures. To fully capture the mechanical response of HPFRCC materials, identification of the material's response regime (*e.g.*, elastic versus strain hardening) including the evolution of micro- and macro-scale cracking is needed. *In-situ* observation of the material's mechanical response could validate many of the behavioral assumptions made during design of a structure using such materials. The sensors currently available for monitoring HPFRCC materials are point sensors that measure the response of an instrumented structure at a specific point. Strain gages are a classic example since they measure strain only at the location of the gage. Generally, these point measurements do not directly measure damage; rather, they are used in conjunction with physics-based models to hypothesize the occurrence of cracking and structural damage. Since HPFRCC are unique materials with energy dissipated through micro- and macro-scale cracks, improved sensing techniques are necessary to directly observe their cracking behavior. In particular, a means of measuring crack occurrence, location and severity are desired. Towards this end, two entirely new approaches are offered for sensing the response of HPFRCC

materials: wireless sensor networks (Chapter 2) and the use of the inherent electromechanical behavior of the HPFRCC materials (Chapters 3 through 6).

Wireless sensors have shown tremendous promise for monitoring civil structures because they eliminate the need for wiring between sensors; hence, wireless sensors are low cost and easy to install (Lynch and Loh 2006). Due to their cost, wireless sensors can be installed in large numbers resulting in extremely dense instrumentations. Dense instrumentation allows the system to target the measurement of individual components such as joints, beams and columns. Before wireless sensors can be contemplated for monitoring structures employing HPFRCC materials, the reliability and accuracy of the sensors must first be validated. Hence, one objective of Chapter 2 was to validate the performance of a wireless sensor prototype by Wang, *et al.* (2007) to monitor a full-scale highway bridge structure in which HPFRCC materials are employed. The Grove Street Bridge was selected with wireless sensors used to monitor the response of the bridge, and more specifically, that of an engineered cementitious composite (ECC) link slab deck element. The second objective of Chapter 2 was to explore the use of the computational intelligence coupled with each wireless sensor to locally process measurement data. The intended purpose of local data processing was to autonomously identify cracking and damage in HPFRCC structural elements. This objective was satisfied by embedding a damage index model proposed by Canbolat, *et al.* (2004) to determine the degree of damage incurred in an HPRFRCC bridge pier loaded under cyclic lateral loading.

While the thesis findings confirm the promise associated with wireless sensing, it can be concluded that wireless sensors alone are not sufficient to provide detailed information on the mechanical response of HPFRCC materials. While a rough assessment of cracking in HPFRCC structural elements (for example, the HPFRCC bridge pier) can be made through embedded interrogation of component responses, the need for a more accurate and detailed assessment of cracking still exists. A radically new approach to sensing cracks based on the electromechanical properties of HPFRCC materials was proposed in Chapters 3 through 5. In Chapter 3, the resistivity (the inverse of conductivity) of ECC materials was studied to establish a direct correlation between the electrical properties

and the mechanical response of the material. A key objective of the chapter was to establish an accurate experimental method for measurement of resistivity. Electrical impedance tomography (EIT) was then proposed in Chapter 4 for the calculation of the spatial distribution of conductivity using electrical measurements made along the boundary of an ECC specimen. The objective of Chapter 5 was to determine the accuracy of the EIT conductivity mapping technique using ECC test specimens loaded under uniaxial tensile loading.

The universality of the EIT approach to spatial mapping of a material's conductivity is shown in Chapter 6 using another multifunctional material. The multifunctional material considered in this chapter was carbon nanotube composites proposed for structural health monitoring by Loh, *et al.* (2007a). The carbon nanotube thin film composite was used as a sensing skin whose conductivity is linearly related to strain. The sensing skin, when epoxy mounted to the surface of a structure, was shown capable of measuring both cracks in ECC structural elements and impact damage in steel plates.

7.2 Achievement and Contribution

As shown in Figure 7-1, the thesis has made many scientific contributions to the fields of HPFRCC materials and structural health monitoring. First, wireless monitoring systems have been tested in an operational structure. Field testing revealed that wireless sensors are accurate in measuring the static and dynamic response of a bridge. In total, 16 accelerometers were installed to measure deck acceleration while six strain gages and four LVDTs were installed to measure the response of an ECC link slab to static live load. Both the static and dynamic responses were accurately measured with no data loss occurring during wireless transmission. With very few field deployments of wireless sensors reported in the literature (Lynch and Loh 2006), the field study conducted in this thesis will contribute empirical evidence supporting the claim that wireless sensors can serve as reliable substitutes for the tethered sensors traditionally used.

The computational power coupled with wireless sensors represents a significant paradigm shift for the structural monitoring field. The thesis offered two illustrations of embedded computing within a wireless sensor network. First, FFT and peak picking algorithms were coded into each wireless sensor to determine modal properties of the Grove Street Bridge. Using acceleration measurements recorded from routine traffic loading, each wireless sensor transformed the data into the frequency domain where modal frequencies were automatically determined. Furthermore, wireless exchange of the imaginary component of the Fourier spectra at each modal frequency yielded the mode shapes of the bridge. For the Grove Street Bridge, the soft-connection functionality of the ECC link slab was accurately verified by observing a lack of response across the link slab in the calculated mode shapes. The in-network determination of bridge mode shapes presented in this thesis is the field's first illustration of automated modal analysis by a wireless sensor network installed in a civil structure.

Building upon the embedded computing illustrated in the field, the thesis has explored the embedment of damage detection algorithms in the wireless sensors. Specifically, a damage index model that used peak component displacements as input was employed to determine the degree of damage in HPFRCC structural components exposed to cyclic loading. Using an HPFRCC bridge pier constructed in the laboratory, the embedded damage model was shown accurate in quantifying the degree of crack damage that had occurred within the loaded bridge pier. Through extensive instrumentation of the pier using LVDT, separate damage index models were developed corresponding to the flexural and shear response of the structure. The wireless sensor was shown capable of separating the pier response into flexural and shear responses in addition to determining flexural and shear damage indices. The thesis's work establishes the damage index method as a powerful damage estimation tool that a monitoring system can use to identify those structural elements requiring immediate inspection.

The most significant achievement of this thesis is the establishment of the use of the electromechanical properties inherent to HPFRCC materials as a tool for quantifying their response to loading. The thesis thoroughly explored the electrical resistivity of ECC

materials. With 2-point probing measurements sensitive to contact impedance and DC methods vulnerable to material polarization, it was concluded that the most accurate method of measuring bulk resistivity of ECC materials was 4-point AC probing. Given the rate of polarization of ECC, it was determined that an AC frequency greater than 1 kHz minimizes the error introduced in the resistivity measurement due to material polarization. Another factor discovered to affect resistivity measurements was the hydration of the ECC material. Specifically, ECC materials exhibited significant variation in measured resistivity over the 35-days after casting. After one day, the resistivity of M-45 ECC was 150 kΩ-cm; after 35 days, the initial resistivity was found to be stable but roughly four times larger with a value of 600 kΩ-cm.

During the elastic tensile response of ECC, a linear piezoresistive behavior was discovered. This finding is consistent with the linear piezoresistivity discovered in other elastically loaded fiber reinforced cementitious materials (Chung 2003). For ECC materials, the gage factor of the material during its elastic response was found to be between 10 and 20. However, the introduction of dense fields of microcracks during strain hardening results in an inconsistent gage factor; gage factors experimentally determined during the strain hardening response regime range from 30 to 80. One reason identified for such variability is that the multi-point resistivity probing technique is effectively averaging the changes in resistivity due to strain and cracking across the volume between the probes.

The inconsistent resistivity measurement inherent to multi-point probing of strain hardened ECC are resolved by adopting electrical impedance tomography for conductivity measurement. To the author's knowledge, this thesis is the first time EIT has been applied to conductivity mapping in cementitious specimens. The method proved extremely powerful in yielding multi-dimensional maps (in the case of this thesis, two dimensional maps) of an ECC specimen conductivity. This was significant because it provides a distributed measurement of strain along with images of crack patterns within ECC structural elements. By exploring the application of EIT to ECC plates elastically loaded in tension, the EIT derived resistivity was determined to be linear as found

previously during 4-point probing. The gage factor determined from the EIT conductivity maps was approximately 15.

The conductivity maps determined for the plates loaded while in their strain hardening regime provided the location of micro-crack fields. The conductivity drop associated with micro-cracking was linearly correlated to the logarithmic of the crack width. At the end of the strain hardening regime, macro-scale cracks that localized were also observed in the EIT maps. Again, the drop in conductivity was correlated to the width of the larger cracks. For example, conductivity drops as large as 500 $nS\text{-}cm^{-1}$ were observed for cracks 2.5 mm wide. The observation of cracks were observed in a variety of test specimens including plates loaded in monotonic and cyclic tension, and for an unreinforced ECC beam loaded in 3-point bending. The EIT method of sensing conductivity offers a powerful method for distributed sensing in HPFRCC materials; such an approach is perfectly scaled to the local nature of cracking in cementitious materials.

Although the EIT method might appear applicable only to cementitious materials, the approach can be applied to other materials exhibiting changes in material conductivity to external stimulus. The universality of distributed sensing of multifunctional materials by EIT was illustrated using thin film sensing skins assembled from carbon nanotubes and polymers. These nanoengineered thin films were shown capable of sensing cracking in ECC materials. Furthermore, residual strain introduced in metallic test specimens was also illustrated. EIT conductivity maps were shown accurate in localizing the point of impact where residual damage was greatest.

7.3 Opportunities for Future's Research

While the thesis has set a foundation for the use of wireless sensors for monitoring HPFRCC structures, more work is needed to fully harness the tremendous potential of the technology. First, work is needed to explore the embedment of other data interrogation algorithms for automated data processing. While the damage index method has shown

promise for rapid detection of crack damage, more accurate damage detection algorithms could be explored for embedment. However, as algorithms grow in complexity, the computational limits (both computational throughput and memory) will be encountered. Hence, fundamental research in distributed computing and parallel data processing architectures are needed to maximize the collective computing resource distributed across the network.

In the area of distributed sensing by EIT, additional work is needed before the method can be deployed in operational structures. Specifically, data acquisition for the EIT analysis conducted in this thesis was manual and required significant time. Therefore, the next step in the development of distributed EIT sensing would be the creation of an automated data acquisition system that can take the repeated measurement of boundary voltages to applied currents. If the EIT data acquisition system can be created to record boundary data at a high rate, it is possible to continuously collect boundary current-voltage measurements leading to real-time EIT conductivity mapping. Therefore, the time evolution of crack fields can be produced. Furthermore, if the data acquisition can be designed to offer a wireless interface, then the extensive wiring that would be associated with boundary electrodes would be eliminated. To develop a wireless system, wireless sensor would have to be equipped with actuation channels to trigger the injection of AC currents into structural elements while the sensing interface of a wireless sensor measures boundary voltages.

In addition to advancing EIT data acquisition, future exploration of the application of EIT to cementitious structural elements is necessary. Specifically, this thesis only explored unreinforced test specimens. Realistically, HPFRCC structural components will employ some amount of steel reinforcement. The influence of steel reinforcement bars on the EIT method must be explored in detailed. Another extension of the EIT technique would be to image, in three-dimensions, cracking occurring within HPFRCC components. While the mathematical framework associated with EIT allows it to be applied in three dimensions, buried steel reinforcement and electrode installation still represent technical challenges to be solved.

It is unlikely that EIT conductivity maps alone will be sufficient for complete characterization of the mechanical behavior of instrumented HPFRCC specimens. Hence, the integration of EIT conductivity maps with other damage detection methods could improve the damage detection process. For example, damage index methods could be improved using information derived from EIT sensing. The shear damage index method proposed in Chapter 2 requires identification of when fiber pullout occurs. Since fiber pullout is correlated to the size of localized cracks, EIT maps imaging large cracks could be used to determine when fiber pullout has occurred and the use of the post-fiber pullout model is appropriate. Of course many other damage detection methods exist that could be combined with EIT conductivity maps to yield more accurate estimates of structural damage.

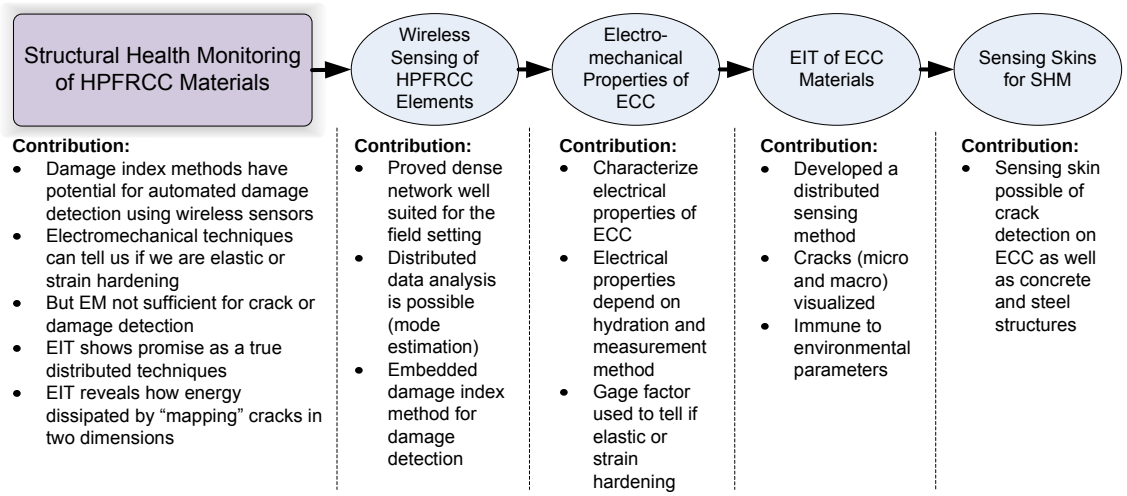

Figure 7-1: Overview of the major contributions of the thesis.

References

California Department of Transportation, 2001. *Caltrans Seismic Design Criteria*, Version 1.2, Caltrans, Sacramento, CA.

ACI-318., 2008. *Building Code Requirements for Structural Concrete and Commentary*, American Concrete Institute, Farmington Hills, MI.

ACI. 1998. *Cause, Evaluation and Repair of Cracks in Concrete Structures*. Report Number ACI224.1R-93, American Concrete Institute: Farmington Hills, MI.

Ali, A., and Wight, J. K., 1990. "Reinforced Concrete Structural Wall with Staggered Opening Configuration under Reversed Cyclic loading," Report Number ECE-8603624, National Science Fundation, Arlington, VA, 241.

Baker, L. E., 1989. "Principles of the Impedance Technique," *IEEE Engineering in Medicine and Biology Magazine*, **8**: 11-15.

Balaguru, P. N., and Shah, S. P., 1992. *Fiber-Reinforced Cement Composites*, McGraw-Hill: New York, NY.

Barber, D. C., and Brown, B. H., 1984. "Applied Potential Tomography," *Journal of Physics E: Scientific Instruments*, **17**: 723-733.

Barsoukov, E., and Macdonald, J. R., 2005. *Impedance Spectroscopy: Theory, Experiment, and Applications*, Wiley: Hoboken, NJ.

Borcea, L., 2002. "Electrical impedance tomography," *Inverse Problems*, **18**: R99-R136.

Brownjohn, J. M. W., Moyo, P., Omenzetter, P., and Lu, Y., 2003. "Assessment of Highway Bridge Upgrading by Dynamic Testing and Finite-Element Modal Updating," *Journal of Bridge Engineering*, **8**: 162-172.

Bryzek, J., 1996. "Impact of MEMS Technology on Society," *Sensors and Actuators A (Physical)*, **A56**: 1-9.

Bungey, J. H., Millard, S. G., and Grantham, M. G., 2006. *Testing of Concrete in Structures*. Taylor and Francis: london, UK.

Calleja, J., 1953. "Determination of Setting and Hardening Time of High-Alumina Cements by Electrical Resistance Techniques," *Journal of American Concrete Institute*, **25**: 249-256.

Canbolat, B. A., Parra-Montesinos, G. J., and Wight, J. K., 2004. "Seismic Behavior of High-Performance Fiber Reinforced Cementitious Composite Beams," Report Number UMCEE 04-11, University of Michigan, MI.

Caner, A., and Zia, P., 1998. "Behavior and Design of Link Slab for Jointless bridge Decks," *PCI Journal*, **43**: 68-80.

Cao, J., and Chung, D. D. L., 2004. "Electric polarization and depolarization in cement-based materials, studied by apparent electrical resistance measurement," *Cement and Concrete Research*, **34**: 481-485.

Carino, N. J., 2004. "Stress Wave Propagation Methods," *Handbook on Nondestructive Testing of Concrete*, (eds. Malhotra V. M. and Carino N. J.), CRC Press: Boca Raton, FL.

Casciati, F., Faravelli, L., and Borghetti, F., 2003. "Wireless Links between Sensor-Device Control Stations in Long Span Bridges," *Proceedings of SPIE - Smart Structures and Materials: Smart Systems and Nondestructive Evaluation*, **5057**: 1-7.

Celebi, M., 2002. "Seismic instrumentation of buildings (with emphasis on federal buildings)," *United States Geological Survey Report No. 0-7460-68170*, USGS, Menlo Park, CA.

Celebi, M., Sanli, A., Sinclair, M., Gallant, S., and Radulescu, D., 2004. "Real-Time Seismic Monitoring Needs of a Building Owner and the Solution: A Cooperative Effort," *Earthquake Spectra*, **20**: 377-394.

Cheng, K. S., Isaacson, D., Newell, J. C., and Gisser, D. G., 1988. "Error Comparison for Different Current Patterns in Electrical Impedance Imaging," *Proceedings of the 10th International Conference of the IEEE Engineering in Medicine and Biology Society*, **1**: 279-280.

Chung, D. D. L., 2001. "Cement-Based Electronics," *Journal of Electroceramics*, **6**: 75-88.

Chung, D. D. L., 2003. *Multifunctional Cement-Based Materials*, Marcel-Dekker: New York, NY.

Clayton, E. H., Lu, C., Koh, B. H., Xing, G., and Fok, C. L., 2005. "Damage Detections and Correlation-Based Localization Using Wireless Mote Sensors," *Proceedings of the 20th IEEE International Symposium on Intelligent Control, ISIC '05 and the 13th Mediterranean Confenence on Control and Altomation, MED '05*, Limassol, Cyprus, 304-309.

Decher, G., and Schlenoff, J. B., 2003. *Multilayer Thin Films: Sequential Assembly of nanocomposite Materials*, Wiley-VCH: Federal Republic of Germany.

Doebling, S. W., Farrar, C. R., and Prime, M. B., 1998. "A Summary Review of Vibration-Based Damage Identification Methods," *Shock and Vibration Digest*, **30**: 91-105.

Doebling, S. W., Farrar, C. R., Prime, M. B., and Shevitz, D. W., 1996. "Damage Identification and Health Monitoring of Structural and Mechanical Systems from Changes in their Vibration Characteristics: A Literature Review," *Report # LA-13070-MS*, Los Alamos National Laboratory, Los Alamos, NM.

Du, Y., Clark, L. A., and Chan, A. H. C., 2007. "Impact of reinforcement corrosion on ductile behavior of reinforced concrete beams," *ACI Structural Journal*, **104**: 285-293.

Fu, X., Ma, E., Chung, D. D. L., and Anderson, W. A., 1997. "Self-monitoring in carbon fiber reinforced mortar by reactance measurement," *Cement and Concrete Research*, **27**: 845-852.

Gower, K. R., and Millard, S. G., 1999. "Measurement of Concrete Resistivity for Assessment of Corrosion Severity of Steel Using Wenner Technique," *ACI Materials Journal*, **96**: 536-541.

Hammond, E., and Robson, T. D., 1955. "Comparison of Electrical Properties of Various Cements and Concrete," *The Engineer*, **199**: 114-115.

Han, N., van Beek, A., and Koenders, E. A. B., 2005. "Elastic Methods," *Advanced Testing of Cement Based Materials during Setting and Hardening - Final Report of RILEM TC 185-ATC*, (Reinhardt, H. W. and Grosse, C. U., eds.) Technical Report 31, RILEM: Bagneux, France.

Hansen, T. M., Stokbro, K., Hansen, O., Hassenkam, T., Shiraki, I., Hasegawa, S., and Boggild, P., 2003. "Resolution Enhancement of Scanning Four-Point Probe Measurement on Two-Dimensional Systems," *Review of Scientific Instruments*, **74**: 3701-3708.

Hansson, I. L. H., and Hansson, C. M., 1983. "Electrical Resistivity Measurement of Portland Cement Based Materials," *Cement and Concrete Research*, **13**: 675-683.

Hasegawa, S., Shiraki, I., Tanikawa, T., Petersen, C. L., Hansen, T. M., Boggild, P., and Grey, F., 2002. "Direct Measurement of Surface-State Conductance by Microscopic Four-Point Probe Method," *Journal of Physics: Condensed Matter*, **14**: 8379-8392.

Holder, D. S., 2005. *Electrical Impedance Tomography - Method, History and Applications*, IOP: Bristol and Philadelphia.

Hou, T. C., Loh, K. J., and Lynch, J. P., 2007a. "Electrical Impedance Tomography of Carbon Nanotube Composite Materials," *Proceedings of SPIE - The International Society for Optical Engineering: Sensors and Smart Structures Technologies for Civil, Mechanical, and Aerospace Systems*, San Diego, **6529**: 65529-1-10.

Hou, T. C., Loh, K. J., and Lynch, J. P., 2007b. "Spatial conductivity mapping of carbon nanotube composite thin films by electrical impedance tomography for sensing applications," *Nanotechnology*, **18**: 315501.

Hou, T. C., and Lynch, J. P., 2005a. "Conductivity-Based Monitoring and Damage Characterization of Fiber Reinforced Cementitious Structural Components," *Proceedings of the SPIE - The International Society for Optical Engineering*, **5765**: 419-429.

Hou, T. C., and Lynch, J. P., 2005b. "Monitoring Strain in Engineered Cementitious Composites Using Wireless Sensors," *Proceedings of the 11th International Conference on Fracture*, Turin, Italy,

Hyman, A. E., 2005. "Inspection, repair and rehabilitation of concrete structures due to corrosion," *International Journal of Materials & Product Technology*, **23**: 309-337.

Jarvenpaa, S., 1996. *A Finite Element Model for the Inverse Conductivity Problem*. Phil. Lic. Thesis, University of Helsinki, Finland.

Kang, I., Schulz, M. J., Kim, J. H., Shanov, V., and Shi, D., 2006. "A Carbon Nanotube Strain Sensor for Structural health Monitoring," *Smart Materials and Structures*, **15**: 737-748.

Kim, Y. Y., Fischer, G., and Li, V. C., 2004. "Performance of Bridge Deck Link Slabs Designed with Ductile Engineered Cementitious Composites," *ACI Structural Journal*, **101**: 792-801.

Kratzig, W. B., Meyer, I. F., and Meskouris, K., 1989. "Damage Evolution in Reinforced Concrete Members Under Cyclic Loading," *Proceedings of the 5th International Conference on Structural Safety and Reliability*, San Francisco, CA, 795-802.

Kunieda, M., and Rokugo, K., 2006. "Recent Progress on HPFRCC in Japan Required Performance and Applications," *Journal of Advanced Concrete Technology*, **4**: 19-33.

Lauer, K. R., 2004. "Magnetic/Electrical Methods," *handbook on Nondestructive Testing of Concrete*, (Malhotra, V. M. and Carino, N. J. eds.), CRC Press, Boca Raton, FL.

Lecompte, D., Vantomme, J., and Sol, H., 2006. "Crack Detection in a Concrete Beam Using Two Different Camera Techniques," *Structural Health Monitoring*, **5**: 59-68.

Levenberg, K., 1944. "A method for the solution of certain problems in least squares," *SIAM Journal of Numerical Analysis*, **16**: 588-604.

Li, H., Xiao, H. G., and Qu, J. P., 2006. "Effects of Compressive Strain on Electrical Resistivity of Carbon Black-Filled Cement-Based Composites," *Cement and Concrete Composites*, **28**: 824-828.

Li, V. C., 2003a. "Durable Overlay Systems with Engineered Cementitious Composites (ECC)," *International Journal for Restoration of Buildings and Monuments*, **9**: 1-20.

Li, V. C., 2003b. "On Engineered Cementitious Composites (ECC) - A Review of the Material and Its Applications," *Journal of Advanced Concrete Technology*, **1**: 215-230.

Li, V. C., Lepech, M., Li, M., Lynch, J. P., and Hou, T. C., 2005. "Field Demonstration of Durable Link Slabs for Jointless Bridge Decks Based on Strain-Hardening

Cementitious Composites," *Research Report RC-1471*, Michigan Department of Transportation, Lansing, MI.

Li, V. C., Wang, S., Ogawa, A., and Saito, T., 2002. "Interface Tailoring for Strain Hardening PVA-ECC," *ACI Materials Journal*, **99**: 463-472.

Li, V. C., Wang, S., and Wu, C., 2001. "Tensile Strain-Hardening Behavior of Polyvinyl Alcohol Engineered Cementitious Composite (PVA-ECC)," *ACI Materials Journal*, **95**: 483-492.

Loh, C. H., Lynch, J. P., Lu, K. C., Wang, Y., and Lin, P. Y., 2008. "Model Identification of a Cable-Stay Bridge Using Wireless Output-Only Monitoring Systems," *Engineering Structures*, (accepted and in press).

Loh, K. J., Kim, J., Lynch, J. P., Kam, N. W. S., and Kotov, N. A., 2007a. "Multifunctional layer-by-layer carbon nanotube-polyelectrolyte thin films for strain and corrosion sensing," *Smart Materials and Structures*, **16**: 429-438.

Loh, K. J., Lynch, J. P., Shim, B. S., and Kotov, N. A., 2007b. "Tailoring Piezoresistive Sensitivity of Multilayer Carbon Nanotube Composite Sensors," *Journal of Intelligent Material Systems and Structures*, **at press**:

Lynch, J. P., 2002. *Decentralization of Wireless Monitoring and Control Technologies for Smart Civil Structures*. Ph.D. Thesis, Department of Civil and Environmental Engineering, Stanford University, Palo Alto, CA.

Lynch, J. P., 2007. "An Overview of Wireless Structural Health Monitoring for Civil Structures," *Philosophical Transactions of the Royal Society of London. Series A*, Mathematical and Physical Science, The Royal Society, London, 365(1851): 345-372.

Lynch, J. P., and Loh, K. J., 2006. "A Summary Review of Wireless Sensors and Sensor Networks for Structural Health Monitoring," *Shock and Vibration Digest*, **38**: 91-128.

Lynch, J. P., Sundararajan, A., Law, K. H., Kiremidjian, A. S., and Carryer, E., 2004. "Embedding damage detection algorithms in a wireless sensing unit for attainment of operational power efficiency," *Smart Materials and Structures*, **13**: 800-810.

Lynch, J. P., Wang, Y., Loh, K. J., Yi, J. H., and Yun, C. B., 2006. "Performance Monitoring of the Geumdang Bridge Using A Dense Network of High-Resolution Wireless Sensors," *Smart Materials and Structures*, **15**: 1561-1575.

MacGreger, J. G., and Wight, J. K., 2005. *Reinforced concrete : mechanics and design 4th ed.*, Upper Saddle River, NJ : Prentice-Hall.

Marquardt, D., 1963. "An algorithm for least squares estimation of nonlinear parameters," *SIAM Journal of Applied Mathematics*, **11**: 431-441.

Mayer, J. W., and Lau, S. S., 1990. *Electronic Materials Science: For Integrated Circuits in Si and GaAs*, Macmillan: New York, NY.

McCarter, W. J., and Afshar, A. B., 1984. "Some aspects of the electrical properties of cement paste," *Journal of Material Science Letters*, **3**: 1083-1086.

McCarter, W. J., and Afshar, A. B., 1985. "Futher studies of the early hydration of Portland cement paste," *Journal of Material Science Letters*, **4**: 405-408.

McCarter, W. J., and Brousseau, R., 1990. "The A.C. Response of Hardened Cement Paste," *Cement and Concrete Research*, **20**: 891-900.

Mehanny, S. F., and Deierlein, G. G., 2001. "Seismic Damage and Collapse Assessment of Composite Moment Frames," *Journal of Structural Engineering*, **127**: 1045-1053.

Millard, S. G., 1991. "Reinforced Concrete Resistivity Measurement Techniques," *Proceedings of the Institution of Civil Engineers, Part 2: Research and Theory*, **91**: 71-88.

Mindess, S., 2004. "Acoustic Emission Methods," *Handbook on Nondestructive Testing of Concrete*, (eds. Malhotra V. M. and Carino N. J), CRC Press: Boca Raton, FL.

Mita, A., and Takahira, S., 2004. "Damage Index Sensor for Smart Structures," *Structural Engineering and Mechanics*, **17**: 331-346.

MnDOT. 2007. *Interstate 35W Mississippi River Bridge Fact Sheet*, http://www.dot.state.mn.us/i35wbridge/pdfs/factsheet.pdf (accessed on: August 21, 2007).

Moore, M. E., Phares, B. M., Graybeal, B. A., Rolander, D. D., and Washer, G. A., 2001. *Reliability of Visual Inspection for Highway Bridge*, Report # FHWA-RD-01-020, Federal Highway Administration, Washington D.C.

Murai, T., and Kagawa, Y., 1985. "Electrical Impedance Computed Tomography Based on a Finite Element Model," *IEEE Transactions on Biomedical Engineering*, **BME-32**: 177-184.

Naaman, A. E., 1987. "High-Performance Fiber Reinforced Cement Composites," *Concrete Structures for the Future, IABSE Symposium*, Zurich, Germany, 371-376.

Naaman, A. E., 1998. "Fiber reinforced cement composites: characterization, properties, and applications," *Proceedings of Advanced Concrete Technology Workshop*, Holderbank, Switzerland,

Naaman, A. E., 2003. "Engineered Steel Fibers with Optimal Properties for Reinforcement of Cement Composites," *Journal of Advanced Concrete Technology*, **1**: 241-252.

Naaman, A. E., and Chandrangsu, K., 2004. "Innovative Bridge Deck System Using High-performance Fiber-Reinforced Cement Composites," *ACI Structural Journal*, **101**: 57-64.

Naaman, A. E., and Reinhardt, H. W., 1996. "Characterization of high performance fiber reinforced cement composites-HPFRCC," *Proceedings of the 2nd International RILEM Workshop: HPFRCC*, 1-23.

Nagayama, T., Spencer Jr., B. F., and Rice, J. A., 2007. "Structural Health Monitoring Utilizing Intel's Imote2 Wireless Sensor Platform," *Proceedings of SPIE--Sensors and Smart Structures Technologies for Civil, Mechanical, and Aerospace Systems*, **6529(2)**: 6592943.

Narenda, N. K., and Mehra, R. K., 1974. "Computational aspects of maximum likelihood estimation and reduction in sensitivity function calculation," *IEEE Transactions on Automatic Control*, **AC-19**: 774-783.

Pakzad, S. N., Fenves, G. L., Kim, S. B., and Culler, D. E., 2008. "Design and Implementation of Scalable Wireless Sensor Network for Structural Monitoring," *Journal of Infrastructure Systems*, **14**: 89-101.

Park, G., Cudney, H. H., and inman, D. J., 2000. "Impedance-Based Health Monitoring of Civil Structural Components," *Journal of Infrastructure Systems*, **6**: 153-160.

Park, S., Ahmad, S., Yun, C. B., and Roh, Y., 2006. "Multiple Crack Detection of Concrete Structure using Impedance-Based Structural Health monitoring Techniques," *Experimental Mechanics*, **46**: 609-618.

Park, Y. J., and Ang, A. H. S., 1985. "Mechanistic Seismic Damage Model for Reinforced Concrete," *Journal of Structural Engineering*, **111**: 722-739.

Parra-Montesinos, G. J., 2003. "HPFRCC in Earthquake-Resistant Structures: Current Knowledge and Future Trends," *High Performance Fiber Reinforced Cement Composites (HPFRCC 4)*, Edited by A. E. Naaman and H. W. Reinhardt, RILEM Publications, France, 453-472.

Parra-Montesinos, G. J., 2005. "High-Performance Fiber-Reinforced Cement Composites: An Alternative for Seismic Design of Structures," *ACI Structural Journal,* **102**: 668-675.

Paulson, K., Breckon, W., and Pidcock, M. K., 1992. "Electrode Modeling in Electrical Impedance Tomography," *SIAM Journal of Applied Mathematics,* **52**: 1012-1022.

Peeters, B., and Ventura, C. E., 2003. "Comparative Study of Modal Analysis Techniques for Bridge Dynamic Characteristics," *Mechanical Systems and Signal processing*, **17**: 965-988.

Peled, A., Torrent, J. M., Mason, T. O., Shah, S. P., and Garboczi, E. J., 2001. "Electrical Impedance Spectra to Monitor Damage during Tensile Loading of Cement Composites," *ACI Materials Journal*, **98**: 313-322.

Perry, C. C., and Lissner, H. R., 1962. *The Strain gage Primer*, McGraw-Hill: New York, NY.

Pidcock, M. K., Kuzuoglu, M., and Leblebicioglu, K., 1995a. "Analytic and Semi-Analytic Solutions in Electrical Impedance Tomography. II. Two-Dimensional Problems," *Physiological Measurement*, **16**: 91-110.

Pidcock, M. K., Kuzuoglu, M., and Leblebicioglu, K., 1995b. "Analytic and Semi-Analytic Solutions in Electrical Impedance Tomography: I. Two-Dimensional Problems," *Physiological Measurement*, **16**: 77-90.

Quyang, C., landis, E., and Shah, S. P., 1991. "Damage Assessment in Concrete Using Quantitative Acoustic Emission," *Journal of Engineering Mechanics,* **17**: 2681-2698.

Raghavan, A., 2007. *Guided-Wave Structural Health Monitoring*. Ph.D. Thesis, The University of Michigan, Ann Arbor, Michigan.

Reddy, J. N., 1993. *An Introduction to the Finite Element Method*, McGraw-Hill: New York, NY.

Reza, F., Yamamuro, J. A., Batson, G. B., and Lee, J. S., 2003. "Smart Behavior of Carbon Fiber Cement Composites in Compact Tension," *Proceedings of the 16th ASCE Engineering Mechanics Conference*, Seattle, WA,

Rose, J. L., 2002. "A baseline and Vision of Ultrasonic Guided Wave Inspection Potential," *Transactions of the ASME Journal of Pressure Vessel Technology*, **124**: 273-282.

Ruiz-Sandoval, M., Spencer Jr., B. F., and Kurata, N., 2003. "Development of a High Sensitivity Accelerometer for the Mica Platform," *Proceedings of the 4th International Workshop on Structural health Monitoring*, 1027-1034.

Sahmaran, M., and Li, V. C., 2008. "Durability of mechanically loaded engineered cementitious composites under highly alkaline environments," *Cement and Concrete Research*, **30**: 72-81.

Saito, R., Dresselhaus, G., and Dresselhaus, M. S., 2004. *Physical Properties of Carbon Nanotubes*, Imperial College Press (ICP): London, UK.

Shah, S. P., and Choi, S., 1999. "Nondestructive Techniques for Studying Fracture Processes in Concrete," *International Journal of Fracture*, **98**: 351-359.

Shinozuka, M., 2003. "Homeland Security and Safety," *Proceedings of Structural Health Monitoring and Intelligent Infrastructure*, Tokyo, Japan, **2**: 1139-1145.

Skakalova, V., Dettlaff-Weglikowska, U., and Roth, S., 2005. "Electrical and Mechanical Properties of nanocomposites of Single Wall Carbon Nanotubes with PMMA," *Synthetic Metals*, **152**: 349-352.

Smits, F. M., 1958. "Measurement of Sheet Resistivities with the Four-Point Probe," *Bell System Technical Journal*, **37**: 711-718.

Sohn, H., and Farrar, C. R., 2001. "Damage Diagnosis Using Time-Series Analysis of Vibrating Signals," *Journal of Smart Materials and Structures*, **10**: 446-451.

Sohn, H., Farrar, C. R., Hemez, F. M., Czarnecki, J. J., Shunk, D. D., Stinemates, D. W., and Nadler, B. R., 2004. "A Review of Structural Health Monitoring Literature:

1996-2001," *Report # LA-13976-MS*, Los Alamos National Laboratory, Los Alamos, NM.

Somersalo, E., Cheney, M., and Isaacson, D., 1992. "Existence and Uniqueness for Electrode Models for Electric Current Computed Tomography," *SIAM Journal of Applied Mathematics*, **52**: 1023-1040.

Stang, H., and Pedersen, C., 1996. "HPFRCC - Extruded Pipes," *Proceedings of the 4th Materials Engineering Conference*, Washington, D. C.,

Straser, E. G., and Kiremidjian, A. S., 1998. *A Modular, Wireless Damage Monitoring System for Structures*. John A. Blume Earthquake Engineering Center, Stanford University, Stanford, CA.

Thomsen, J. H., and Wallace, J. W., 1995. "Displacement-Based Design of RC Structural Walls: Experimental Studies of Walls with Rectangular and T-Shaped Cross Sections," Report Number CU/CEE-95/06, Department of Civil and Environmental Engineering, Clarkson University, Potsdam, NY, 353.

Thostenson, E. T., and Chou, T. W., 2006. "Carbon Nanotube Networks: Sensing of Distributed Strain and Damage for Life Prediction and Self Healing," *Advanced Materials*, **18**: 2837-2841.

Toussaint, E., Destrebecq, J. F. O., and Grediac, M., 2005. "A Detailed Study of Crack Propagation in Cement-Based Fiber Composite Beams under Bending," *Cement and Concrete Composites*, **27**: 399-411.

Valentini, L., Mengoni, F., Armentano, I., Kenny, J. M., Ricco, L., Alongi, J., Trentini, M., Russo, S., and Mariani, A., 2006. "Enhancement of Photoelectrical Properties in Polymer Nanocomposites Containing Modified Single-Walled Carbon Nanotubes by Conducting Dendrimer," *Journal of Applied Physics*, **99**: 114305.

Vauhkonen, M., 1997. *Electrical Impedance Tomography and Prior Information*. Ph.D. Thesis, Kuopio University, Kuopio, Finland.

Vilhunen, T., Kaipiom, J. P., Vauhkonen, P. J., Savolainen, T., and Vauhkonen, M., 2002. "Simultaneous Reconstruction of Electrode Contact Impedance and Internal Electrical Properties: I. Theory," *Measurement Science and Technology*, **13**: 1848-1854.

Wang, Y., Lynch, J. P., and Law, K. H., 2005. "Wireless Structural Sensors Using Reliable Communication Protocols for Data Acquisition and Interrogation," *Proceedings of the International Modal Analysis Conference (IMAC-XXIII)*, Orlando, FL,

Wang, Y., Lynch, J. P., and Law, K. H., 2007. "A Wireless Structural Health Monitoring System with Multithreaded Sensing Devices: Design and Validation," *Structure and Infrastructure Engineering*, **3**: 103-120.

Webster, J. G., 1990. *Electrical Impedance Tomography*, Hilger: Bristol, England.

Whiting, D. A., and Nagi, M. A., 2003. *Electrical Resistivity of Concrete - A Literature Review*. PCA R&D Serial No. 2457, Portland Cement Association, Skokie, IL.

Wight, J. K., Parra-Montesinos, G. J., and Canbolat, A., 2006. "HPFRCC Coupling Beams for Earthquake-Resistant Wall Structures," *Proceedings of the IABSE Symposium on Structures and Extreme Events*, Lisbon, Portugal, 114-115.

Woo, E. J., Hua, P., Webster, J. G., and Tompkins, W. J., 1994. "Finite Element Method in Electrical Impedance Tomography," *Medical & Biological Engineering & Computing*, **32**: 530-536.

Xu, M. W., Hantschel, T., and Vandervorst, W., 2002. "Three-Dimensional Carrier Profiling of InP-Based Devices Using Scanning Spreading Resistance Microscopy," *Applied Physics Letters*, **81**: 177-179.

Yorkey, T. J., Webster, J. G., and Tompkins, W. J., 1987. "Comparing Reconstruction Algorithms for Electrical Impedance Tomography," *IEEE Transactions on Biomedical Engineering*, **BME-34**: 843-852.

Yu, H., Cao, T., Zhou, L., Gu, E., Yu, D., and Jiang, D., 2006. "Layer-by-Layer Assembly and Humidity Sensitive Behavior of Poly(ethyleneimine)/Multiwall Carbon nanotube Composite Films," *Sensors and Actuators*, **119**: 512-515.

Zhang, W., Suhr, J., and Koratkar, N., 2006. "Carbon Nanotube/polycarbonate Composites as Multifunctional Strain Sensors," *Journal of Nanoscience and Nanotechnology*, **6**: 960-964.

Zhdanov, M. S., and Keller, G. V., 1994. *Geoelectrical Methods in Geophysical Exploration*, Elsevier: Amsterdam.